# Studies of Electron Ionization

**Natalie Anne Love**

**University College London**

**Thesis submitted for the**

**degree of Doctor of Philosophy**

**2005**





ProQuest LLC
789 East Eisenhower Parkway
P.O. Box 1346
Ann Arbor, MI 48106-1346

*To Mum and Dad*

# Acknowledgments

I would like to begin by thanking my supervisor, Steve Price, for his dedication to helping me improve my scientific understanding and written work. His help in both my undergraduate and postgraduate years has been invaluable. I would also like to thank members of the physical chemistry group, past and present, for being great listeners, readers and most importantly friends. Without of course forgetting to thank all the technical staff in the workshops for their expertise in helping me solve design problems and fix those inevitable breakages!

I would also like to say a special thank you to my Mum and Dad for their never failing love and support, and a space on the coffee table to have this thesis on permanent display. I would also like to thank Dominic for his great support and for keeping me on the ground when everything seemed too much.

# Publications

The following publications are based on the work discussed in this thesis;

"The formation of boron containing fragment ions from the ionization of $BCl_3$", Natalie. A. Love and Stephen. D. Price, *International Journal of Mass Spectrometry* **233,** 145 (2004).

"Electron ionization of $N_2O$", Natalie. A. Love and Stephen. D. Price, *Physical Chemistry Chemical Physics* **6,** 4558 (2004).

# Abstract

This thesis presents the results of experimental investigations to determine the electron ionization cross-sections of gases used in plasma etching processes. The small molecules studied include boron trichloride ($BCl_3$), nitrous oxide ($N_2O$), sulphur hexafluoride ($SF_6$) and acetylene ($C_2H_2$). The knowledge of accurate electron ionization cross-sections is essential for the modelling and optimization of plasmas used in industry and for the purposes of atmospheric modelling. It is therefore surprising that despite the widespread industrial use of these small molecules there have been few investigations of their ionization. It is the lack of available electron ionization cross-section data that provides the motivation for the investigations detailed in this thesis.

The formation and dissociation of singly charged (monocations), doubly charged (dications) and triply charged molecular ions (trications) are studied using pulsed electron ionization (30-200 eV) coupled with time-of-flight (TOF) mass spectrometry and a two-dimensional (2D) ion coincidence technique. The experimental technique and data analysis procedures adopted allow the contribution to the total ion yield from single and multiple ionization to be distinguished and quantified. Such information yields relative partial ionization cross-sections (PICSs) and also allows relative precursor specific PICSs to be determined, which quantify the contribution from single, double and triple ionization to the relative yields of the fragment ions formed following electron-molecule collisions. Relative precursor specific PICSs therefore provide a more 'in-depth' chemical picture of each PICS. The relative precursor specific PICSs determined, following electron interaction with $N_2O$, provide clear evidence of energetic ion loss in previous cross-section determinations detailed in the literature. In addition, the 2D ion coincidence technique provides information on the energetics involved in the dissociation of any multiply charged ions formed. In the case of $BCl_3$, further insight on the possible dissociation dynamics of $BCl_3^{2+}$ is reported.

Following the investigations of $N_2O$, $BCl_3$ and $SF_6$, the apparatus was commissioned to produce absolute partial ionization cross-sections and absolute precursor specific partial ionization cross-sections from 30-200 eV. Experimentally, the commissioning involved the addition of a Spinning Rotor Gauge (SRG) and a new gas inlet line to the source region. These investigations have extended the data determined for the electron ionization of $N_2O$ and have also enabled the absolute cross-section data for the electron ionization of $C_2H_2$ to be determined.

# Contents


## Chapter 1 7

### Introduction

1.1 Background 7

1.2 Laboratory techniques for forming positive ions in mass spectrometry 10

1.3 Product ions 14

1.4 Electron Ionization Cross-Sections 24

1.5 Theoretical determination of electron ionization cross-sections 32

1.6 Other experimental methods to study ionization 34

1.7 Summary 39

1.8 References 40

## Chapter 2 48

### Experimental Details

Section 1 Experimental Arrangement

2.1 Introduction 48

2.1.1 Time-of-flight mass spectrometry 49

2.1.2 Data Sets 57

2.1.3 Conclusions 68

Section 2 Commissioning an absolute cross-section measurement technique

2.2 Introduction 69

2.2.1 Normalization techniques – absolute PICSs 71

2.2.2 New gas inlet system 72

2.2.3 Pressure measurements 74

2.2.4 Experimental Procedure 84

2.2.5 Conclusions 84

2.3 References 85

# Chapter 3 86

## Data Collection and Data Analysis

### Section 1 Relative Partial Ionization Cross-Sections

3.1 Introduction 86

3.1.1 Partial ionization cross-section determination 86

3.1.2 Relative partial ionization cross-section determination 99

3.1.3 Relative precursor specific partial ionization cross-section determination 102

3.1.4 Kinetic energy release determination 103

3.1.5 Review of errors 108

3.1.6 Conclusions 113

### Section 2 Absolute Partial Ionization Cross-Sections

3.2 Introduction 114

3.2.1 Argon and Nitrogen 114

3.2.2 Gas pressure in the source region 119

3.2.3 Summary 124

3.2.4 Absolute precursor specific partial ionization cross-section determination 124

3.2.5 Further improvements 126

3.2.6 Review of Errors 127

3.2.7 Conclusions 128

3.3 References 123

# Chapter 4 132

## Electron Ionization of $N_2O$

4.1 Introduction 132

4.2 Experimental Procedures 133

4.3 Data Analysis 134

4.4 Relative PICSs 138

4.5 Energetic ion loss 140

4.6 Discussion 142

4.7 Conclusions 154
4.8 References 156

**Chapter 5** **158**

**Electron Ionization of $BCl_3$**

5.1 Introduction 158
5.2 Experimental Procedures 159
5.3 Data Analysis 160
5.4 Relative PICSs 164
5.5 Discussion 165
5.6 Conclusions 173
5.7 References 174

**Chapter 6** **176**

**Electron Ionization of $SF_6$**

6.1 Introduction 176
6.2 Experimental Procedures 178
6.3 Data Analysis 179
6.4 Relative PICSs 184
6.5 Discussion 186
6.6 Conclusions 205
6.7 References 206

**Chapter 7** **208**

**Absolute Electron Ionization Cross-Sections of $N_2O$ and $C_2H_2$**

7.1 Introduction 208

Electron Ionization of $N_2O$

7.2 Introduction 209
7.3 Experimental procedures 210
7.4 Data Analysis 210

Electron Ionization of $C_2H_2$

7.5 Introduction 220

7.6 Experimental procedures 221

7.7 Data Analysis 222

7.8 Discussion 228

7.9 Overall Conclusions 236

7.10 References 237

**Chapter 8** **239**

Further Work

**Appendices** **242**

Appendix A 242

Appendix B 245

Appendix C 248

Appendix D 252

Appendix E 255

Appendix F 260

Appendix G 264

Appendix H 267

Appendix I 273

# Chapter 1

# Introduction

## 1.1 Background

This thesis presents the results of experimental investigations to determine the electron ionization cross-sections of gases used in plasma etching processes. In this work, the emphasis is placed on quantifying the contribution from single, double and triple ionization to the total ion yield.

Electron ionization of molecules occurs within many environments including plasmas and planetary atmospheres.[1,2] Knowledge of the electron ionization cross-sections, including partial ionization cross-sections (PICSs), is essential when trying to understand the electron induced processes occurring in such environments. PICSs provide information on the identity and abundance of the different charged species formed in ionizing electron-molecule collisions. The production of accurate PICSs is therefore vital for the modelling and optimization of plasmas used in industry and for the purposes of atmospheric modelling.

As mentioned above, PICSs are important as they provide information on the identity and abundance of the different charged species formed in ionizing electron-molecule collisions. To identify the products formed following ionization events a mass spectrometer is required. In using a mass spectrometer to produce accurate PICS measurements the apparatus must be able to detect all ions, regardless of their mass or initial kinetic energy, with equal efficiency. Some earlier experiments used to determine PICSs did not efficiently detect energetic fragment ions formed by dissociative multiple ionization.[3-6] It has therefore been widely recognised that the reliability of some earlier PICS determinations is questionable.[7,8] Indeed, the contribution to the total ion yield from multiple ionization was then thought to be of little importance and was thus often recognised but ignored.[2] Recent studies of the electron ionization cross-sections of small molecules have shown that dissociative multiple ionization can contribute significantly to fragment ion yields.[4,9-11] For example, following electron ionization of the chlorine molecule, at electron energies above 50 eV, the yield of fragment ions from multiple ionization is comparable with the yield of fragment ions from single ionization.[9] Specifically, at 100 eV dissociative

multiple ionization represented 26% of the total fragment ion yield following electron ionization of chlorine. Therefore, to obtain accurate PICS data, the contribution from energetic fragment ions cannot be neglected. Consequently, earlier PICS determinations produced using experimental apparatus where the problem of inefficient energetic ion detection was not addressed, often underestimated the true PICS for fragment ions. Appreciation of the shortcomings of previous work has led to renewed activity in the area of PICS determinations over the last decade.[12-16] However, in spite of this increased interest, there still remain significant gaps in the availability of accurate electron ionization cross-sections, even for small molecules. Indeed, even where there are several PICS data sets determined for certain molecules, the agreement between these data sets often varies and, in some cases, all data sets for the same molecule disagree.

With the continued growth in the semiconductor and related industries, the demand for accurate electron ionization cross-sections for a large variety of gases used in the feed gas mixtures for plasma etching applications continues to increase.[2,17-19] A recent report from the National Research Council addressing the 'Database Needs for Modeling and Simulation of Plasma Processing',[20] highlights the lack of reliable PICSs for molecules such as $N_2O$. It is the lack of reliable and available PICSs for the ionization of many molecules used in technologically important plasmas, and those molecules abundant in planetary atmospheres, that provide the clear motivation for the investigations discussed in this thesis. This thesis details the determination of relative PICSs for the formation of fragment ions following electron ionization of nitrous oxide ($N_2O$), boron trichloride ($BCl_3$) and sulphur hexafluoride ($SF_6$). PICSs are determined by simultaneously recording mass and two-dimensional (2D) ion-ion coincidence spectra, as a function of ionizing electron energy from 30-200 eV. The data analysis procedure adopted in this thesis allows the contribution to the total ion yield from single and multiple ionization to be distinguished and quantified. Specifically, the contribution from single, double and triple ionization, to the relative yields of the fragment ions formed following electron-molecule collisions is determined. These cross-sections are termed precursor specific PICSs. The ability to determine the individual components of the PICS for the formation of a particular fragment ion provides a more in-depth chemical picture of each PICS.

The shape of the ion pair peaks produced from the data recorded by the 2D ion-ion coincidence technique can also be interpreted to yield an estimate of the kinetic

energy released upon fragmentation of the multiply charged ion. Such kinetic energy releases (KER) can be used to estimate the energy of the electronic state of the multiply charged ion that dissociated to yield the fragments of interest. Where comparison is available, KER estimates produced in this way generally agree well with values produced by photoionization coincidence techniques,[21] and more sophisticated methods, such as Doppler-free KER (DFKER) spectroscopy[22,23] and threshold photoelectrons coincidence (TPEsCO) spectroscopy.[24,25]

The development of quantitative theoretical descriptions of the chemistry occurring in environments such as plasmas and planetary atmospheres generally requires absolute electron ionization cross-section data. It is therefore useful to be able to provide a complete set of electron ionization cross-sections on an absolute scale from a single laboratory. One of the aims of this thesis was to enable the determination of absolute PICSs and absolute precursor specific PICSs, as opposed to relative ionization cross-sections. To obtain absolute electron ionization cross-sections it was necessary to modify the experimental apparatus, these modifications are detailed in Chapter 2. Following this apparatus modification, absolute PICSs and absolute precursor specific PICSs for the fragment ions formed following electron ionization of $N_2O$ and $C_2H_2$ were determined, and are discussed in Chapter 7.

This thesis uses a time-of-flight (TOF) mass spectrometer, coupled with a 2D ion-ion coincidence technique to investigate the electron ionization of $N_2O$, $BCl_3$, $SF_6$ and $C_2H_2$ from 30-200 eV. This experimental technique enables the single product ions, pairs of product ions or three product ions formed following ionization of the individual target molecules to be detected, identified and quantified. The experimental apparatus and methodology are described in Chapter 2. The procedures used to analyse the experimental data are discussed in detail in Chapter 3. The remainder of this thesis (Chapters 4-7) presents the results of the experimental work, and a discussion of the results for each target molecule. However, to put the results and conclusions of Chapters 4-7 into context, a brief introduction detailing some of the ionization methods used to form positive ions and the different types of ion produced following electron ionization, are presented. The various types of electron ionization cross-sections determined in this thesis, together with the relevant terminology, are then discussed, with an additional comment on two commonly used theoretical methods for calculating the electron ionization cross-section. Other experimental techniques used to detect and identify ions formed following ionization are then briefly presented.

## 1.2 Laboratory techniques for forming positive ions for mass spectrometry

The four main ionization techniques used, together with mass spectrometry, to produce ionized media are briefly discussed below. Electron ionization is the ionization method used in this study and is discussed in more detail in Chapter 2.

### 1.2.1 Electron ionization

Electron ionization generally involves the formation of ions following collisions between electrons and neutral gas species. Electrons are usually produced *via* thermionic emission from a filament with subsequent acceleration. Electron energies from 30-200 eV were used to ionize the molecules studied in this thesis. Electron ionization is a long standing, well proven method of ion formation and is still widely used in many current experiments investigating ion formation and fragmentation.[6,26,27]

If the energy of an electron beam colliding with a gas phase target molecule is greater than a critical value, termed the ionization energy, some target species, depending on the corresponding cross-section, will be ionized. The majority of ions formed by electron ionization are singly charged parent ions, shown in Reaction (1.I), and singly charged fragment ions formed from dissociative single ionization, shown in Reaction (1.II).[28]

$$XY + e^- \rightarrow XY^+ + 2e^- \qquad (1.I),$$

$$XY + e^- \rightarrow X^+ + Y + 2e^- \qquad (1.II).$$

The Wannier law describes the relationship between the cross-section $\sigma_{ion}$ for forming an ion *via* single ionization to the amount $E$ by which the energy of the system exceeds the ionization energy of the species. The Wannier law is expressed below:[29]

$$\sigma_{ion} \propto E^{1.127} \qquad (1.1).$$

The electron ionization cross-section for the single ionization process $\sigma_{ion}$, therefore depends on the amount $E$ by which the energy of the system exceeds the ionization energy of the species. The Wannier law is a threshold law, as it only applies when $E$ is small.[28,29] It should be noted that Eq. (1.1) is only applicable to the formation of ground state ions in the lowest lying ionic state.

As the ionizing electron energy is increased above the threshold value, there is an initial increase in the number and variety of ions produced, due principally to dissociative ionization channels and to a lesser extent multiple ionization. Wannier also

considered multiple electron ionization processes, defined in Reaction (1.III), where $N \geq 3$ and $N$ represents the resulting number of electrons following multiple ionization.[28]

$$XY + e^- \rightarrow XY^{(N-1)+} + e_1 + ....+ e_N \qquad (1.III).$$

Wannier proposed that without the inclusion of long-range interactions the cross-section of a double electron ionization process is approximately proportional to $E^2$. While this may be true for just near threshold, at high electron energies direct ionization processes are not the main means of multiple ionization.[30] Experimental electron ionization cross-sections for the formation of multiply charged ions generally rise from zero at threshold to a maximum at electron energies of one to a few hundred electronvolts. The convenience of electron generation and subsequent formation of multiply and singly charged ions must be balanced against the lack of information regarding the energy transferred to the target molecule upon ionization, and thus the distribution of internal energies with which they are formed.[30]

Over the past 30 years there have been numerous investigations of the single ionization of atoms and molecules following electron ionization. These investigations include ($e$, $2e$) experiments, which involve the electron ionization of neutral targets in which the kinematics in the final state are completely determined (energies, momenta, angles and the coincident detection of all outgoing electrons) to yield ($e$, $2e$) triply differential cross-sections.[31] Such measurements have provided an increased understanding of the ionization mechanism and of the momentum distributions for outgoing electrons.[32,33] As a result of these investigations (and numerous others) a large amount of information about the single ionization mechanisms such as direct ionization and autoionization is now known.[2] However, investigations of the electron double ionization processes are more limited, due principally to the smaller ionization cross-sections. However, there are now detailed investigations of the electron double ionization of the rare gases that completely determine the kinematics. These experiments use triple coincidence techniques, and are termed ($e$, $3e$) experiments.[34,35] The ($e$, $3e$) experiments simultaneously analyse the three outgoing electrons from the double ionization process in both direction and energy and are detected in coincidence. The angular distributions in initial ($e$, $3e$) experiments on argon were consistent with a two-step model for the double ionization[34] and further ($e$, $3e$) experiments, using a lower collision energy, have again shown the importance of such a mechanism in double ionization.[36,37]

## 1.2.2 Photoionization

The increasing availability of synchrotron radiation sources and improving laser technology means that photoionization is now a commonly used method of ionization. Photoionization involves the interaction of a photon, of known energy, emitted by a discharge lamp, synchrotron radiation source or laser, with a neutral target species, as shown in Reaction (1.IV).[38,39,40]

$$XY + h\nu \rightarrow XY^{+} + e^{-} \qquad (1.IV).$$

The advantage of photoionization, in comparison with electron ionization, is that the energy of the incident photon is, in principle, known. This means that the energy transfer to the target molecule upon ionization is also known.[39]

The near threshold region is defined as being too low for any inner-shell excitations or ejections.[30] In 1948, Wigner[41] discussed the behaviour of cross-sections near threshold, with the aim of improving the knowledge of how the product yield approaches zero with decreasing energy. Wigner's threshold laws therefore describe the behaviour of cross-sections (as a function of energy) near threshold, specifically for the two-particle break up under different kinds of interaction potentials (no interaction, short and long-range Coulomb forces). This formalism is often applied to the photoionization of molecules. Following the work of Wigner, in 1953 Wannier[29] derived a threshold law in the form of a power law, shown in Eq. (1.1). The Wannier threshold law, discussed earlier for electron ionization, can also be applied to the double photoionization process shown in Reaction (1.V),[28,29] where direct two electron ejection is assumed.

$$XY + h\nu \rightarrow XY^{2+} + 2e^{-} \qquad (1.V).$$

A technique developed specifically to study double photoionization, namely photoelectron-photoelectron coincidence (PEPECO), enables both electron energies to be analysed. Using the PEPECO technique a major fraction of the double photoionization of ordinary molecules, at low energy, is shown to be indirect (a process other than simultaneous ejection of two electrons).[30] The indirect process first forms a superexcited singly charged ion which then autoionizes to the doubly charged final product. This means that doubly charged ions can also be formed outside the Franck-Condon zone due to the two-step nature of the transition.[30]

### 1.2.3 Chemical Ionization

In chemical ionization (CI), for example employed in mass spectrometry (CIMS), CI is the result of the reaction between sample molecules and reagent ions. The reagent ions are generally formed from a reagent gas by electron ionization and subsequent ion-molecule reactions. Commonly used reagent gases include methane, isobutane and ammonia. For example, in methane CI the reagent ion is $CH_5^+$, which arises from the following sequence:

$$CH_4 + e^- \rightarrow CH_4^{+\bullet} + 2e^- \quad (1.VI),$$

$$CH_4^{+\bullet} + CH_4 \rightarrow CH_5^+ + CH_3 \quad (1.VII).$$

In order to achieve high efficiency in the formation of the reagent ion a high pressure of reagent gas is generally used. The $CH_5^+$ reagent ion then reacts by proton transfer with the sample molecules X (of sufficiently high proton affinity), shown in Reaction (1.VIII). However, CI may also involve charge exchange, electron capture or adduct formation.

$$CH_5^+ + X \rightarrow MH^+ + CH_4 \quad (1.VIII).$$

Two distinct advantages of CI over electron ionization are firstly its specificity, in being able to select a reagent gas for the system and secondly that CI is a softer ionization technique. CI is therefore used primarily to enhance the abundance of the molecular ion. For this reason CI and electron ionization techniques are often used to complement each other.

### 1.2.4 Collisional Ionization

Collisional ionization involves the formation of ions following collisions between neutrals and high-energy ions. The discussion presented in this thesis will focus only on the formation of doubly charged ions (dications) *via* collisional ionization. The collision results in ionization of the projectile ion or the neutral target.[30] A singly charged projectile cation $X^+$, possessing several kiloelectronvolts (keV) of kinetic energy, is collided with a target gas Y. The projectile $X^+$ is ionized *via* charge stripping (CS), shown in Reaction (1.IX).[42]

$$X^+ + Y \rightarrow X^{2+} + Y + e^- \quad (1.IX).$$

The energy required to ionize the projectile is taken from the kinetic energy of the projectile cation itself. A velocity measurement of the product dication $X^{2+}$ then enables the double ionization energy of the projectile to be determined.[39] To a first approximation this represents the ionization energy required to proceed with a vertical

transition from the geometry of the singly charged cation. Ionization of the neutral target species can also occur by charge transfer, shown in Reaction. (1.X).[38]

$$X^+ + Y \rightarrow X^- + Y^{2+} \qquad (1.X).$$

The cross-sections for this type of reaction are small, but such charge transfer experiments are especially useful in measuring spectra of dications that do not exist as stable species. The double ionization energy of Y can be deduced if the product anions $X^-$ are detected within a small angle of the original projectile direction, using the observed change in velocity of X.[43-45] Provided that the transition from projectile cation to product anion is well understood, information about the electronic states of the dication of interest can be determined.

## 1.3 Product ions

Following electron ionization of the target molecules, many different product ions are formed. In this thesis the product ions formed following ionization are singly and doubly charged. It should be noted that no triply charged ions were directly observed. By simultaneously recording mass and coincidence spectra, the monocations and dications formed *via* dissociative multiple ionization are distinguished from those monocations and dications formed 'directly' *via* single and double ionization. The following sections briefly discuss the different types of ion formed following an electron-molecule collision, and how the distinction is made between ions formed by dissociative and non-dissociative ionization.

### 1.3.1 Parent and fragment ions

Single ionization of a neutral gas phase target molecule involves a transition between two well-defined electronic states of the molecule and the molecular ion. This results in the removal of an electron from the neutral molecule to form a singly charged ion. Vibrational and rotational excitation also accompany this transition, however, the energy transferred into vibration and rotation excitation is usually significantly smaller than the energy transfer during electronic excitation. The Franck-Condon principle states that during ionization there is no change in molecular geometry, as the nuclei remain stationary during the fast excitation. The transition from the ground electronic state to the electronic state of the molecular ion is therefore vertical, and is shown in Figure 1.1. The Franck-Condon principle is discussed here for diatomic molecules but it is of course also true for polyatomic molecules.

Upon ionization, different fragmentation channels may be accessed, depending on the relative shape of the neutral and cationic potential energy curves of the chosen system and the ionizing electron energy. In general, but not exclusively, following electron ionization of the target gas species, parent monocation formation is dominant at all ionizing electron energies, shown in Reaction (1.XI). Figure 1.1 (a) illustrates parent monocation formation $XY^+$ on a bound surface.

$$XY + e^- \rightarrow XY^+ + 2e^- \qquad (1.XI).$$

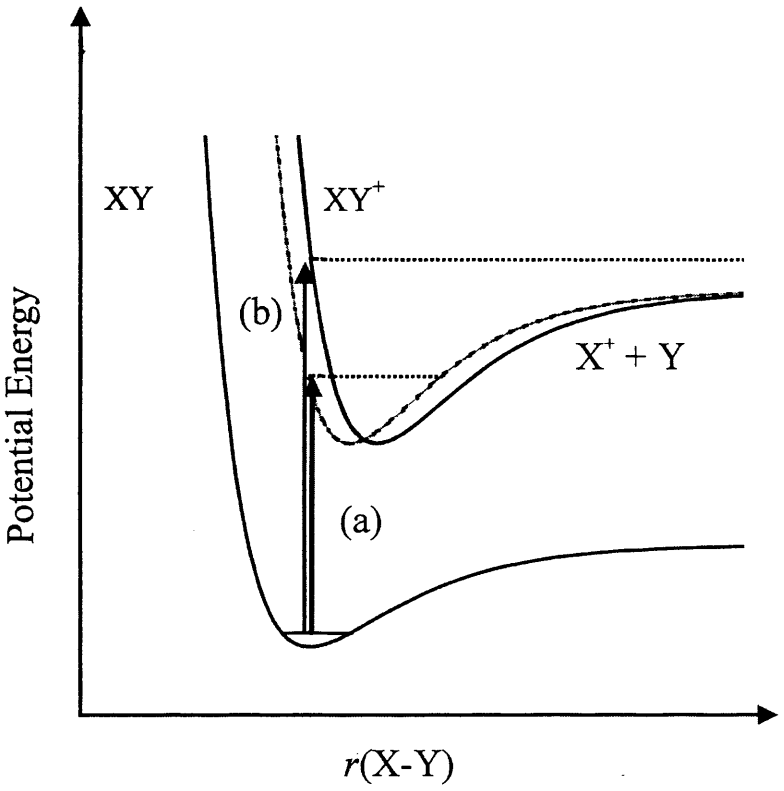


Figure 1.1: Schematic potential energy curves for the single ionization of the molecule XY, (a) forming the parent monocation $XY^+$ on a bound surface. (b) formation of the $XY^+$ parent monocation at an energy above its dissociation limit, and thus the $XY^+$ parent monocation dissociates to form a singly charged fragment ion and neutral.

In some cases, the relative shape of the monocation and neutral potential energy curves mean that the bound region of the cationic state cannot be accessed *via* a vertical transition from the ground electronic state of the neutral molecule. If no bound region can be accessed, the parent monocation rapidly fragments to form a singly charged ion and a neutral product, $X^+ + Y$, as shown in Reaction (1.XII) and in Figure 1.1 (b). The $X^+$ monocation is termed a fragment ion.

$$XY + e^- \rightarrow XY^{+} + 2e^- \rightarrow X^{+} + Y \qquad (1.XII).$$

Of course, the cationic state accessed *via* a vertical transition may be a repulsive state, and therefore the parent monocation will dissociate immediately. However, for the experiments detailed in this thesis, fragment ion formation will not only proceed *via* the ground state, as using ionizing electron energies of 30-200 eV ions are produced in a wide range of highly excited vibrational and electronic energy levels, as shown in Reaction (1.XIII).

$$XY + e^- \rightarrow XY^{+*} + 2e^- \rightarrow X^{+} + Y \qquad (1.XIII).$$

It is therefore likely that the many fragment ions will be formed by direct dissociation *via* predissociation. Herzberg[46] classified predissociations into three ideal cases where the electronic, vibrational and rotational energy levels overlap. Here, the electronic predissociation and internal conversion with vibrational predissociation will be briefly discussed. Electronic predissociation occurs when two excited electronic states (potential energy curves) of a particular molecular ion intersect; one bound excited state and the other a repulsive excited state. When a dissociative state crosses a bound state, monocations excited to vibrational levels near the crossing may dissociate. The transition to a dissociative curve is non-radiative (no energy is absorbed or emitted).

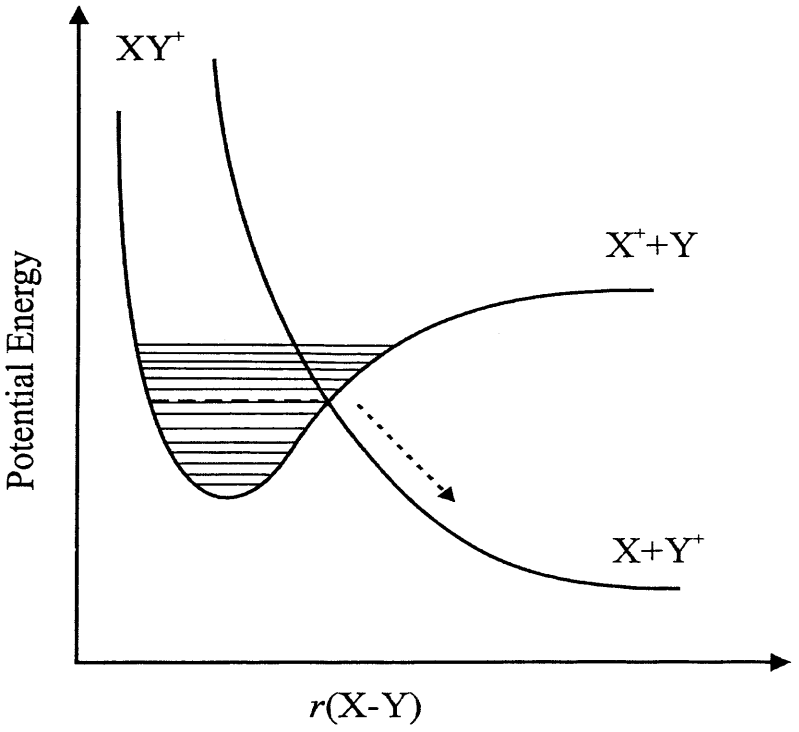


Figure 1.2: A schematic diagram showing how predissociation *via* curve crossing to dissociative potentials provides a common dissociation mechanism.

In the case of polyatomics, the multi-dimensional potential energy surfaces are complex, and the resulting polyatomic ion can undergo internal transitions leading to subsequent unimolecular decomposition.[2] Therefore, for polyatomic ions a statistical approach is required to predict the fragmentation of molecular ions in excited states. The two essentially identical statistical theories used are the quasi-equilibrium theory (QET)[47] and the Rice, Ramsperger, Kassel and Marcus (RRKM) theory.[48] These theories state that ions in excited electronic states relax rapidly by conversion of their electronic excitation energy into vibrational energy (internal conversion) of the molecular ion in its electronic ground state. The internal energy in the excited ion is statistically distributed *via* transitions into the electronic ground state before fragmentation by vibrational predissociation. The RRKM/QET equation yields the rate constant for a molecule at a given energy. A further description of statistical RRKM/QET theory calculations in mass spectrometry is given by Baer *et al.*[49,50]

In general the relative abundance of any fragment ion is related to its rate of formation and its rate of dissociation by unimolecular decomposition.[2] Hence, a mass spectrum is a record in time of the position of this 'quasi-equilibrium' of those rates and thus the respective PICSs of the fragment ions will depend on the time after formation of the parent ion.[2] The RRKM/QET statistical theories can therefore be used to calculate a mass spectrum by determining the rate coefficients of formation and dissociation of the fragment ions.[51]

Following electron ionization, the majority of ions formed are monocations, either parent or fragment ions. However, at ionizing electron energies above the double ionization energy of the target gas molecule, many fragment monocations are formed *via* dissociative multiple ionization. The following section discusses the observation of multiply charged ions, and the method by which monocations formed *via* dissociative multiple ionization are differentiated from monocations formed *via* single ionization. The stability of molecular dications is then examined in terms of the lifetimes of the dication electronic states.

#### 1.3.1.1 Multiply charged ions

At ionizing electron energies above the double ionization threshold, molecular doubly charged ions, termed dications, are observed in low abundance in the mass spectra of each target molecule studied in this thesis. The reason for their observed low abundance, even at ionizing electron energies of 200 eV, is due to the inherently small

ionization cross-section (ICS) for the formation of long-lived dications. In fact, the majority of molecular dications are unstable and rapidly dissociate to yield a pair of singly charged ions, as shown in Reaction (1.XIV).

$$XY^{2+} \rightarrow X^{+} + Y^{+} \qquad (1.XIV).$$

Specifically, the majority of dication electronic states are thermodynamically unstable, as they lie at energies above the asymptote for charge-separating dissociation, shown in Figure 1.3 (b).[21] 'Unstable' molecular dications generally have lifetimes of less than a nanosecond, precluding the detection of such species prior to their dissociation in conventional mass spectrometric experiments. Therefore, in conventional mass spectrometric experiments, the singly charged ions formed as an ion pair following dissociative double ionization will be indistinguishable from those singly charged ions formed *via* single ionization. However, the TOF mass spectrometer used in this thesis is coupled with a 2D ion-ion coincidence technique, enabling such ion pairs to be detected in coincidence. This 2D ion-ion coincidence technique is similar to the photoelectron photoion-photoion coincidence technique (PEPIPICO), pioneered by Eland and co-workers in the 1980s,[52] but uses electron ionization. Unlike PEPIPICO, which is a three-particle coincidence technique, the ion-ion coincidence technique used in this thesis records only the ion pair arrival times. These ion arrival times are stored individually as a list, for off-line inspection, and subsequent data processing following completion of the experiment. From this list of arrival times a 2D mass spectrum, termed pairs spectrum, is generated from the multiple ion arrival data by construction of a 2D histogram of the ion flight-times of both ions. The ion pair peaks formed in the pairs spectra also yield information regarding the fragmentation mechanism involved in the dissociation reaction forming each ion pair.[53] Indeed, the PEPIPICO technique has elucidated the dynamics of three-body dissociation reactions for many dications from molecules such as OCS, $CH_3I$ and $SF_6$.[52,54-56] Owing to the mutual repulsion between these fragment cations, upon dicationic dissociation, a kinetic energy release (KER) of typically more than 5 eV may occur.[21] By examining particular ion pair peaks in the coincidence spectra, the ion arrival data can be manipulated and subsequently modelled to provide an estimate of the kinetic energy released in such dissociations. KER determinations are further detailed in Chapter 3 and results are presented in Chapter 4.

Triply charged molecular ions, termed trications, were not directly observed in the TOF mass spectra presented in this thesis. This is perhaps not surprising given the stronger Coulomb repulsion between three like charges, together with the fact that the

cross-section for formation of such ions is smaller than the double ionization cross-section. As discussed for dications, the majority of trication electronic states are thermodynamically unstable, and thus the ions do not survive on the timescale necessary for detection in a mass spectrometer. In fact, most molecular trications have lifetimes in the sub-nanosecond region. However, trications including diatomic rare gas clusters,[57-59] diatomic fluorides,[60,61] other diatomics[62,63] and small polyatomics[57,63,64] have been observed using different experimental techniques, and are predicted using various theoretical techniques. Indeed, $CS^{3+}$, $CS_2^{3+}$, $COS^{3+}$, $Cl_2^{3+}$ and $SO_2^{3+}$ trications have been observed in low abundance in mass spectrometric experiments.[9,63-65] Despite the observation of such ions, described above, the majority of molecular trications are unstable and rapidly dissociate. If two ions are formed following a tricationic dissociation event, an ion pair consisting of a dication and monocation is observed in the pairs spectra, as shown in Reaction (1.XV). Such ion pairs were observed in the pairs spectra following electron ionization of $N_2O$ and $SF_6$.

$$XYZ^{3+} \rightarrow X^{2+} + YZ^{+} \qquad (1.XV).$$

In addition to the collection of two ion arrival times, the data collection electronics were set to record three ion arrival times following each start signal from the pulse generator. The ability to collect ion triples creates an ion-ion-ion coincidence experiment, enabling three fragment ions formed following a tricationic dissociation event to be detected, see Reaction (1.XVI).

$$XYZ^{3+} \rightarrow X^{+} + Y^{+} + Z^{+} \qquad (1.XVI).$$

Such events are termed triples, and triples data were recorded following the electron ionization of $N_2O$ and $SF_6$. In fact, the coincidence studies conducted in this thesis on triatomic trication dissociation determined that complete charge-separation to three monocations appears to have the largest probability.[66]

The experimental and data analysis techniques used in this thesis allows these singly and doubly charged ions formed *via* dissociative multiple ionization to be distinguished from the singly and doubly charged ions formed *via* non-dissociative single and double ionization. Such data enables precursor specific PICSs to be quantified.

#### 1.3.1.1.1 Stability of multiply charged ions

To understand why the majority of electronic states of molecular dications and

trications immediately dissociate, it is useful to look at the energy of the electronic states with respect to the asymptote for charge-separation. The following discussion is exclusively presented for dications, but is also applicable to trications. The thermodynamic stability of multiply charged ions with respect to the asymptotes of the corresponding charge-separated fragments, $X^+ + Y^+$ for a diatomic dication (or $X^{2+} + Y^+$ for a diatomic trication) are illustrated schematically in Figure 1.3. With reference to Figure 1.3, some electronic states of a dication can be (a) thermodynamically unstable, (b) thermodynamically stable or (c) metastable.

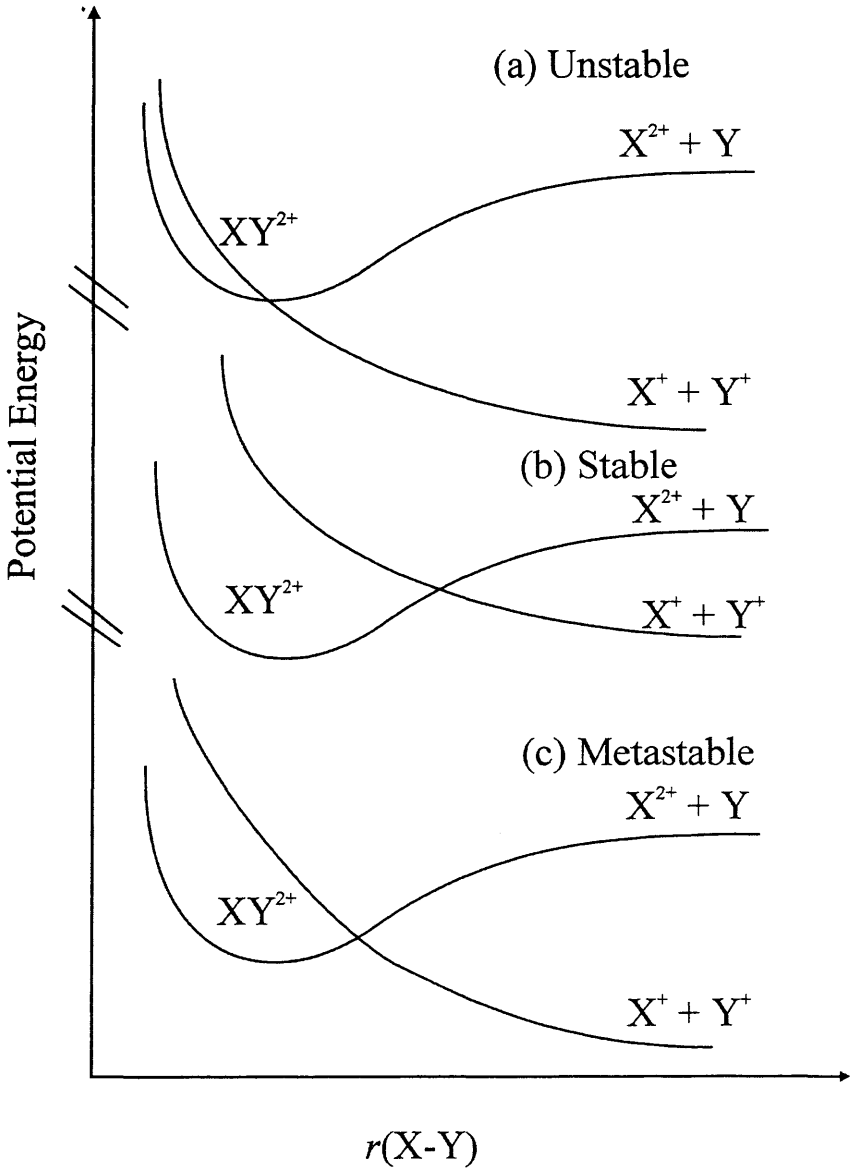


Figure 1.3: A schematic diagram of the diabatic potential energy curves for a diatomic molecular dication: leading to (a) thermodynamically unstable states, (b) thermodynamically stable states and (c) metastable states of the dication.[38]

When presented with a doubly charged molecular ion (dication), one may expect such species to be extremely short-lived, due to the Coulomb repulsion between the two positive charges. Indeed, a large number of the electronic states of molecular dications do rapidly fragment to produce a pair of monocations.[21,67] Figure 1.3 (a) illustrates the case where the energy of the monocation fragments $X^+ + Y^+$ is lower than the energy of $XY^{2+}$ and thus the dication is thermodynamically unstable. Although the majority of dication electronic states lie above the charge separating dissociation asymptote, there are some 'thermodynamically stable' dications, for which the bound $XY^{2+}$ state is lower in energy than the lowest asymptotes $X^+ + Y^+$ and $X^{2+} + Y$, see Figure 1.3 (b).[38] Recent interest in small thermodynamically stable dications such as $XeHe^{2+}$, $KrHe^{2+}$, $AlF^{2+}$ and $FeNH^{2+}$ has arisen, as it is believed that these may provide an insight into the nature of chemical bonding in the presence of multiple charges.[38]

Despite being thermodynamically unstable with respect to charge-separation, many molecular dications, such as $CO^{2+}$, were first observed and identified using conventional mass spectrometric experiments.[68] Indeed, dications are observed in the mass spectra presented in this thesis. Such ions must survive for at least a microsecond to be detected in mass spectrometric experiments. Therefore, not all dication electronic states dissociate rapidly, despite being thermodynamically unstable with respect to charge-separation.[69] These dication electronic states have a barrier to charge-separation, as shown in Figure 1.3 (c).[66] Such a barrier is illustrated schematically for a diatomic dication in Figure 1.4 and confers kinetic stability on the dication electronic state. These 'long-lived' dication electronic are termed 'metastable'. Metastable dication electronic states have lifetimes of at least the order of microseconds. The lifetime of such a metastable electronic state of a dication is dependent on the height and width of the barrier to charge-separation.[69-71] In several cases, the potential well of the dication is relatively deep and thus can support several bound vibrational levels. The $O_2^{2+}$ dication possesses a relatively deep potential well, and its potential energy curves are presented inset in Figure 1.4 (a). In an idealised, collision-free environment, the lifetimes of metastable dications should vary significantly depending on the degree of vibrational excitation. High-lying vibrational levels can more easily tunnel through the barrier to charge-separating dissociation, and will therefore have significantly shorter lifetimes than low-lying vibrational levels, which are effectively trapped behind the barrier. Recent storage ring experiments have determined that dications in low-lying vibrational states can live for longer than one second.[69,71] In fact, the potential energy

surface of the metastable states varies approximately as $r^{-1}$ at large $r$. Therefore, the barrier to charge-separation becomes very wide as the vibrational excitation of the dication decreases,[67] which rapidly increases the tunnelling lifetime of such low-lying vibrational levels.[72] It therefore appears that predissociation *via* curve crossings to repulsive electronic states, as shown in Figure 1.4, actually provide a common decay mechanism for the low-lying vibrational states of molecular dications.[73-75]

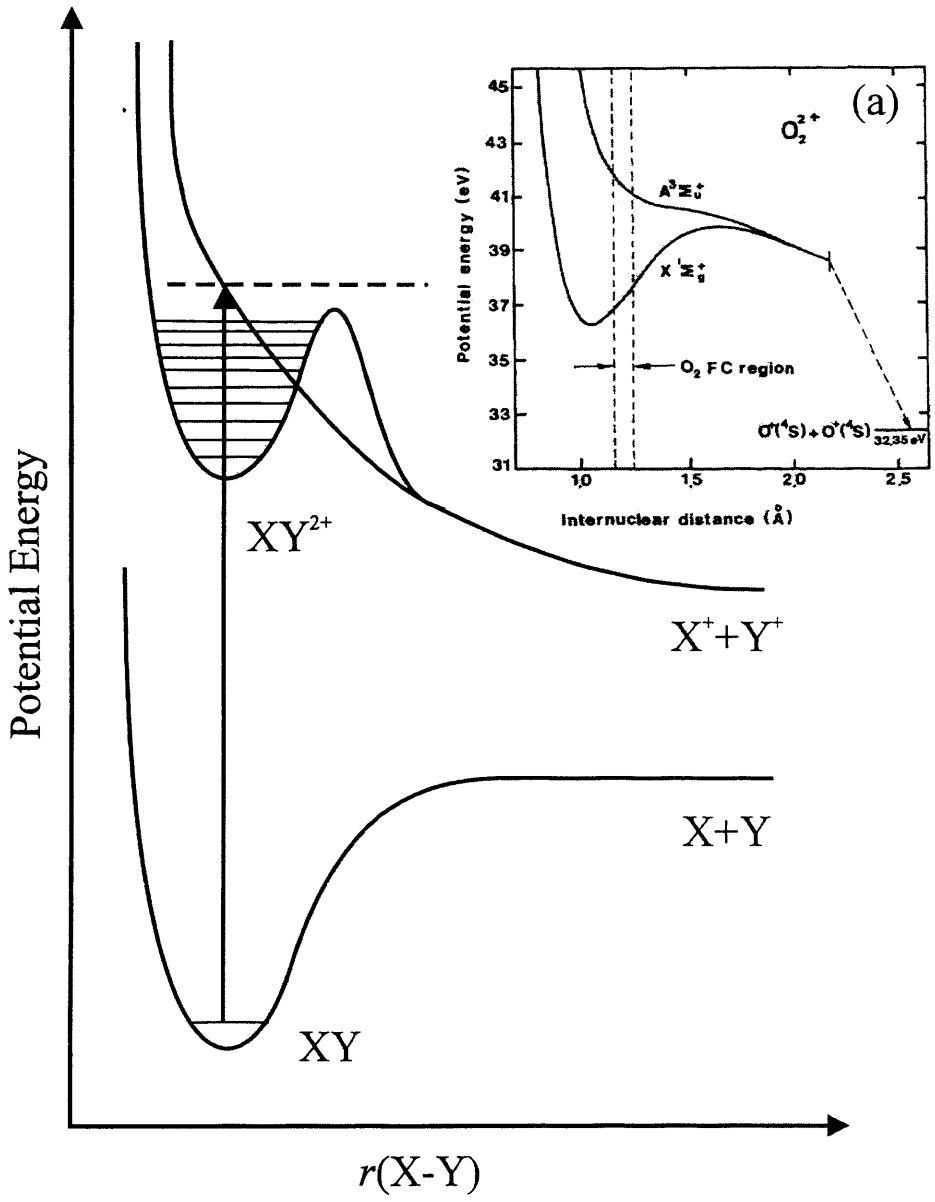


Figure 1.4: Schematic potential energy curves for a diatomic molecular dication. The inset diagram (a) shows the potential energy diagram for $O_2^{2+}$, illustrating the relatively deep potential well of the $O_2^{2+}$ dication that supports many vibrational levels, taken from Larsson *et al*[76] and Hall *et al.*[77]

There are currently two rationales proposed to explain the existence of the metastable dication states. The first proposal suggests these metastable states arise from an avoided crossing between two diabatic electronic states of the dication.

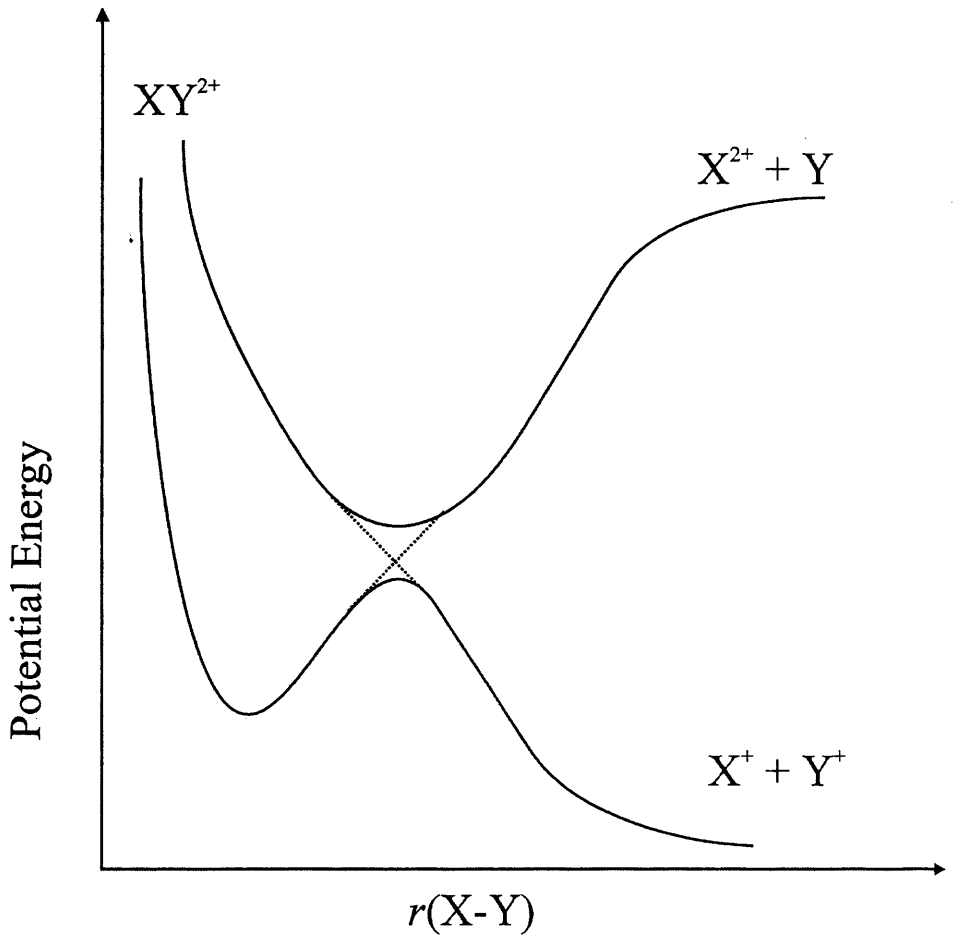


Figure 1.5: A schematic diagram illustrating how metastable dication states can arise from the avoided crossing of the potential energy curves of the dication leading to charge-separating dissociation and neutral loss.

These electronic states converge at large internuclear distances to the purely repulsive charge-separation potential energy curve ($X^+ + Y^+$) and the neutral loss potential energy curve ($X^{2+} + Y$), shown schematically in Figure 1.5. An avoided crossing occurs when two electronic states of the same symmetry do not actually cross, due to the repulsion between them, but would cross if there were no perturbation. Such an avoided crossing may give rise to a potential well, whose depth and width allow the existence of metastable dication states.[66,78]

The second rationale for the existence of metastable dication states was proposed following theoretical investigations of the electronic structure of $F_2^{2+}$. O'Neil and co-workers[79] found that the potential energy curves of this dication could be reproduced by the addition of the Coulomb repulsion potential to the potential energy curves of the isoelectric neutral, $O_2$.[79] From this proposal, it followed that dication states could be pictured as arising from the combination of the chemical binding potential of the neutral isoelectronic molecule and the Coulomb repulsion of the constituent ion pair. [79] Therefore, metastable dication states will exist when the strength of the chemical bond is sufficient to overcome the repulsion between the two positive charges. However, this 'additive' interpretation is not suitable for some heteronuclear diatomic dications, such as $HCl^{2+}$, because at small internuclear distances both positive charges reside on one of the atoms.[72]

In recent years, following increased experimental[80-82] and theoretical[83-87] efforts to address the fundamental questions regarding the structure, stability and the bonding of small molecular dications, our understanding of the properties of molecular dications continues to develop.

## 1.4 Electron Ionization Cross-Sections

In an ongoing effort to understand the electron ionization processes and develop models of the chemistry occurring in technologically important plasmas and planetary atmospheres, reliable electron ionization cross-sections are required. Any ionization cross-section can be expressed mathematically using a variation of the Beer-Lambert law:

$$I = I_0 e^{-nl\sigma} \qquad (1.2),$$

where $I$ is the electron flux after passing through the target gas, $I_0$ is the initial electron flux, $n$ is the number density of the gas, $l$ is the electron pathlength and $\sigma$ is the cross-section. Experimental determinations of the electron ionization cross-section usually involve an experimental arrangement similar to that shown in Figure 1.6, which is discussed in the following section.

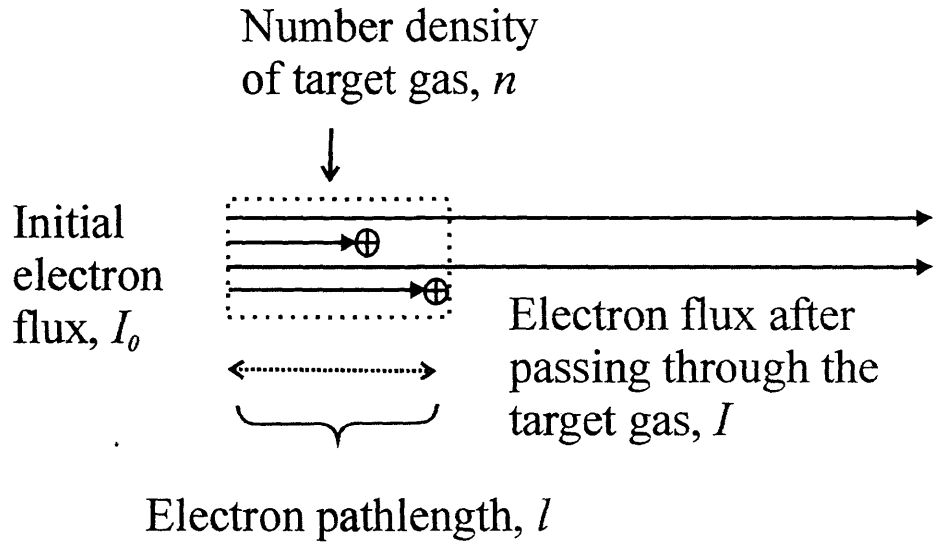


Figure 1.6: A schematic diagram of an electron ionization experiment.[2]

The following sections also detail the various types of cross-section determined in this thesis and the terminology used.

### 1.4.1 Total ionization cross-section

As discussed in Section 1.2.1, electron ionization of a polyatomic target gas results in the production of ions, neutrals and ejected electrons. A measure of the probability of producing positive charge, regardless of identity, is the total ionization cross-section[2] (ICS), $\sigma_t$. The total ICS is therefore a sum of the single ($\sigma^+$), double ($\sigma^{2+}$), triple ($\sigma^{3+}$) and higher level ionization cross-sections, as shown in Eq. (1.3).

$$\sigma_t = \sigma^+ + \sigma^{2+} + \sigma^{3+} + \ldots \quad (1.3).$$

For the majority of molecules the single ionization cross-section will be significantly larger than the multiple electron ionization cross-sections.[2]

The total electron ICS can therefore be defined by expressing the number of ionization events forming positive charge $I_{charge}$ (total positive ion flux), as being equal to $I_o$–$I$.

$$I_{charge} = I_o - I \quad (1.4).$$

The general definition for an ICS given in Eq. (1.2) can then be defined in terms of the total ICS for formation of positive charge:

$$I_{charge} = I_0(1 - e^{-nl\sigma_t}) \quad (1.5).$$

Of course, $nl\sigma_t$ is small, and thus an expression for the number of ionizing events forming a positive charge is produced and shown below in Eqs. (1.6) and (1.7).

$$I_{charge} = I_o nl\sigma_t \quad (1.6),$$

$$\sigma_t = \frac{I_{charge}}{I_0 nl} \quad (1.7).$$

Consequently, the measurement of the total ICS for a gaseous sample requires the determination of four quantities, the total positive ion flux, the initial electron flux, the number density of the gas and the electron pathlength, as defined in Eq. (1.7). A brief description of the principles involved in the measurements of these four quantities is given using the 'classic' apparatus of Tate and co-workers,[88] illustrated schematically in Figure 1.7. In fact, such apparatus is still used to determine $\sigma_t$ with only slight modifications.

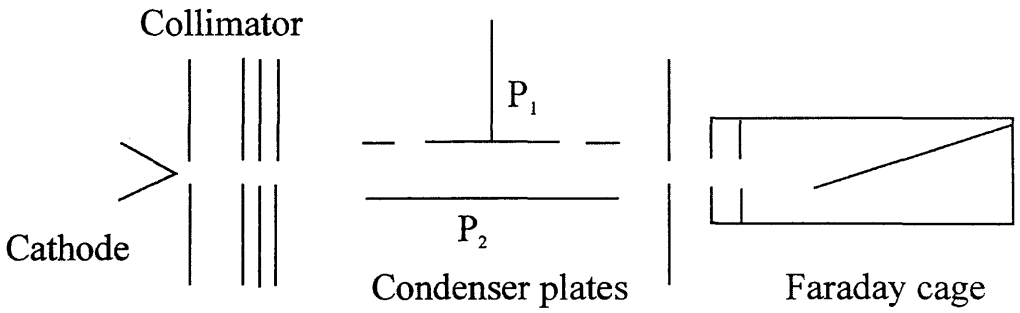


Figure 1.7: A schematic diagram of the apparatus used by Tate and Smith[88] and similar to the apparatus used by Rapp *et al.*[89]

Electrons emerge from a cathode and pass through a collimator and receive acceleration where they enter the gas filled collision chamber. An electric field is applied across the condenser plates, so that the positive ions can be collected at $P_1$ and the total positive ion flux, $I_{charge}$, can be determined. An axial magnetic field prevents any electron beam deflection and suppresses secondary electron emission from $P_1$. The electron beam is then trapped in the Faraday cage, so the electron flux, $I_0$, can be determined. The pathlength, $l$, is the length of $P_1$ following in the electron beam direction. Finally, the number density, $n$, is evaluated using the gas pressure and temperature of the collision chamber.

Total electron ICSs are not directly determined in this thesis. The primary aim of this thesis is to provide cross-section data that could aid in the modelling of electron ionization processes in plasmas and planetary atmospheres. It is therefore vital that the identity of the species formed following electron ionization is determined. Where the identity of the product ion is determined, the ICS for the formation of the particular ion is termed the partial ionization cross-section (PICS).

### 1.4.2 Partial ionization cross-sections

As described above, PICSs provide information on the identity and abundance of different charged species formed following electron ionization. Hence, the determination of PICSs is more challenging than the determination of total ICSs, as to identify all the product ions formed following electron ionization a mass spectrometer is required.

If we consider electron ionization of a polyatomic molecule $XY_2$, there are a number of different ions that may be formed, for example $X^+$, $Y^+$, $XY_2^{2+}$, $XY^+$, $XY_2^+$. The probability of forming an individual ion is quantified by the PICS.[2] The PICS for the formation of each fragment ion is expressed as $\sigma$[ion]. The sum of the PICS for each ion formed following ionization is therefore equivalent to the total ICS, as shown below in Eq. (1.8):

$$\sigma[X^+] + \sigma[Y^+] + \sigma[XY_2^{2+}] + \sigma[XY^+] + \sigma[XY_2^+] = \sigma_t \qquad (1.8).$$

The total ICS for each small molecule studied in this thesis could be determined by summing the PICS for the formation of each detected fragment ion.

By expressing the number of particular ionization events $I_{events}$, as being equal to $I_o$–$I$, the ionization cross-section definition given in Eq. (1.2), can be defined in terms of the PICS for that particular ionization event $\sigma_p$:

$$I_{events} = I_o - I \qquad (1.9),$$

$$I_{events} = I_0(1 - e^{-nl\sigma_p}) \qquad (1.10).$$

As $nl\sigma_p$ is small, an expression for the number of ionizing events is produced and shown in Eq. (1.11).

$$I_{events} = I_o nl\sigma_p \qquad (1.11).$$

From Eq. (1.11), the number of ionization events, and thus the intensity of the peaks in the mass spectrum, is directly related to the absolute PICS for the production of a specific ion. Determination of the absolute PICS for a given ion is therefore more challenging than total ICS determination, as together with the parameters $I_o$, $n$ and $l$, the

number of ionizing events forming each detected ion must also be accurately determined.[12,90]

When determining accurate PICSs, it is essential to ensure that the experimental apparatus is capable of complete collection of all the fragment ions. As discussed in Section 1.1, it has recently become apparent that earlier experimental investigations of PICSs, involving quadrupoles or magnetic sector instruments, were often not capable of efficiently detecting the energetic fragment ions formed by dissociative multiple ionization, as shown in Reaction (1.XVII).

$$XY_2 + e^- \rightarrow XY_2^{2+} + 3e^- \rightarrow XY^+ + Y^+ + 3e^- \qquad (1.XVII).$$

In these earlier experiments, the problem of efficient energetic ion detection was frequently recognised, but the loss of such signals was considered to be of little importance, as multiple ionization was thought to provide only a small contribution to the total ion yield. In recent years, experiments that allow the efficient collection of high kinetic energy ions have shown that such ions, from multiple ionization, actually contribute significantly to the ion yields following electron ionization of small molecules, often comprising around 10-26 % of the total ion yield. Careful consideration was therefore given to the collection of energetic fragment ions formed following dissociative multiple ionization in the experimental apparatus used to perform the experiments detailed in this thesis, which is further discussed in Chapter 2.

The experimental set-up used for the work presented in this thesis couples a TOF mass spectrometer with the capability of recording ion-ion coincidences. Clearly, this enables the identification of ions formed following electron ionization. Furthermore, by simultaneously recording mass and coincidence spectra, ions formed *via* dissociative multiple ionization are distinguished from ions formed from single ionization. The contribution from various levels of ionization, such as single, double and triple, to the individual ion yields can therefore be determined. These cross-sections are termed precursor specific PICSs and are described below.

### 1.4.3 Precursor specific partial ionization cross-sections

The precursor specific PICS expresses the probability for forming a particular fragment ion, *via* single, double, triple and higher levels of ionization. The sum of the precursor specific PICSs for the formation an $X^+$ ion *via* single ($\sigma_1$), double ($\sigma_2$), triple ($\sigma_3$), etc. ionization is equivalent to the PICS for formation of the $X^+$ ion, shown in Eq. (1.12):

$$\sigma_p[X^+] = \sigma_1[X^+] + \sigma_2[X^+] + \sigma_3[X^+] + .... \quad (1.12).$$

In Chapters 4-7 precursor specific PICSs are presented for $N_2O$, $BCl_3$, $SF_6$ and $C_2H_2$. As discussed above, when determining PICSs, one must ensure that all energetic ions formed are detected. Determining precursor specific partial ionization cross-sections can help conclusively identify incomplete energetic ion detection in earlier experiments, as demonstrated in Chapter 4 for the electron ionization of $N_2O$.

### 1.4.4 Relative partial and relative precursor specific partial ionization cross-sections

As described above, PICSs quantify the individual ionization cross-section for the formation of a particular ion, Eq. (1.8). To accurately determine the absolute PICS for the formation of a particular ion, the electron pathlength, $l$, the number density of the target gas in the source region, $n$, the initial electron flux, $I_0$, and the number of ionizing events, $I_{events}$, forming that particular ion must all be determined. Determination of these variables is experimentally non-trivial and therefore, more often then not, relative PICSs are determined. Relative PICSs are determined by taking a ratio of the PICS for forming a selected fragment ion, against the PICS of a specific ion, usually the most abundant ion such as the parent ion. The relative PICS for forming an $X^+$ ion, $\sigma_r[X^+]$, is shown in Eq.(1.13).

$$\sigma_r[X^+] = \frac{\sigma_p[X^+]}{\sigma_p[\text{Parent}]} = \frac{I_{events}[X^+]/I_0 nl}{I_{events}[\text{Parent}]/I_0 nl} = \frac{I_{events}[X^+]}{I_{events}[\text{Parent}]} \quad (1.13).$$

As a consequence of using a ratio, the electron pathlength, the number density of the target gas and the initial electron flux are equivalent for each ion and thus do not need to be experimentally determined.[10] Therefore, only the number of ionizing events forming the $X^+$ and parent ion need to be determined, as shown in Eq. (1.13). Relative PICSs are useful as these values can be normalised to available total ICS data for the molecule being studied to produce absolute PICSs. In fact, the total ICSs determined by Rapp and Englander-Golden[89] in 1965 for a number of different molecules are still used by many groups to normalise their data to produce absolute PICSs. In this thesis relative PICSs for $N_2O$, $BCl_3$ and $SF_6$, are presented in Chapters 4-6.

Relative precursor specific PICSs are determined using the same principle described above for relative PICSs. Relative precursor specific PICSs for the formation of fragment ions following electron ionization of $N_2O$ and $SF_6$ *via* single, double and triple ionization, and $BCl_3$ *via* single and double ionization, are presented in Chapters 4-6.[91,92]

### 1.4.5 Absolute partial and absolute precursor specific partial ionization cross-sections

To develop models of the chemistry occurring in plasmas and planetary atmospheres we have established the need for the production of reliable electron ionization cross-sections. In modelling the conditions in these environments, it is useful to be able to provide a complete set of electron ionization cross-sections on an absolute scale from a single laboratory. With the growing industrial demand for such data, there are an increasing number of electron ionization experiments specifically designed to investigate and determine the absolute PICSs for gases such as $N_2O$, $C_2F_6$ and $TiCl_4$ to name but a few.[5,26,93-95] Indeed, this thesis presents absolute PICSs and absolute precursor specific PICSs determinations following the modification of the experimental apparatus. In this thesis the absolute PICS of a particular ion $X^+$ is indicated by a prime, $\sigma'[X^+]$. Two experimental methodologies are commonly used to determine absolute PICSs. These methods are briefly outlined below and are discussed in more detail in Chapters 2 and 3.

#### 1.4.5.1 Method 1: Individual parameter determination

The first method involves the definitive determination of each of the variables, expressed in Eq. (1.11), which is experimentally non-trivial.[96] For the discussion presented here, the focus is placed on the experimental methods used by Straub and co-workers.[94] The apparatus of Straub and co-workers consists of an electron gun, TOF mass spectrometer with a position sensitive detector and an absolute capacitance pressure gauge. A pulsed electron beam is directed through an interaction region, filled with the target gas. After each electron pulse, a pulsed voltage is applied to the top plate to drive any positive ions formed towards the bottom plate, where they are accelerated and subsequently impact on the position sensitive detector. The experimental design is similar to the parallel plate arrangement used by Rapp and Englander-Golden[97] coupled with a short pathlength mass spectrometer.[97] A schematic diagram of the apparatus used by Straub and co-workers[94] is displayed in Figure 1.8.

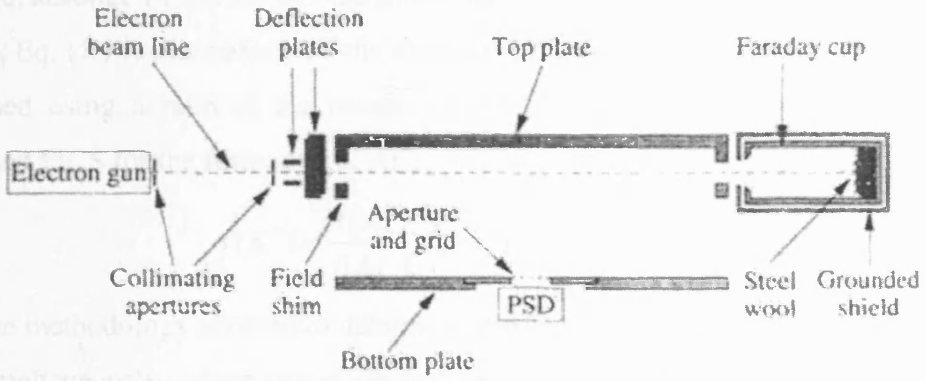


Figure 1.8: A schematic diagram of the apparatus used by Straub and co-workers.[94]

The use of a position sensitive detector enables the demonstration of complete fragment ion collection. As discussed above, if complete ion collection is shown, accurate determinations of the absolute PICSs should be possible. To determine absolute PICSs the electron flux is found by collecting the electron beam in a Faraday cup and measuring the current with an electrometer. The number of particular ionization events is determined by recording a TOF mass spectrum and counting the number of ions in an appropriate portion of the spectrum. In the experimental set-up used by Straub and co-workers[94] the length of the aperture directly in front of the detector provides the pathlength. Finally, the target number density is obtained from measurements of the target gas pressure, using a capacitance diaphragm gauge (not shown in Figure 1.8). Measurements of these quantities allow the direct determination of absolute PICSs, but it is clear that the determination of these quantities, particularly the target gas density, is time consuming.[94]

### 1.4.5.2 Method 2: Utilising two gases

The second method involves two target gases, one target gas with well-defined absolute PICSs, such as argon or nitrogen, and the other target gas with 'unknown' absolute PICSs. This method may be thought of as a normalisation technique.[95,98] The two target gases can be used separately or mixed in the source region of the experiment. If the experimental conditions are known to be equivalent between each experimental run, the two target gases can be used separately. However, if there is a variation in experimental conditions between experiments both target gases must be used simultaneously. In using the target gases separately or simultaneously a ratio of selected ion intensities can then be normalised to the well-defined absolute PICSs.

Therefore, absolute PICSs for the 'unknown' target gas can then be determined.[95,98] For example, Eq. (1.14) illustrates how the absolute PICS for the formation of the $X^+$ ion is determined using a ratio of the intensities $I[X^+]$ and $I[Ar^+]$ multiplied by the well established PICS for the formation of $Ar^+$:

$$\sigma'[X^+] = \frac{I[X^+]}{I[Ar^+]}\sigma'[Ar^+] \qquad (1.14).$$

The methodology adopted to determine absolute PICSs within this thesis uses two gases simultaneously, where one of the two gases has well-defined absolute PICSs. A full description of this methodology is given in Chapters 2 and 3. This thesis presents absolute PICSs and absolute precursor specific PICSs for $N_2O$ and $C_2H_2$, in Chapter 7, following apparatus modification outlined in Chapters 2 and 3.

## 1.5 Theoretical determination of electron ionization cross-sections

Calculated electron ionization cross-sections are increasingly used in comparison with experimental data and indeed for molecules where no experimental data is available. The binary-encounter-Bethe (BEB) theory of Kim and Rudd[99] and the Deutsch-Märk (DM) formalism are the two most widely used semi-rigorous methods to calculate absolute electron ionization cross-sections for molecules. Both methods were originally developed for the calculation of atomic ionization cross-sections and were subsequently extended to neutral molecular targets and molecular ions. However, the accurate theoretical determination of total ionization cross-sections for polyatomic molecules still remains challenging. A brief description of each method is given in the following sections.

### 1.5.1 Binary encounter Bethe (BEB) model

In 1994 Kim and Rudd[99] developed a collision theory for electron ionization of atoms and molecules, known as the binary-encounter-dipole (BED) model. The BED model combines a modified form of the Mott cross-sections and the Bethe cross-section. However, to determine ionization cross-sections for atoms and molecules the differential oscillator strengths are required. This quantity is often difficult to obtain experimentally or theoretically for each subshell of the target.[100,101] Consequently, Kim and Rudd devised a simplified version of the BED model, called the binary-encounter-Bethe (BEB) model,[99,102] which does not require the differential oscillator strengths.

The BEB model is frequently used in the theoretical determination of total electron ionization cross-sections.[100,101] The BEB model relies on information and data that are, for the most part, readily available in the literature or theoretically obtainable. This simplification allows the determination of reliable total ionization cross-sections for theoretically challenging targets such as polyatomic molecules.[102] The achievement of the BEB model is in its relative simplicity, requiring theoretical data from the ground state wavefunction of the target atom or molecule. This theoretical data includes the binding energy, kinetic energy and electron occupation number of each bound orbital. Comparisons with available experimental ionization cross-section data indicate that the BEB model produces ionization cross-sections in agreement to ± 15% at the cross-section peak.[103] The BEB model has been successfully tested for both atoms and molecules.[104-106]

### 1.5.2 Deutsch-Märk (DM) formalism

The DM formalism combines a Gryzinski-type energy dependence (continuous velocity distribution for atomic electrons) of the cross-section[107] with quantum mechanically calculated molecular structure information, based on the additivity concept.[3,108] The DM formula expresses the atomic ionization cross-section as the sum over all partial ionization cross-sections, corresponding to the removal of a single electron from a given atomic sub-shell.[100] The simple extension of this formula to molecular ionization cross-sections is achieved by performing molecular orbital population analysis.[3,109-112] Subsequent modifications have also enabled the cross-section determination for radicals,[112] small clusters,[113] atomic ions[114] and multiple ionization of atoms.[108,115] In all these cases ionization cross-section calculation using the DM formalism only includes direct ionization processes. Therefore, agreement is generally observed between the experimental data and the calculated data for small molecules and radicals, as a result of the dominance of the direct ionization processes.[100] However, for molecules with cross-sections that have a significant yield from ion-pair formation or indirect ionization processes, not considered in the DM formula, agreement is often poorer.[100]

The DM formalism and the BEB approach rely on information and data that is readily available in the literature, or easily obtained using quantum chemistry codes. This has allowed a growing number of theoretical ionization cross-section studies to be performed. As a consequence, it is now becoming easier to compare the rapidly

increasing number of experimentally determined molecular ionization cross-sections with theoretical studies.

## 1.6 Other experimental methods to study ionization

It is interesting to briefly review other experimental techniques used to investigate singly and multiply charged ions, and describe some of the important experimental developments that continue to increase the information available for such species.

### 1.6.1 Singly charged ions

Experimental developments over the past 50 years have enabled a detailed understanding of the structure, spectroscopy and dynamics of singly charged positive atomic and molecular ions (monocations).[66,69] Due to the numerous and varied nature of the experimental studies investigating the properties of monocations, only a brief list of some of the applicable experimental techniques is given here, as a detailed review is beyond the scope of this thesis. The majority of these experimental techniques probe the electronic spectroscopy of these ions, and there now exists a large database of information on the structures, spectroscopy and dynamics of monocations.[116] The spectroscopic techniques commonly used include photoelectron spectroscopy,[116,117] photoionization mass spectrometry,[116,118,119] ion emission and absorption spectroscopy,[120-122] electron energy-loss spectroscopy[123-125] and increasingly laser spectroscopy including the zero kinetic energy (ZEKE) spectroscopic technique,[126-129] to name but a few.[116] Coincidence techniques have also been employed to investigate the dissociation of monocations, these include photoelectron-photoion coincidence (PEPICO)[116,130,131] and threshold photoelectron-photoion coincidence (TPEPICO).[25,116,132-134] These techniques simultaneously detect electrons and ions produced together in single ionization events.

In this thesis parent monocation formation and dissociation is studied using electron ionization mass spectrometry, which enables the identification of every product ion formed following electron ionization of a selected molecule.

### 1.6.2 Multiply charged ions

Despite early mass spectrometric experiments that observed the first atomic doubly charged ion (dication) over 80 years ago,[135] followed by the observation of doubly charged carbon monoxide molecules in the 1930s,[68,136] molecular dications were

rarely the target of experimental investigations before 1980. Therefore, the information available on the properties of molecular dications, from both an experimental and theoretical perspective, is still limited. The restricted study of the properties of molecular dications, before 1980, was primarily due to the inherent instability of such ions and the relatively high energies required for their formation, which complicated experimental studies.[21,137] However, the development of new experimental techniques in the 1980s instigated a resurgence in the study of molecular dicationic properties, and now many experimental groups are investigating these short-lived species.[25,38,69,71,72,75,78,138-142] As a consequence of these experiments, the reactivity of molecular dications, following collisions with neutral species, molecular species, or photons is now also an active area of experimental and theoretical investigation.[67,137,143,144] As discussed in Section 1.3.1.1, the majority of molecular dications rapidly dissociate to yield a pair of singly charged ions, which are difficult to distinguish from the products of single ionization events. Conventional mass spectrometric studies are therefore limited to the observation of metastable states of the dications, that are stable on a lifetime that enables detection. The fact that the double ionization cross-section of a molecule is typically an order of magnitude smaller than its single ionization cross-section,[2] further complicates the study of molecular dications. However, in overcoming these difficulties, several long standing experimental techniques were further developed, together with some novel experimental techniques, to study molecular dications and trications.[22,25,145,146] These experimental techniques include multiple ion-electron coincidence,[53] Auger electron spectroscopy (AES) (often coupled with coincidence techniques)[147], Doppler-free kinetic energy release spectroscopy (DFKER),[75,148,149] threshold photoelectrons coincidence spectroscopy (TPEsCO)[25,150,151] and laser predissociation spectroscopy,[152,153] for which additional discussion is presented below. These experimental techniques have increased the understanding of molecular dications and allowed detailed studies of the chemical and physical processes which occur in various dicationic systems.

There is also a growing experimental and theoretical interest in molecular triply charged ions (trications). Molecular trications are commonly produced in various experimental arrangements, due to the increasing availability of photon sources such as synchrotrons or intense lasers, particle accelerator beams and also high-energy electrons. For more information on the current and future directions in this area of study, the reader is referred to recent reports by Mathur.[69,154]

As discussed in Section 1.3.1.1, the investigations detailed in this thesis are performed on a TOF mass spectrometer coupled with a 2D ion-ion coincidence technique. It is the 2D ion-ion coincidence technique together with the data processing, that enables dissociative multiple ionization events, involving two or three ion arrivals, to be distinguished and quantified from non-dissociative ionization events. This distinction allows the contribution from single, double and triple ionization to the individual ion yields to be quantified. Using this data the PICSs and precursor specific PICSs are determined. From the data obtained in this thesis, estimates of the double ionization energy of certain dications can be made, the pairs spectra yields information on the type of dissociation mechanisms responsible for certain ion pairs, and the KER associated with certain ion pairs can also be estimated. This KER estimate can then be used to determine the energy of the dication state responsible for the dissociation. However, no detailed information on the electronic or vibrational structure of dications or trications can be determined. Different experimental techniques must therefore be relied upon to provide such data. Some of these experimental techniques are briefly discussed below.

As a result of the instability of multiply charged ions, coincidence techniques are paramount in the study of such species. Pioneering techniques such as AES provided some of the earliest information on the electronic states of doubly charged molecules.[155] Recently, AES spectroscopy has been used with coincidence techniques, to study $CO_2$ and $CS_2$ molecules,[156-158] in a similar fashion to the PEPIPICO technique. AES (coupled with coincidence techniques) is particularly valuable in improving the understanding of the fragmentation dynamics of core-excited molecules. In 1995, a technique termed Doppler-free kinetic energy release spectroscopy (DFKERS) was developed,[22] enabling the investigation of the electronic structure, as well as the dissociation dynamics of molecular dications, to be advanced. In previous experiments, the energy resolution in KER spectra has been limited by the Doppler broadening, caused by the thermal motion of the parent molecules. Such Doppler broadening may be in the order of 1 eV in the spectrum, effectively precluding the observation of both vibrational and electronic states.[22] DFKERS eliminates this broadening by using a coincidence TOF instrument. DFKERS has been used to investigate the dissociation of dications, formed upon 200 eV electron ionization, and has resolved dissociative vibrational lines in various electronic states of $CO^{2+}$, $N_2^{2+}$, $O_2^{2+}$ and $NO^{2+}$.[75,148,149] The DFKER spectra also showed that the majority of cation pairs from diatomic precursors

are formed with continuous KER distributions. Hsieh and Eland[23] then determined DFKER distributions for the dissociative double ionization of $N_2$, CO, $O_2$ and NO, using PIPICO and PEPIPICO techniques with a position sensitive detector, at photon energies of 40.8 and 48.4 eV. Although these methods give a poorer energy resolution in comparison to the DFKERS apparatus used by Lundqvist *et al*,[22] advantages include better mass resolution, elimination of angular discrimination effects and the use of a wavelength selected photon source instead of an electron beam which provides precise upper limits to the energy transfer. These features enabled the direct comparison with distributions calculated for direct transitions to dissociative dication states, for which potential energy curves were calculated.[23] TPEsCO studies, performed in the last decade, also give detailed information of the energy levels in doubly charged molecules and complement the information provided by DFKERS. The TPEsCO technique records the spectra of coincidences between two nearly zero energy electrons, ejected each time a dicationic state is formed within a few meV of its threshold (less than 20 meV), as the photon energy is scanned across the range of interest.[159,160] The coincidence spectrum displays a peak every time the photon energy is scanned across a double ionization threshold of the species. Direct observation of the formation of dicationic states essentially at their thresholds is therefore possible, and yields information regarding the energies and relative peak intensities of the states in existence for a particular molecule. The only other technique capable of this is double ZEKE electron coincidence spectroscopy.[161] However, the double ZEKE technique suffers from larger background contributions than the TPEsCO technique.[151] Dications studied using TPEsCO include $HCl^{2+}$, $Cl_2^{2+}$, $CO^{2+}$, $N_2^{2+}$, $O_2^{2+}$, $HI^{2+}$, $CS_2^{2+}$ and $C_6H_6^{2+}$.[24,25,162,163]

Both DFKER and TPEsCO techniques provide detailed information on the vibrational structure of dication electronic states. However, for certain molecular dications, the older technique of laser predissociation spectroscopy can provide hyperfine components of the rotational fine structure in certain vibrational bands. In this technique dications are formed *via* electron ionization of the selected gas and coaxially combined with a laser beam in an interaction region. In general, a kinetic energy release of several electronvolts (eV) results from the photo-induced predissociation of the chosen electronic state of the dication.[145] The two photofragments formed following dicationic predissociation are monitored using coincidence detection. Laser predissociation spectroscopy has provided detailed studies of the metastable electronic states of $N_2^{2+}$.[145,164] However, laser predissociation

spectroscopy is limited to its applicability to other molecular dications, although a recent IR laser predissociation spectrum of $HCl^{2+}$ has achieved hyperfine resolution, and thus will hopefully be applied to other dications in the future.

Following technological advances, such as position sensitive detectors,[154] and the knowledge that certain molecular dication electronic states have lifetimes of up to 1 second, the reactivity of molecular dications following 'collisions' with neutral species or photons has become an active area of study. The reactivity of molecular dications with neutrals (bimolecular chemistry) has revealed a rich and unusual chemistry, where electron transfer, chemical reactions, charge-separation or neutral loss reactions can occur. Such chemistry may have an interesting influence on the chemistry of energised media.[67] A recently developed position sensitive coincidence (PSCO) spectrometer has been designed to study the dynamics of dication reactions by detecting, in coincidence, the pair of monocations frequently formed in the processes of making and breaking of chemical bonds.[165] Using a position sensitive detector, pairs of product ions are recorded in coincidence from an individual reactive event. From this data it is possible to determine the initial velocity vectors of all the ionic fragments. Such data yields detailed information on the scattering dynamics of the particular process.[67,166] The coincidence technique is particularly suited for the study of reactions which produce three products. Unlike conventional techniques, the PSCO experiment allows the initial velocity vectors of all three products to be determined for each reactive event. To illustrate the power of the PSCO experiment, the dynamics of two of the product channels formed following reaction of the $CF_2^{2+}$ dication with $H_2O$ are shown below in Reactions (1.XVIII) and (1.XIX):[167]

$$\begin{array}{l} CF_2^{2+} + H_2O \rightarrow [H_2O\text{-}CF_2]^{2+} \rightarrow H^+ + HOCF_2^+ \\ \qquad\qquad\qquad\qquad\qquad\qquad\qquad\qquad\qquad\qquad \downarrow \\ \qquad\qquad\qquad\qquad\qquad\qquad\qquad\qquad\qquad\qquad OCF^+ + HF \end{array} \qquad \text{(1.XVIII)},$$

$$\begin{array}{l} CF_2^{2+} + H_2O \rightarrow HCF_2^+ + OH^+ \\ \qquad\qquad\qquad\qquad\qquad\qquad\qquad\qquad\qquad\qquad \downarrow \\ \qquad\qquad\qquad\qquad\qquad\qquad\qquad\qquad\qquad\qquad O + H^+ \end{array} \qquad \text{(1.XIX)}.$$

For example Reaction (1.XVIII) occurs *via* the formation of a long-lived collision complex $[H_2O\text{-}CF_2]^{2+}$ which undergoes charge-separating dissociation to form $H^+$ and $HOCF_2^+$. This area of study offers exciting prospects and has already been shown to be a valuable tool for probing reaction dynamics.[165]

## 1.7 Summary

This chapter begins by providing clear motivation for the need to determine accurate electron ionization cross-sections for molecules used in plasmas and present in planetary atmospheres. Discussion on the ionization method used in this thesis, and other available ionization methods, is then presented together with the type of ions formed following ionization. The various forms of electron ionization cross-sections determined are then detailed along with the most common experimental and theoretical techniques used to determine electron ionization cross-sections. A brief overview of the current experimental techniques used to study the formation, dissociation and properties of singly, doubly and triply charged molecular ions is also presented.

In this thesis, the formation and fragmentation of molecular ions formed following electron ionization are investigated. Time-of-flight mass spectrometry is used to study the formation of monocations and dications and also the dissociation of monocations and is used with an ion-ion coincidence technique to study the dissociation of dications and trications. This data is then used to determine partial and precursor specific partial ionization cross-sections for selected small molecules.

## 1.8 References


1 T. D. Märk, *Electron-Molecule Interactions and their Applications* (Academic, London, 1984).

2 T. D. Märk and G. H. Dunn, *Electron Impact Ionization* (Springer-Verlag, New York, 1985).

3 D. Margreiter, G. Walder, H. Deutsch, H. U. Poll, C. Winkler, K. Stephan, and T. D. Mark, *Int. J. Mass Spectrom. Ion Process.* **100,** 143 (1990).

4 M. R. Bruce and R. A. Bonham, *Int. J. Mass Spectrom. Ion Process.* **123,** 97 (1993).

5 I. Iga, M. Rao, and S. K. Srivastava, *J. Geophys. Res.-Planets* **101,** 9261 (1996).

6 S. H. Zheng and S. K. Srivastava, *J. Phys. B-At. Mol. Opt. Phys.* **29,** 3235 (1996).

7 K. H. Becker and V. Tarnovsky, *Plasma Sources Sci. Technol.* **4,** 307 (1995).

8 R. F. Stebbings and B. G. Lindsay, *J. Chem. Phys.* **114,** 4741 (2001).

9 P. Calandra, C. S. S. O'Connor, and S. D. Price, *J. Chem. Phys.* **112,** 10821 (2000).

10 S. Harper, P. Calandra, and S. D. Price, *Phys. Chem. Chem. Phys.* **3,** 741 (2001).

11 M. R. Bruce, L. Mi, C. R. Sporleder, and R. A. Bonham, *J. Phys. B-At. Mol. Opt. Phys.* **27,** 5773 (1994).

12 B. G. Lindsay, R. Rejoub, and R. F. Stebbings, *J. Chem. Phys.* **118,** 5894 (2003).

13 M. Rao and S. K. Srivastava, *J. Phys. B-At. Mol. Opt. Phys.* **29,** 1841 (1996).

14 C. Tian and C. R. Vidal, *J. Phys. B-At. Mol. Opt. Phys.* **31,** 5369 (1998).

15 J. Lopez, V. Tarnovsky, M. Gutkin, and K. Becker, *Int. J. Mass Spectrom.* **225,** 25 (2003).

16 C. Q. Jiao, A. Garscadden, and P. D. Haaland, *Chem. Phys. Lett.* **310,** 52 (1999).

17 D. Smith and P. Spanel, *Mass Spectrom. Rev.* **14,** 255 (1995).

18 L. G. Christophorou and J. K. Olthoff, *J. Phys. Chem. Ref. Data* **28,** 967 (1999).

19 L. G. Christophorou and J. K. Olthoff, *Adv. At. Mol. Opt. Phys.* **44,** 59 (2001).

20 Database needs for modeling and simulation of plasma processing, National Research Council, (National Academy Press, 1996).

21 D. M. Curtis and J. H. D. Eland, *Int. J. Mass Spectrom. Ion Process.* **63,** 241 (1985).

22 M. Lundqvist, P. Baltzer, D. Edvardsson, L. Karlsson, and B. Wannberg, *Phys. Rev. Lett.* **75,** 1058 (1995).

23 S. Hsieh and J. H. D. Eland, *J. Phys. B-At. Mol. Opt. Phys.* **29,** 5795 (1996).

24 A. G. McConkey, G. Dawber, L. Avaldi, M. A. MacDonald, G. C. King, and R. I. Hall, *J. Phys. B-At. Mol. Opt. Phys.* **27,** 271 (1994).

25 R. I. Hall, L. Avaldi, G. Dawber, A. G. McConkey, M. A. Macdonald, and G. C. King, *Chem. Phys.* **187,** 125 (1994).

26 C. Tian and C. R. Vidal, *J. Chem. Phys.* **108,** 927 (1998).

27 R. Basner, M. Schmidt, E. Denisov, K. Becker, and H. Deutsch, *J. Chem. Phys.* **114,** 1170 (2001).

28 F. H. Read, in *Electron Impact Ionization*, edited by Springer-Verlag (New York, 1985), pp. 42.

29 G. H. Wannier, *Phys. Rev.* **90,** 817 (1953).

30 J. H. D. Eland, in *Vacuum Ultraviolet Photoionization and Photodissociation of Molecules and Clusters* (World Scientific, Singapore, 1991), pp. 297.

31 U. Amaldi, A. Egidi, R. Marconero, and G. Pizzella, *Rev. Sci. Instrum.* **40,** 1001 (1969).

32 P. J. O. Teubner, in *Electron Impact Ionization* (Springer-Verlag, New York, 1985), pp. 89.

33 A. Lahmam-Bennani, *J. Electron. Spectrosc. Relat. Phenom.* **123,** 365 (2002).

34 A. Lahmam-Bennani, C. Dupre, and A. Duguet, *Phys. Rev. Letts.* **63,** 1582 (1989).

35 H. Ehrhardt, K. Jung, G. Knoth, and P. Schlemmer, *Z. Phys. D.* **1,** 3 (1986).

36 A. Lahmam-Bennani and A. Duguet, Correlations, Polarization, and Ionization in Atomics Systems, Proceedings of the International Symposium on (e, 2e), Double Photoionization and Related Topics and the Eleventh International Symposium on Polarization and Correlation in Electronic and Atomic Collisions. (Missouri, 2001), pp. 96.

37 C. C. Jia, A. Lahmam-Bennani, A. Duguet, L. Avaldi, M. Lecas, and C. Dal Cappello, *J. Phys. B-At. Mol. Opt. Phys.* **35,** 1103 (2002).

38 D. Schröder and H. Schwarz, *J. Phys. Chem. A* **103,** 7385 (1999).

39 J. H. D. Eland, F. S. Wort, P. Lablanquie, and I. Nenner, *Z. Phys. D-Atoms Mol. Clusters* **4,** 31 (1986).

40 R. Locht, G. Hagenow, K. Hottmann, and H. Baumgartel, *Chem. Phys.* **151,** 137 (1991).

41 E. P. Wigner, *Phys. Rev.* **73,** 1002 (1948).

42 J. L. Holmes, *Org. Mass. Spectrom.* **20,** 169 (1985).

43 J. Appell, J. Durup, F. C. Fehsenfeld, and J. Fournier, *J. Phys. B-At. Mol. Opt. Phys.* **6,** 197 (1973).

44 P. G. Fournier, F. Fournier, F. Salama, D. Stark, S. D. Peyerimhoff, and J. H. D. Eland, *Phys. Rev. A* **34,** 1657 (1986).

45 M. Lange, O. Pfaff, U. Muller, and R. Brenn, *Chem. Phys.* **230,** 117 (1998).

46 G. Herzberg, *Electronic Spectra and Electronic Structure of Polyatomic Molecules* (D. Van Nostrand Company, New York, 1966).

47 H. M. Rosenstock, M. B. Wallenstein, A. L. Wahrhaftig, and H. Eyring, *Proc. Nat.*

*Acad. Sci. U.S.A.* **38,** 667 (1952).

48 R. A. Marcus and O. K. Rice, *J. Phys. Colloid Chem.* **55,** 894 (1951).

49 T. Baer and W. L. Hase, *Unimolecular Reaction Dynamics: Theory and Experiments* (Oxford University Press, Oxford, 1996).

50 T. Baer and P. M. Mayer, *J. Am. Soc. Mass Spectrom.* **8,** 103 (1997).

51 A. Maccoll, *Org. Mass Spec.* **26,** 235 (1991).

52 J. H. D. Eland, F. S. Wort, and R. N. Royds, *J. Elec. Spect. Rel. Phen.* **41,** 297 (1986).

53 J. H. D. Eland, *Mol. Phys.* **61,** 725 (1987).

54 T. Masuoka, *J. Chem. Phys.* **98,** 6989 (1993).

55 P. Lablanquie, I. Nenner, P. Millie, P. Morin, J. H. D. Eland, M. J. Hubinfranskin, and J. Delwiche, *J. Chem. Phys.* **82,** 2951 (1985).

56 L. J. Frasinski, M. Stankiewicz, K. J. Randall, P. A. Hatherly, and K. Codling, *J. Phys. B-At. Mol. Opt. Phys.* **19,** L819 (1986).

57 G. Frenking, W. Koch, D. Cremer, J. Gauss, and J. F. Liebman, *J. Chem. Phys.* **93,** 3397 (1989).

58 T. T. Tsong and T. J. Kinkus, *J. Phys. Scr.* **T4,** 201 (1983).

59 M. Hotokka, T. Kindstedt, P. Pyykko, and B. O. Roos, *Mol. Phys.* **52,** 23 (1984).

60 K. Nagesha, V. R. Marathe, and D. Mathur, *Chem. Phys.* **154,** 125 (1991).

61 D. Schröder, J. N. Harvey, and H. Schwarz, *J. Phys. Chem. A* **102,** 3639 (1998).

62 H. Sakai, H. Stapelfeldt, E. Constant, M. Y. Ivanov, D. R. Matusek, J. S. Wright, and P. B. Corkum, *Phys. Rev. Lett.* **81,** 2217 (1998).

63 C. P. Safvan, M. Krishnamurthy, and D. Mathur, *J. Phys. B-At. Mol. Opt. Phys.* **26,** L837 (1993).

64 N. Jeffreys, I. W. Griffiths, D. E. Parry, and F. M. Harris, *Chem. Phys. Lett.* **266,** 537 (1997).

65 M. Lavollee and V. Brems, *J. Chem. Phys.* **110,** 918 (1999).

66 D. Mathur, *Phys. Reps.* **225,** 193 (1993).

67 S. D. Price, *Phys. Chem. Chem. Phys.* **5,** 1717 (2003).

68 R. Conrad, *Physik. Z* **31,** 888 (1930).

69 D. Mathur, L. H. Andersen, P. Hvelplund, D. Kella, and C. P. Safvan, *J. Phys. B-At. Mol. Opt. Phys.* **28,** 3415 (1995).

70 J. Senekowitsch, S. O' Neil, P. J. Knowles, and H. J. Werner, *J. Chem. Phys.* **95,** 1847 (1991).

71 L. H. Andersen, J. H. Posthumus, O. Vahtras, H. Agren, N. Elander, A. Nunez, A. Scrinzi, M. Natiello, and M. Larsson, *Phys. Rev. Lett.* **71,** 1812 (1993).

72 F. R. Bennett and I. R. McNab, *Chem. Phys. Lett.* **251,** 405 (1996).

73 G. Parlant, J. Senekowitsch, S. O' Neil, and D. R. Yarkony, *J. Chem. Phys.* **94,** 7208 (1991).

74 A. S. Mullin, D. M. Szaflarski, K. Yokoyama, G. Gerber, and W. C. Lineberger, *J. Chem. Phys.* **96,** 3636 (1992).

75 M. Lundqvist, D. Edvardsson, P. Baltzer, M. Larsson, and B. Wannberg, *J. Phys. B-At. Mol. Opt. Phys.* **29,** 499 (1996).

76 M. Larsson, P. Baltzer, S. Svensson, B. Wannberg, N. Martensson, A. N. Debrito, N. Correia, M. P. Keane, M. Carlssongothe, and L. Karlsson, *J. Phys. B-At. Mol. Opt. Phys.* **23,** 1175 (1990).

77 R. I. Hall, G. Dawber, A. McConkey, M. A. MacDonald, and G. C. King, *Phys. Rev. Lett.* **68,** 2751 (1992).

78 D. Mathur, *Phys. Rep.* **225,** 193 (1993).

79 J. Senekowitsch and S. O'Neil, *J. Chem. Phys.* **95,** 1847 (1991).

80 S. G. Cox, A. D. J. Critchley, P. S. Kreynin, I. R. McNab, R. C. Shiell, and F. E. Smith, *Phys. Chem. Chem. Phys.* **5,** 663 (2003).

81 A. J. Yencha, A. M. Juarez, S. P. Lee, G. C. King, F. R. Bennett, F. Kemp, and I. R. McNab, *Chem. Phys.* **303,** 179 (2004).

82 A. E. Slattery, T. A. Field, M. Ahmad, R. I. Hall, J. Lambourne, F. Penent, P. Lablanquie, and J. H. D. Eland, *J. Chem. Phys.* **122,** 084317. (2005).

83 M. Urban, G. H. F. Diercksen, and M. Jurek, *Mol. Phys.* **94,** 199 (1998).

84 R. Polak, *Chem. Phys.* **232,** 25 (1998).

85 J. S. Wright, G. A. DiLabio, D. R. Matusek, P. B. Corkum, M. Y. Ivanov, C. Ellert, R. J. Buenker, A. B. Alekseyev, and G. Hirsch, *Phys. Rev. A* **59,** 4512 (1999).

86 M. M. Teixidor, F. Pirani, P. Candori, S. Falcinelli, and F. Vecchiocattivi, *Chem. Phys. Lett.* **379,** 139 (2003).

87 M. Alagia, B. G. Brunetti, P. Candori, S. Falcinelli, M. M. Teixidor, F. Pirani, R. Richter, S. Stranges, and F. Vecchiocattivi, *J. Chem. Phys.* **120,** 6985 (2004).

88 J. T. Tate and P. T. Smith, *Phys. Rev.* **39,** 270 (1932).

89 D. Rapp, P. Englander-Golden, and D. D. Briglia, *J. Chem. Phys.* **42,** 4081 (1965).

90 L. J. Kieffer and G. H. Dunn, *Rev. Mod. Phys.* **38,** 1 (1966).

91 N. A. Love and S. D. Price, *Int. J. Mass Spectrom.* **233,** 145 (2004).

92 N. A. Love and S. D. Price, *Phys. Chem. Chem. Phys.* **6,** 4558 (2004).

93 H. C. Straub, B. G. Lindsay, K. A. Smith, and R. F. Stebbings, *J. Chem. Phys.* **105,** 4015 (1996).

94 H. C. Straub, P. Renault, B. G. Lindsay, K. A. Smith, and R. F. Stebbings, *Phys.*

72 F. R. Bennett and I. R. McNab, *Chem. Phys. Lett.* **251,** 405 (1996).

73 G. Parlant, J. Senekowitsch, S. O' Neil, and D. R. Yarkony, *J. Chem. Phys.* **94,** 7208 (1991).

74 A. S. Mullin, D. M. Szaflarski, K. Yokoyama, G. Gerber, and W. C. Lineberger, *J. Chem. Phys.* **96,** 3636 (1992).

75 M. Lundqvist, D. Edvardsson, P. Baltzer, M. Larsson, and B. Wannberg, *J. Phys. B-At. Mol. Opt. Phys.* **29,** 499 (1996).

76 M. Larsson, P. Baltzer, S. Svensson, B. Wannberg, N. Martensson, A. N. Debrito, N. Correia, M. P. Keane, M. Carlssongothe, and L. Karlsson, *J. Phys. B-At. Mol. Opt. Phys.* **23,** 1175 (1990).

77 R. I. Hall, G. Dawber, A. McConkey, M. A. MacDonald, and G. C. King, *Phys. Rev. Lett.* **68,** 2751 (1992).

78 D. Mathur, *Phys. Rep.* **225,** 193 (1993).

79 J. Senekowitsch and S. O'Neil, *J. Chem. Phys.* **95,** 1847 (1991).

80 S. G. Cox, A. D. J. Critchley, P. S. Kreynin, I. R. McNab, R. C. Shiell, and F. E. Smith, *Phys. Chem. Chem. Phys.* **5,** 663 (2003).

81 A. J. Yencha, A. M. Juarez, S. P. Lee, G. C. King, F. R. Bennett, F. Kemp, and I. R. McNab, *Chem. Phys.* **303,** 179 (2004).

82 A. E. Slattery, T. A. Field, M. Ahmad, R. I. Hall, J. Lambourne, F. Penent, P. Lablanquie, and J. H. D. Eland, *J. Chem. Phys.* **122,** 084317. (2005).

83 M. Urban, G. H. F. Diercksen, and M. Jurek, *Mol. Phys.* **94,** 199 (1998).

84 R. Polak, *Chem. Phys.* **232,** 25 (1998).

85 J. S. Wright, G. A. DiLabio, D. R. Matusek, P. B. Corkum, M. Y. Ivanov, C. Ellert, R. J. Buenker, A. B. Alekseyev, and G. Hirsch, *Phys. Rev. A* **59,** 4512 (1999).

86 M. M. Teixidor, F. Pirani, P. Candori, S. Falcinelli, and F. Vecchiocattivi, *Chem. Phys. Lett.* **379,** 139 (2003).

87 M. Alagia, B. G. Brunetti, P. Candori, S. Falcinelli, M. M. Teixidor, F. Pirani, R. Richter, S. Stranges, and F. Vecchiocattivi, *J. Chem. Phys.* **120,** 6985 (2004).

88 J. T. Tate and P. T. Smith, *Phys. Rev.* **39,** 270 (1932).

89 D. Rapp, P. Englander-Golden, and D. D. Briglia, *J. Chem. Phys.* **42,** 4081 (1965).

90 L. J. Kieffer and G. H. Dunn, *Rev. Mod. Phys.* **38,** 1 (1966).

91 N. A. Love and S. D. Price, *Int. J. Mass Spectrom.* **233,** 145 (2004).

92 N. A. Love and S. D. Price, *Phys. Chem. Chem. Phys.* **6,** 4558 (2004).

93 H. C. Straub, B. G. Lindsay, K. A. Smith, and R. F. Stebbings, *J. Chem. Phys.* **105,** 4015 (1996).

94 H. C. Straub, P. Renault, B. G. Lindsay, K. A. Smith, and R. F. Stebbings, *Phys.*

*Rev. A* **52,** 1115 (1995).

95 R. Basner, M. Schmidt, K. Becker, V. Tarnovsky, and H. Deutsch, *Thin Solid Films* **374,** 291 (2000).

96 B. G. Lindsay, H. C. Straub, K. A. Smith, and R. F. Stebbings, *J. Geophys. Res.-Planets* **101,** 21151 (1996).

97 D. Rapp and P. Englander-Golden, *J. Chem. Phys.* **43,** 1464 (1965).

98 C. C. Tian and C. R. Vidal, *J. Phys. B-At. Mol. Opt. Phys.* **31,** 895 (1998).

99 Y.-K. Kim and M. E. Rudd, *Phys. Rev. A* **50,** 3954 (1994).

100 H. Deutsch, K. Becker, S. Matt, and T. D. Märk, *Int. J. Mass Spectrom.* **197,** 37 (2000).

101 M. A. Ali, Y. K. Kim, W. Hwang, and M. E. Rudd, *J. Korean Phys. Soc.* **32,** 499 (1998).

102 W. Hwang, Y. K. Kim, and M. E. Rudd, *J. Chem. Phys.* **104,** 2956 (1996).

103 H. Nishimura, W. M. Huo, M. A. Ali, and Y. K. Kim, *J. Chem. Phys.* **110,** 3811 (1999).

104 Y.-K. Kim, W. Hwang, N. M. Weinberger, M. A. Ali, and M. E. Rudd, *J. Chem. Phys.* **106,** 1026 (1997).

105 Y.-K. Kim and P. M. Stone, *Phys. Rev. A* **64,** 052707 (2001).

106 Y.-K. Kim and J. P. Desclaux, *Phys. Rev. A* **66,** 012708 (2002).

107 M. Gryzinski, *Phys. Rev. A* **138,** 305 (1965).

108 H. Deutsch, K. Becker, and T. D. Märk, *J. Phys. B-At. Mol. Opt. Phys.* **29,** L497 (1996).

109 H. Deutsch, K. Becker, S. Matt, and T. D. Märk, *J. Phys. B-At. Mol. Opt. Phys.* **32,** 4249 (1999).

110 H. Deutsch, K. Becker, R. Basner, M. Schmidt, and T. D. Märk, *J. Phys. Chem. A* **102,** 8819 (1998).

111 H. Deutsch, K. Becker, P. Defrance, U. Onthong, R. Parajuli, M. Probst, S. Matt, and T. D. Märk, *J. Phys. B-At. Mol. Opt. Phys.* **35,** L65 (2002).

112 H. Deutsch, C. Cornelissen, L. Cespiva, V. Bonacic-Koutecky, D. Margreiter, and T. D. Märk, *Int. J. Mass. Spectrom. Ion. Process.* **129,** 43 (1993).

113 H. Deutsch, K. Becker, and T. D. Märk, *Int. J. Mass Spectom. Ion Process.* **144,** L9 (1995).

114 H. Deutsch and T. D. Märk, *Nucl. Instrum. Meth. Phys. Res. B* **98,** 135 (1995).

115 H. Deutsch, K. Becker, S. Matt, and T. D. Märk, *Plasma Phys. Controlled Fusion* **40,** 1721 (1998).

116 J. H. D. Eland, *Photoelectron Spectroscopy*, Second Edition (1984).

117 I. Fischer, *Int. J. Mass Spectrom.* **216,** 131 (2002).

118 B. P. Tsai and J. H. D. Eland, *Int. J. Mass. Spectrom. Ion. Phys.* **36,** 143 (1980).

119 T. Masuoka, *J. Chem. Phys.* **115,** 264 (2001).

120 J. P. Maier, *Chimia* **34,** 219 (1980).

121 J. H. D. Eland, in *Electron Spectroscopy: Theory, Techniques and Applications*, edited by C. R. Brundle (Academic Press, London, 1979).

122 R. J. Saykally and R. C. Woods, *Ann. Rev. Phys. Chem.* **32,** 403 (1981).

123 J. F. Rendina and R. E. Grojean, *Appl. Spectrosc.* **25,** 24 (1971).

124 T. Veszpremi, *Chem. Phys. Lett.* **88,** 325 (1982).

125 P. Limao-Vieira, S. Eden, P. A. Kendall, N. J. Mason, A. Giuliani, J. Heinesch, M. J. Hubin-Franskin, J. Delwiche, and S. V. Hoffmann, *Int. J. Mass Spectrom.* **233,** 335 (2004).

126 J. P. Maier, *J. Electron Spectrosc. Relat. Phenom.* **66,** 15 (1993).

127 S. Willitsch, J. M. Dyke, and F. Merkt, *Mol. Phys.* **102,** 1543 (2004).

128 M. Sommavilla and F. Merkt, *J. Phys. Chem. A* **108,** 9970 (2004).

129 S. A. Boggis, J. M. Dyke, M. Tabrizchi, and R. Richter, *Mol. Phys.* **97,** 81 (1999).

130 T. Baer, *Adv. Chem. Phys.* **64,** 111 (1986).

131 J. H. D. Eland, *Int. J. Mass. Spectrom. Ion. Physics.* **12,** 389 (1973).

132 J. C. Creasey, D. M. Smith, R. P. Tuckett, K. R. Yokall, K. Codling, and P. A. Hatherly, *J. Phys. Chem.* **100,** 4350 (1996).

133 P. M. Guyon, *Laser Chem.* **11,** 131 (1991).

134 P. Lablanquie, M. Lavollee, J. H. D. Eland, F. Penent, and R. I. Hall, *Meas. Sci. Technol.* **6,** 939 (1995).

135 J. J. Thomson, *Philos. Mag.* **24,** 668 (1912).

136 A. L. Vaughan, *Phys. Rev.* **38,** 1687 (1931).

137 Y. Lee, S. R. Leone, P. Champkin, N. Kaltsoyannis, and S. D. Price, *J. Chem. Phys.* **106,** 7981 (1997).

138 S. D. Price, *J. Chem. Soc.-Faraday Trans.* **93,** 2451 (1997).

139 P. G. Fournier, J. H. D. Eland, P. Millie, S. Svensson, S. D. Price, J. Fournier, G. Comtet, B. Wannberg, L. Karlsson, P. Baltzer, A. Kaddouri, and U. Gelius, *J. Chem. Phys.* **89,** 3553 (1988).

140 J. C. Severs, W. J. Griffiths, F. M. Harris, S. R. Andrews, and D. E. Parry, *J. Chem. Soc. Faraday Trans.* **92,** 3293 (1996).

141 P. A. Hatherly, M. Stankiewicz, L. J. Frasinski, K. Codling, and M. A. Macdonald, *Chem. Phys. Lett.* **159,** 355 (1989).

142 W. Koch, B. Liu, T. Weiske, C. B. Lebrilla, T. Drewello, and H. Schwarz, *Chem.*

*Phys. Lett.* **142,** 147 (1987).

143 D. Kearney and S. D. Price, *Phys. Chem. Chem. Phys.* **5,** 1575 (2003).

144 N. Tafadar and S. D. Price, *Int. J. Mass Spectrom.* **223,** 547 (2003).

145 D. M. Szaflarski, A. S. Mullin, K. Yokoyama, M. N. R. Ashfold, and W. C. Lineberger, *J. Phys. Chem.* **95,** 2122 (1991).

146 J. H. D. Eland and D. Mathur, *Rapid Commun. Mass Spectrom.* **5,** 475 (1991).

147 D. M. Hanson, C. I. Ma, K. Lee, D. Lapianosmith, and D. Y. Kim, *J. Chem. Phys.* **93,** 9200 (1990).

148 M. Lundqvist, D. Edvardsson, P. Baltzer, and B. Wannberg, *J. Phys. B-At. Mol. Opt. Phys.* **29,** 1489 (1996).

149 D. Edvardsson, M. Lundqvist, P. Baltzer, B. Wannberg, and S. Lunell, *Chem. Phys. Lett.* **256,** 341 (1996).

150 A. D. J. Critchley, G. C. King, P. Kreynin, M. C. A. Lopes, I. R. McNab, and A. J. Yencha, *Chem. Phys. Lett.* **349,** 79 (2001).

151 M. Hochlaf, R. I. Hall, F. Penent, H. Kjeldsen, P. Lablanquie, M. Lavollee, and J. H. D. Eland, *Chem. Phys.* **207,** 159 (1996).

152 M. Larsson, G. Sundstrom, L. Brostrom, and S. Mannervik, *J. Chem. Phys.* **97,** 1750 (1992).

153 Y. Y. Lee, S. R. Leone, P. Champkin, N. Kaltsoyannis, and S. D. Price, *J. Chem. Phys.* **106,** 7981 (1997).

154 D. Mathur, *Phys. Rep.-Rev. Sec. Phys. Lett.* **391,** 1 (2004).

155 T. A. Carlson, *Photoelectron and Auger Spectroscopy* (New York, 1975).

156 C. I. Ma, K. D. Lee, D. Ji, D. Y. Kim, and D. M. Hanson, *Nucl. Instrum. Methods Phys. Res. Sect. A-Accel. Spectrom. Dect. Assoc. Equip.* **347,** 453 (1994).

157 D. Ceolin, C. Miron, M. Simon, and P. Morin, *J. Electron Spectrosc. Relat. Phenom.* **141,** 171 (2004).

158 U. Alkemper and F. von Busch, *J. Electron Spectrosc. Rel. Phenom.* **93,** 115 (1998).

159 G. Dawber, A. G. McConkey, L. Avaldi, M. A. MacDonald, G. C. King, and R. I. Hall, *J. Phys. B-At. Mol. Opt. Phys.* **27,** 2191 (1994).

160 A. J. Yencha, G. C. King, M. C. A. Lopes, J. D. Bozek, and N. Berrah, *Chem. Phys. Lett.* **315,** 37 (1999).

161 B. Krässig and V. Schmidt, *J. Phys. B-At. Mol. Opt. Phys.* **25,** L327 (1992).

162 A. J. Yencha, A. M. Juarez, S. P. Lee, G. C. King, F. R. Bennett, F. Kemp, and I. R. McNab, *Chem. Phys.* **303,** 179 (2004).

163 M. Hochlaf, R. I. Hall, F. Penent, J. H. D. Eland, and P. Lablanquie, *Chem. Phys.* **234,** 249 (1998).

164 T. E. Masters and P. J. Sarre, *J. Chem. Soc. Faraday Trans.* **86,** 2005 (1990).

165 S. M. Harper, W. P. Hu, and S. D. Price, *J. Phys. B-At. Mol. Opt. Phys.* **35,** 4409 (2002).

166 W. P. Hu, S. M. Harper, and S. D. Price, *Meas. Sci. Technol.* **13,** 1512 (2002).

167 S. M. Harper, W. P. Hu, and S. D. Price, *J. Chem. Phys.* **121,** 3507 (2004).

# Chapter 2

# Experimental Details

## Section 1 Experimental arrangement

## 2.1 Introduction

In this thesis two-dimensional (2D) time-of-flight (TOF) mass spectrometry is used to study the electron ionization of $N_2O$, $BCl_3$, $SF_6$ and $C_2H_2$. This experimental technique enables the single product ions, pairs of product ions and triples of product ions formed following the interaction of an electron with individual precursor gas molecules, to be detected, identified and quantified. The 2D technique also provides information on the energetics involved in the dissociation of any multiply charged ions formed. In this chapter the techniques and experimental set-up are discussed in detail for both the standard methodology used to determine relative partial ionization cross-sections (PICSs) and precursor specific PICSs and for the extension of this work to determine absolute PICSs and absolute precursor specific PICSs. These terms are defined in Chapter 1 and enable the contributions from various levels of ionization to the individual product ion yields to be quantified following an electron-molecule collision.

The experimental apparatus was originally designed[1,2] to study the ionization of reactive gas species. In these experiments the time that the gaseous molecules reside in the inlet system, before reaching the ionization region of the TOF mass spectrometer, was minimised to reduce species decomposition and thus produce reliable data for inherently unstable molecules. Hence, the gas inlet system consists of a wide bore, high conductance Teflon/glass inlet and was kept at low pressures so that the molecules rapidly enter the ionization region before significant decomposition could occur. The individual preparation of each target molecule studied in this thesis is presented within the relevant chapter. However, the gaseous species selected for use in this thesis were generally commercial products used without further purification.

### 2.1.1 Time-of-flight mass spectrometry

TOF mass spectrometry is a widely used experimental technique due to the relative conceptual simplicity of its design. TOF mass spectrometry works on the principle that when ions of different mass are accelerated to the same kinetic energy by a set of electric fields, they will have different velocities and, therefore, will have different flight times over a set distance. The flight time of a particular ion $t_{tof}$ can be derived, as shown in Appendix A, using a combination of Newtonian mechanics and electrostatics, which yields a proportionality relationship between $t_{tof}$, and the square root of the ion's mass, $m$:

$$t_{tof} = k\sqrt{m} \qquad (2.1.1),$$

where $k$ is a constant dependent on the electric fields and apparatus geometry.

TOF mass spectrometry has a number of advantages over other mass spectrometric techniques. For example, ions of all masses can be detected simultaneously and at high speed. Therefore, a complete spectrum can be collected in a few microseconds and as such an entire mass spectrum can be recorded for each ionizing event. Another significant advantage is the simplicity of the design of a TOF mass spectrometer, as other mass spectrometric methods, such as magnetic sector mass spectrometry, rely on expensive or heavy magnets, and are often complex to align and construct. These properties make TOF mass spectrometry a good experimental technique for use in conjunction with pulsed ionization.

### 2.1.2 Time-of-flight mass spectrometer

The TOF mass spectrometer used for the experiments described in this thesis is of a standard Wiley-McLaren[3] two-field design with first order 'space focusing'. The TOF mass spectrometer incorporates three distinct regions; the source region, second acceleration region and a field-free drift region, with lengths $2D_1$, $D_2$ and $D_3$ respectively. The values of $D_1$, $D_2$ and $D_3$ used currently are presented in Section 2.1.2.1

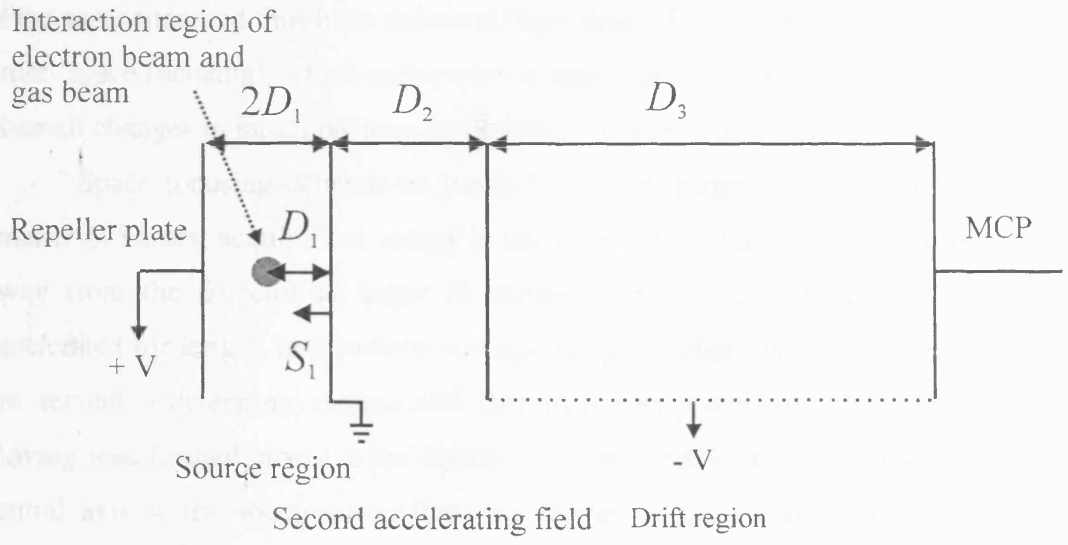


Figure 2.1.1: A schematic diagram of a two-field TOF system.

Ions are formed in the source region by electron ionization, and are then accelerated out of the source region by a pulsed positive voltage applied to the repeller plate. The ions then enter the second accelerating region where they are further accelerated before entering the field-free drift region and impinge on a multi-channel plate (MCP) detector. Therefore, to record a mass spectrum the ion flight time between the source region and the detector must be determined, Eq. (2.1.1).

### 2.1.2.1 Focusing

Using the experimental set-up shown in Figure 2.1.1, ions with the same mass-to-charge ratio should ideally have an identical flight time in the TOF mass spectrometer. However, when the electric field is applied to the source region, the ions will have some initial spatial distribution and therefore each ion will have an initial potential energy dependent on its initial position in the source region. The variable $S_1$, shown in Figure 2.1.1, represents the displacement of an individual ion's position in the source region from the entrance to the second accelerating region. After acceleration, the final energy of identical mass ions will therefore not be single-valued. As a consequence there will be a distribution in ion flight times dependent on the ion's initial position in the source region, centred on the 'predicted' ion flight time (if all ions were formed at $S_1$=$D_1$). To reduce this detected ion flight time distribution and produce the highest possible mass resolution, the mass spectrometer is designed so that the ions are 'focused'. Focusing attempts to ensure that, regardless of an ion's initial velocity or position in the source region, ions of the same mass-to-charge ratio arrive at the detector

at the same time and thus have the same flight time. This experimental set-up uses first order 'space focusing', which endeavours to ensure that ion flight times are independent of small changes in initial position in the source region to first order.[4]

Space focusing depends on the fact that ions formed closer to the detector, at smaller $S_1$ values, acquire less energy in the source field than those ions formed further away from the detector at larger $S_1$ values. Ions formed at larger $S_1$ values are accelerated for longer, and so have correspondingly higher kinetic energies on entering the second accelerating region, and therefore may eventually overtake the slower moving ions formed closer to the detector. Consequently, there is a position along the central axis of the spectrometer that ions formed at large and small $S_1$ values reach simultaneously; this is the space focus plane. Wiley and McLaren[3] found the position at which the ions with initial source positions $S_1 = D_1 \pm \frac{1}{2}\delta S_1$ pass each other by setting the derivative of the TOF to zero with respect to $S_1$, shown in Eq. (2.1.2). To clarify this statement, first order 'space focusing' requires that there should be no variation in the ion flight time, $t_{tof}$, with respect to the initial position of the ion in the source region, $S_1$, under conditions where the ion's initial energy $U_0$=0 and $S_1$=$D_1$:[4]

$$\left(\frac{\partial t_{tof}}{\partial S_1}\right)_{(U_0=0,S_1=D_1)} = 0 \qquad (2.1.2).$$

Eq. (2.1.2) can then be applied to the equation for the total flight time of an ion in a two-field TOF mass spectrometer, shown in Appendix A and B, to obtain an expression for the first order focus requirements, Eq. (2.1.3). An expression for $D_3$ is obtained in terms of a new parameter $k_0$, where it is assumed that the ion's initial kinetic energy is zero and that the ion is formed in the centre of the source region ($S_1$=$D_1$):[3]

$$D_3 = 2S_1 k_0^{\frac{3}{2}}\left(1 - \frac{D_2}{S_1(k_0 + k_0^{\frac{1}{2}})}\right) \qquad (2.1.3),$$

$$k_0 = \frac{S_1E_{S_1} + D_2E_{D_2}}{S_1E_{S_1}} = 1 + \frac{D_2E_{D_2}}{S_1E_{S_1}} \qquad (2.1.4).$$

Where $E_{S_1}$ and $E_{D_2}$ represent the electric field strength in the source and accelerating regions respectively. Eq. (2.1.4) shows that for a two-field TOF mass spectrometer it is the ratios of electric field strength and lengths, both with respect to the source region, that are key in the space focusing conditions. Therefore, 'space focusing' can be achieved by adjusting the ratio of $E_{D_2}/E_{S_1}$, with fixed values of $S_1$, $D_2$ and $D_3$ values for a two-field experiment, in contrast with a one-field TOF mass spectrometer which

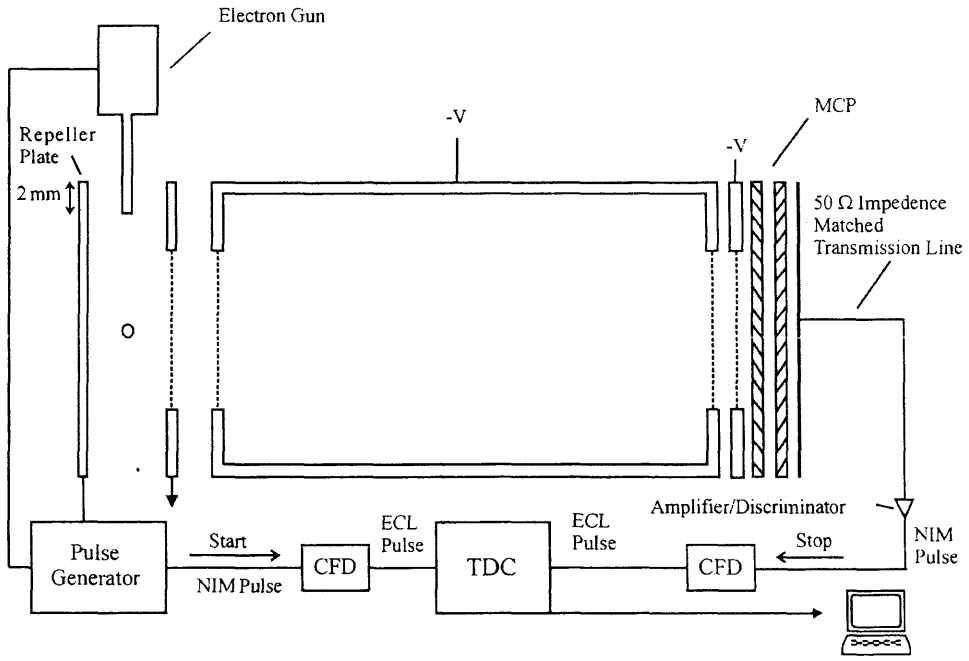


Figure 2.1.2: A schematic diagram of the TOF mass spectrometer set-up. The gas inlet is perpendicular to the plane of the figure and is not shown.

### 2.1.2.3 Source Region

Target gas molecules are ionized following interaction with a pulsed electron beam in the source region of the mass spectrometer. Ionization occurs at the centre of the source region where the target gas jet intersects with the pulsed electron beam. The target gas molecules and the electron beam are transported to the centre of the source region *via* hypodermic needles. The end of the hypodermic needle transporting the target gas molecules was positioned approximately 2 mm from the TOF mass spectrometer's axis. The end of the hypodermic needle transporting the electron beam was positioned approximately 2 mm into the source region. The target gas and electron beam hypodermic needles are mounted perpendicular to one another.

A pulse generator, run at 50 kHz, controls the pulsing of the electron gun, the pulsing of the repeller plate within the source region and also sends the 'start' signal to the data collection electronics. The electron gun, Figure 2.1.3, consists of a filament, stainless steel base plate and optics (extraction lens and focusing lens), which serve to extract and transport the electrons from the filament to the needle entrance in the source region. Without a 'start' trigger from the pulse generator the electron gun base plate is

held at a bias potential to stop the electrons reaching the needle entrance (between –65 to -250 V). When a 'start' trigger is received from the pulse generator a pulsed voltage is briefly applied to the base plate to allow the electrons to reach the needle entrance and enter the source region. To obtain well-resolved spectra the applied pulsed voltage is optimised at each electron energy.

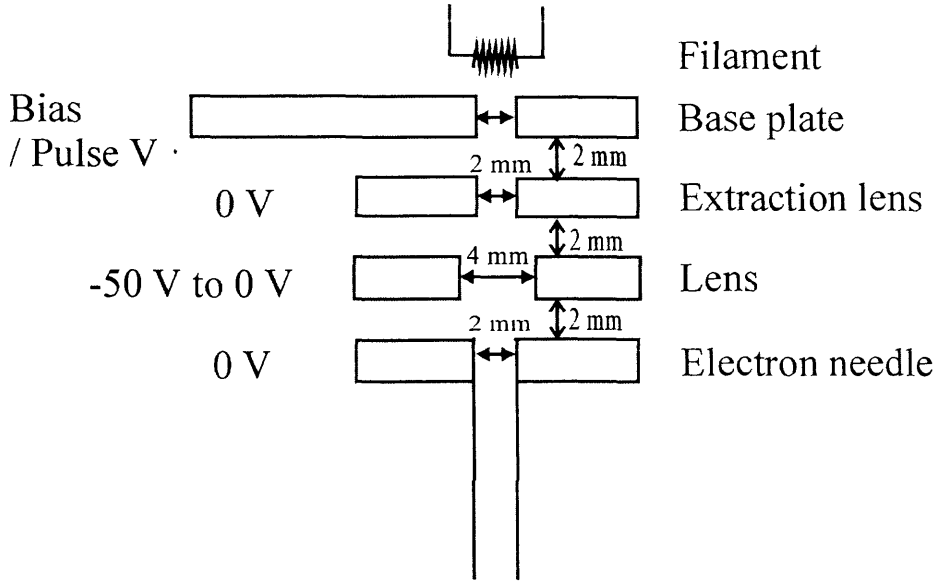


Figure 2.1.3: A schematic diagram of the electron gun. Voltages and approximate dimensions are indicated.

The electron gun produces 50 ns pulses of ionizing electrons at 50 kHz, at electron energies in the range 30-200 eV. Approximately 110 ns after the electron trigger pulse the repeller plate of the TOF mass spectrometer is pulsed from 0 V to +400 V to extract the ions formed following interaction of the target gas with the pulse of electrons from the source region. Then 340-400 ns after the extraction voltage is applied to the repeller plate a 'start' signal is sent to the Le Croy 3377 time-to-digital converter (TDC), see Figure 2.1.4. The 'start' signal is sent to the data collection electronics after application of the extraction voltage to the repeller plate to prevent any RF noise created by this extraction voltage pulse from being detected and recorded. The 'start' signal is sent from the pulse generator to the TDC *via* a constant fraction discriminator (CFD) in order to convert the NIM pulse produced by the pulse generator to an emitter coupled logic (ECL) pulse required by the TDC.

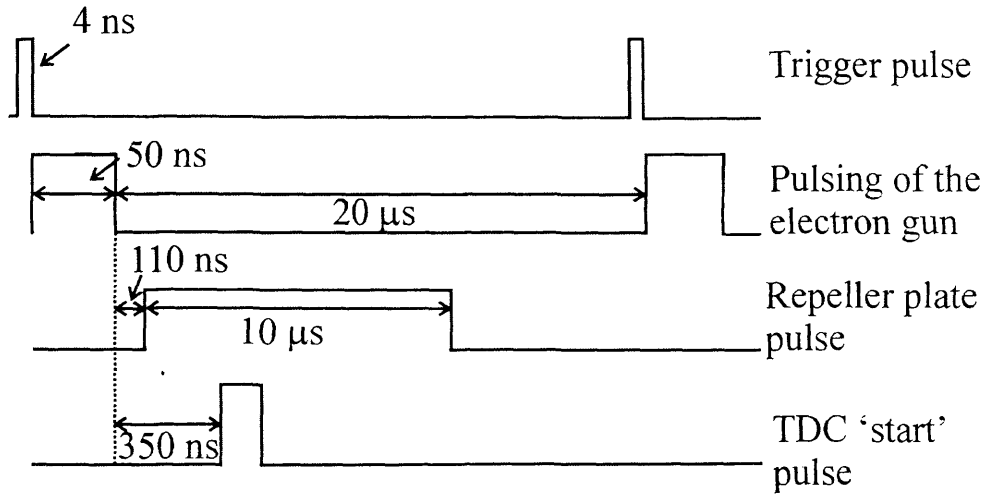


Figure 2.1.4: A schematic diagram of pulse timings for the TOF mass spectrometer.

Using a pulsed electron beam ensures that ionization occurs immediately before the ion extraction voltage is applied to the repeller plate, and thus the majority of discrimination effects in the mass spectra are removed.[6] The pulsed electron beam serves to reduce the time ions reside in the source region, ensuring that there is limited time for the energetic fragment ions formed, such as lighter monocations or dications, to leave the focused volume and therefore the majority of these energetic ions will be detected at the MCP. As detailed by Bruce and Bonham,[6] to enable quantitative data to be extracted from mass spectra one must carefully confirm that no mass discrimination effects exist. Mass discrimination effects include a variety of subtle points. Specifically, Bruce and Bonham found that following the electron ionization of argon the relative intensity of $Ar^{2+}$ and $Ar^{+}$ ions were dependent on the background argon pressure, the energy with which the ions hit the MCP detector and the setting used on the CFD in their system. In accord with their recommendations, the experimental operating conditions, defined below, were tested by measuring the relative intensities of $Ar^{2+}$ to $Ar^{+}$ in the mass spectra. The results confirmed that no mass discrimination effects were occurring in the experimental apparatus described in this thesis.

Ions formed following the interaction of the target gas with the pulse of electrons are then further accelerated in the second acceleration region into the field-free drift region of the TOF mass spectrometer.

#### 2.1.2.4 Detection region and data collection

The MCP detector used in these experiments is comprised of two identical plates constructed by Burle and made of special glass[7] with a diameter of 40 mm. These plates have an array of channels that pass through them of approximately 25 μm in diameter. These channels have a low work-function coating that releases electrons when the ions impact their surface. Each channel acts as a miniature electron multiplier, so for each detected ion approximately $10^6$ electrons are produced in the output pulse of the MCP.[7,8] The pulse of electrons from the back of the MCP is collected on a copper anode mounted on glass/epoxy circuit board and passed to a fast quad preamplifier and then to a pair of CFDs. The first CFD performs the discrimination process, whilst the second is used to produce an ECL pulse from the NIM output of the first CFD. The second CFD has an adjustable dead-time set to 32 ns. The dead-time is defined as the time following the discriminator output when the CFD cannot trigger again. To minimise the loss of ions, the minimum available dead-time of 32 ns was selected. Typical operating parameters are listed below in Table 2.1.1.

Table 2.1.1: Typical operating parameters for the TOF mass spectrometer used to record spectra at 200 eV.

| Parameter | Typical value |
|---|---|
| Electron energy | 200 eV |
| Pulsing period | 20 μs |
| Usual repeller plate voltage | +300 V to +400 V |
| Onset of repeller plate voltage | 110 ns after electron gun |
| Repeller plate pulse width | 10 μs |
| Drift tube voltage | -2000 V |
| Onset of TDC start pulse | 350 ns after voltage applied to repeller plate |
| MCP back/front voltage | -250/-2450 V |
| CFD dead-time | 32 ns |
| Discriminator threshold | 40 mV |

The ion arrival signals from the MCP are then amplified and discriminated and passed to the TDC. Once the TDC has received a 'start' pulse there is a finite period of time (a 10 μs 'time window') during which the TDC will count up to 32 'stop' pulses.

After this time period has elapsed any recorded ion flight times are then transferred from the TDC to a Le Croy 4302 memory module using a Fast Encoding and Readout ADC (FERA) interface to quickly pass data. If during this 'time window' a single stop pulse is received, one ion flight time is stored as an event in the memory, if the TDC receives two or three stop pulses in the 'time window' then two or three ion flight times are stored as a single event in each case, enabling the simultaneous recording of TOF mass spectra and coincidence spectra. The memory module accumulates 512 kbytes of data, which is then read by a PC *via* a SCSI interface in a DDC3000/PCI crate using a specially written data acquisition algorithm.[9] Whilst the contents of the memory module are downloaded to the PC the TDC is briefly stopped. This process takes around 1.5 s, and in this time no data is collected. Once the data contained in the memory module has been extracted the data acquisition continues, until the memory module is full again. This cycle of emptying and filling the memory module is continued until sufficient data is collected. Upon extraction of the data from the memory module, the specially written data acquisition algorithm (written in Visual Basic) is able to distinguish which memory events contain one, two or three ion flight times. This produces three individual data sets, containing events that have single ion flight times, two ion flight times (pairs) and three ion flight times (triples). The singles data is immediately downloaded onto a PC, while the pairs and triples data is stored for off-line processing. These data sets are discussed below.

### 2.1.3 Data Sets

The Visual Basic algorithm allows the distinction between memory events that contain one, two or three ion arrival times, which produces three data sets of ion flight times. The first data set contains events that have a single ion flight time. This list of ion flight times is continuously added to a histogram showing the number of ions versus the ion flight time (TOF mass spectrum), and is displayed on the PC. The spectrum is called a singles spectrum. As discussed previously, the coincident data sets, involving two or three ion flight times, are recorded and kept for offline analysis, unlike the singles data. The second data set contains events that have two ion flight times (a pair of ion flight times). This list of pairs of ion flight times is displayed as a 2D histogram of the number of ion pairs versus the two ion flight times, $t_1$ and $t_2$. This plot forms a coincidence spectrum, called a pairs spectrum. The third data set contains events that have three ion flight times. This list of ion flight times is initially displayed as a

histogram showing the number of ions versus the ion flight time. This histogram is called a triples mass spectrum. A series of pairs spectra are then plotted in coincidence with the different 'reference' ions present in the triples mass spectrum. These plots are termed coincident pairs spectra.

The calibration and presentation of the singles, pairs and triples spectra are discussed in the following sections.

### 2.1.3.1 Singles spectrum

A singles spectrum is a histogram showing the number of ions versus ion mass, recorded at a particular ionizing electron energy. A singles spectrum is calibrated by selecting two known ion peaks and their respective ion flight times, Eq. (2.1.5). For example, Figure 2.1.5 shows a singles spectrum of $N_2O$ gas, recorded at an ionizing electron energy of 200 eV. The ions $N^+$ and $N_2O^+$ were detected and the respective ion flight times were used to calibrate the mass spectrum by solving Eq. (2.1.5) simultaneously for both ions.

$$t_{tof} = k\sqrt{m} + c \qquad (2.1.5),$$

where $c$ is a constant required due to the time delays inherent with the electronics. Therefore, once values for $k$ and $c$ have been determined any ion peaks in the singles spectrum can be identified using Eq. (2.1.5).

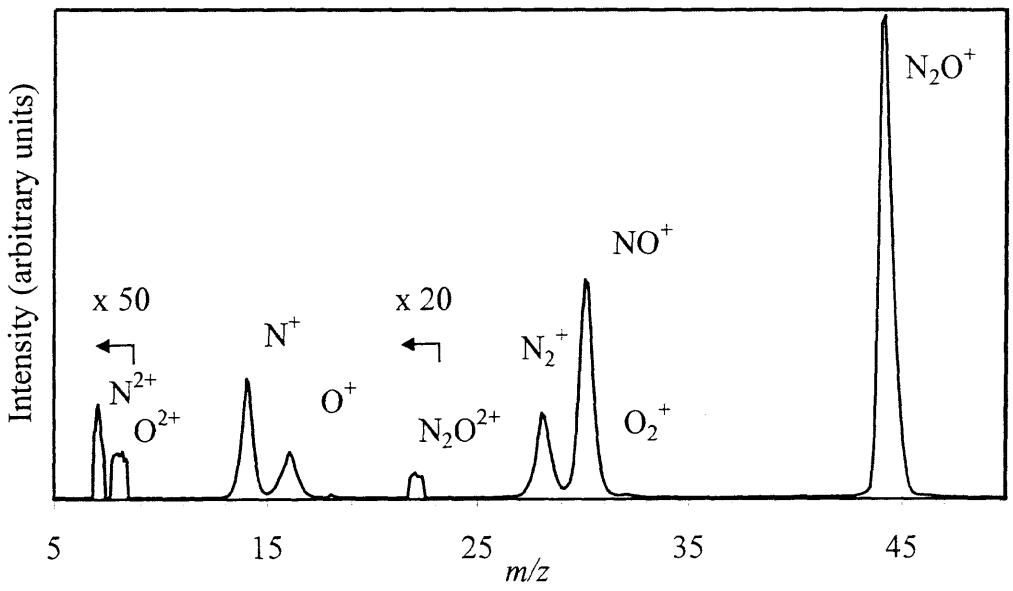


Figure 2.1.5: Singles spectrum of $N_2O$ recorded at 200 eV. The $N^{2+}$, $O^{2+}$ and $N_2O^{2+}$ ions are shown enlarged by 50, 50 and 20 times respectively.

#### 2.1.3.1.1 Ions from multiple ionization

When separating these ion flight times into the data sets containing one, two or three ion flight times, described in Section 2.1.3, there are complications associated with the collection and assignment of the number of ion flight times. For example, if an ion from dissociative double ionization is detected at the MCP but its correlated ion pair partner is missed due to the detection efficiency being less than 1, this ion flight time will be assigned to the data set containing single ion flight times, and plotted in the singles spectrum. The contribution of fragment ions from dissociative multiple ionization to the singles spectra is impossible to prevent experimentally. However, as detailed in Chapter 3, the contribution of fragment ions from multiple ionization to the singles spectrum can be numerically determined and is then subtracted from the intensity data of the singles spectrum in the data processing.

### 2.1.3.2 2D ion coincidence technique

To distinguish between monocations formed *via* dissociation of a singly charged ion and those resulting from dissociation of a dication or trication the experiment described in this thesis is coupled with a 2D ion coincidence technique. The 2D ion coincidence technique allows ion pairs formed following multiply charged ion dissociation to be detected and identified. Using a technique such as 2D ion coincidence, information regarding the type of dissociation pathways, appearance energies and kinetic energy released upon multiply charged ion dissociation can be determined. In this thesis, the 2D ion coincidence technique is used primarily to identify ion pairs formed following dissociative double ionization and ion triples formed following dissociative triple ionization to quantify the proportion of ions formed *via* dissociative double and/or triple ionization to the total ion yields. However, where additional information can be provided regarding the energetics involved in a particular dissociation event, further investigations were performed and are detailed in the results presented in Chapters 4 and 5.

#### 2.1.3.2.1 Pairs spectrum

Events involving two ion arrivals at the detector are termed pairs, and generally consist of a pair of monocations or occasionally a dication and a monocation. In this thesis, quadruple ionization is assumed to be negligible, as will be discussed in more detail in Chapter 3. At electron energies up to 200 eV, the majority of the monocation pairs are formed *via* dissociative double ionization, and the ion pairs including a monocation and dication are formed largely *via* dissociative triple ionization. To produce a 'real' ion pair all ions must be formed from the same dissociation event, for example two fragment ions formed following a dicationic dissociation in the source region of the TOF mass spectrometer. Both ions are then accelerated out of the source region by a pulsed positive voltage applied to the repeller plate and into the second accelerating region where they reach the field-free drift tube and then impinge on the MCP detector. As these fragment ions are formed at the same instant in time, their arrival times at the detector will be correlated, where the lightest ion will arrive first followed by its correlated ion partner, see Figure 2.1.6.

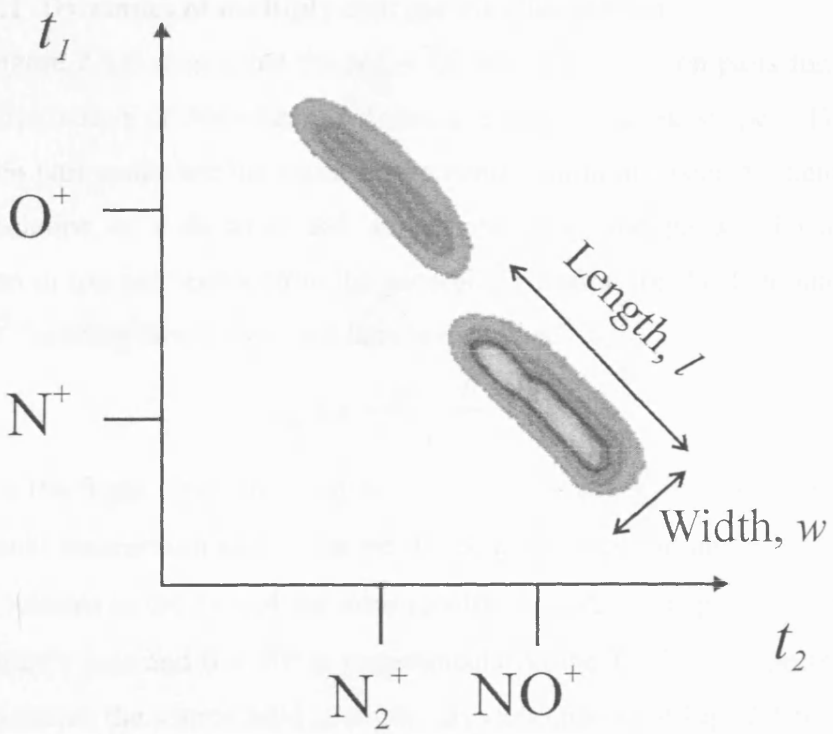


Figure 2.1.6: A schematic diagram of a pairs spectrum formed following electron ionization of $N_2O$ at 200 eV. The ion pairs: $N_2^+ + O^+$ and $NO^+ + N^+$ are shown.

The pairs data therefore allows the distinction between monocations formed following dissociative double and triple ionization and the monocations formed *via* single ionization, shown in the singles spectra. Additionally, the pairs spectrum allows dications formed *via* dissociative triple ionization to be distinguished from those dications formed *via* dissociative double ionization. By collecting the pairs data a much more detailed understanding of the formation and fragmentation of a molecule following ionization is obtained.

The pairs data are processed offline. A pairs spectrum is generated by plotting the flight times of coincident ion pairs, in a 2D histogram, which is equivalent to a 2D mass spectrum. The flight time of the lightest ion, $t_1$, is plotted on the $y$-axis against the flight time, $t_2$, of the correlated ion partner on the $x$-axis. Therefore, a histogram is produced of the ion pair peak intensity as a function of the flight times of the ion pairs formed *via* a dissociation event.

#### 2.1.3.2.1.1 Dynamics of multiply charged ion dissociation

Figure 2.1.6 shows that the $N_2^+ + O^+$ and $NO^+ + N^+$ ion pairs formed following electron ionization of $N_2O$ have a distinctive ion pair peak shape. These 'lozenge' shaped ion pair peaks are the result of the conservation of linear momentum following the dissociation of a dication and are termed 'real' ion pairs. To understand the correlation in ion pair momentum the general expression for the TOF under the Wiley-McLaren[3] focusing conditions used here is examined:

$$t_{\text{tof}} = t_0 - \frac{p\cos\theta}{E} \qquad (2.1.6),$$

where $t_0$ is the flight time for an ion with zero kinetic energy release, $p$ is the magnitude of the initial momentum of the ion on dissociation, $\theta$ is the angle of the dissociation direction relative to the axis of the mass spectrometer ($\theta = 0$ is parallel to the TOF mass spectrometer's axis and $\theta = 90°$ is perpendicular to the TOF mass spectrometer's axis) and $E$ represents the source field strength. By examination of Eq. (2.1.6), 'real' ion pair peak shapes should be linear with a gradient of -1, a detailed proof is shown in Section 3.1.1.3.5 of Chapter 3. However, experimentally recorded ion pair peaks are seen to be lozenge shaped because there will be a distribution of ion flight times resulting from the kinetic energy release (KER) upon dissociation and the direction of the initial impulse

upon dissociation, giving the ion pair peaks length and width, see Figure 2.1.6 and Figure 2.1.7.[10-12] The length, *l*, shown on Figure 2.1.6, of the ion pair peak is due to the deviation of the ion flight time from $t_0$, as the ion flight time may be shorter or longer depending on the KER and the direction of dissociation.[10-12] The width, *w*, shown on Figure 2.1.6, of the ion pair peak arises from random thermal velocities of the dication or trication before ionization/dissociation, the temporal resolution and, of course, the dication or trication dissociation mechanism.[10-12] The gradient of the ion pair peaks observed in the pairs spectra can provide information on the mechanism of a given multiply charged ion dissociation and is further described in Chapter 3.

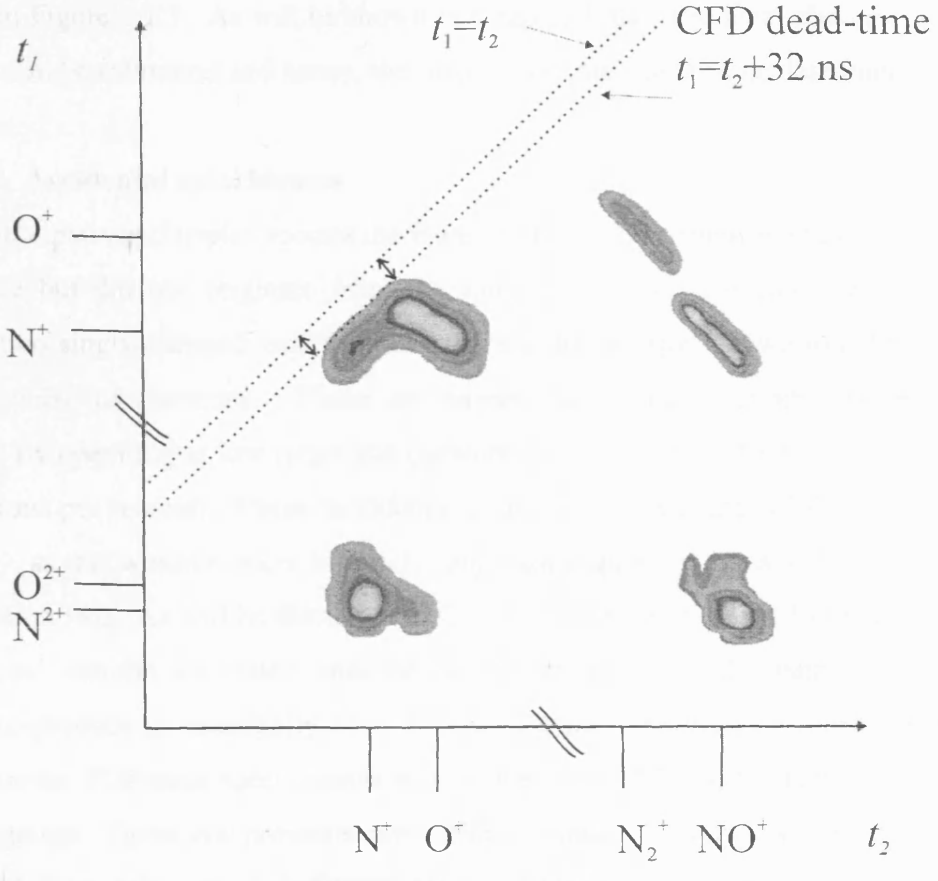


Figure 2.1.7: A schematic diagram of a pairs spectrum for $N_2O$, recorded at 200 eV. Eight dissociation channels were observed: $NO^+ + N^+$, $N_2^+ + O^+$, $N^+ + N^+ + O$, $N^+ + O^+ + N$, $N^{2+} + N^+ + O$, $N^{2+} + O^+ + N$, $O^{2+} + N^+ + N$ and $N^{2+} + NO^+$.

When a peak corresponding to an ion pair of the same or very similar mass is detected, the peak will be centred near the $t_1=t_2$ diagonal of the pairs spectrum. As previously discussed in Section 2.1.2.4, the CFD has a 32 ns dead-time, which prevents all the second stop pulses arriving within 32 ns of the first stop pulse being sent to the TDC. In such cases the first ion flight time will be recorded but its correlated partner ion will not, therefore this single ion arrival signal is plotted in the singles spectrum. For the majority of identical ion pairs this dead-time does not obscure the whole ion pair peak, as the ion pairs that have a large difference in flight times (>32 ns) are still detected and assigned to the pairs spectrum, for example the $N^+ + N^+ + O$ ion pair peak observed in Figure 2.1.7. As will be shown in Chapter 3, the 'lost area' obscured by the dead-time can be estimated and hence, the 'lost ion counts' can also be determined.

#### 2.1.3.2.1.2 Accidental coincidences

In the pairs and triples spectra there are ion pairs and triples that have arrived in coincidence but did not originate from the same dissociative ionization event. For example, two singly charged ions formed from the dissociation of two ions formed in the same pulse of electrons. These are termed 'accidental coincidences' and are minimised by operating at low target gas pressure ($1x10^{-6}$ Torr) and low ionization rate (200-300 ions per second). These 'accidental coincidences' are impossible to eliminate completely, as this would involve infinitely long data acquisition rates with an infinitely low ionization rate. As will be discussed in Chapter 3, the contribution from 'accidental coincidences' can be estimated and, hence, subtracted from the pairs and triples spectrum to produce an essentially 'true' pairs and triples spectrum. Typical operating pressures in the TOF mass spectrometer were in the order of 1-2 $x10^{-6}$ Torr, as recorded by an ion gauge. These low pressures are used in conjunction with low ionization rates of 200-300 ions per second (adjusted by the filament emission current). These experimental conditions ensure that there is very much less than one ionization event per pulse, hence dramatically decreasing the likelihood of 'accidental coincidences' in the coincidence spectra for both pairs and triples data and avoiding detector saturation.[13-15]

#### 2.1.3.2.1.3 Energetic ion collection

To accurately determine PICSs, it is crucial that the apparatus detects *all* ions with equal efficiency, irrespective of the initial kinetic energy or mass of the fragment ion. Ions formed *via* multiple ionization are highly energetic, as removal of more than one electron from a molecule requires a large amount of energy. Also, fragment ions formed *via* dissociative multiple ionization may have kinetic energy releases greater than 10 eV.

Given that ionization occurs in the centre of the source region, our experimental apparatus is designed to detect any ions with a translational energy component of less than 11 eV (from Eq. (2.1.7)) perpendicular to the axis of the mass spectrometer.[16] The maximum translational energy, $E$, an ion can possess perpendicular to the axis of the TOF mass spectrometer, and still be detected, is calculated by assuming a point ion source using Eq. (2.1.7):

$$E = \frac{1}{2} m v_t^2 \qquad (2.1.7),$$

where $v_t$ is the transverse velocity of the ion perpendicular to the axis of the TOF mass spectrometer. The transverse velocity of an ion can be calculated using Eq. (2.1.8). The example shown below is for the $O^+$ ion, of course this calculation is mass independent, where $r_{det}$ is the radius of the detector (20 mm) and the ion flight time $t_{tof}$ of the $O^+$ ion is 1.75 μs:

$$v_t = \frac{r_{det}}{t_{tof}} = \frac{2.00}{1.75} = 1.15 \text{ cm } \mu s^{-1} \qquad (2.1.8).$$

Using the value calculated for $v_t$, the value of $E$ = 11 eV is determined from Eq. (2.1.7).

Curtis and Eland[17] determined the kinetic energy release (KER) from a dicationic dissociation to be commonly less than 9 eV, so the majority of energetic fragment ions formed *via* dissociative double ionization should reach the detector in this apparatus, Figure 2.1.8 (a). However, ions with a significant velocity component (>11 eV) perpendicular to the axis of the TOF mass spectrometer will miss the detector, as shown schematically in Figure 2.1.8 (b).

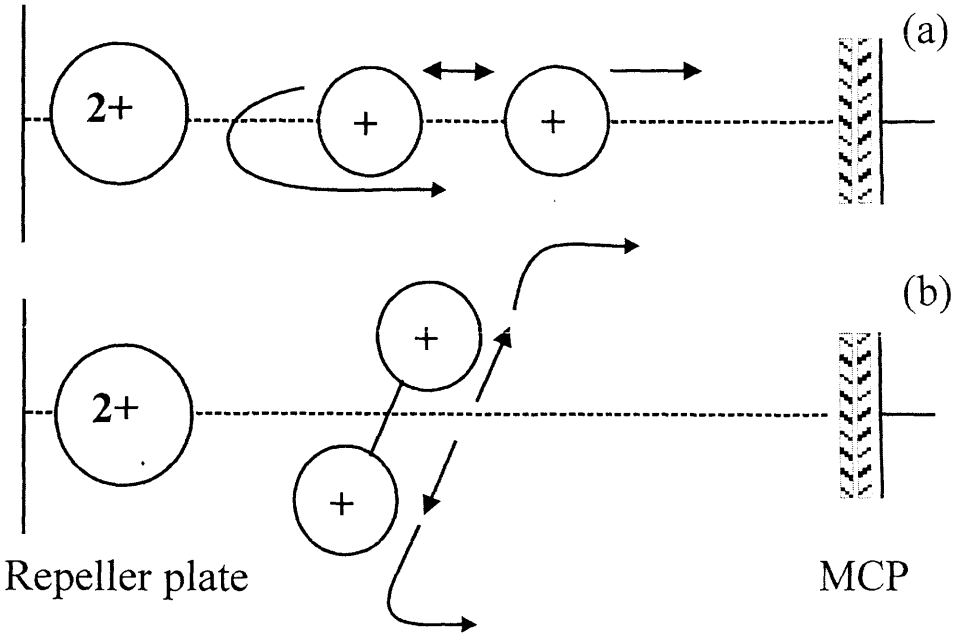


Figure 2.1.8: A schematic diagram to show how ions formed with a translational energy component of less than 11 eV perpendicular to the axis of the mass spectrometer (a) will be detected but ions formed with a translational energy component of more than 11 eV perpendicular to the axis of the mass spectrometer (b) will not be detected in the experimental set-up used in this thesis.

Experimentally, the ionic collection efficiency for energetic ions, formed *via* multiple ionization, can be determined from the shape of the signals in the relevant TOF difference spectrum. A TOF difference spectrum histograms the differences in ion flight times for each ion pair of interest from the pairs data. Figure 2.1.9(a) shows a TOF difference spectrum for the $NO^+ + N^+$ ion pair formed following dissociation of $N_2O^{2+}$. This ion coincidence peak is 'square topped', indicating no energetic ion loss. The peak width, $\omega$, arises because the TOF of each ion pair is strongly dependent on the direction of the initial impulse given to it by the multiply charged ion dissociation with respect to the axis of the TOF mass spectrometer. In contrast, Figure 2.1.9(b) shows a TOF difference spectrum for the $N^+ + O^+$ ion pair formed following dissociation of $N_2O^{2+}$. This ion coincidence peak is 'hollow' around $\Delta t_0$, that is the TOF difference the ions would have if they were formed with no kinetic energy, when there is energetic ion loss. Where energetic ion loss is observed the number of counts lost can be estimated using the fact that the peak shape should be 'square topped'. This procedure was used

for the $N^+ + O^+$ ion pair and is discussed in Chapter 4.

However, it should be noted that any fragment ion loss from single ionization cannot be quantified if such ions are formed with kinetic energies greater than 11 eV.

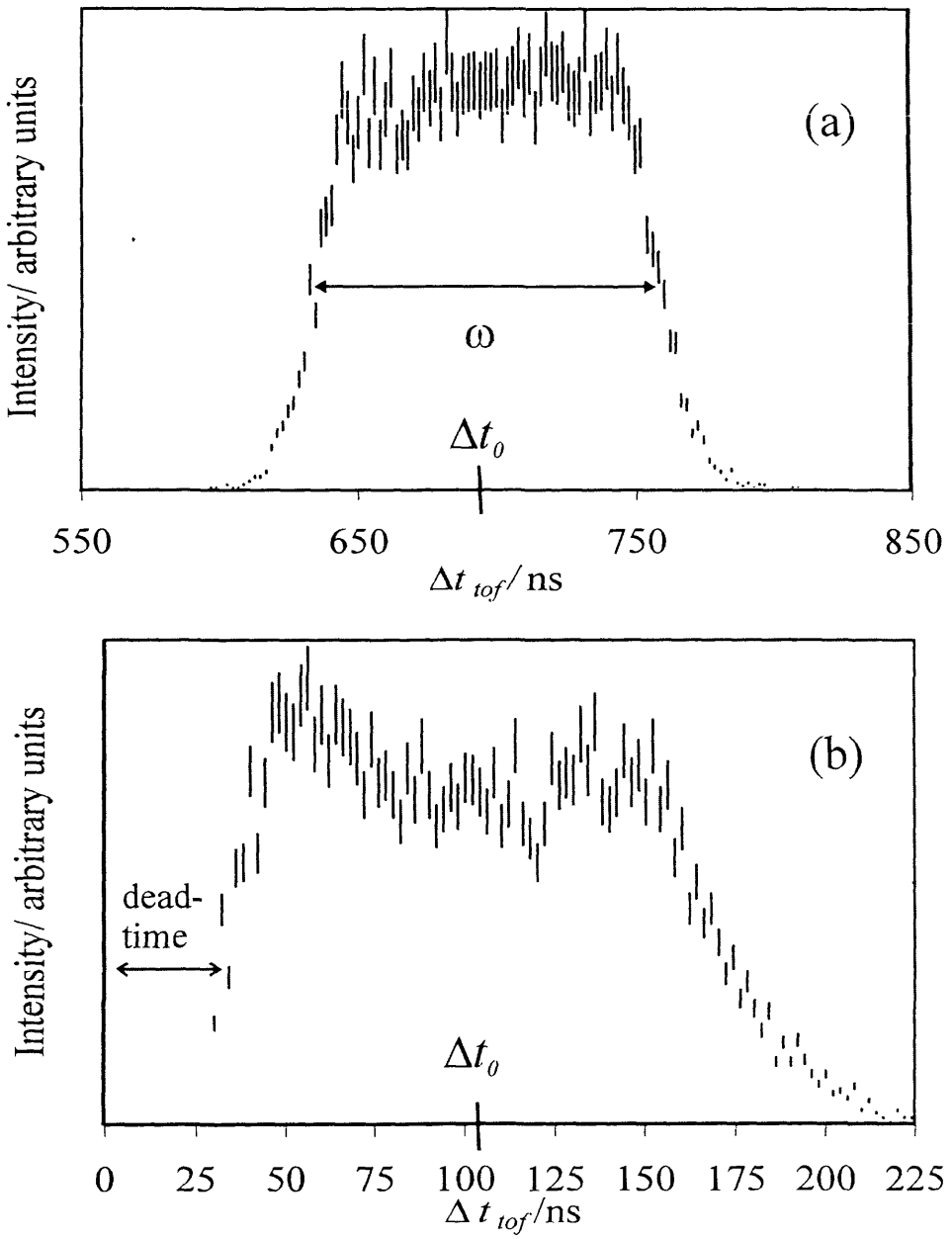


Figure 2.1.9: TOF difference spectra: (a) the $NO^+ + N^+$ ion pair demonstrates a prototypical 'square topped' TOF difference peak where there is no energetic ion loss. The peak width ω is shown and can be related to the KER upon dication fragmentation. (b) the $N^+ + O^+$ ion pair shows a TOF difference peak shape when there is energetic ion loss forming a characteristic 'hollow' appearance.

#### 2.1.3.2.2 Triples spectrum

Events involving three ion arrivals at the detector following a repeller plate pulse are termed 'triples'. To produce a 'real' ion triple spectrum all ions must be formed from the same dissociation event. Triples are initially displayed as a histogram showing the number of ions versus ion flight time, called a triples mass spectrum, Figure 2.1.10.

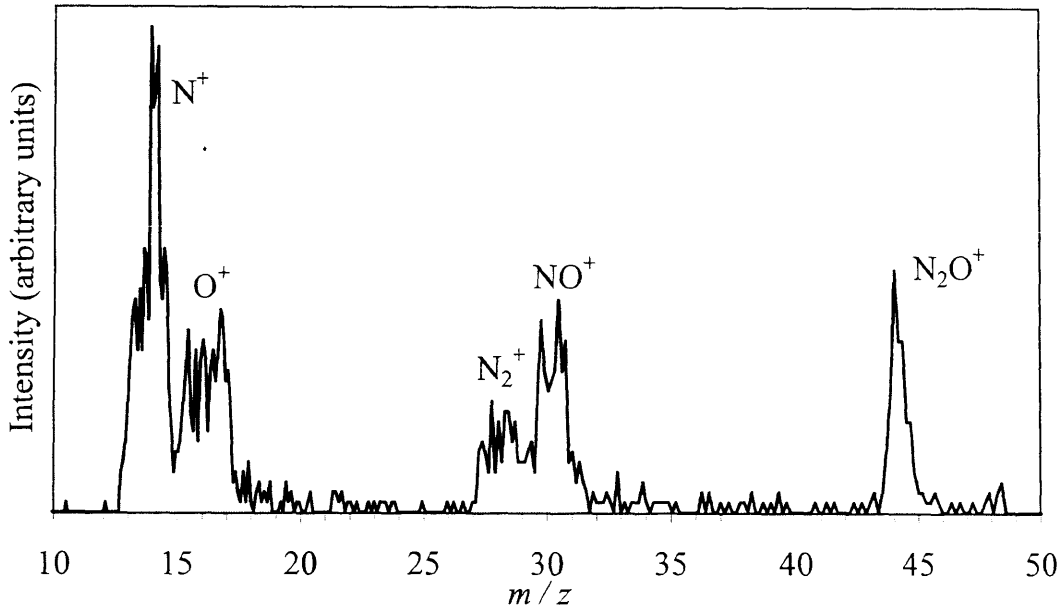


Figure 2.1.10: A triples mass spectrum for $N_2O$ recorded at 200 eV. The $N_2^+$, $NO^+$ and $N_2O^+$ ion peaks show that accidental coincidences are significant.

From the triples mass spectrum a particular reference ion is selected. A coincidence spectrum is then generated by plotting the flight times of ions coincident with the selected reference ion. Such a pairs spectrum is termed a coincident pairs spectrum (a histogram of the ion pair peak intensity coincident with the reference ion as a function of the flight times).

In the electron ionization experiments reported in this thesis, the majority of coincidence signals recorded consisted of two monocation arrivals. At the electron energies under investigation in this thesis of 30-200 eV, the probability of dissociative triple ionization, forming a dication and monocation pair and three monocations (triple), is significantly lower than the probability of dissociative double ionization. In a typical experiment performed and detailed in this thesis, at an electron energy of 200 eV, 50000 ion pairs and approximately 700 ion triples (including accidental coincidences) were recorded. Figure 2.1.10 shows the reduced quality of the triples mass spectrum due to

the small number of triples collected and the presence of accidental coincidences. The small number of triple coincidences detected further supports the neglect of quadruple and higher order ionization in the experiments reported in this thesis.

#### 2.1.3.2.2.1 Dynamics of multiply charged ion dissociation

The momentum correlation is more complicated for the triples than the pairs spectrum as the third charged body has some momentum. As such the ion pair peaks formed *via* the triples spectrum will not have the same characteristic peak shape as observed in the pairs spectrum. As a result of the low number of triple ionization events reported in this thesis, for the electron ionization of $N_2O$ and $SF_6$, no detail is given regarding the dynamics of these dissociative triple ionization events. To enable better counting statistics to be obtained, and hence information on the dynamics of dissociation, it would be necessary to significantly increase the data acquisition time and ionizing electron energy.[12] For the data presented in this thesis it was not feasible to increase the data acquisition time, but the experiments could, of course, be repeated to increase the data recorded following dissociative triple ionization.

## 2.1.4 Conclusions

These sections describe how the 2D TOF mass spectrometer is used to investigate single, double and triple ionization of gaseous molecules, which enables relative PICSs and relative precursor specific PICSs to be determined. This is further discussed in Chapter 3.

The following sections of this chapter will discuss how modification of the experimental technique, described in this chapter, will enable absolute PICSs and absolute precursor specific PICSs to be determined.

# Section 2 Commissioning an absolute cross-section measurement technique

## 2.2 Introduction

Any electron ionization cross-section can be defined by an equation analogous to the Beer-Lambert Law, previously discussed in Chapter 1:

$$I = I_0 e^{-nl\sigma} \qquad (2.2.1),$$

where $I$ is the electron flux after passing through the target gas, $I_0$ is the initial electron flux, $n$ is the number density of the target gas, $l$ is the electron pathlength and $\sigma$ is the cross-section. Using Eq. (2.2.1) the number of ionization events of a particular type is defined as $I_{events}$, where $I_{events} = I_0 - I$:

$$I_{events} = I_0(1 - e^{-nl\sigma}) \qquad (2.2.2),$$

and as $nl\sigma$ is small Eq.(2.2.2) can be recast:

$$I_{events} = I_0 nl\sigma \qquad (2.2.3).$$

Therefore, to determine an absolute cross-section, the initial electron flux, number density of the target gas, electron pathlength and the number of ionization events must all be known for each experiment.[18] Determination of these variables is non-trivial and experimentally challenging to achieve with acceptable levels of accuracy. To determine the experimental variables listed above (Eq. (2.2.3)) using the current experimental set-up, described in Section 1 of this chapter, would require several major modifications to the apparatus and would be difficult to achieve. Therefore, a normalisation technique was selected to determine absolute ionization cross-sections, enabling the current experimental set-up to be utilised with some 'simpler' experimental modifications. As described in Chapter 1, a normalisation technique decreases the requirement of Eq. (2.2.3) to determine all the experimental variables needed to produce an absolute cross-section, usually requiring only one of these variables to be known. A normalisation technique involves two gases, one with well-defined absolute PICSs such as argon or nitrogen, the other, X, with 'unknown' cross-sections which are to be determined. With

reference to Eq. (2.2.3), the number of particular ionizing events can be defined by introducing the ion detection efficiency, $f_i$, and equating this product to the recorded total ion signal intensity, $S$, for example of the $Ar^+$ ion:

$$I_{\text{events}} f_i = S(\text{Ar}^+) \tag{2.2.4},$$

$$nl\sigma'[\text{Ar}^+]I_0 f_i = S(\text{Ar}^+) \tag{2.2.5}.$$

With reference to Eq. (2.2.5), the absolute PICS of a particular ion is indicated by a prime. Using the gas laws, the number density of each gas is proportional to the gas pressure, $p_{\text{gas}}$, divided by the product of the gas constant, $R$, and temperature, $T$. These values can then be substituted into Eq. (2.2.5) to produce a definition for the signal intensity of each ion in terms of the individual pressure, gas constant, temperature, electron pathlength, absolute PICS for each ion, initial electron flux and the ion detection efficiency:

$$\frac{p_{\text{Ar}}}{RT} l\sigma'[\text{Ar}^+]I_0 f_i = S(\text{Ar}^+) \tag{2.2.6},$$

$$\frac{p_{\text{X}}}{RT} l\sigma'[\text{X}^+]I_0 f_i = S(\text{X}^+) \tag{2.2.7}.$$

The next stage involves taking a ratio of Eqs. (2.2.6) and (2.2.7), giving Eq.(2.2.8). The signal intensity of each selected ion is now only dependent on the product of the ratio of the individual gas pressure and individual ionization cross-section. Under identical experimental conditions the other parameters, defined in Eqs. (2.2.6) and (2.2.7), are approximately constant for each gas.

$$\frac{p_{\text{Ar}}}{p_{\text{X}}} \frac{\sigma'[\text{Ar}^+]}{\sigma'[\text{X}^+]} = \frac{S(\text{Ar}^+)}{S(\text{X}^+)} \tag{2.2.8}.$$

Utilising the present experimental set-up, the total signal intensities of each selected ion can already be determined, and thus, if the pressure of each gas can also be determined, this data can be normalised to the well-defined $\sigma'[Ar^+]$ values, enabling the absolute PICS for $X^+$, $\sigma'[X^+]$, to be determined at each electron energy. With reference to the methodology described above, it is also possible to extend the data analysis to determine values for the absolute precursor specific PICSs. The determination of absolute precursor specific PICSs is discussed in more detail in Chapter 3.

To determine absolute PICSs and absolute precursor specific PICSs, the experimental apparatus, described previously in Section 2.1.2.2, required modifications. These modifications involved the installation of a new gas inlet system and required a new gauge with the ability to measure low gas pressure. A new gas inlet system was

required to enable the simultaneous introduction of two gases for each experimental run. The filament current is known to fluctuate, and therefore, as discussed above, to ensure that the experimental conditions are equivalent for each gas, it was necessary to use both precursor gases simultaneously. The simultaneous use of two different gases creates a potential pressure measurement problem, as a pressure measurement of a gas mixture is then required. By forming a well-defined gas mixture prior to entry into the source region, or by allowing the gases to mix in the source region prior to ionization, individual gas pressures can be determined and therefore the problem of measuring the pressure of a gas mixture is overcome. In this thesis a single gas is allowed to enter the source region to a certain pressure, the second gas then enters the source region to form a gas mixture. By using various pressure measurements the gas mixture can then be defined, and is discussed in the following sections of this chapter.[19-21] Absolute PICSs can also be determined experimentally using the normalisation technique, described above, by employing only one input gas per experiment, or by normalising to one particular electron energy, which are preferable techniques if the experimental conditions remain stable throughout all experiments.[22,23] A brief overview of the methods used to determine absolute PICSs is presented in the following section.

### 2.2.1 Normalization techniques – absolute PICSs

There are two methods currently adopted that determine absolute PICSs by normalization to a gas with experimentally well-defined absolute PICSs. Firstly, Tian and Vidal[22] have obtained absolute PICSs by normalizing the recorded ion counts of a selected ion to those of argon, using a TOF mass spectrometric technique. The ion counts of argon are recorded at all electron energies with a particular argon gas pressure. The experiment is then performed with the 'unknown' molecule using the same backing pressure and identical experimental conditions, the ion counts are then recorded for each ion produced. A ratio of each ion intensity to the ion counts of $Ar^+$ is determined and normalised to the known absolute PICS[24] of $Ar^+$ for each electron energy.[22] This method produces absolute PICSs for each selected ion formed following ionization. The identical experimental conditions in the apparatus of Tian and Vidal[22] allow each gas to be used separately. Another approach used by Basner and co-workers[19,21,25] involves the simultaneous use of two gases, one with well-defined absolute PICSs such as argon. The experimental technique also utilises TOF mass

spectrometry where the source region is filled with the target gas under investigation and argon, which is used as a reference gas. The gases were used simultaneously and the pressures were determined using a spinning rotor gauge (SRG). At each electron energy, the relative PICSs for the ions formed following ionization of argon and from the 'unknown' molecule in the gas mixture were determined. The relative PICSs for the fragment ions formed following ionization of the unknown molecule were then put on an absolute scale by normalisation to the total argon ionization cross-section at 70 eV,[24] producing absolute PICSs for each selected ion formed following electron ionization.

The following sections detail the installation and testing of the second gas inlet system. The method of gas pressure measurement is also discussed along with a summary of the progress in understanding how to achieve the most accurate gas pressure measurements.

### 2.2.2 New gas inlet system

To enable the simultaneous use of two gases the apparatus was modified to incorporate a second gas inlet system. The second gas inlet is a replica of the first inlet system, having a wide bore, high gas conductance inlet system of glass and Teflon, used to rapidly draw molecules into the TOF mass spectrometer. Glass and Teflon are used to try to limit any species decomposition that may occur on metallic and non-metallic surfaces and to limit the time the gaseous molecules spend in the inlet system. The gas inlet systems are mounted on opposite sides of the stainless steel chamber and both produce a jet of gas into the source region perpendicular to the electron gun. The gas inlet systems are positioned so that ionization of both the reference and target molecules occurs at the centre of the source region, defined by 6 cm diameter plates supporting the grids. Both gas inlets are perpendicular to the electron gun, which serves to minimise the area occupied by the target gases before ionization occurs.

After installation of the second gas inlet, this new gas inlet system was tested to ensure that the mass and coincidence spectra produced were in agreement with the first gas inlet system. To do this several experiments were performed using argon and nitrogen gas. The intensity ratios of ions were determined and the new and old gas inlet needles were compared, see Figure 2.2.1 and Figure 2.2.2.

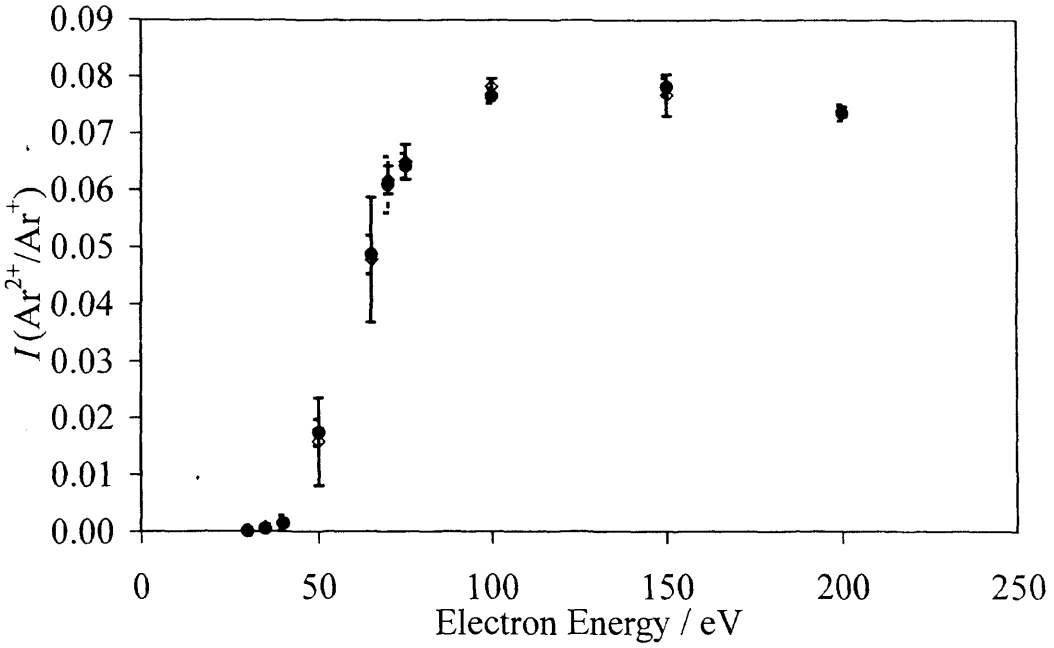


Figure 2.2.1: Intensity ratio of $Ar^{2+}/Ar^{+}$ using the old (●) and new gas needle inlets (◇). The points shown represent the average of 3 experimental determinations and the associated errors represent the standard deviation of these determinations.

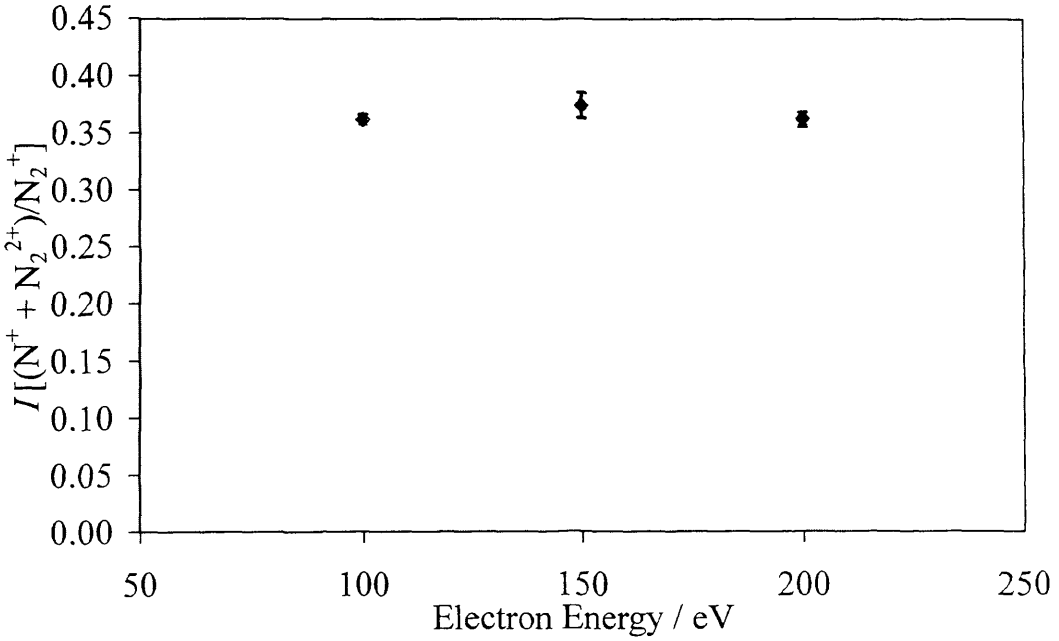


Figure 2.2.2: Intensity ratio of $(N^{+} + N_2^{2+})/N_2^{+}$ using the old (●) and new gas needle inlets (◇). The points shown represent the average of 10 experimental measurements and the associated errors represent the standard deviation of these determinations.

Figure 2.2.1 and Figure 2.2.2 illustrate that agreement is observed between the old and

new gas inlet systems for both argon and nitrogen, thus confirming that both gas inlet needles are essentially equivalent.

### 2.2.3 Pressure measurements

The experiments are performed at pressures of around $10^{-6}$ Torr as measured by an ion gauge. To achieve accurate gas pressure measurements at pressures of $10^{-6}$ Torr, only a Spinning Rotor Gauge (SRG) could be used, as a Baratron is not capable of accurately measuring pressures below $10^{-5}$ Torr.[26] The SRG gauge used in the following work was the SRG-2 CE model from MKS instruments. A cross-section through the SRG is illustrated in Figure 2.2.3. The key component of a SRG is a freely rotating stainless steel sphere (R), located in the vacuum (V), which is decelerated by friction when in contact with gas molecules. It is this relative deceleration that is proportional to the pressure of the gas. The stainless steel ball is accelerated to free spin (D) and held by two permanent magnets (M), the ball is stabilised by two opposing coils (A) that amplify the upper and lower magnetic fields as necessary. Four coils prevent any horizontal deviation (L). The signal is picked up by two coils that are switched in series (P).

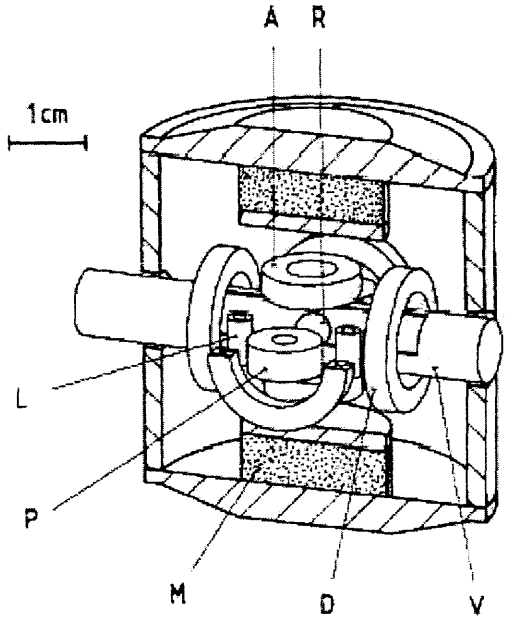


Figure 2.2.3: A cross-section through the SRG head. R is the stainless steel sphere (rotor), V is the vacuum enclosure, D is one of the four drive coils, M is one of the two permanent magnets, P is one of the two pick-up coils, L is one of the four coils of the lateral damping system and A is one of the two coils that pick-up and control the axial rotor position.[26]

The SRG was attached to the stainless steel chamber of the TOF mass spectrometer, ensuring the gauge was vertical to ±1°, which enabled the sphere to spin freely. The SRG was installed in the only available site near the source region of the mass spectrometer. It was imperative to locate the SRG as near to the source region as possible to provide accurate measurements of the pressure in the source region where both gas inlets are located.

The theory behind how the SRG works can be derived using several assumptions and is then modified to try to mimic reality more closely. Firstly, the surface of the stainless steel ball is assumed to be a 'technical' (perfectly smooth) surface. On a technical metal surface the angular distribution of molecules leaving the surface is approximately symmetrical with respect to the plane of the surface. Thus, gas molecules colliding with such a rotating technical surface will momentarily adsorb and then be re-emitted, without leading to any tangential force on the surface of the sphere, therefore only the tangential force of the incoming gas molecules needs to be considered.[27,28]

The spin axis of the sphere is taken to be the polar axis, where θ is the co-latitude angle along any meridian which increases from 0 at one pole to π at the opposite pole.[28] The incoming gas molecules are assumed to have an isotropic velocity distribution, giving a tangential surface velocity at $\theta$ of $r\omega\sin\theta$.

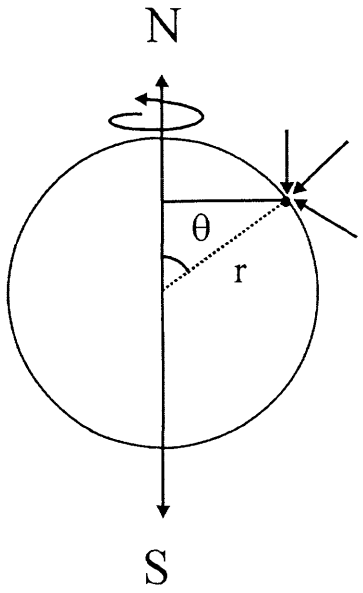


Figure 2.2.4: A schematic diagram of the spinning sphere, the arrows represent the incoming gas molecules and θ the angle of co-latitude created by the average incoming gas molecule arrival.

The axial angular momentum component of a molecule on the surface moving with the tangential surface velocity is given by Eq. (2.2.9). The rate of molecular impingement, $F$, (molecules per unit area per unit time) is also defined by Eq. (2.2.10)[28]:

$$L = mr^2\omega\sin^2\theta \qquad (2.2.9),$$

$$F = \frac{p\bar{c}}{4kT} \qquad (2.2.10),$$

where $m$ is the molecular mass, $r$ is the distance from the axis of rotation, $\omega$ is the angular velocity (equivalent to frequency) of the sphere, $\bar{c}$ is the mean molecular velocity, $p$ is the pressure, $k$ is Boltzmann's constant and $T$ is the absolute gas temperature. Eq. (2.2.9) represents the mean angular momentum transferred from the sphere by molecules striking at a given co-latitude angle, θ. The rate of momentum transfer to the molecules is therefore equal to the loss rate of angular momentum of the sphere due to molecular drag. To allow for the motion of the sphere, the loss rate of angular momentum is multiplied by the surface element of a sphere and integrated over the surface, Eq. (2.2.11), to produce Eq. (2.2.12), where $I$ is the moment of inertia of the sphere, $\rho$ is the density of the sphere and $RD$ is the residual drag on the sphere due to eddy currents created by the magnetic field.[26]

$$-\frac{\partial(I\omega)}{\partial t} = 2\pi r^4\omega mF\int_0^{\pi}\sin^3\theta d\theta + I\omega(RD) \qquad (2.2.11),$$

$$-I\dot{\omega} - \omega\dot{I} = \frac{8\pi r^4\omega mF}{3} + I\omega(RD) \qquad (2.2.12).$$

By substituting a value for $F$ into Eq. (2.2.12) and dividing by the angular momentum, $I\omega$, the relative retardation $(-\dot{\omega}/\omega)$ of the sphere can be expressed:

$$-\frac{\dot{\omega}}{\omega} = \frac{10p}{\pi r\rho\bar{c}} + RD + \frac{\dot{I}}{I} \qquad (2.2.13).$$

Eq. (2.2.13) represents the relative retardation (gaseous drag) of the sphere per unit time due to gas friction. The expression $\dot{I}/I$ represents changes in the sphere's moment of inertia due to thermal expansion, created predominantly when spinning the sphere to free spin. However, there is no way to directly correct for perturbations in the temperature of the sphere but these temperature fluctuations can be minimised by ensuring the stability of the residual drag, and as such are incorporated into the residual drag value.

Eq. (2.2.13) can also be expressed in terms of the time, $t$, required for a certain

number of sphere rotations:[26]

$$-\frac{\dot{\omega}}{\omega}=\frac{t_n-t_{n-1}}{t_n t_{n-1}} \qquad (2.2.14).$$

These time intervals are arranged so that the start of $t_n$ corresponds with the end of $t_{n-1}$. Eqs. (2.2.13) and (2.2.14) are limited by the assumption that there is total transfer of tangential impulse for a technical surface. For a 'rough' surface this assumption breaks down and not all molecules exchange tangential momentum upon collision. Hence it is necessary to correct for this assumption by using a gas friction coefficient, $\sigma_{coeff}$. For a rotating sphere, $\sigma_{coeff}$.normally lies between 0 and $4/\pi$. To determine a value for $\sigma_{coeff}$ a pressure calibration is necessary. The sphere is calibrated by MKS instruments against a gas friction manometer, which serves as a transfer standard.[28,29] Therefore, a value for $\sigma_{coeff}$ of 0.984 is known together with the diameter of the calibrated sphere, 4.50 mm, which has a density of 7.70 $gcm^{-3}$.[29] Note that it is still assumed that the gas molecules do not collide with one another.

Using Eqs. (2.2.13) and (2.2.14) an expression in terms of the pressure can be derived, the constants are defined below.

$$p=\left(\frac{1}{\sigma_{coeff}}K\frac{t_n-t_{n-1}}{t_n t_{n-1}}\right)-RD \qquad (2.2.15),$$

where $K=\frac{\pi}{10}r\rho\bar{c}$ and $\bar{c}=\sqrt{\frac{8RT}{\pi M}}$.

The term '*RD*' shown in Eq. (2.2.15) represents the additional correction to the pressure measurement caused by the residual drag (also termed offset), which is produced by the suspension of the stainless steel sphere in the magnetic field.[26,27] The origin and value of the residual drag is further discussed in Section 2.2.3.2.1.

### 2.2.3.1 Calibration of the SRG

The gas pressure measurement produced by the SRG is principally gas independent. However, the parameters of molecular mass, viscosity and temperature coefficient of viscosity must be input to produce an accurate gas pressure measurement. The SRG has preset parameters for some commonly used gases, but when using two gases simultaneously a methodology needed to be adopted to allow for the combination of these different gas parameters.

#### 2.2.3.1.1 Mass difference

The effect of the gas calibration on the pressure measurement produced by the SRG was first investigated by recording a background pressure measurement on the SRG when no gas was added to the source region. The SRG was calibrated to the preset air calibration, as the background residual gases present in the mass spectrometer are predominantly nitrogen and hydrogen, which are detected as $N_2^+$ and $H^+$ ions. However, when a gas such as argon is added to the source region, the gas pressure measurement on the SRG may be unreliable when calibrated to air. To test the effect that the gas calibration had on pressure measurements of different gases, the gas calibration was set to air and the individual gas. The intensity of the $N_2^+$ and $Ar^+$ ions formed following electron interaction with nitrogen and argon (added separately) was monitored as a function of the nitrogen or argon gas pressure, recorded on the SRG, when calibrated to air and the gas being studied, see Figure 2.2.5.

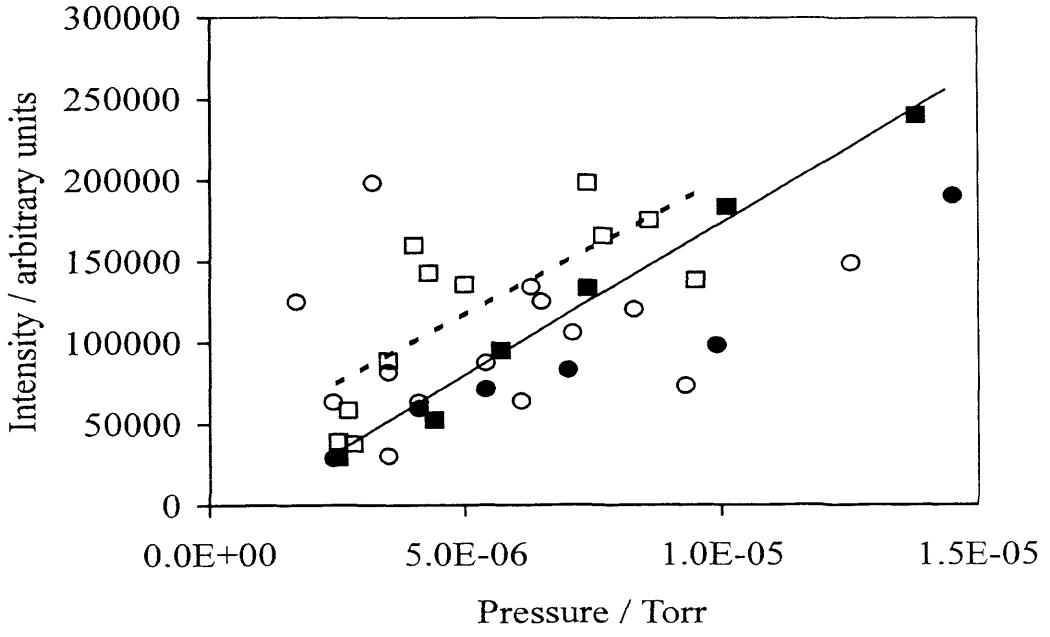


Figure 2.2.5: The intensity of $Ar^+$ and $N_2^+$ ions as a function of argon and nitrogen pressure measured on the SRG respectively. The intensity of $Ar^+$ ions is shown when the SRG is calibrated to air (○) and argon (□). The intensity of $N_2^+$ ions is shown when the SRG is calibrated to air (●) and nitrogen (■). The guidelines illustrate the 'increased' linear relationship observed for both argon and nitrogen when calibrated to argon and nitrogen respectively on the SRG.

Figure 2.2.5 illustrates that the intensity of the $N_2^+$ ions increases linearly with nitrogen pressure when the SRG is calibrated to air, due to the abundance of nitrogen in air. However, the intensity of $Ar^+$ ions is non-linear with increasing argon pressure when the SRG is calibrated to air. Therefore, Figure 2.2.5 shows a linear relation was observed between the pressure and the intensity of each gas when the gas calibration on the SRG was set to the respective gas (see the guidelines). A 'less' linear relationship was produced when the gas calibration was set to air, especially for the intensity of $Ar^+$ with increasing respective gas pressure. Figure 2.2.6 clearly illustrates that if the gas calibration used on the SRG is that of the respective gas, a linear relationship is indeed observed between the intensity of the $Ar^+$ and $N_2^+$ ions with respect to the gas pressure of argon and nitrogen.

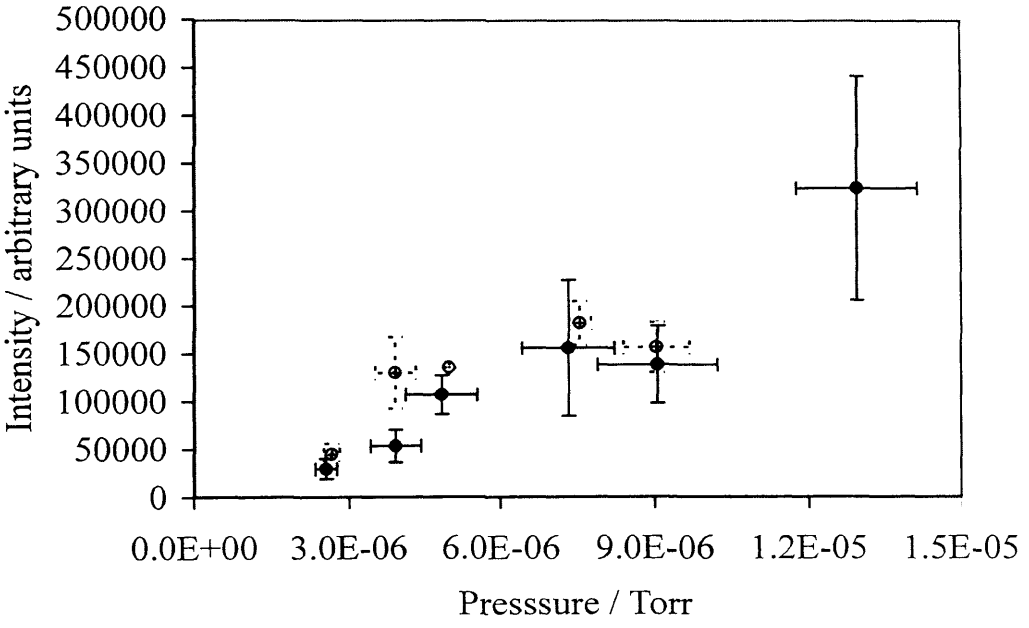


Figure 2.2.6: The intensity of $Ar^+$ (O) and $N_2^+$ (●) ions with respect to gas pressure, measured by the SRG, when using the gas calibration for argon and nitrogen respectively. The bars shown represent the standard deviation in the intensity range of three determinations over a range of pressures, where the range is also shown as the standard deviation of three determinations.

The gas calibration information discussed above, and illustrated in Figure 2.2.5 and Figure 2.2.6, shows that in order to produce a more realistic gas pressure measurement it is desirable to use the correct gas calibration for the precursor gas being used. However, as described previously, two gases are used simultaneously for each

experiment, and thus a strategy was adopted to allow for a pressure measurement of a gas mixture. Altering the gas calibration input changes the pressure measurement displayed on the SRG controller. The gas calibration on the SRG was therefore set to the first gas added (in general the reference gas) for each experiment and remained calibrated to this gas throughout the experimental run. When the second gas was added, this 'mixed' pressure measurement was still calibrated to the reference gas. It was therefore assumed that when the gas pressure ratio was determined this value must be corrected to allow for any mass difference between the two gases being utilised. To correct the pressure ratio for any difference in the mass of the gases a new term of 'mass factor' is introduced. To obtain this 'mass factor' a single precursor gas, for example argon or nitrogen gas, was let into the mass spectrometer to a range of constant pressures (measured with an ion gauge). For each constant pressure, the gas calibration on the SRG was altered from argon to nitrogen and *vice versa* for both argon and nitrogen gas. The pressure measurements obtained from the SRG were recorded and compared for each gas calibration on the SRG. This exchange of gas calibrations, whilst the gas pressure was constant, produced an approximately constant value, termed the 'mass factor' for the argon and nitrogen two-gas system. Having determined a mass factor, depending on the calibration of the SRG, the mixed pressure measurement was adjusted using this mass factor. However, after rigorous testing with combinations of gases with both differing and similar molecular mass systems, such as $Ar/N_2O$, $N_2/C_2H_2$ and $Ar/C_2H_2$, the method of utilising a 'mass factor' correction value for each two-gas system was determined to be unreliable. The 'mass factor' correction values determined experimentally for each two-gas system did not always concur with subsequent mathematical definitions, described below. It is therefore concluded that the 'mass factor' correction value determined experimentally for each system may also be dependent on other experimental variables, not yet fully understood, such as the individual gas flow into the source region. Consequently, a purely mathematical strategy was used to provide a definitive method for deriving the 'mass factor' correction for each two-gas system. It is still not fully understood why the experimental methodology does not agree with the mathematical approach and further experimental work is necessary to clarify the reason(s) for the disagreement. With the benefit of hindsight, a mathematical approach should have been adopted initially, to determine how the simultaneous use of gases with different molecular masses would effect the pressure measurements.

A mathematical strategy was adopted for determining the required gas pressure measurements to increase the confidence of the methodology. Using Eq. (2.2.15) each stage of the gas pressure measurements was defined in terms of a product of the constants and the time required for a certain number of sphere rotations.[26] When using two different gases simultaneously, obtaining an absolute pressure measurement of the 'gas mixture' becomes complicated. To produce reliable absolute gas pressures for each gas, six pressure measurements were recorded from the SRG per experiment. An initial pressure measurement, with no gas added, was recorded with the SRG calibrated to the reference gas, typically argon or nitrogen. This initial (background) pressure measurement is termed $p_1$. $p_1$ is expressed in terms of $t_{back}$, where $t_{back}$ represents the time for a certain number of sphere rotations, which incorporates the residual drag and sphere retardation due to background gas (background + offset). A pressure measurement is then recorded after addition of the reference gas (for example argon) before and after the experimental run is conducted. This produces an average pressure measurement termed $p_2$. The second gas, X, is then added to a required pressure, with the SRG still calibrated to the reference gas (argon). A pressure measurement is then recorded before and after the experimental run is conducted producing an average measurement, $p_3$. An average pressure measurement, over the duration of the experiment, was obtained for each term; $p_1$, $p_2$ and $p_3$:

$$p_1 = k\bar{c}_{Ar}(t_{back}) \qquad (2.2.16),$$

$$p_2 = k\bar{c}_{Ar}(t_{Ar} + t_{back}) \qquad (2.2.17),$$

$$p_3 = k\bar{c}_{Ar}(t_X + t_{Ar} + t_{back}) \qquad (2.2.18).$$

Eqs. (2.2.16)-(2.2.18) define each pressure measurement with respect to the time for a certain number of rotations for each situation when gas is added, $p_1$, $p_2$ and $p_3$, where $k$ and $\bar{c}$ are defined below as:

$$k = \frac{\pi r \rho}{10\sigma_{coeff}},$$

$$\bar{c} = \sqrt{\frac{8RT}{\pi M}},$$

noting that $\sigma_{coeff}$ is assumed to remain constant for different gases.[26] So using Eqs. (2.2.16)-(2.2.18) the gas pressure of argon can be defined, $p_{Ar}$, and the gas mixture of argon and gas X, $p_{mix}$, in terms of the average gas pressures read directly from the SRG, $p_1$, $p_2$ and $p_3$.

$$p_{Ar} = p_2 - p_1 = k\bar{c}_{Ar}(t_{Ar} + t_{back}) - k\bar{c}_{Ar}(t_{back}) \qquad (2.2.19),$$
$$p_{Ar} = k\bar{c}_{Ar}(t_{Ar})$$

$$p_{mix} = p_3 - p_2 = k\bar{c}_{Ar}(t_x + t_{Ar} + t_{back}) - k\bar{c}_{Ar}(t_{Ar} + t_{back}) \qquad (2.2.20).$$
$$p_{mix} = k\bar{c}_{Ar}(t_x)$$

However, the 'true' pressure $p_X$ of gas X should be calibrated to gas X, and not argon, and thus can be expressed as:

$$p_x = k\bar{c}_x(t_x) \qquad (2.2.21).$$

Consequently, a ratio of gas pressures is then determined using Eqs.(2.2.19) and (2.2.21). Eq. (2.2.20).is then substituted into Eq. (2.2.22) for $T_X$:

$$\frac{p_x}{p_{Ar}} = \frac{k\bar{c}_x(t_x)}{k\bar{c}_{Ar}(t_{Ar})} = \frac{k\bar{c}_x p_{mix}}{k\bar{c}_{Ar}(t_{Ar})k\bar{c}_{Ar}} \qquad (2.2.22).$$

Substituting Eq.(2.2.19) into Eq. (2.2.22) yields:

$$\frac{p_x}{p_{Ar}} = \frac{k\bar{c}_x(t_x)}{k\bar{c}_{Ar}(t_{Ar})} = \frac{\bar{c}_x p_{mix}}{\bar{c}_{Ar} P_{Ar}} \qquad (2.2.23).$$

From examination of Eq. (2.2.23) the only values that do not cancel are $\sqrt{(1/M_{gas})}$ for each gas within the constants $\bar{c}_{Ar}$ and $\bar{c}_x$. Therefore, the required gas pressure ratio can be expressed:

$$\frac{p_x}{p_{Ar}} = \frac{p_{mix}}{p_{Ar}} \frac{\sqrt{M_{Ar}}}{\sqrt{M_X}} \qquad (2.2.24).$$

By examining the mathematics behind the gas pressure measurement determined by the SRG, the only variable dependent on the gas in the pressure measurement ratio was determined to be equal to the ratios of the different molecular masses, $\sqrt{M_1}/\sqrt{M_2}$, of the two gases used. Therefore, the measured gas pressure ratio must be multiplied by the ratio of molecular masses to determine the gas pressure ratio of the two gases used.

This mathematical strategy, defined above, yields a relatively straightforward methodology for the determination of reliable gas pressure ratios for the selected two-gas systems being investigated. Indeed, as mentioned above, the gas pressure ratio is dependent on the molecular masses of the gases used for the two-gas system.

The methodology outlined above is further tested and discussed in detail in Chapter 3. Chapter 3 also illustrates that reliable absolute PICSs are determined, these results are presented in Chapters 3 and 7.

### 2.2.3.2 Gas flow

The $p_{mix}$ pressure measurement will always be the most challenging quantity to

determine accurately, as it assumes uniform mixing of the gases in the source region *ie* no gas density effects. However, the gas inlets produce jets of effusive gas, and thus the two gases may not mix as assumed. To achieve a uniform gas mixture of the two precursor gases in the source region of the TOF mass spectrometer the PTFE gas inlet tubing was removed from both the gas needles and re-located towards the back of the chamber. Following this relocation, the gases formed a more homogenous gas mixture prior to ionization, as demonstrated in Chapters 3 and 7.

#### 2.2.3.2.1 Residual Drag

The rotation of the stainless steel sphere in the magnetic field, used to suspend the sphere, produces eddy currents in the sphere, which lead to an additional drag on the sphere, called the residual drag (*RD*) or offset, Eq.(2.2.15).[26,27] The residual drag is dependent on the dimensions of the apparatus used with the SRG, the magnitude and direction of the sphere's magnetic moment and the temperature of the sphere. Therefore, the residual drag should be determined every time the sphere suspension is deactivated. The experimental methodology adopted above to determine the individual gas pressures already incorporates both the residual drag and the drag imparted by the gas or gases present at the instant of measurement, Eqs. (2.2.16)-(2.2.18). The actual gas pressure derived from the pressure measurements will be independent of the offset value used in the SRG, provided that all the pressure measurements required to produce the actual gas pressure for each gas are made with the same offset value.

For the initial absolute PICS determinations the pre-calibrated offset (residual drag) value of $2.50 \times 10^{-5}$ mbar ($1.43 \times 10^{-5}$ Torr) was utilised.[29] The value of the residual drag was subsequently set equal to zero on the SRG and used for all subsequent absolute PICS determinations detailed in Chapter 7. For experiments where the offset value was non-zero, the resultant actual gas pressures are equivalent, but the recorded pressure measurements, defined above, forming $p_1$, $p_2$ and $p_3$, are on a 'shifted' pressure scale. Table 2.2.1 illustrates the independence of the actual gas pressure with respect to the offset value.

To demonstrate experimentally the relationship between the actual gas pressure and the offset value an approximately constant argon gas pressure was used whilst the offset value was altered. Pressure measurements of $p_1$ and $p_2$ were recorded for each offset value. Table 2.2.1 shows the argon gas pressure to be identical, within the limits of error, for both offset values.

Table 2.2.1: Argon gas pressure determination using the pre-calibrated offset value and an offset value of zero. All pressure measurements are shown in Torr.

| Offset=$1.43\times10^{-5}$ | Offset=0 |
|---|---|
| $p_1=2.14\times10^{-5}$ | $p_1=3.57\times10^{-5}$ |
| $p_2=2.53\times10^{-5}$ | $p_2=3.95\times10^{-5}$ |
| $p_2-p_1=(2.53\times10^{-5})-(2.14\times10^{-5})$ | $p_2-p_1=(3.95\times10^{-5})-(3.57\times10^{-5})$ |
| $=\underline{0.39\times10^{-5}}$ | $=\underline{0.38\times10^{-5}}$ |

#### 2.2.3.2.2 Sampling Interval

The SRG has the option to produce a separate pressure measurement at time intervals of 1-60 seconds. It is preferable to use the largest time intervals possible between pressure measurements, as this increases the stability and accuracy of the measurement obtained. For practical purposes a 30 second sampling interval was used in these experiments, which provided adequate stability and accuracy of the pressure measurement and was applicable to the pressure range investigated here ($10^{-6}$ Torr).[26]

## 2.2.4 Experimental Procedure

The experimental procedure is unchanged from that previously described in Section 2.1.2.2 to Section 2.1.3. The ionization rate is kept low to try to limit the number of accidental coincidences in the pairs spectra.

#### 2.2.4.1 Experimental runtime

Experiments to determine the absolute PICSs were run until approximately 5000 ion pairs were collected. The collection of 5000 ion pairs represents a compromise between experimental runtimes that will produce sufficient counting statistics, whilst minimising any gas pressure change.

## 2.2.5 Conclusions

These sections describe how the 2D TOF mass spectrometer was modified to determine absolute PICSs and absolute precursor specific PICSs. These modifications included a new gas inlet system and pressure measurement gauge. The experimental methodology is discussed and is further tested and described in the following chapter.

## 2.3 References


1 C. S. S. O'Connor, N. C. Jones, and S. D. Price, *Int. J. Mass Spectrom. Ion Process.* **163,** 131 (1997).
2 C. S. S. O'Connor, N. C. Jones, and S. D. Price, *Chem. Phys.* **214,** 131 (1997).
3 W. C. Wiley and I. H. McLaren, *Rev. Sci. Instrum.* **26,** 1150 (1955).
4 D. P. Seccombe and T. J. Reddish, *Rev. Sci. Instrum.* **72,** 1330 (2001).
5 J. H. D. Eland, *Meas. Sci. Technol.* **4,** 1522 (1993).
6 M. R. Bruce and R. A. Bonham, *Z. Phys. D-Atoms Mol. Clusters* **24,** 149 (1992).
7 J. L. Wiza, *Nucl. Instrum. Meths.* **162,** 587 (1979).
8 Philips, *Data Handbook, Electron Multipliers,* (1991).
9 C. S. S. O'Connor, PhD Thesis: *The Properties of Molecular Ions*, University College London, 1999.
10 J. H. D. Eland, F. S. Wort, and R. N. Royds, *J. Elec. Spect. Rel. Phen.* **41,** 297 (1986).
11 J. H. D. Eland, *Mol. Phys.* **61,** 725 (1987).
12 J. H. D. Eland, in *Vacuum Ultraviolet Photoionization and Photodissociation of Molecules and Clusters* (World Scientific, Singapore, 1991), pp. 297.
13 M. R. Bruce, C. Ma, and R. A. Bonham, *Chem. Phys. Lett.* **190,** 285 (1992).
14 D. A. Hagan and J. H. D. Eland, *Org. Mass Spectrom.* **27,** 855 (1992).
15 L. J. Frasinski, M. Stankiewicz, P. A. Hatherly, and K. Codling, *Meas. Sci. Technol.* **3,** 1188 (1992).
16 P. Calandra, C. S. S. O'Connor, and S. D. Price, *J. Chem. Phys.* **112,** 10821 (2000).
17 D. M. Curtis and J. H. D. Eland, *Int. J. Mass Spectrom. Ion Process.* **63,** 241 (1985).
18 T. D. Märk and G. H. Dunn, *Electron Impact Ionization* (Springer-Verlag, New York, 1985).
19 R. Basner, M. Schmidt, K. Becker, V. Tarnovsky, and H. Deutsch, *Thin Solid Films* **374,** 291 (2000).
20 R. Basner, M. Schmidt, E. Denisov, K. Becker, and H. Deutsch, *J. Chem. Phys.* **114,** 1170 (2001).
21 R. Basner, M. Schmidt, E. Denisov, P. Lopata, K. Becker, and H. Deutsch, *Int. J. Mass Spectrom.* **214,** 365 (2002).
22 C. C. Tian and C. R. Vidal, *J. Phys. B-At. Mol. Opt. Phys.* **31,** 895 (1998).
23 M. Rao and S. K. Srivastava, *J. Phys. B-At. Mol. Opt. Phys.* **25,** 2175 (1992).
24 H. C. Straub, P. Renault, B. G. Lindsay, K. A. Smith, and R. F. Stebbings, *Phys. Rev. A* **52,** 1115 (1995).
25 R. Basner, M. Schmidt, and H. Deutsch, *J. Chem. Phys.* **103,** 211 (1995).
26 J. K. Fremerey, *J. Vac. Sci. Technol.* **A3,** 1715 (1985).
27 J. K. Fremerey, *Rev. Sci. Instrum.* **42,** 753 (1971).
28 Course material given at the National Institute of Standards and Technology, Vacuum Calibrations Using the Molecular Drag Gauge, (NIST, 1991).
29 Calibration sheet, MKS Instruments, (Germany, 2001).

# Chapter 3

# Data Collection and Data Analysis

## Section 1 Relative partial ionization cross-sections

## 3.1 Introduction

As discussed in Chapter 2, electron ionization 2D TOF mass spectrometry is utilised to study the single, double and triple ionization of gaseous molecules. In this chapter the analysis procedures used to extract information from the recorded spectra are detailed to determine both relative partial ionization cross-sections (PICSs) and relative precursor specific PICSs. This chapter then details the extension to the data analysis procedure, used after the apparatus modification discussed in Chapter 2, to determine absolute PICSs and absolute precursor specific PICSs.

### 3.1.1 Partial ionization cross-section determination

#### 3.1.1.1 Singles spectrum

Events involving a single ion arrival at the detector, following the repeller plate pulse, are termed 'singles' and the flight times associated with these events are displayed as a histogram of ion counts against flight time. This data produces a singles (mass) spectrum.

##### 3.1.1.1.1 Peak intensity determination

The intensities of these ion peaks in the singles spectra, $I[X^+]$, are determined by summing the counts in the peak, and applying a suitable background correction for the non-zero baseline, see cases (a) and (b) in Figure 3.1.1.

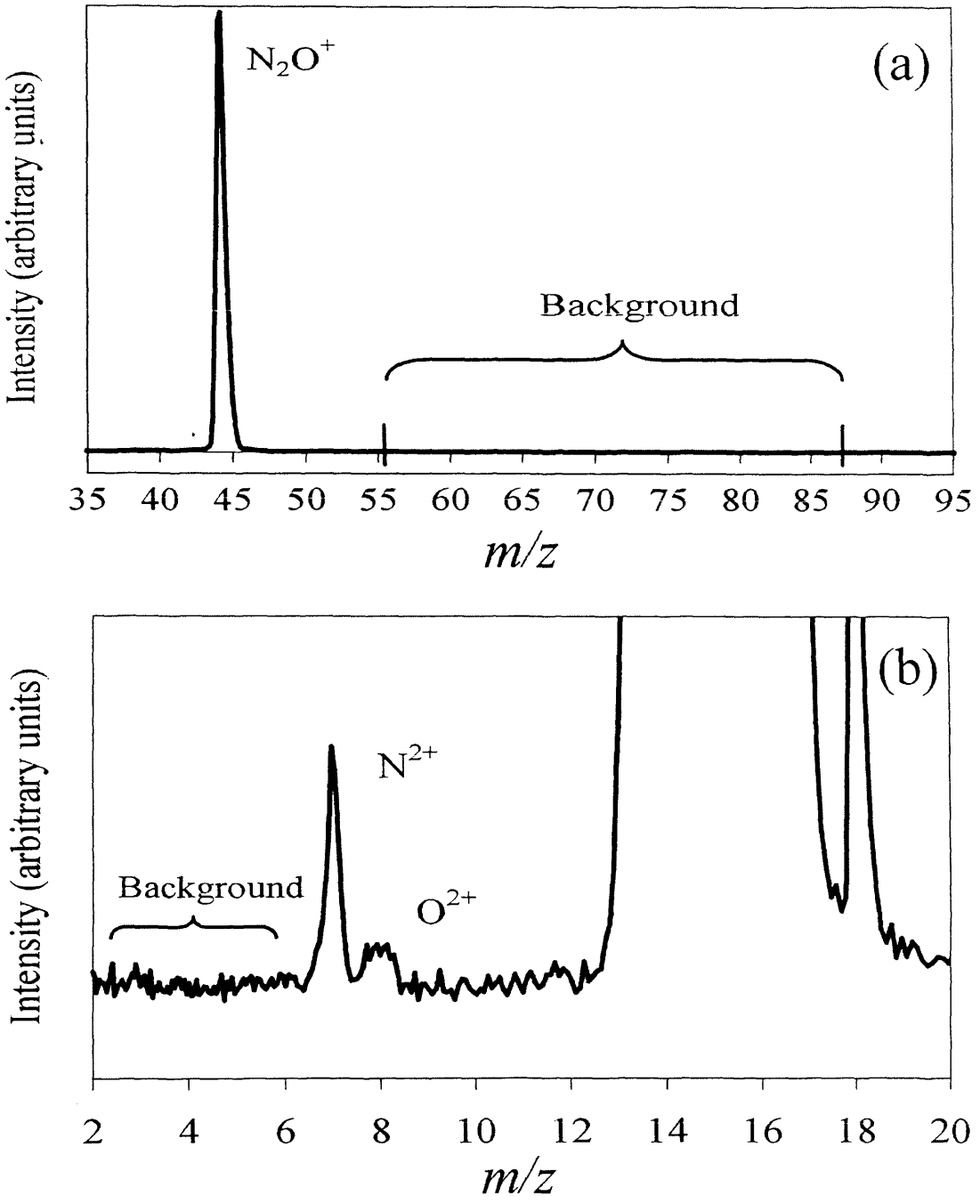


Figure 3.1.1: A diagram showing the background chosen for correction of a cation peak (a) and a dication peak (b) in the singles spectrum of $N_2O$, recorded at 200 eV.

Typically, a part of the singles spectrum where no ion peaks are observed is chosen to be a representative level of background, Figure 3.1.1 (a). This background is subsequently subtracted from the initially determined ion peak intensity. However, for ions with a smaller intensity in the singles spectrum, such as dications, a representative background is selected close to the dication peak, Figure 3.1.1 (b).

### 3.1.1.2 Pairs and triples spectrum

Events involving two ion arrivals and three ion arrivals at the detector, following a repeller plate pulse, are referred to as 'pairs' and 'triples', as described in Chapter 2. These events are stored individually and processed offline. The majority of coincidence signals will consist of two ion arrivals, as the probability of dissociative triple ionization occurring is significantly lower than that of dissociative double ionization at the electron energies under investigation.[1]

### 3.1.1.3 Pairs Spectrum

#### 3.1.1.3.1 Peak intensity determination

As previously described in Chapter 2 the pairs spectrum is displayed as a coincidence spectrum: a two-dimensional histogram of $t_1$ (first ion arrival time) against $t_2$ (second ion arrival time) for each ion pair. The intensities of a given product ion in the pairs spectrum, $P[X^+]$, are determined by summing the number of counts within each characteristic 'lozenge' shaped peak which involves the $X^+$ ion, Figure 3.1.2.[2-7]

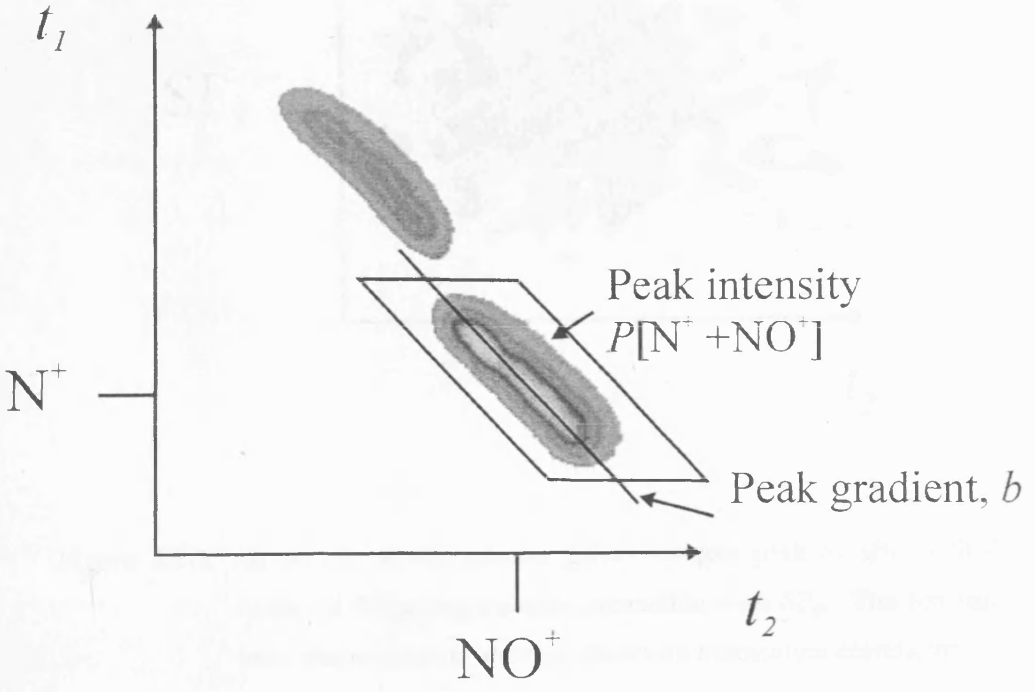


Figure 3.1.2: A schematic diagram of a peak in the pairs spectrum, illustrating how the intensity and gradient of an ion pair peak is evaluated.

As discussed in Section 2.1.3.2 of Chapter 2, the pairs spectrum may contain

contributions from ions that did not originate from the same dissociative ionization event, but are detected in coincidence; for example, two singly charged ions formed from the dissociation of two ions formed in the same pulse of electrons. Such events are termed 'accidental coincidences'.[8-10] Any accidental coincidence ion pair peaks in the pairs spectrum can be readily identified by their characteristic 'round' shape and are labelled as a 'false' ion pair peak. The ion counts producing a 'false' ion pair peak form a round peak shape because the ions show no momentum correlation, resulting from their separate formation. A 'false' ion pair peak therefore usually consists of two ion pair masses that cannot be formed from the same dissociative ionization event, such as the parent ion and another fragment ion, shown in Figure 3.1.3.

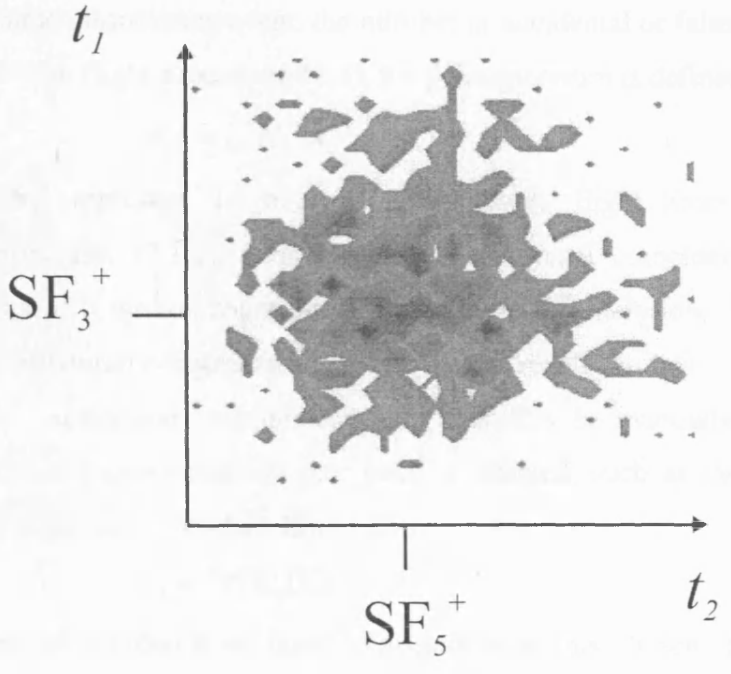


Figure 3.1.3: An accidental coincidence (false) ion pair peak of $SF_3^+ + SF_5^+$ observed following electron interaction with $SF_6$. The ion pair peak shape is round and thus shows no momentum correlation.

There is also a contribution from accidental coincidences to 'real' ion pair peaks (ions originating from the same dissociative event). The ion counts from accidental coincidences that contribute to 'real' ion pair peaks cannot be distinguished by direct observation of the peaks in the pairs spectrum. Instead, the contribution from accidental

coincidences to 'real' ion pair peaks is estimated, and subtracted using a procedure termed accidental coincidence subtraction. If a significant number of false coincidence peaks are observed in the pairs spectrum, then accidental coincidence subtraction is performed on the pairs spectrum to produce 'real' ion pair peaks and thus 'real' ion pair peak intensities.

#### 3.1.1.3.2 Accidental coincidence subtraction

The contribution from accidental coincidences to the pairs spectrum is minimized by operating with a low target gas pressure (below $10^{-6}$ Torr), and a low ion count rate (approximately 200-300 ions per second). Despite these experimental conditions, accidental coincidences still contribute to 'real' ion pair peaks in the pairs spectra. As false ion pair peaks are formed of two singly charged ions that were not produced in the same dissociation event, the number of accidental or false coincidences, $F_{12}$, between ions with flight times $t_1$ and $t_2$ in the pairs spectrum is defined as:

$$F_{12} = f_i^2 N_1^+ N_2^+ \qquad (3.1.1),$$

where $N_1^+$ and $N_2^+$ represent the number of ions with flight times of $t_1$ and $t_2$ respectively. From Eq. (3.1.1), it is clear that accidental coincidences could be completely eliminated if the ion count rates utilised were infinitely low. However, this approach is experimentally impractical, as it would result in infinitely long data acquisition times. Accidental coincidences must therefore be manually assessed and subtracted. Firstly, a known false ion pair peak is selected, such as shown in Figure 3.1.3. Eq. (3.1.1) is re-cast to produce Eq. (3.1.2):

$$F_{12} = CI[X_1]I[X_2] \qquad (3.1.2).$$

Where the number of accidental or false coincidences in this chosen 'false' ion pair peak, $F_{12}$, is expressed as being equal to a constant, $C$, multiplied by the individual ion intensities observed in the singles spectrum for the ions seen in this false ion pair peak, $I[X_1]$ and $I[X_2]$, Eq. (3.1.2). As the singles spectrum is recorded concurrently with the pairs spectrum, the singles spectrum can be used to estimate, and subsequently subtract the false coincidences from the recorded pairs spectrum. This concurrent recording of the singles and pairs spectrum enables the 'expected' false coincidence spectrum to be calculated and normalised to the recorded pairs spectrum in a known false coincidence region where no 'real' ion pair peaks are observed.

Accidental coincidence subtraction is performed by initially constructing an

accidental coincidence array containing the product of the individual ion intensities $I[X_1]$ and $I[X_2]$ in the singles spectrum. With reference to Eq. (3.1.2) this product needs to be scaled by $C$ to produce an estimate of the number of accidental coincidences present at any coordinate in the pairs spectrum. To determine the constant $C$ the number of accidental coincidences in the chosen 'false' ion pair peak is determined and then the accidental coincidence array is normalised to this value. This constant, $C$, can then be used to determine the number of accidental coincidences present in 'real' ion pair peaks, Eq. (3.1.2). The accidental coincidences can then be subtracted to leave a 'true' pairs spectrum.[9-11]

At an electron energy of 200 eV accidental coincidences in the pairs spectra were typically found to be less than 1-3% of a 'real' ion pair peak intensity.

#### 3.1.1.3.3 Ion pair peak intensity

In the data processing, discussed in Sections 3.1.2 and 3.1.3, a distinction is made between different types of ion pair: $P_2[X^+]$ and $P_3[X^+]$. $P_2[X^+]$ is the intensity of an $X^+$ ion in pairs of monocations (e.g. the $N^+ + O^+$ ion pair formed following electron interaction with $N_2O$). Such pairs of monocations can arise from double ionization or from triple ionization where an ion is missed. In contrast, $P_3[X^+]$ represents the intensity of an $X^+$ ion in ion pairs involving a dication and a monocation (e.g. the $N^{2+}+ O^+$ ion pair formed following electron interaction with $N_2O$), and such pairs of ions can only arise from triple or higher levels of ionization. A small contribution from triple ionization is observed at the electron energies used in the experimental investigations detailed in this thesis, and thus the neglect of higher order ionization is appropriate.

As detailed in Chapter 2, the experimental set-up is such that no ion pairs are recorded if the second ion arrives within 32 ns of the first ion, due to the dead-time of the discrimination circuitry, see Figure 3.1.4. Following ionization of $N_2O$ such dead-time losses affects the $N^+ + N^+$ and, to a lesser extent, the $N^+ + O^+$ peaks in the pairs spectra. These ion losses are easily estimated by extrapolating the visible part of the pairs peak to the diagonal $t_1=t_2$ using simple geometry. The area of the peak obscured by the dead-time is then determined and scaled accordingly, as demonstrated in Figure 3.1.4 and in Eq. (3.1.3).[6,9]

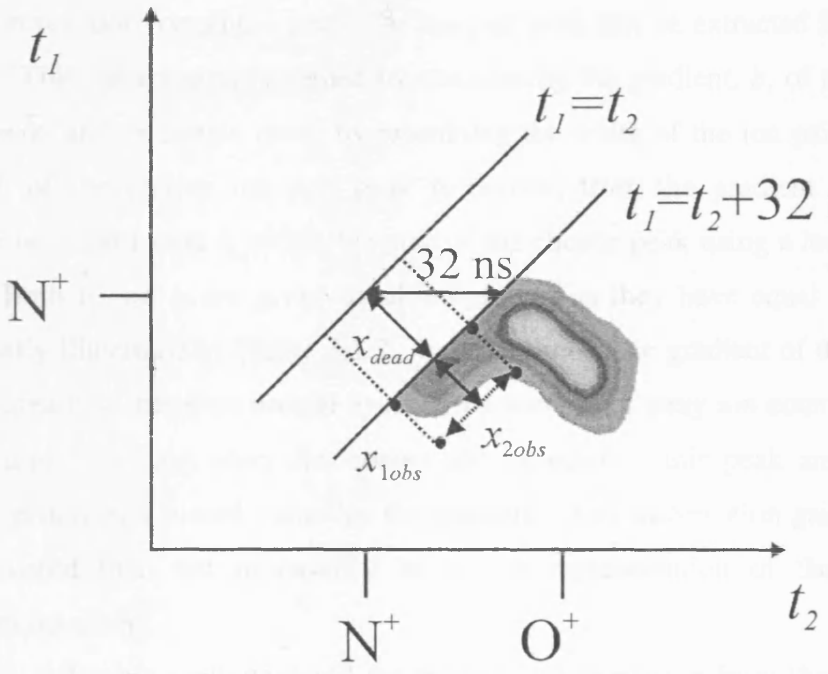


Figure 3.1.4: A schematic diagram of a peak corresponding to an identical ion pair, centred on the diagonal $t_1=t_2$, illustrating how the area obscured by the CFD dead-time is evaluated.

With reference to Figure 3.1.4, as the dead-time is known (32 ns), the length of the obscured peak, $\chi_{dead}$, can be calculated using trigonometry. The area occupied by the counts in the observed peak, $A_{obs}$, is determined using the approximate ion pair peak length $\chi_{1obs}$ and width $\chi_{2obs}$. The area occupied by the unobservable counts in the portion of the ion pair peak obscured by the dead-time, $A_{dead\text{-}time}$, is then determined using the length of the obscured peak, $\chi_{dead}$, and the width of the observed peak, $\chi_{2obs}$. The ratio of these areas is taken and multiplied by the number of ion counts recorded in the observed area, $P_{obs}[X^+]$, to produce an estimate for the number of ion counts obscured by the dead-time. Therefore, an estimate of the total number of ion counts for the entire ion pair peak is determined and expressed in Eq. (3.1.3):

$$P[X^+] = \frac{A_{dead\text{-}time}}{A_{obs}} P_{obs}[X^+] + P_{obs}[X^+] \qquad (3.1.3).$$

### 3.1.1.3.4 Ion pair peak gradient determination

Information concerning the fragmentation mechanism involved in a given dissociation reaction forming a particular ion pair peak can be extracted from the pairs spectrum. This information is gained by considering the gradient, $b$, of that particular ion pair peak, and in certain cases by examining the width of the ion pair peak.[2] The gradient $b$ of the chosen ion pair peak is derived from the gradient of the linear regression between $t_1$ and $t_2$ within the area of the chosen peak using a least squares fit method. Both $t_1$ and $t_2$ are given equal weightings as they have equal uncertainties, schematically illustrated in Figure 3.1.2. In determining the gradient of the chosen ion pair peak area it is therefore crucial to limit the number of stray ion counts included in the peak area. If many stray ion counts are included in this peak area, the fitting procedure produces a biased value for the gradient. Any information gained from this gradient would then not necessarily be a true representation of the dissociation mechanism occurring.

The following sections detail the possible interpretation from the experimental coincidence data regarding the fragmentation mechanisms involved in two-body and three-body dicationic dissociation reactions.

### 3.1.1.3.5 Two-body dissociation reactions

For a two-body dissociation reaction there is only one possible decay pathway, the direct dissociation of the molecular dication or trication to form a pair of product ions, [Reaction (3.1.I)].

$$m^{2+} \rightarrow m_1^{+} + m_2^{+} \qquad (3.1.I).$$

As discussed in Section 3.1.1.3.1, each ion pair peak in the pairs spectrum exhibits a characteristic 'lozenge' shape with an individual gradient $b$. For example, the ion pair peak produced following the two-body dissociation reaction of $N_2O^{2+}$ to form $NO^+ + N^+$, is orientated diagonally in the pairs spectrum, see Figure 3.1.2. The orientation of this ion pair peak can be explained by the conservation of linear momentum upon dicationic dissociation, forming a pair of monocations, where both ions (1 and 2) have the same magnitude of initial momentum $p$, in opposite directions:

$$p_1 + p_2 = 0 \qquad (3.1.4).$$

Therefore, under Wiley-McLaren focusing conditions[12] general expressions for each ion flight time can be expressed:[13]

$$t_1 = t_1^{\circ} + kp\cos\theta \qquad (3.1.5),$$

$$t_2 = t_2^{\circ} - kp\cos\theta \qquad (3.1.6),$$

where $t^0$ is the respective ion flight time in the absence of energy release for each ion, $k$ is a constant inversely proportional to the electric field strength and $\theta$ is the angle between the initial momentum vector and the axis of the mass spectrometer. With reference to Eqs. (3.1.5) and (3.1.6), the sum of the ion flight times ($t_1$+$t_2$) is constant, as the summation is independent of any kinetic energy release. The ion pair peak in the pairs spectrum corresponding to a two-body dissociation is therefore observed to be diagonal with a gradient of –1, shown by Eq. (3.1.7).[2,13,14]

$$t_1 = -t_2 + (t_1^{\,0} + t_2^{\,0}) \qquad (3.1.7).$$

Figure 3.1.2 shows that both the $NO^+ + N^+$ and $N_2^+ + O^+$ ion pair peaks formed following dissociation of $N_2O^{2+}$ have a gradient of –1, as predicted by Eq. (3.1.7), as they can only result from the direct dissociation of the $N_2O^{2+}$ dication.

### 3.1.1.3.6 Three-body dissociation reactions

For three-body dissociation reactions yielding two detectable fragment ions and one unobserved neutral species, the dynamics upon dissociation can be far more complex, as these reactions can occur *via* a variety of different pathways. These different pathways can be approximately separated into three classes of dissociation mechanism. Firstly, a 'direct' mechanism, *ie* an instantaneous explosion where all the bonds are broken simultaneously and thus the two monocations are formed with equal and opposite momenta. Following an instantaneous explosion, the neutral fragment receives no impulse, providing there are no collisions between the fragments. This dissociation mechanism therefore produces an ion pair peak with a gradient of –1 in the pairs spectrum, [Reaction (3.1.II)], due to the correlation in momenta of the fragment ions, described above for a two-body dissociation.

$$m^{2+} \rightarrow m_1^{\,+} + m_2^{\,+} + m_3 \qquad (3.1.II).$$

However, if the three-body dissociation reaction occurs *via* a sequential mechanism, such as deferred charge separation (DCS), [Reaction (3.1.III)], or an initial two-body charge separation (ICS) followed by a further dissociation to give an ion pair and neutral(s), [Reaction (3.1.IV)] the analysis is further complicated.

$$m^{2+} \rightarrow m_1 m_2^{2+} + m_3$$

$$m_1 m_2^{2+} \rightarrow m_1^{+} + m_2^{+} \qquad \text{(3.1.III)},$$

$$m^{2+} \rightarrow m_1^{+} + m_2 m_3^{+}$$

$$m_2 m_3^{+} \rightarrow m_2^{+} + m_3 \qquad \text{(3.1.IV)}.$$

In the case of a DCS mechanism, the dominant energy release will occur on the second dissociation step [Reaction(3.1.III)], comparable to a simple two-body dissociation producing an ion pair peak gradient of –1 in the pairs spectrum.[2,14]

In the case of ICS, the monocations formed [Reaction (3.1.IV)] will have equal and opposite momenta:

$$p_1 = -p_{23} \qquad (3.1.8).$$

$$(m_1 v_1 + m_2 m_3 v_{23} = 0)$$

However, the secondary dissociation [Reaction (3.1.IV)] affects the momenta, by introducing a factor involving a mass ratio of fragment ions.

$$p_2 = m_2 v_{23} = \frac{m_2}{m_2 + m_3} p_{23} \qquad (3.1.9).$$

From Eq. (3.1.8), Eq. (3.1.9) is re-cast in terms of $p_1$ and $p_2$:

$$p_1 = -\frac{m_2 + m_3}{m_2} p_2 \qquad (3.1.10).$$

Eq. (3.1.10) demonstrates that the ion pair peak gradient observed in the pairs spectrum is equal to $-(m_2+m_3)/m_2$. That is the ratio of masses from the secondary dissociation, when the heaviest ion is plotted on the $x$-axis.[15] However, this gradient illustrates the limiting case where the ion ($m_2m_3^+$) has sufficient time to freely rotate and leave the Coulomb field of the other monocation before secondary dissociation occurs. This type of reaction is indicative of a slow dissociation because the fragment ions formed following ICS have time to leave the other ions' Coulomb field. If this monocation dissociates before leaving the Coulomb field of the correlated partner monocation (fast dissociation), the monocation subsequently produced, *via* the secondary dissociation step, will possess an increased momentum and thus the gradient will move towards –1. For example, the three-body dissociation reaction of $N_2O^{2+}$ to form the $N^+ + O^+ + N$ ion pair, shown in Figure 3.1.4, exhibits an ion pair peak gradient of –1. The possible dissociation mechanisms are illustrated in Table 3.1.1, with the associated gradients shown in Reactions [3.1.V], [3.1.VI] and [3.1.VII].

Table 3.1.1: Possible sequential mechanisms for the formation of the $N^+ + O^+$ ion pair from $N_2O^{2+}$.

| Deferred charge separation (DCS) | Initial charge separation (ICS) | |
|---|---|---|
| $N_2O^{2+} \rightarrow NO^{2+} + N$<br>$\downarrow \quad \downarrow$<br>$N^+ + O^+ + N$<br>Gradient = -1 | $N_2O^{2+} \rightarrow NO^+ + N^+$<br>$\downarrow \quad \downarrow$<br>$N + O^+ + N^+$<br>Gradient = $-\frac{m_O + m_N}{m_O}$ (-1.88) to -1 | $N_2O^{2+} \rightarrow N_2^+ + O^+$<br>$\downarrow \quad \downarrow$<br>$N^+ + N + O^+$<br>Gradient = $-\frac{m_N + m_N}{m_N}$ (-2) to -1 |
| [3.1.V] | [3.1.VI] | [3.1.VII] |

From Table 3.1.1, each possible sequential mechanism could produce an ion pair peak in the pairs spectrum with a gradient of –1. Consequently a pathway cannot be definitively specified for some ion pair peaks, such as the $N^+ + O^+$ ion pair peak, using the coincidence technique described in this thesis. Using triple coincidence techniques, other details that assist the interpretation into the type of three-body dissociation reactions, forming a certain fragment ion pair, have been found. [2,4,15-18] These details are usually observed in the mass and/or coincidence spectra. For example, an ion pair peak formed *via* a dissociation reaction involving DCS may exhibit a metastable 'tail.' This 'tail' is observed from the ion pair peak to the diagonal $t_1=t_2$ of the dissociated dication [Reaction (3.1.III)] forming that particular fragment ion pair.[17] Such a metastable 'tail' is observed following the electron ionization of $SF_6$ detailed in Chapter 6.

In photoelectron-photoion-photoion coincidence (PEPIPICO) experiments, detailed mechanisms have been proposed following the investigation of three-body dissociations in many small molecules. These mechanisms are obtained from the ion pair peak shapes and are generally consistent with the observed angular correlations and initial momenta of the fragment ions.[5] The resolution of ion pairs obtained using PEPIPICO experiments is superior to the resolution possible in the pairs spectra presented in this thesis, and is discussed in the following section.

### 3.1.1.3.7 Resolution

The pairs spectra presented in this thesis are of poorer resolution than PEPIPICO experiments[1,2,15,16,19] because there is a finite time during which dications or trications

can be formed in the electron pulse, and hence there is a small uncertainty as to when the dissociation event occurred. This uncertainty is observed as a greater ion pair peak 'width' if directly compared with ion pair peaks recorded in PEPIPICO experiments. Figure 3.1.5 schematically illustrates this 'width' difference.

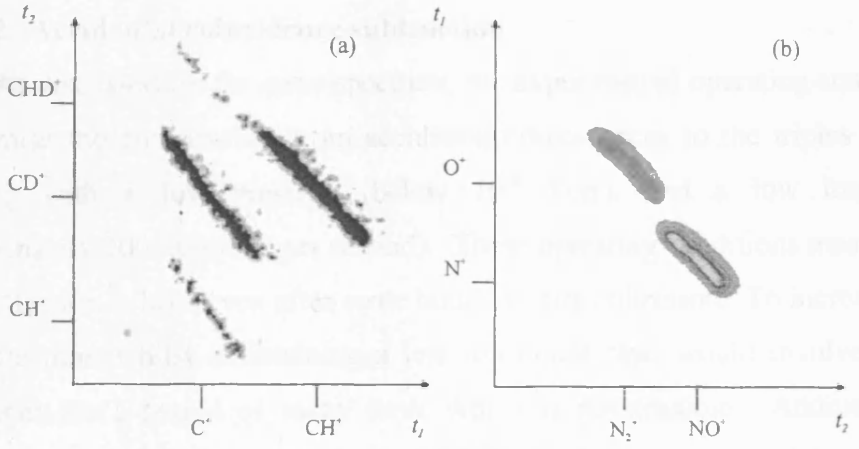


Figure 3.1.5: Schematic diagram illustrating the difference in ion pair peak widths measured (a) using PEPIPICO, example shown for HCCD[20] and (b) coincidence technique used in this thesis, example shown for $N_2O$.

In PEPIPICO experiments the detection of the photoelectron as a time zero precisely defines the moment of dissociation and thus 'slimmer' ion pair peaks are observed. This enables further information concerning the dynamics of multiply charged ion dissociation to be obtained from the PEPIPICO experiments than are possible using the apparatus described in this thesis.

### 3.1.1.4 Triples spectrum

#### 3.1.1.4.1 Peak intensity determination

This set of data is first visualized by simply plotting a mass spectrum of the ions recorded as ion triple arrivals, termed a triples mass spectrum and illustrated in Chapter 2. A series of pairs spectra are then plotted in coincidence with the different ions present in the triples mass spectrum. The intensities of the peaks in these 'coincident pairs' spectra are determined by summing the counts in each peak to give $T[X^+]$.

As discussed in Section 3.1.1.3.2 for the pairs spectrum, the triples spectrum may also contain contributions from ions that did not originate from the same

dissociative ionization event but are detected in coincidence, termed 'accidental coincidences'.[8-10] As described for the pairs spectrum, if a significant number of accidental coincidences are observed in the triples spectrum then accidental coincidence subtraction is performed to produce 'real' ion triples.

### 3.1.1.4.2 Accidental coincidence subtraction

As discussed for the pairs spectrum, the experimental operating conditions serve to minimise the contribution from accidental coincidences to the triples spectrum by operating with a low pressure (below $10^{-6}$ Torr), and a low ion count rate (approximately 200-300 ions per second). These operating conditions mean that the ion triple collection is low, even after some hours of data collection. To increase the triples data collection, whilst maintaining a low ion count rate, would involve running the experiment for a period of many days, which is not feasible. Additionally, at the electron energies utilised in this thesis, 30-200 eV, the occurrence of dissociative triple ionization is expected to be low.

As a result of the pictorial representation of the ion triples data any accidental coincidence ion peaks in the triples spectrum are more complicated to assign, as not all coincidences in the triples spectra exhibit momentum correlation. However, the methodology, discussed for the pairs spectrum, is modified to account for the third ion, and is used to estimate the contribution to 'real' ion pair peaks from accidental coincidences in the triples spectrum. With reference to the triples mass spectrum, Figure 2.1.10, displayed in Chapter 2, it is clear that the triples data contain accidental coincidences. Observation of ion peaks corresponding to $N_2^+$, $NO^+$ and $N_2O^+$ following electron ionization of $N_2O$ cannot be formed with any other two fragment monocations in the same dissociative event from $N_2O^{3+}$. Accidental coincidence peaks in the triples spectrum are formed of three singly charged ions not formed in the same dissociation event. The number of accidental coincidences, $F_{123}$, between ions with flight times $t_1$, $t_2$ and $t_3$ in the pairs spectrum are defined as:

$$F_{123} = f_i^{\,3} N_1^{\,+} N_2^{\,+} N_3^{\,+} \qquad (3.1.11),$$

where $N_1^+$, $N_2^+$ and $N_3^+$ represent the number of ions with flight times of $t_1$, $t_2$ and $t_3$ respectively. As detailed for the accidental coincidence subtraction of the pairs spectrum, Eq. (3.1.11) can be re-cast:

$$F_{123} = CI[X_1]I[X_2]I[X_3] \qquad (3.1.12).$$

When a 'false' ion triple is observed in the triples spectrum, the number of counts in this

triple is then normalised to the three-dimensional auto-correlation function of the singles spectrum for this peak. A value of $C$ is then determined. An example of an accidental coincidence ion triple peak is the $F^+ + SF_3^+ + SF_5^+$ ion triple, (Chapter 6) formed following electron interaction with $SF_6$. A three-dimensional auto-correlation function of the singles spectrum for each 'real' ion pair peak is then determined and scaled by the value of $C$ to produce an estimate of the number of accidental coincidences contributing to each peak. The number of accidental coincidences, $F_{123}$, can then be subtracted from each 'real' ion triple to produce a 'true' triples spectrum. At 200 eV, accidental coincidences in the triples spectrum were found to be typically less than 1-3% of the ion triple peak intensity.

#### 3.1.1.4.3 Dissociation mechanisms

In this thesis, ion triples are only studied following electron interaction with $N_2O$ and $SF_6$. The observed ion triples are formed of three monocations with low intensities, even at 200 eV. Therefore, any information on the type of dissociation mechanism occurring is impossible to provide with any accuracy under the current experimental set-up. Although, as discussed in Section 3.1.1.3.3, ion pairs formed *via* dissociative triple ionization are also observed.

Creation of molecular ions in charge states greater than two is almost always followed by charge-separation reactions, although, as discussed in Chapter 1, quite a few 'long-lived' triply charged ions have been experimentally observed.[21] For triply charged polyatomic molecules, complete charge-separation has the highest probability of occurring, although dissociation channels where one or more neutral product ions are formed with charge-separation have been shown to be the principal channels in triply charged benzene ions.[22]

### 3.1.2 Relative partial ionization cross-section determination

The ion intensities recorded in the singles, pairs and triples spectra are processed to yield the relative PICSs and relative precursor specific PICSs. This data processing is described in detail in Sections 3.1.2.1 to 3.1.3.1. The relative PICS for the formation of fragment ion $X^+$ is symbolized as $\sigma_r[X^+]$, where the cross-section for the formation of $X^+$ is expressed relative to the cross-section for forming the parent ion. Similarly, the precursor specific PICS $\sigma_n[X^+]$ ($n$=1-3) expresses the cross-section for forming the fragment ion $X^+$, relative to the cross-section for forming the parent ion of the system,

*via* single ($n$=1), double ($n$=2) or triple ($n$=3) ionization. As discussed in Section 3.1.1.2, any contribution from quadruple ionization is assumed to be negligible in this analysis.

### 3.1.2.1 Peak intensities in the singles spectrum

The intensity of each singly charged product ion in the singles spectrum is described by Eq. (3.1.13), neglecting any contribution from dissociative quadruple ionization:

$$I[X^+]=f_iN_1[X^+]+f_i(1-f_i)N_2[X^+]+f_i(1-f_i)N_3^{pairs}[X^+]+f_i(1-f_i)^2N_3^{triples}[X^+] \qquad (3.1.13).$$

The experimental ion detection efficiency is denoted by $f_i$, and $N_n[X^+]$ represents the number of ions, $X^+$, formed *via* the loss of $n$ electrons from the parent molecule. The distinction is made between the number of ions formed *via* dissociative triple ionization $N_3^{pairs}[X^+]$ which generate a pair of fragment ions, a dication and a monocation, such as $N^{2+}+ O^+$, and the number of ions formed *via* dissociative triple ionization $N_3^{triples}[X^+]$ which generate three monocations, such as $N^+ + N^+ + O^+$. In Eq. (3.1.13) the terms involving $N_2[X^+]$, $N_3^{pairs}[X^+]$ and $N_3^{triples}[X^+]$ represent the number of ions contributing to the singles spectrum from dissociative double and triple ionization where an $X^+$ ion is formed and the second ion from the dissociative double ionization event, or the second and third ion from the dissociative triple event, are not detected. Such ion losses occur, that is $f_i<1$, because of the 90% transmission of the grids that define the electric fields in the apparatus and the less than unit efficiency of the electronics and detector, discussed in Section 2.1.2.2 of Chapter 2.

For clarity, the intensity of a dication $X^{2+}$ observed in the singles and pairs spectra is given by Eq. (3.1.14). The intensity of a dication $X_n^{2+}$ observed only in the singles spectrum is given by Eq. (3.1.15). The intensity of the parent ion of the system $Y^+$ observed only in the singles spectrum is represented by Eq. (3.1.16). Examples of selected ion intensities are given in each results Chapter (4-6).

$$I[X^{2+}]= f_iN_2[X^{2+}]+ f_i(1-f_i)N_3^{pairs}[X^{2+}] \qquad (3.1.14),$$

$$I[X_n^{2+}]= f_iN_2[X_n^{2+}] \qquad (3.1.15),$$

$$I[Y^+]= f_iN_1[Y^+] \qquad (3.1.16).$$

To determine the $\sigma_r$ values, it is noted that $\sigma_r[X^+]$, the relative PICS for formation of a fragment ion $X^+$ with respect to the parent ion $Y^+$, is equal to the sum of the relative precursor specific PICSs, $\sigma_n[X^+]$:

$$\sigma_r[X^+] = \frac{\sum_{n=1}^{n=3}\sigma_n[X^+]}{\sigma_n[Y^+]} = \frac{\sigma_1[X^+]+\sigma_2[X^+]+\sigma_3[X^+]}{\sigma_1[Y^+]} \quad (3.1.17).$$

Now, under our experimental conditions of low electron flux and ionization rate, $N_n[X^+]$ is proportional to $\sigma_n[X^+]$:

$$\sigma_n[X^+] = kN_n[X^+] \quad (3.1.18),$$

where $k$ is a constant for each experiment and is dependent on experimental variables such as the target gas pressure, electron flux in the source region, the duration of the experiment and electron path within the ionization volume.[11]

As defined in Eq. (3.1.17), the relative PICS for the formation of a fragment ion can be considered as a sum of the cross-sections for forming the ion *via* single, double and triple ionization. Therefore, in addition to the singles data, the data from the pairs and triples spectra must also be used, and are defined below.

### 3.1.2.2 Peak intensities in the pairs and triples spectra

The intensities of the signals in the pairs, $P_2[X^+]$ and $P_3[X^+]$, and triples, $T[X^+]$, spectra can be written:

$$P_2[X^+] = f_i^2 N_2[X^+] + 2f_i^2(1-f_i)N_3^{\text{triples}}[X^+] \quad (3.1.19),$$

$$P_3[X^+] = f_i^2 N_3[X^+] \quad (3.1.20),$$

$$T[X^+] = f_i^3 N_3^{\text{triples}}[X^+] \quad (3.1.21),$$

where $N_n[X^+]$ represents the number of $X^+$ ions formed *via* loss of $n$ electrons, $P_n[X^+]$ and $T[X^+]$ therefore represent the number of $X^+$ ions detected in the pairs and triples spectra respectively. The contribution to the intensity of the monocation ion pair peaks from ion triple arrivals where one of the correlated ion triples is not detected is expressed in the second term of Eq. (3.1.19). Every ion triple observed in this thesis has two identical ions, such that $2X^+ + Z^+$. The factor of '2' in the second term of Eq. (3.1.19) arises as a consequence of the definitions adopted in the analysis procedure, where the number of ions formed by the various ionization encounters are used and not the number of events.

Using Eqs. (3.1.14)-(3.1.16) and (3.1.19)-(3.1.21), Eq. (3.1.18) can now be re-cast to express the relative PICS in terms of the intensities determined from the singles, pairs and triples spectra. Representative equations are shown for a fragment ion $X^+$ seen in every spectrum and for a dication $X^{2+}$ observed in the singles and pairs spectra:

$$\sigma_r[X^+]=\frac{N_1[X^+]+N_2[X^+]+N_3[X^+]}{N_1[Y^+]}=\frac{I[X^+]+P_2[X^+]+P_3[X^+]+T[X^+]}{I[Y^+]} \quad (3.1.22),$$

$$\sigma_r[X^{2+}]=\frac{N_2[X^{2+}]+N_3[X^{2+}]}{N_1[Y^+]}=\frac{I[X^{2+}]+P_3[X^{2+}]}{I[Y^+]} \quad (3.1.23).$$

Note that the $\sigma_r$ values determined above do not depend on $f_i$. However, if a value of $f_i$ is available, then the data analysis can be extended to determine $\sigma_n[X^+]$ values, quantifying the contributions to each ion yield from single, double and triple ionization.

## 3.1.3 Relative precursor specific partial ionization cross-section determination

As discussed in Section 3.1.2.2, in order to determine $\sigma_n[X^+]$ values, a value for $f_i$ must be determined. For each molecule studied in this thesis an individual $f_i$ determination is performed and each value is given within the relevant chapter.

### 3.1.3.1 Ion detection efficiency determination

The ion detection efficiency, $f_i$, can be determined experimentally by recording the singles and the pairs spectra for $CF_4$. $CF_4$ is used, as the cross-sections for forming an individual ion, $\sigma^+$, and ion pairs, $\sigma_D{}^{++}$, are well-characterised for this molecule and can be extracted from published literature.[6,8,23] The $CF_4$ data is collected at an ionization energy of 100 and 200 eV. At these electron energies there are no data available in the published literature regarding the triple ionization of $CF_4$, and thus triple ionization is assumed to be small (1-2%) and is therefore neglected in this analysis. Expressions for the total number of ions in the singles spectrum, $\sum I$, and the total number of ions in the pairs spectrum, $\sum P$, are expressed below:

$$\sum P = 2f_i{}^2 k\sigma_D{}^{++} \quad (3.1.24),$$

$$\sum I = f_i k\sigma^+ + 2f_i(1-f_i)k\sigma_D{}^{++} \quad (3.1.25),$$

$$\frac{\sum P}{\sum I}=\frac{2f_i\sigma_D{}^{++}}{\sigma^+ + 2(1-f_i)\sigma_D{}^{++}} \quad (3.1.26).$$

Using Eqs. (3.1.24)-(3.1.26) a value for $f_i$ was determined for each experimental study, and is presented within each individual results chapter (4-7). The average $f_i$ value determined over the course of all experimental investigations, discussed in this thesis, is approximately 0.17. Typical values of $f_i$ obtained for similar experimental set-ups are

10-20%.[24]

Having determined a value for the ion detection efficiency, $f_i$, relative precursor specific PICSs can be defined. Eqs. (3.1.27)-(3.1.29) are used to evaluate the precursor specific PICS for formation of a fragment ion $X^+$ *via* single, double and triple ionization:

$$\sigma_1[X^+] = \frac{N_1[X^+]}{N_1[Y^+]} \qquad (3.1.27),$$

$$= \frac{I[X^+] - (1-f_i)/f_i P_2[X^+] - (1-f_i)/f_i P_3[X^+] + (1-f_i)^2/f_i^2 T[X^+]}{I[Y^+]}$$

$$\sigma_2[X^+] = \frac{N_2[X^+]}{N_1[Y^+]} = \frac{P_2[X^+]/f_i - 2(1-f_i)/f_i^2 T[X^+]}{I[Y^+]} \qquad (3.1.28),$$

$$\sigma_3[X^+] = \frac{N_3^{\text{pairs}}[X^+] + N_3^{\text{triples}}[X^+]}{N_1[Y^+]} = \frac{P_3[X^+]/f_i + T[X^+]/f_i^2}{I[Y^+]} \qquad (3.1.29).$$

Within each of the experimental Chapters 4-7, examples of the data analysis equations used for a selected fragment ion are presented. Detailed derivations are also given for each of the experimental chapters in Appendices C-F.

### 3.1.4 Kinetic energy release determination

Information regarding the energetics associated with a given dissociation reaction, such as the kinetic energy release (KER), is difficult to obtain from simply observing the ion pair peaks in the pairs spectra. However, by transforming a chosen ion pair peak from the pairs spectrum into a TOF difference ($\Delta t_{tof}$) spectrum it is then possible to estimate the kinetic energy release(s) (KER), for the formation of the particular ion pair. Figure 3.1.6 illustrates the KER in terms of the energy of the dication state that gives rise to the dissociation reaction.

As discussed in Section 3.1.1.3.7, due to the length of the electron pulse, the perpendicular width of the pairs peaks presented in this thesis is greater than other experimental methods, such as PEPIPICO. This additional perpendicular ion pair peak width adds to the uncertainty when evaluating the KER(s) for a certain ion pair. Therefore, experimental methods such as PEPIPICO produce more accurate KER values than are possible using the experimental set-up presented in this thesis. Consequently, for each dissociation channel observed in the pairs spectra the KER determinations are only presented where there is currently little information available in

the literature or to confirm the determinations of existing experimental investigations.

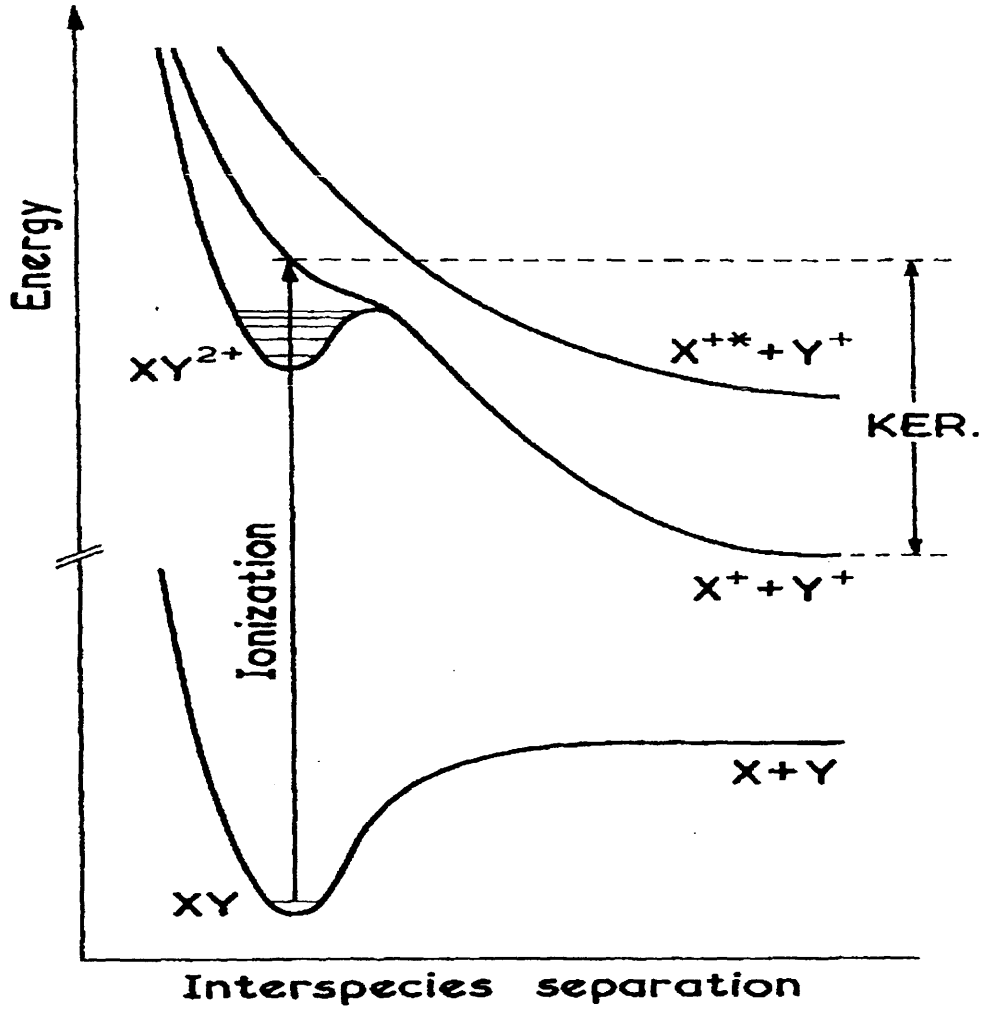


Figure 3.1.6: Schematic potential energy curves showing the relationship of the KER to the energy of the diatomic dication state giving rise to the dissociation reaction.

### 3.1.4.1 Time-of-flight difference spectrum

Information regarding the KER upon multiply charged ion dissociation is obtained by forming a TOF difference $\Delta t_{tof} = (t_2 - t_1)$ plot from the pairs data, where the differences in ion flight times are histogrammed for each ion pair of interest. This ion coincidence spectrum will have a prototypical 'square top' (discussed in Chapter 2) if all the ions are being collected, shown in Figure 3.1.7.[25]

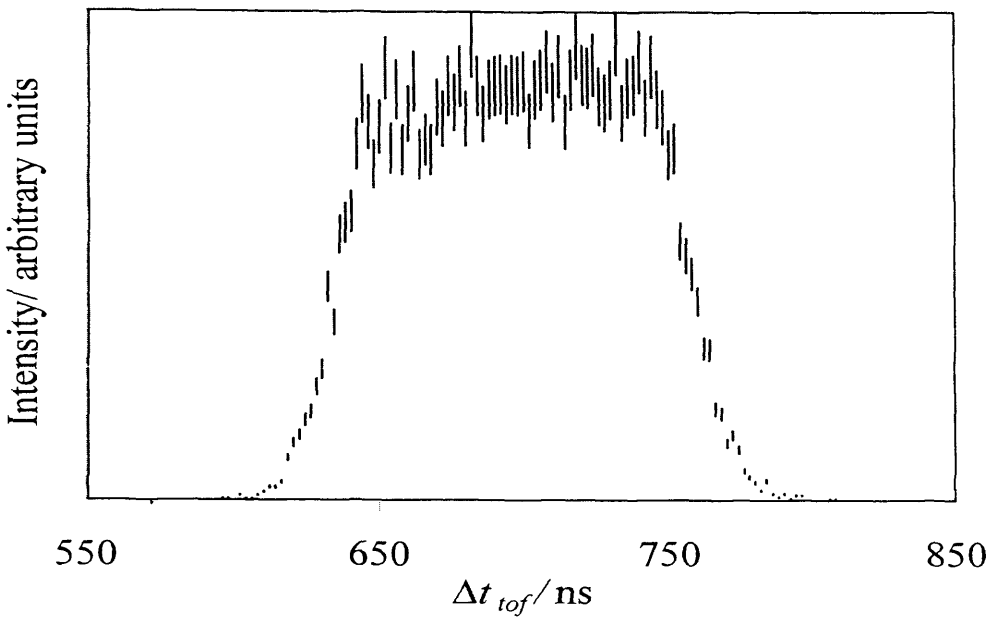


Figure 3.1.7: An ion coincidence peak for the $NO^+ + N^+$ ion pair transformed from the pairs spectrum recorded following electron interaction with $N_2O$. The error bars shown represent a typical data spread of approximately 7 %.

To provide an estimate of the KER for each dicationic dissociation channel, the TOF difference spectrum is used alongside a Monte Carlo simulation of the dication dissociation of interest. The Monte Carlo simulation can be directly compared with the experimental TOF difference spectrum. The fit of the simulated TOF difference spectrum to the experimental data is refined until agreement is achieved.[10,25,26]

### 3.1.4.2 Monte Carlo simulation

The Monte Carlo simulation allows the inclusion of all experimental parameters affecting the peak shape, such as the size of the ionization region and the distribution of KERs and has been shown to produce KERs in excellent agreement with literature.[11,27,28] The Monte Carlo simulation uses repeated ion trajectories and calculates the ion flight times under an electrostatic model of the experimental conditions. The dication dissociation is modelled with a Gaussian kinetic energy release distribution (KERD), a Gaussian spatial distribution of ionization events about the centre of the source region and represents the initial velocity of the neutral molecule before ionization by a Maxwell-Boltzmann distribution. The KERDs are modelled as a sum of Gaussian energy release distributions as the KERD of the detected fragments is expected to be a direct function of the reflection of the Gaussian ground state

wavefunction on the respective repulsive potential energy curves of the dication states in the Franck-Condon region (reflection approximation).[14,24]

The treatment of the ions in the simulation is important. The initial direction of the motion of the molecules before ionization is random, and as the ions are formed their movement will be isotropic, but detection is only on a single plane. Most ions detected will therefore have a significant transverse velocity away from the axis of the TOF mass spectrometer. To allow for the projection of a spherical velocity distribution onto the plane of the detector, the distribution of initial velocities following ionization must be sinusoidally weighted, thus ensuring that a higher proportion of ions have large velocity components along the axis of the TOF mass spectrometer than small angles. This modelling results in the satisfactory production of a 'square topped' peak.[25]

#### 3.1.4.2.1 Apparatus and ion parameters

To set up a simulation the apparatus parameters are entered: source length, acceleration length, drift tube length, source voltage and the voltage on the drift tube. This ensures that an electrostatic model of the experimental conditions is achieved. The values concerning the dissociation reaction under investigation are then entered; these include the masses of the detected ion pairs and the mass of the parent dication. The masses of the primary ions formed in the initial dicationic charge separation, which then dissociate to form the detected ion pair, are also included in the program, and used if necessary to enable the simulation of all possible decay pathways, see Reactions [3.1.V] to [3.1.VII].

The energetics for the individual dissociation reactions can then be entered into the program. Initially an estimate of the KER or KERs upon dissociation of the dication to form each ion pair is entered with the probability of each release if the KER is multi-valued. The detector radius, initial gas temperature along the jet axis and initial gas temperature perpendicular to the jet axis are then defined and entered into the program.

#### 3.1.4.2.2 Simulation parameters

The simulation parameters consist of the number of ion trajectories required, half-width of KER distribution for each ion pair and the half-width of the Gaussian distribution of ionization events in the source region. Once the apparatus, ion and simulation parameters have been entered into the program, the simulation is run and the simulated spectrum can then be compared with the experimental data. The Monte Carlo

simulation is displayed as a histogram of the number of ions with a particular TOF difference. If agreement is not found between the simulated data and the experimental data the simulation can be re-run with different energetics and simulation parameters until satisfactory agreement, judged by eye, with the experimental data is found, see Figure 3.1.8. The uncertainties in the determined KER(s) are determined by the deviations necessary to significantly degrade the fit with experimental data, and are generally in the order of ±1.0 eV.

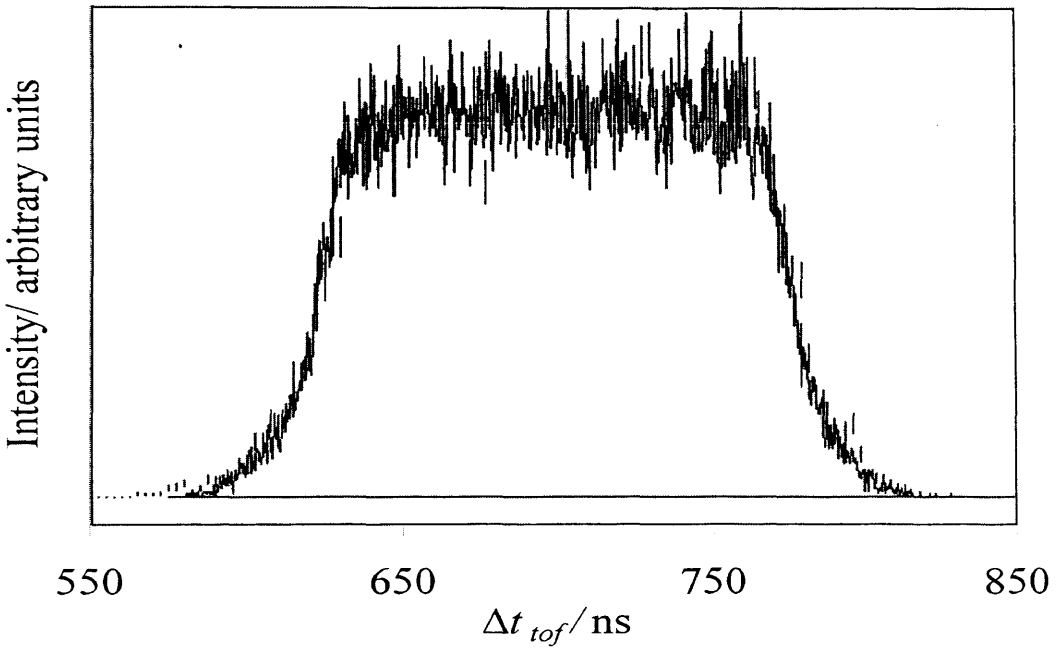


Figure 3.1.8: An ion coincidence peak for the $NO^+ + N^+$ ion pair, transformed from the pairs spectrum, and shown together with a Monte Carlo simulation. Good agreement is observed between the simulation and the experimental data.

It should be noted that, as discussed above, the KER has only been investigated for molecules where novel information can be obtained and where comparison with other techniques is relevant. As discussed in Section 3.1.1.3.7, the resolution of the pairs spectra presented in this thesis is lower than other techniques, such as PEPIPICO, which also means greater uncertainty in the TOF difference plots. Thus, only estimates of the KER are produced, although agreement with more accurate techniques is observed. Chapter 4 presents KER estimates for selected dicationic dissociations and compares these results with available data.

### 3.1.5 Review of errors

At this point it is appropriate to discuss the sources of error associated with the current experiment and provide estimates of the relative magnitude of these errors in relation to the ionization cross-sections presented for each target gas. The main sources of error are detailed in Chapters 2 and 3, and include the determination of the ion detection efficiency ($f_i$), corrections of the singles spectra for contributions from the background gas and correction to the pairs spectra for loss of ion counts due to the CFD dead-time, accidental coincidences in the pairs spectra and the loss of energetic ions from ion pairs in the pairs spectra. The following discussion is divided into two parts, the first part provides details of the uncertainty from different sources of error to the relative PICSs ($\sigma_r$ values) and the second part details the uncertainty from the sources of error to the relative precursor specific PICSs ($\sigma_1$ and $\sigma_2$ values). In the present discussion the magnitude of the error in the triples data is neglected due to the difficulty in accurately quantifying an error in numbers which represent less than 1% of the total ion yield.

#### 3.1.5.1 Relative PICS data

The statistical error in the relative PICSs is minimised for each precursor gas by performing at least four measurements for each electron energy, and obtaining an average value with an associated standard deviation for each electron energy. As discussed in Chapter 2, the overlap of the electron beam with the target gas is maximised for each electron energy. Hence, there is an error associated with any change in the overlap between the electron beam and the target gas beam. The magnitude of this error is difficult to quantify, but it should be approximately constant for the relative ionization cross-section measurements and minimized by the procedure of optimizing the ion signal at a given electron energy. Indeed, this is shown to be true for argon using the ion trajectory simulation program SIMION.

The relative PICSs values are independent of $f_i$ (ion detection efficiency) and therefore are not influenced by the uncertainty in this parameter. However, there are other sources of error, mentioned above, that can affect the $\sigma_r$ values. These sources of error are now quantified, and their magnitudes discussed, for the electron ionization of $N_2O$. The magnitudes of these errors are of course similar for the electron ionization of $BCl_3$ (Chapter 5) and $SF_6$ (Chapter 6), and are therefore not individually detailed here.

**Background contribution**

As discussed in Chapter 3, each peak in the singles spectrum is corrected for the presence of background gas in the mass spectrometer. The correction for the background contribution to the singles spectra for cations represents approximately 1% of the cation peak observed in the spectrum. The background correction to the dication peaks depends on the location and intensity of the dication peak in the spectrum. Typically, the correction for the background contribution to dication peaks is approximately 15%. However, if the dication peak is located next to a cation peak of high intensity, and is itself low intensity, the correction can be approximately 85% of the observed dication peak. Allowing for the statistical error in these subtractions gives the resulting counting uncertainty for cation signals as less than ±0.5% and for dications as ±2-3% at 100 eV.

**Accidental coincidences**

As discussed in Chapter 3, accidental coincidences are given by pairs of ions that did not originate from the same dissociative event but are nonetheless detected in coincidence. Such accidental coincidences inevitably contribute to 'real' ion pair peaks in the pairs spectra. For the electron ionization of $N_2O$ no accidental coincidence subtraction was performed, as the contribution from accidental coincidences to each ion pair peak was less than 2%. However, if accidental coincidence subtraction is performed at 100 eV the value of $\sigma_1[N^+]$ increases by 1% and the value of $\sigma_2[N^+]$ decreases by 1%, resulting in the $\sigma_r[N^+]$ value remaining approximately unchanged. The magnitude of this error justifies the neglect of accidental coincidence subtraction in Chapter 4.

**Dead-time correction**

As detailed in Chapter 2, the experimental set-up is such that no ion pairs are recorded if the second ion arrives within 32 ns of the first ion, due to the dead-time of the discrimination circuitry. Section 2.1.3.2.1.3 of Chapter 2 details how the $N^+ + N^+$ and $N^+ + O^+$ ion pair peaks were corrected for the ion counts lost due to the dead-time of the CFD. To quantify this correction the lost ion counts represented 30% of the detected ion counts for both ion pair peaks, and 12% of the total $N^+$ ions observed in ion pairs. If the correction for the lost ion counts was accurate to ±15% of the 'true' lost ion

counts, the value of $\sigma_1[N^+]$ at 100 eV increased by 5% and the value of $\sigma_2[N^+]$ decreased by 7%, leading to an overall decrease in the $\sigma_r[N^+]$ value of less than 2%. It should be remembered that only identical or nearly identical ion pairs are affected by the dead-time correction, and the uncertainty in the $\sigma_r$ value is less than the typical standard deviation of ±2-5% shown with the relative PICS data.

**Energetic ion loss**

As discussed in Chapters 3 and 4, energetic ion loss is observed for the $N^+ + O^+$ ion pair in the form of a hollow TOF difference spectrum. Such energetic ion loss may also occur for the $N^+ + N^+$ ion pair, but due to the dead-time is difficult to quantify with any accuracy. A 'best-fit' TOF difference peak was used to correct the $N^+ + O^+$ ion pair peak which produced an 18% increase in the ion pair intensity, equating to a less than 1% increase in the $\sigma_r[N^+]$ value at 100 eV. To complement the 'best-fit' peak a 'worst-fit' TOF difference peak was analysed and produced an increase of 25% to the ion counts of the $N^+ + O^+$ ion pair peak. Again, these variations result in the value of $\sigma_r[N^+]$, at 100 eV, increasing by just over 1%, due to the 1% decrease in $\sigma_1[N^+]$ and a 2% increase in the value of $\sigma_2[N^+]$. The magnitude of this error is again lower than the typical standard deviation presented with the relative PICSs.

The magnitude of the errors discussed above for the correction to the singles spectra for the contribution of the background gas, the loss of ion pairs due to the dead-time, the contribution of accidental coincidences and energetic ion loss each contribute no more than, and often much less than, a ±2% error in the relative PICSs. Statistical combination of these relative errors gives an overall error of ±4% ($\sqrt{4x2^2}$) if all the above errors contribute, which they often do not. The magnitude of this error is generally less than, or equivalent to, the typical standard deviation of ±2-5% shown with the relative PICSs. For that reason the preferred use of the standard deviation in the experimental measurements, as a measure of the error for each average measurement, is justified.

### 3.1.5.2 Relative precursor specific PICSs

In determining the precursor specific values, the sources of error discussed above will all apply. However, as shown below, in the determination of relative precursor specific PICSs the greatest source of uncertainty is undoubtedly the determination of the ion detection efficiency, $f_i$. As described in Chapter 3, $f_i$ is

determined experimentally by recording singles and pairs spectra of $CF_4$, which are normalised to the 'known' cross-sections for forming individual ions and ion pairs following electron ionization of $CF_4$.[6,8,23] The $CF_4$ data of Bruce and Bonham.[6,8,23] are used for this normalization as both the single and ion-pair ionization cross-sections are determined in their work. The experiments of Bruce and co-workers[6,8,23] utilise a pulsed electron source crossed with an effusive gas jet, with two identical TOF mass spectrometers at 180°. Positive ions are accelerated down one flight tube assembly towards one of the MCP detectors while electrons and negative ions are extracted down the other flight tube towards another MCP detector.[6] Bruce and co-workers[8,29] performed a thorough error analysis which detailed statistical counting uncertainties for ions, variation in the electron and gas beams and ion current and errors in the normalization procedures and in their alternative absolute scaling determination. This error analysis produced an *absolute* error for each PICS of ±15%. The ion pair production cross-sections generally had greater absolute uncertainties of around ±20%. The absolute errors given with the data of Bruce and Bonham[6,8,23] represent three standard deviations. Therefore, for the current statistical error analysis one standard deviation is used.

Before embarking on an analysis of the errors in the data presented in this thesis, it is interesting to compare the $CF_4$ data of Bruce and Bonham,[6,8,23] and its listed uncertainty, with recently determined absolute PICSs and absolute ion pair cross-sections of Sieglaff *et al*[30] who utilise electron ionization with a TOF mass spectrometer and position sensitive detector. As discussed in Chapters 2 and 3, the absolute PICSs determined by this experimental group are used to normalise the absolute ICS experiments presented in this thesis, and are generally considered to be the most reliable data for comparison with the current experiments. Unfortunately, for the electron ionization of $CF_4$, Seiglaff *et al*[30] do not determine the cross-sections for all the significant ion pair production channels which are required to determine a value for $f_i$ for the experiments presented in this thesis. Indeed only the $CF^+ + F^+$ and $CF_2^+ + F^+$ ion pair channels are recorded by Seiglaff *et al.*[30] However, comparison of the absolute PICSs is useful: for example, the absolute PICS for the formation of $C^+$ at 140 eV (the peak of the ICS) determined by Sieglaff *et al*[30] is approximately 7% greater than the value determined by Bruce and Bonham.[23] For other less energetic ions formed following electron ionization of $CF_4$ the absolute cross-section data of Seiglaff *et al*[30] are consistently greater (about 5%), but close to, the data of Bruce and Bonham. In fact,

the data of Seiglaff *et al*[30] actually show better agreement with earlier data of Bruce and Bonham prior to a revision by these authors.[8,29,31] This good agreement between the work of these two groups provides further justification for the use of one standard deviation for the data of Bruce and Bonham.[6,8,23] Indeed the error quoted for the absolute ICSs of Seiglaff *et al*[30] is ±5%, justifying the use of this relative error in propagating the errors induced by the variation in the $CF_4$ cross-sections into the current data.

One standard deviation of the errors reported by Bruce and Bonham[6,8,23] (±5%) is propagated with the counting errors of the singles (±3%) and pairs (±4%) data from the current $CF_4$ calibration experiments. This propagation gives deviations of ±15% in the determined values of $f_i$ for the current experiment. For the electron ionization of $N_2O$, detailed in Chapter 4, an average value for $f_i$ was determined to be 0.17 with a standard deviation of ±0.01 (conservatively a ±10% relative error). The systematic error in $f_i$ of ±15%, due to the uncertainty in the calibrating $CF_4$ data, is therefore slightly greater than the statistical standard deviation we determine. Incorporating the systematic error, $f_i$ may have values between 0.14 and 0.20. Performing a "worst case analysis", by using these limiting values of $f_i$, the relative precursor specific PICSs for the formation of $N^+$ vary by ±20%. For example, at 100 eV the value of $\sigma_1(N^+)$ decreases by 20% when a lower value of $f_i$ is utilised and increases by 20% when a higher value of $f_i$ is employed. Such a "worst case" error should be associated with three standard deviations, indicating the associated standard deviation from the possible variations in $f_i$ is about 7%. The exactly opposite trend is of course found for the values of $\sigma_2(N^+)$. The statistical error bars plotted with the relative precursor specific PICS values are typically ±10%, comparable with the 7% variance introduced from the possible variations in $f_i$. Combining the 7% statistical error from the variations in $f_i$ with the 4% relative error from the other sources of error described in the previous section gives a predicted statistical error of 8%, in good accord with the error bars given for this data derived from the statistical spread of the averaged determinations. Again, this shows that the statistical approach employed in determining the uncertainties in the precursor specific PICSs is appropriate and the uncertainty predicted by propagating the errors in determining a value for $f_i$ does not change the conclusions detailed in the results chapters.

As demonstrated in the above analysis, the largest source of uncertainty in the relative precursor specific PICSs results from the determination of $f_i$. The main source

of error in the determination of a value for $f_i$ results from the current methodology that requires experimental data from the literature to be used, and thus the confidence in the value of $f_i$ relies on the level of confidence of the literature data. For future experimental investigations the error in $f_i$ may be minimised by directly measuring $f_i$ and thus significant improvements in the uncertainty of the relative precursor specific PICS data would be accomplished. This could be achieved by using an ion-electron coincidence experiment, although this would require considerable experimental modification.

### 3.1.6 Conclusions

The data analysis methods used to obtain relative PICSs and relative precursor specific PICSs from the singles, pairs and triples spectra have been discussed.

In addition, the analysis of the peak slopes in the pairs spectrum is explained. Detailed discussion is presented on how information regarding multiply charged dissociation dynamics is obtained. Also, the transformation of the pairs spectrum to a TOF difference spectrum is shown, and the methodology used to obtain estimates for the KER(s) is presented.

Chapters 4-6 demonstrate that the analysis procedures described within this chapter yield accurate data on the relative PICSs and relative precursor specific PICSs of $N_2O$, $BCl_3$ and $SF_6$.

The following section of this chapter illustrates the data analysis techniques used following experimental modification to enable the determination of absolute PICSs and absolute precursor specific PICSs from the singles, pairs and triples spectra.

# Section 2 Absolute partial ionization cross-sections

## 3.2 Introduction

The commissioning of an absolute ionization cross-section measurement technique was described in Chapter 2. In this section of Chapter 3 detailed information is presented regarding how initial absolute partial ionization cross-section (PICS) determinations were performed using argon and nitrogen gas. Argon and nitrogen gas were selected as suitable 'test' gases because both have well-defined absolute PICSs available in the literature.[32,33] Whilst performing experiments on this test system, the effect of additional experimental parameters such as gas input order, gas pressure ratio and gas flow were considered. Following these experiments the uncertainties in the determined absolute PICSs were shown to be reduced.

The data analysis is then extended to show how absolute precursor specific PICSs are determined for a 'test' system of argon and nitrous oxide. In this thesis, absolute PICSs, $\sigma'[X^+]$, and absolute precursor specific PICSs, $\sigma_n'[X^+]$, are represented by an additional prime to differentiate an absolute cross-section determination from a relative PICS, $\sigma_r[X^+]$, or relative precursor specific PICS, $\sigma_n[X^+]$.

### 3.2.1 Argon and Nitrogen

#### 3.2.1.1 Absolute partial ionization cross-section determination

With reference to Chapter 2, by taking a ratio of Eqs. 2.2.6 and 2.2.7, an expression dependent only on the gas pressure, individual cross-section and signal intensity of each selected ion is determined, which for the nitrogen/argon gas system is expressed in Eq. (3.2.1). Since the gases are used together, the electron pathlength, initial electron flux and ion detection efficiency are equivalent for each gas used. The nitrogen and argon gas system can be defined in terms of a gas pressure ($p$) ratio, total ion signal intensity ($S$) ratio and the well-defined absolute PICSs of the $Ar^+$ and $N_2^+$ ions:

$$\frac{p_{Ar}}{p_{N_2}}\frac{\sigma'[Ar^+]}{\sigma'[N_2^+]} = \frac{S(Ar^+)}{S(N_2^+)} \qquad (3.2.1).$$

The total ion signal, $S(X^+)$, of an $X^+$ ion, includes ions in the singles and pairs. It should

be noted that no triples were collected due to the short runtimes necessary to minimise gas pressure change over experimental runtime. However, for the 'test' system, the $N_2^+$ and $Ar^+$ signal intensity will, of course, only occur in the singles spectrum and therefore $S(N_2^+)=I(N_2^+)$ and $S(Ar^+)=I(Ar^+)$. For example, to determine $\sigma'[N_2^+]$ values, Eq. (3.2.1) can be re-arranged:

$$\sigma'[N_2^+] = \frac{S(N_2^+)}{S(Ar^+)} \times \frac{p_{Ar}}{p_{N_2}} \times \sigma'[Ar^+] \qquad (3.2.2).$$

$$\left[\sigma'[N_2^+] = \frac{I(N_2^+)}{I(Ar^+)} \times \frac{p_{Ar}}{p_{N_2}} \times \sigma'[Ar^+]\right]$$

Using Eq. (3.2.2), the values of $\sigma'[N_2^+]$ can be determined if all the values on the right hand side of Eq. (3.2.2) are known for each electron energy under investigation. In the following experiments argon is used as the reference gas. The experimental set-up, described in Section 2.1.2.2 of Chapter 2, enables the total ion signal intensity ratio and the gas pressure ratio to be determined, where the absolute PICS of one gas is known from the literature. Sections 3.2.1.2 to 3.2.1.4 briefly explain how these values are determined.

### 3.2.1.2 Total ion signal

The singles and pairs data were recorded and analysed as described in Chapters 2 and 3.

#### 3.2.1.2.1 Singles spectrum

Briefly, events involving a single ion arrival at the detector following the repeller plate pulse are termed 'singles' and the flight times associated with these events are displayed as a histogram of ion counts against flight time. This data makes up the singles spectrum. The intensities of peaks in the singles spectrum, $I(X^+)$, are determined by summing the counts in the peak and applying a suitable background correction for any non-zero baseline. The non-zero background is formed of the ionized residual gas present in the mass spectrometer.

For the $Ar/N_2$ system a singles spectrum is produced showing ion peaks of $N^{2+}$, $N^+$, $Ar^{2+}$, $N_2^+$ and $Ar^+$ ions, Figure 3.2.1. This singles spectrum is analysed as described in Section 3.2.1.

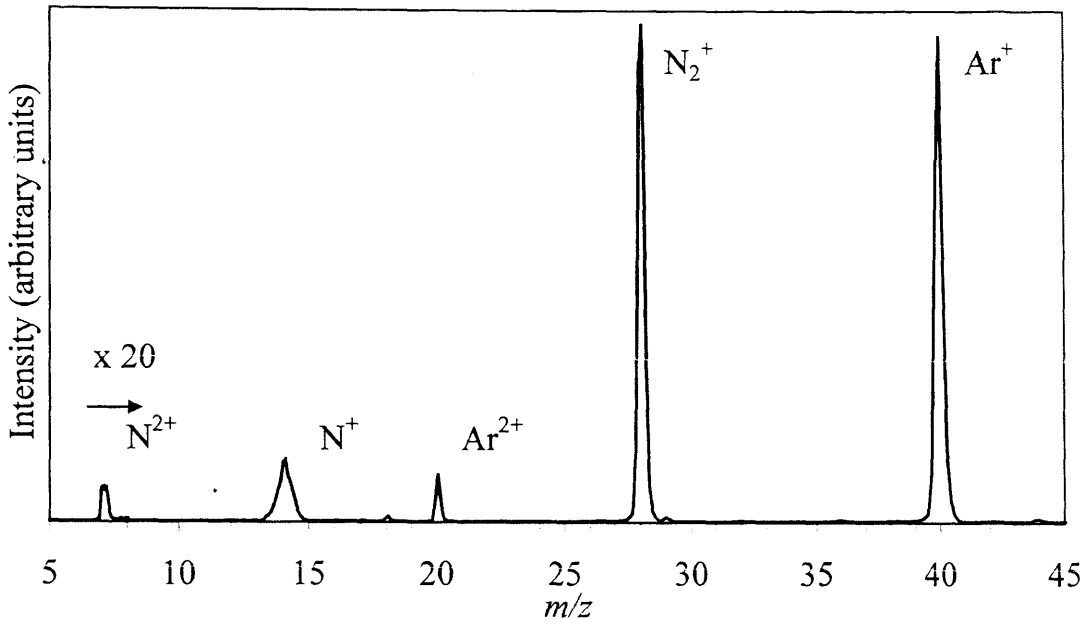


Figure 3.2.1: A singles spectrum of the two-gas system $N_2$/Ar recorded at 200 eV. As indicated in the figure the intensity scale has been increased by a factor of 20 over the *m/z* values of 6-8, to show the signal due to $N^{2+}$. Ion peaks of $O^+$, $H_2O^+$, $O_2^+$ and hydrocarbon residues are also observed from ionization of the background gas.

#### 3.2.1.2.2 Pairs spectrum

The pairs spectrum is displayed as a coincidence spectrum: a two-dimensional histogram of $t_1$ (first ion arrival time) against $t_2$ (second ion arrival time) for each ion pair. The intensities of a given product ion in the pairs spectrum $P[X^+]$ can be determined by summing the number of counts within each characteristic 'lozenge' shaped peak which involves the $X^+$ ion.

If an $X^+$ ion is observed in both the singles and pairs spectra, the total ion signal will be a summation of the intensities observed in the singles and pairs spectra, $S(X^+)=I[X^+]+P[X^+]$. For the Ar/$N_2$ system only one ion pair peak is observed in the pairs spectrum of $N^+ + N^+$. The intensity of the identical ion pair peak is analysed as described in Section 3.1.1.3.

### 3.2.1.3 Gas pressures

The absolute gas pressures of nitrogen and argon are determined using a SRG, as detailed in Chapter 2. Argon is introduced initially, followed by nitrogen. Using the methodology described in Chapter 2, the gas pressure ratio can then be expressed in terms of a 'measured' pressure ratio $p_{mix}/p_{Ar}$, and a ratio of molecular mass $\sqrt{M_{Ar}}/\sqrt{M_{N2}}$,

shown in Eq. (3.2.3):

$$\frac{p_{N_2}}{p_{Ar}} = \frac{p_{mix}}{p_{Ar}} \frac{\sqrt{M_{Ar}}}{\sqrt{M_{N_2}}} \qquad (3.2.3),$$

where $p_{mix}$ and $p_{Ar}$ are defined in Eqs. (2.2.19) and (2.2.20) using the recorded pressure measurements from the SRG and are discussed in detail in Section 2.2.3 of Chapter 2.

#### 3.2.1.3.1 Stable gas pressures

Gases used in the experiments to determine relative PICSs (Section 3.1.3) were stored in a glass globe at atmospheric pressure. A Young's needle valve was used to regulate the gas flow into the source region from the glass globe located on the first gas inlet system. The absolute PICS experiments required both gases to be maintained at a near constant gas pressure in the source region over the experimental runtime, which proved difficult to achieve using gas from the glass globe and gas from the second, 'new' inlet system which had no such gas storage, see Figure 3.2.2. Therefore, gases were used directly from the gas cylinder regulator at a pressure of 1-2 bar which helped to achieve a near constant gas pressure of each gas in the source region. The installation of the second gas inlet system, used together with the first gas inlet system for the absolute PICS experiments, was discussed in detail in Section 2.2.2 of Chapter 2.

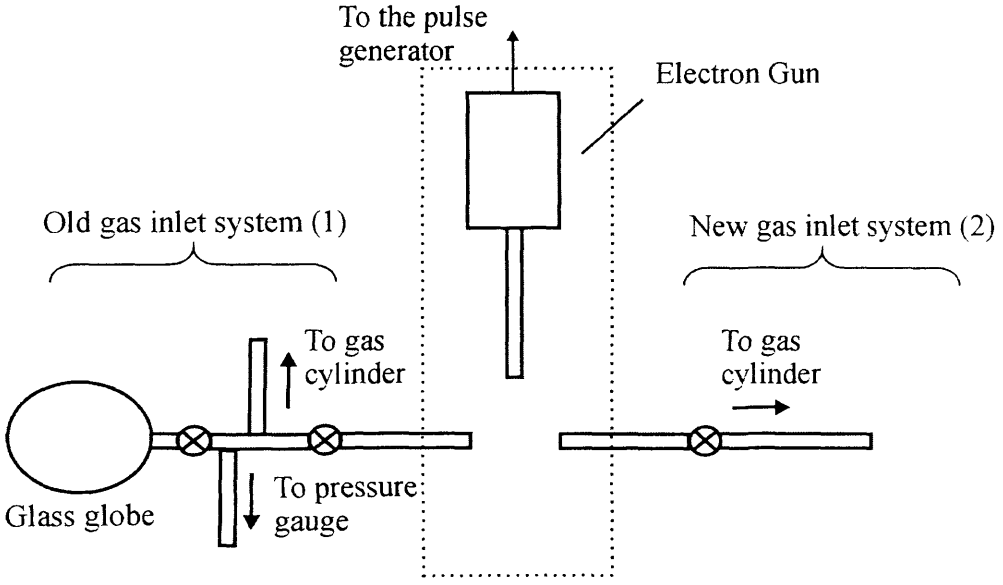


Figure 3.2.2: A schematic diagram of the gas inlet system into the source region, shown by the dotted line. The old gas inlet system, labelled as (1), has the capability of gas storage. However, the new gas inlet system, labelled (2), which has been installed to allow the simultaneous use of two gases has no such gas storage capability.

However, gases could not always be used directly from the cylinder. For example, when using acetylene (Chapter 7), it was necessary to store an atmosphere of gas in the glass globe, due to the hazardous nature of the gas. This method proved sufficient for one day's experimental usage but decreased the stability of the acetylene gas pressure over the experimental runtime.

#### 3.2.1.4 Literature values of absolute partial ionization cross-sections

The absolute PICSs of argon and nitrogen are detailed in the literature. From comparison of the relative PICS determinations, detailed in this thesis for $N_2O$ (Chapter 4) and $SF_6$ (Chapter 6), the cross-section data of Stebbings and co-workers[32,33] are believed to be the most reliable. The cross-section data of Stebbings and co-workers are determined from threshold to 1000 eV, a range which encompasses the 30-200 eV range of electron energies used in this thesis. Stebbings and co-workers experimentally determined each of the variables necessary to derive absolute PICSs (Eq. 2.2.3) and utilised an experimental set-up where energetic ion collection is shown to be 100%. Therefore, the absolute PICS data for $Ar^+$ and $N_2^+$ ions of Stebbings and co-workers are used as the selected reference gas in the electron ionization studies detailed in this chapter and Chapter 7.[32,33] The absolute PICSs of argon determined by Stebbings and co-workers are also used in the determination of absolute PICSs by Tian and Vidal[34] and Basner and co-workers.[35,36] As described in Section 2.2.1 of Chapter 2, these experimental groups utilise similar techniques to determine absolute PICSs to those described in this thesis.

#### 3.2.1.5 Initial results

The experimental methodology used initially for the $Ar/N_2$ 'test' experiments involved adding the reference gas to the source region first, not specifying the use of a certain gas pressure ratio, and using the gas needle inlets into the source region. As expressed in Section 2.2.3.1 of Chapter 2, the experimental aspects of gas inlet order, gas pressure ratio and the position of gas inlets in the source region are believed to be crucial in the determination of accurate absolute PICSs. Therefore, this section will begin by using the experimental conditions outlined above and will then systematically assess the effect of each variable, with the aim of trying to improve the absolute PICS values obtained. The data analysis discussed in Section 3.2.1.1, was used to determine values of $\sigma'[N_2^+]$ from 30-200 eV. With reference to Figure 3.2.3, the currently

determined values of $\sigma'[N_2^+]$ were encouraging.

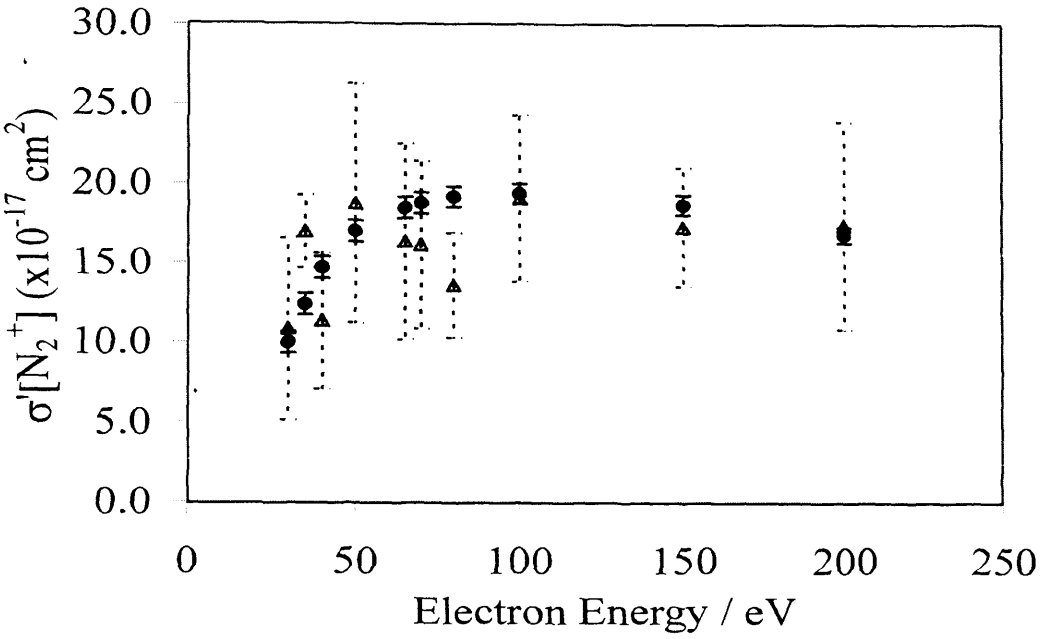


Figure 3.2.3: Values of $\sigma'[N_2^+]$ (△). The points shown represent the average of 10 determinations. The dotted error bars shown represent the standard deviation of 10 determinations for each electron energy. This data is compared with the absolute PICS data for $N_2^+$ of Straub *et al*[33] (●), with appropriate error bars shown.

Agreement was observed between the $\sigma'[N_2^+]$ values determined here and the recently determined absolute PICS data for $N_2^+$ of Straub *et al.*[33] Figure 3.2.3 shows that the $\sigma'[N_2^+]$ values determined here have significant error bars associated with each point. As discussed in Section 2.2.3.2 of Chapter 2, the mixed pressure measurement $p_{mix}$ is the most challenging quantity to accurately determine, as it assumes uniform mixing of the gases in the source region. The large spread of data seen in Figure 3.2.3 indicated that experimental variables that have an effect on this pressure measurement needed to be investigated further. These variables were initially discussed in Section 2.2.3.2 of Chapter 2, for example, the order of gas addition into the source region, the gas pressure ratio of the system and the position of the gas inlets into the source region are important factors. The effects of these factors on the $\sigma'[N_2^+]$ values are reported in Section 3.2.2.

## 3.2.2 Gas pressure in the source region

The experimental technique used in this thesis to determine absolute PICSs is

dependent on the assumption that the individual gas densities approximate the individual gas pressures, see Section 2.2.3.2 of Chapter 2. This assumption relies on the two gases forming a uniform mixture in the source region prior to ionization and thus the pressure readings obtained from the SRG are giving a true representation of the individual gas pressures. The following sections investigate the gas mixture formed and endeavour to obtain a homogeneous gas mixture in order to produce the most accurate absolute PICSs and absolute precursor specific PICSs.

### 3.2.2.1 Gas input order

In Section 2.2.2 of Chapter 2 the second gas inlet system was shown to be equivalent to the original gas inlet system. However, if the gases are not forming a uniform gas mixture in the source region the input order may affect the gas density at the point of ionization, and thus the subsequently recorded pressure measurements may not accurately represent the ratio of densities in the ionization region. Absolute PICS determinations were performed where argon was introduced first followed by nitrogen and *vice versa*, at selected electron energies of 70 and 100 eV. These experiments were performed to ascertain if any difference in the $\sigma'[N_2^+]$ values was observed, Figure 3.2.4.

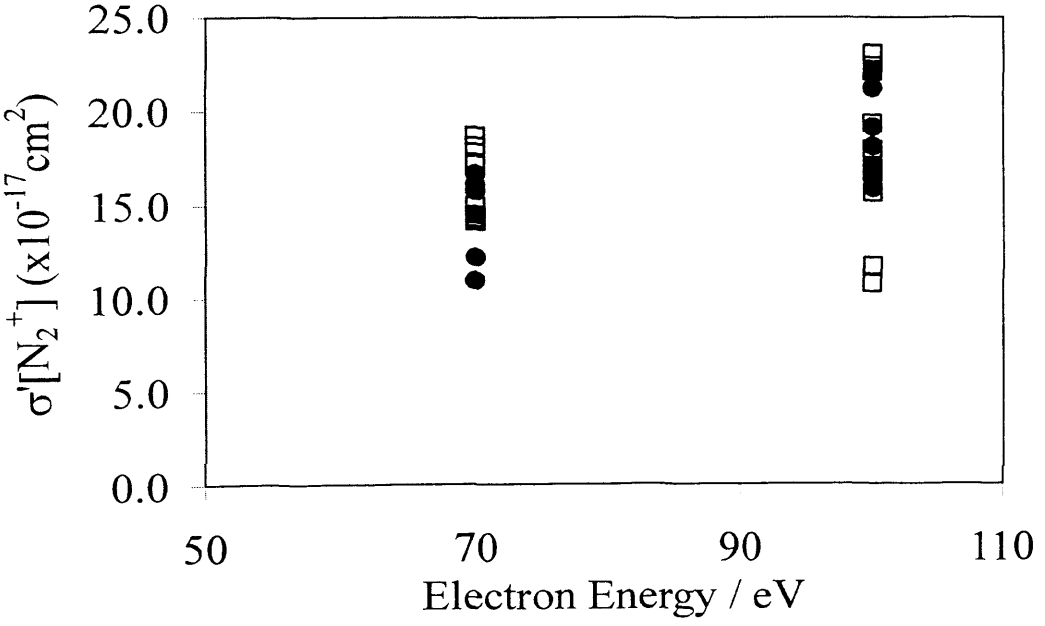


Figure 3.2.4: Values of $\sigma'[N_2^+]$ at 70 and 100 eV, determined for addition of argon first (●) and nitrogen first (□).

Figure 3.2.4 illustrates a significant standard deviation of $\sigma'[N_2^+]$ values for each

case, but the order of gas addition produced no consistent difference between addition of argon first or nitrogen first. To further investigate the large standard deviation, observed in Figure 3.2.4, the gas pressure ratio is examined in Section 3.2.2.2.

### 3.2.2.2 Gas pressure ratio

Having established in Section 3.2.2.1 that there was no consistent difference in the $\sigma'[N_2^+]$ values determined when the order of gas addition was altered, the reference gas, argon, was first introduced to the source region through the old gas inlet system and the 'unknown' gas, nitrogen was subsequently added through the new gas inlet system. Both gases were still introduced into the source region *via* the gas inlet needles. The gas pressure ratio of nitrogen to argon was altered for each experiment by changing one gas pressure whilst the other was kept constant and *vice versa*. The gas pressure ratio is shown with respect to the value of $\sigma'[N_2^+]$ determined at an electron energy of 200 eV, Figure 3.2.5.

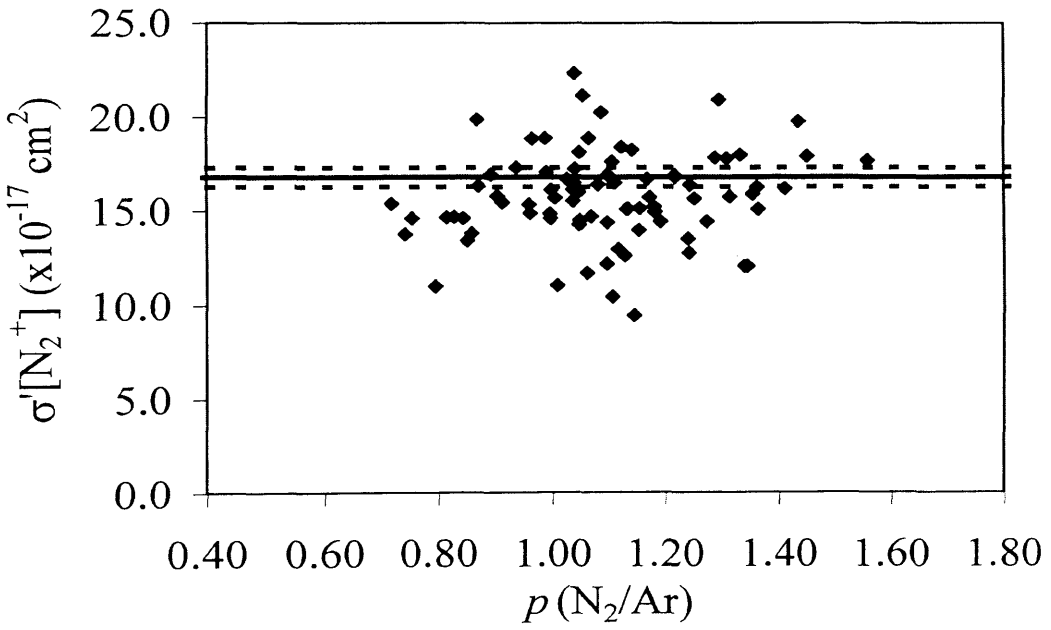


Figure 3.2.5: Values of $\sigma'[N_2^+]$ determined for a range of gas pressure ratios of $N_2$/Ar at an electron energy of 200 eV. The solid line represents the literature value of $\sigma'[N_2^+]$ from the data of Straub *et al.*[33] The two dashed lines show the upper and lower limits of the value determined by Straub *et al.*[33]

Figure 3.2.5 demonstrates that it is desirable to achieve a gas pressure ratio of approximately 1:1, for each experimental run. By utilising gas pressure ratios of

approximately 1:1, the values of $\sigma'[N_2^+]$ determined above show increased reproducibility when compared to both larger and smaller gas pressure ratios.

Another absolute PICS experiment was performed where a gas pressure ratio of approximately 1:1 was produced for each experimental run. The resultant $\sigma'[N_2^+]$ determinations were indeed improved, both in value and certainty, shown in Figure 3.2.6, when compared with the initial experiment displayed in Figure 3.2.3.

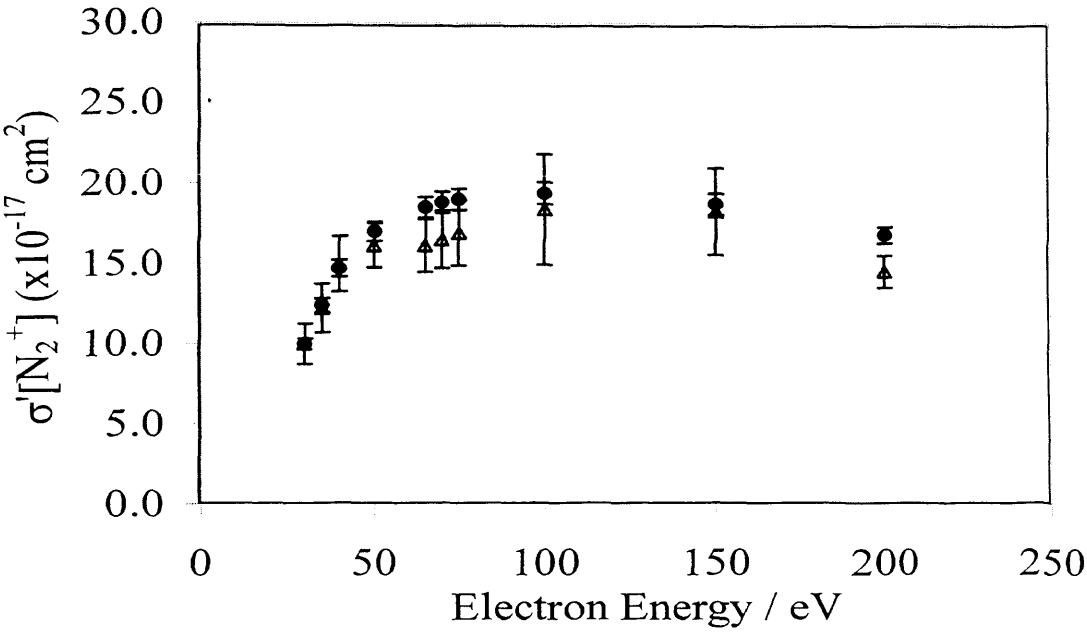


Figure 3.2.6: Values of $\sigma'[N_2^+]$ (△) from 30-200 eV. The points shown represent the average of 4 determinations. The errors shown represent the standard deviation of 4 separate determinations for each electron energy. The absolute PICS data of Straub *et al*[33] (●) are shown with the associated errors.

Figure 3.2.6 illustrates that by achieving a gas pressure ratio of approximately 1:1 for each experimental run, the absolute PICS determinations are significantly improved. The agreement observed between this current data and the absolute PICS data of Straub *et al*[33] is striking. The improvement in the absolute PICS determinations may be explained by considering that by utilising a 1:1 gas pressure ratio, the individual gas density in the source region will be approximately equal, and thus will give the most accurate pressure measurement for each gas.

In the following section the position of the gas inlet needles in the source region is addressed to try to improve the mixing of the two gases before ionization, previously discussed in Section 2.3.3.2 of Chapter 2.

### 3.2.2.3 Gas flow

Following the gas pressure ratio investigation, discussed in Section 3.2.2.2, some additional uncertainty in the absolute PICS determinations remains, see Figure 3.2.6. It is possible that this uncertainty may be due to the nature of the gas inlet systems. Specifically, the gas inlets produce jets of effusive gas, and thus the two gases may not mix as assumed in the source region and may even form two distinct gas regions prior to ionization. To investigate this effect, as described in Section 2.2.3.2 of Chapter 2, the PTFE tubing that connected the glass gas inlet needles to the stainless steel inlet needles within the source region were removed from the stainless steel inlet needles and positioned near the walls of the chamber. Moving the position of the gas inlets provides additional time for the gases to adequately mix in the source region prior to ionization. To test the new location of the PTFE tubing, a further absolute PICS experiment was performed with the $Ar/N_2$ system to determine values of $\sigma'[N_2^+]$ at electron energies from 30-200 eV, shown in Figure 3.2.7.

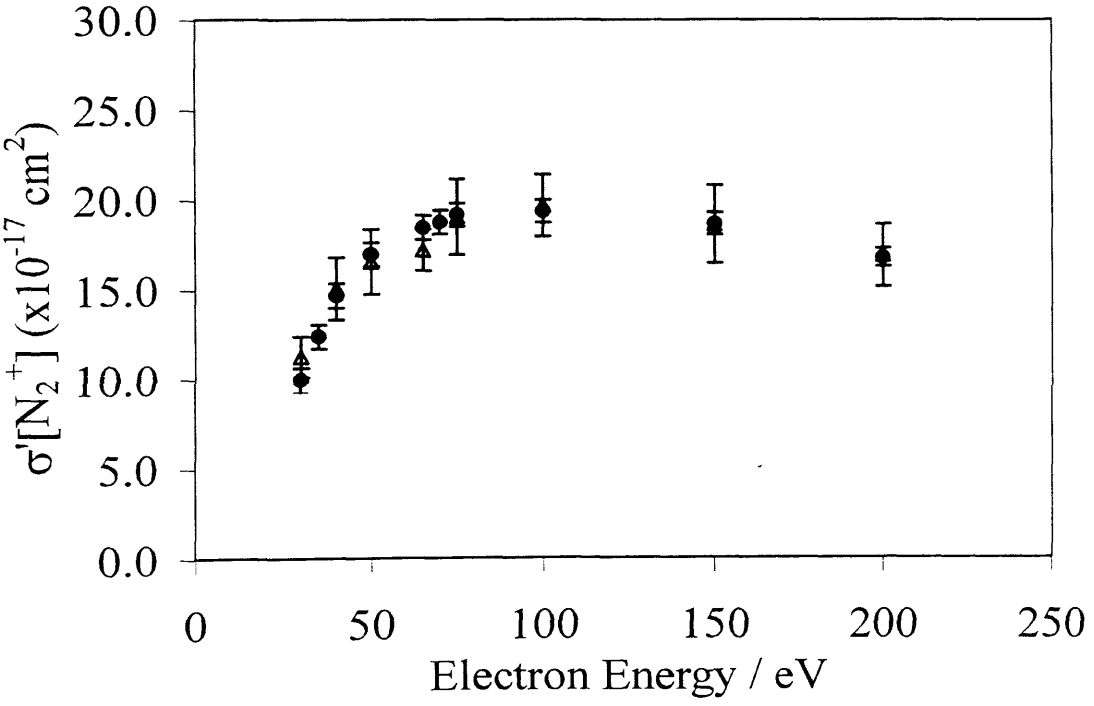


Figure 3.2.7: Values of $\sigma'[N_2^+]$ (△) as a function of electron energy. The points shown represent the average of 4 determinations. The errors shown represent the standard deviation of 4 separate determinations for each electron energy. The absolute PICS data of Straub *et al*[33] (●) are shown with the associated errors.

With reference to Figure 3.2.7 it is evident that the values and uncertainties of the $\sigma'[N_2^+]$ determinations were significantly improved and indeed are in excellent agreement with the absolute PICS data of Straub *et al.*[33] These improvements in the $\sigma'[N_2^+]$ determinations show that in the initial absolute PICS experiments the two gases were not forming a uniform gas mixture prior to ionization in the source region. The positions of the gas inlets may therefore have led to the formation of two distinct gas regions, and thus variable gas densities in the source region, leading to variable and inaccurate gas pressure measurements.

Following the investigations, discussed above, concerning the order of gas addition into the source region, the gas pressure ratio of the system, and the position of the gas inlets in the source region, significantly improved absolute PICSs were determined. In summary, the order of gas addition was determined to make no significant difference to the absolute PICS determinations. However, the gas pressure ratio and position of the gas inlets in the source region were found to be key experimental factors. This is a result of the original assumption utilised in this work that each gas density can be well represented by the respective gas pressure, as discussed in Section 2.2.3.2 of Chapter 2. Therefore, when the two-gas system is well mixed in the source region, prior to ionization, and is composed of approximately equal quantities of gas, reliable absolute PICSs were determined. For all subsequent absolute PICS experiments, performed and detailed in Chapter 7, a gas pressure ratio of 1:1 was utilised together with the relocated gas inlets.

### 3.2.3 Summary

The $N_2$/Ar two-gas 'test' system has shown that a sound methodology has been developed to determine absolute PICSs. By additionally utilising a gas pressure ratio of approximately 1:1 and enabling the gases to form a more uniform gas mixture in the source region the determined values of $\sigma'[N_2^+]$ were in good agreement with Straub *et al*[33] and show improved reproducibility, Figure 3.2.7.

The extension of this data analysis to enable absolute precursor specific PICSs to be determined is described in Section 3.2.4 for the Ar/$N_2O$ 'test' system.

### 3.2.4 Absolute precursor specific partial ionization cross-section determination

To extend the data analysis to determine absolute precursor specific PICSs a

two-gas system of Ar/$N_2O$ was selected. In this two-gas system argon is used as the reference gas and thus the absolute precursor specific PICSs of the fragment ions formed following electron interaction with $N_2O$ are to be determined. This combination of gases was chosen as they met the following criteria: similar molecular mass (40/44), $N_2O$ exhibits dissociative multiple ionization (pairs spectrum, Section 3.1.1.3) and has previously been studied in detail in this laboratory, detailed in Chapter 4. From initial investigations detailed in Chapter 2, the gas pressure ratio was shown to be dependent on the ratio of the square root of the molecular mass of each gas. Thus, by selecting gases with a similar molecular mass, the effect on the gas pressure ratio would be minimised.

Both gases were introduced into the source region using the experimental procedure outlined in Chapter 2 and the additional modifications discussed in Sections 3.2.2.1 to 3.2.2.3. The singles and pairs data were recorded and analysed as described in Chapters 2 and 3.

To enable the absolute precursor specific PICSs to be determined, it is necessary to begin by determining the relative precursor specific PICS for a particular product ion (Eq. (3.2.4) and (3.2.5)), as described in Section 3.1.3. The relative precursor specific PICS for formation of the $N^+$ ion *via* single ($\sigma_1[N^+]$) and double ($\sigma_2[N^+]$) ionization formed following electron interaction with $N_2O$ are expressed below:

$$\frac{I[N^+]-(1-f_i)/f_iP[N^+]}{I[N_2O^+]}=\frac{N_1[N^+]}{N_1[N_2O^+]}=\frac{\sigma_1[N^+]}{\sigma_1[N_2O^+]} \qquad (3.2.4),$$

$$\frac{P[N^+]}{I[N_2O^+]f_i}=\frac{N_2[N^+]}{N_1[N_2O^+]}=\frac{\sigma_2[N^+]}{\sigma_1[N_2O^+]} \qquad (3.2.5).$$

By multiplying Eq. (3.2.4) and (3.2.5) by the value of $\sigma'[N_2O^+]$ determined for each electron energy using Eq. (3.2.8), the absolute precursor specific PICS for formation of the $N^+$ ion *via* single ($\sigma_1'[N^+]$) and double ($\sigma_2'[N^+]$) ionization formed following electron interaction with $N_2O$ are defined:

$$\frac{\sigma_1[N^+]}{\sigma_1[N_2O^+]}\times\sigma'[N_2O^+]=\sigma_1'[N^+] \qquad (3.2.6),$$

$$\frac{\sigma_2[N^+]}{\sigma_1[N_2O^+]}\times\sigma'[N_2O^+]=\sigma_2'[N^+] \qquad (3.2.7),$$

$$\sigma'[N_2O^+]=\frac{S(N_2O^+)}{S(Ar^+)}\times\frac{p_{Ar}}{p_{N_2O}}\times\sigma'[Ar^+] \qquad (3.2.8).$$

In Eq. (3.2.8), the values of the $S(N_2O^+)$, $S(Ar^+)$, $P_{Ar}$ and $P_{N2O}$ were determined from the

singles spectrum and measurements from the SRG respectively, as described in Sections 3.2.1.1 to 3.2.1.4, where,

$$\frac{S(N_2O^+)}{S(Ar^+)} = \frac{I[N_2O^+]}{I[Ar^+]} \quad (3.2.9),$$

$$\frac{p_{Ar}}{p_{N_2O}} = \frac{p_{Ar}}{p_{mix}} \frac{\sqrt{M_{N_2O}}}{\sqrt{M_{Ar}}} \quad (3.2.10).$$

The $\sigma'[N^+]$ values, shown in Chapter 7, were determined using a summation of the individual absolute precursor specific PICSs; $\sigma_1'[N^+]$ and $\sigma_2'[N^+]$, shown in Eq. (3.2.11). The values of $\sigma'[N^+]$ can, of course, be determined 'directly' utilising the same method as that used to determine the $\sigma'[N_2O^+]$ values, shown in Eq. (3.2.12).

$$\sigma'[N^+] = \sigma_1'[N^+] + \sigma_2'[N^+] \quad (3.2.11),$$

$$\sigma'[N^+] = \frac{S(N^+)}{S(Ar^+)} \times \frac{p_{Ar}}{p_{N_2O}} \times \sigma'[Ar^+] \quad (3.2.12).$$

Both methods are mathematically equivalent and thus produce the same absolute PICS values and errors. As the aim of this study is to produce absolute precursor specific PICSs, the absolute PICSs presented in this thesis are determined from the summation of the absolute precursor specific PICSs.

The $Ar/N_2O$ system was used as a test case for the determination of absolute precursor specific PICSs. Absolute precursor specific PICSs for the formation of $N^+$, $O^+$, $N_2^+$ and $NO^+$ ions *via* single and double ionization were determined at electron energies of 30-200 eV, and these results are detailed in Chapter 7. As shown in Chapter 7, the $Ar/N_2O$ test case system produced absolute precursor specific PICS determinations in agreement with data from the literature, providing further evidence that the experimental methodology and analysis procedures, detailed in this chapter, enable accurate absolute PICSs and absolute precursor specific PICSs to be determined.

## 3.2.5 Further improvements

As noted above, for the $Ar/N_2O$ 'test' case system, the contribution to the total ion yield from triple ionization was not determined. In fact, the contribution from triple ionization was neglected throughout the absolute PICS experiments. The contribution from triple ionization to the total ion yield is determined to be only 1% at 200 eV, for the electron ionization of $N_2O$. As discussed in Section 2.2.4.1 of Chapter 2, the experimental runtimes were shortened for the absolute PICS experiments. It was

necessary to use shortened experimental runtimes to minimise any changes in gas pressure and therefore increase the gas pressure stability for each experiment. However, using shorter experimental runtimes results in an increased statistical uncertainty in the absolute PICSs. Therefore, neglect of the contribution from triple ionization to the total ion yield for the absolute PICS experiments is appropriate. The unavoidable fluctuation in gas pressure seen over the time needed to record coincidence spectra remains a source of experimental inaccuracy. In the future it may be advantageous to install precision leak valves for both gas inlet systems to try to minimise the change in pressure over the time needed to record a coincidence spectrum (Section 3.1.1.3). Such increased gas pressure stability may also enable the experimental runtime to be increased and hence enable ion triples to be collected. With the installation of precision leak valves a gas pressure ratio of 1:1 may also be easier to attain.

## 3.2.6 Review of errors

It is now appropriate to discuss the sources of error within the experimental apparatus for the determination of absolute ICSs. The relative magnitude of these errors is presented and the overall error for the absolute ionization cross-sections is assessed.

### 3.2.6.1 Absolute PICSs

As detailed in Chapters 2 and 3, the determination of absolute PICSs and absolute precursor specific PICSs requires the simultaneous use of two gases and the pressure measurements using the SRG. The most challenging quantity to measure in this situation is the pressure and therefore the pressure measurements have the largest associated error. As detailed in Chapters 2 and 3, the gas flow was carefully controlled to ensure that a gas mixture was being formed in the ionization region. However, a systematic error in the pressure readings is a possibility. Consequently, the pressure measurements were assigned a ±10% error. Errors also result from the use of the literature cross-section data for the $Ar^+$ and $N_2^+$ ions. However, the error associated with these cross sections is given to be ±5% and ±3.5% respectively by Straub *et al.*[32,33,37] The counting statistics for the cations were ±1%. By propagating these errors the absolute PICSs have a ±12% error associated with them. The magnitude of this error is reasonable for the experimental determination of absolute PICSs and comparable with the error for similar ionization experiments on molecules.[34,36,38-40] Such an error is in good accord with the error bars given for this data derived from the

statistical spread of the averaged determinations which are approximately ±10%. Again, this shows that the statistical approach employed in determining the uncertainties in the PICSs is appropriate. To reduce the size of the error for future absolute PICS investigation the estimated error derived from the pressure measurements can be investigated and improved with a detailed study of the SRG and the effect of the mass difference for various two-gas systems.

#### 3.2.6.2 Absolute precursor specific PICSs

It is clear from the discussion of the errors for the relative PICSs and relative precursor specific PICSs, presented in Chapter 3, that the absolute precursor specific PICSs will have a greater associated error than the absolute PICSs because $f_i$ must be used in the derivation of these values. Indeed, when including the errors discussed above from the pressure measurements, counting statistics, literature data and the ion detection efficiency (7%) the overall error for the absolute precursor specific PICSs is ±14%, at 100 eV. The displayed standard deviations from repeated determinations of these absolute precursor specific PICSs are usually at least 10%. Such a figure is in good accord with the overall error and shows that the statistical approach employed in determining the uncertainties in the absolute precursor specific PICSs is appropriate. As discussed in Chapter 3, the systematic error could be improved by decreasing the error in the value of $f_i$, and, as discussed above for the absolute PICSs, by increasing the confidence in the pressure measurements.

### 3.2.7 Conclusions

This chapter discusses the data analysis methods used to determine absolute PICSs and absolute precursor specific PICSs in the modified experimental apparatus where two gases are used simultaneously.

The $Ar/N_2$ two-gas system is presented as a 'test' case to illustrate that the experimental methodology and analysis produces accurate absolute PICSs. In the process of performing experiments to determine values of $\sigma'[N_2^+]$, further modifications to the methodology were found to significantly improve the values and uncertainties in the $\sigma'[N_2^+]$ determinations. These improvements include using a gas pressure ratio of 1:1 and moving the gas inlet tubing to form a more uniform gas mixture in the source region. The gas inlet order had no significant effect on the $\sigma'[N_2^+]$ values obtained.

The data analysis methods used to determine absolute precursor specific PICSs are discussed. Chapter 7 illustrates a 'test' case for the absolute precursor specific PICS determinations of $N^+$, $O^+$, $N_2^+$ and $NO^+$ ions using the two-gas system of $Ar/N_2O$ from 30-200 eV.

## 3.3 References


1 J. H. D. Eland, in *Vacuum Ultraviolet Photoionization and Photodissociation of Molecules and Clusters* (World Scientific, Singapore, 1991), pp. 297.

2 J. H. D. Eland, *Mol. Phys.* **61,** 725 (1987).

3 L. J. Frasinski, A. J. Giles, P. A. Hatherly, J. H. Posthumus, M. R. Thompson, and K. Codling, *J. Electron Spectrosc. Relat. Phenom.* **79,** 367 (1996).

4 S. Hsieh and J. H. D. Eland, *Int. J. Mass Spectrom.* **167,** 415 (1997).

5 S. Hsieh and J. H. D. Eland, *J. Phys. B-At. Mol. Opt. Phys.* **30,** 4515 (1997).

6 M. R. Bruce, L. Mi, C. R. Sporleder, and R. A. Bonham, *J. Phys. B-At. Mol. Opt. Phys.* **27,** 5773 (1994).

7 P. Jukes, A. Buxey, A. B. Jones, and A. J. Stace, *J. Chem. Phys.* **109,** 5803 (1998).

8 M. R. Bruce, C. Ma, and R. A. Bonham, *Chem. Phys. Lett.* **190,** 285 (1992).

9 D. A. Hagan and J. H. D. Eland, *Org. Mass Spectrom.* **27,** 855 (1992).

10 L. J. Frasinski, M. Stankiewicz, P. A. Hatherly, and K. Codling, *Meas. Sci. Technol.* **3,** 1188 (1992).

11 P. Calandra, C. S. S. O'Connor, and S. D. Price, *J. Chem. Phys.* **112,** 10821 (2000).

12 W. C. Wiley and I. H. McLaren, *Rev. Sci. Instrum.* **26,** 1150 (1955).

13 J. H. D. Eland, F. S. Wort, and R. N. Royds, *J. Elec. Spect. Rel. Phen.* **41,** 297 (1986).

14 M. Lange, O. Pfaff, U. Muller, and R. Brenn, *Chem. Phys.* **230,** 117 (1998).

15 J. H. D. Eland, *Chem. Phys. Lett.* **203,** 353 (1993).

16 I. Nenner and J. H. D. Eland, *Z. Phys. D-At. Mol. Clusters* **25,** 47 (1992).

17 T. A. Field and J. H. D. Eland, *Chem. Phys. Lett.* **211,** 436 (1993).

18 T. A. Field and J. H. D. Eland, *Chem. Phys. Lett.* **303,** 144 (1999).

19 S. Hsieh and J. H. D. Eland, *Int. J. Mass Spectrom. Ion Process.* **167/168,** 415 (1995).

20 R. Thissen, J. Delwiche, J. M. Robbe, D. Duflot, J. P. Flament, and J. H. D. Eland, *J. Chem. Phys.* **99,** 6590 (1993).

21 D. Mathur, *Phys. Rep.* **225,** 193 (1993).

22 D. A. Hagan and J. H. D. Eland, *Rapid Commun. Mass Spectrom.* **3,** 186 (1989).

23 M. R. Bruce and R. A. Bonham, *Int. J. Mass Spectrom. Ion Process.* **123,** 97 (1993).

24 D. M. Curtis and J. H. D. Eland, *Int. J. Mass Spectrom. Ion Process.* **63,** 241 (1985).

25 S. Leach, J. H. D. Eland, and S. D. Price, *J. Phys. Chem.* **93,** 7575 (1989).

26 P. G. Fournier, J. H. D. Eland, P. Millie, S. Svensson, S. D. Price, J. Fournier, G. Comtet, B. Wannberg, L. Karlsson, P. Baltzer, A. Kaddouri, and U. Gelius, *J. Chem. Phys.* **89,** 3553 (1988).

27 C. S. S. O'Connor, N. Tafadar, and S. D. Price, *J. Chem. Soc.-Faraday Trans.* **94,** 1797 (1998).

28 C. S. S. O'Connor and S. D. Price, *Int. J. Mass Spectrom.* **184,** 11 (1999).

29 C. Ma, C. R. Sporleder, and R. A. Bonham, *Rev. Sci. Instrum.* **62,** 909 (1991).

30 D. R. Sieglaff, R. Rejoub, B. G. Lindsay, and R. F. Stebbings, *J. Phys. B-At. Mol. Opt. Phys.* **34,** 799 (2001).

31 C. Ma, M. R. Bruce, and R. A. Bonham, *Phys. Rev. A* **44,** 2921 (1991).

32 R. Rejoub, B. G. Lindsay, and R. F. Stebbings, *Phys. Rev. A* **65,** 042713 (2002).

33 H. C. Straub, P. Renault, B. G. Lindsay, K. A. Smith, and R. F. Stebbings, *Phys. Rev. A* **54,** 2146 (1996).

34 C. C. Tian and C. R. Vidal, *J. Phys. B-At. Mol. Opt. Phys.* **31,** 895 (1998).

35 R. Basner, M. Schmidt, E. Denisov, K. Becker, and H. Deutsch, *J. Chem. Phys.* **114,** 1170 (2001).

36 R. Basner, M. Schmidt, E. Denisov, P. Lopata, K. Becker, and H. Deutsch, *Int. J. Mass Spectrom.* **214,** 365 (2002).

37 H. C. Straub, P. Renault, B. G. Lindsay, K. A. Smith, and R. F. Stebbings, *Phys. Rev. A* **52,** 1115 (1995).

38 S. H. Zheng and S. K. Srivastava, *J. Phys. B-At. Mol. Opt. Phys.* **29,** 3235 (1996).

39 B. G. Lindsay, R. Rejoub, and R. F. Stebbings, *J. Chem. Phys.* **118,** 5894 (2003).

40 J. Lopez, V. Tarnovsky, M. Gutkin, and K. Becker, *Int. J. Mass Spectrom.* **225,** 25 (2003).

# Chapter 4

# Electron Ionization of $N_2O$

## 4.1 Introduction

Nitrous oxide ($N_2O$) is a colourless, odourless gas, which was first discovered in 1793 by Joseph Priestly.[1] It was not, however, until the 1840s that $N_2O$ was used as an anaesthetic and analgesic, giving $N_2O$ the common name 'laughing gas'. Today, because $N_2O$ is unreactive with most substances at room temperature, it is used as a propellant in aerosols to replace CFCs.[1] Nitrous oxide is also widely used in plasma etching processes for semiconductor manufacturing and it is also a minor, but significant, constituent of the Earth's atmosphere.[2,3] A recent report from the National Research Council addressing the 'Database Needs for Modeling and Simulation of Plasma Processing'[3] highlights the lack of reliable partial ionization cross-sections (PICSs) for molecules such as $N_2O$. Accurate electron ionization cross-sections are essential for the modelling and optimization of plasmas used in industry, and for atmospheric modelling. It is this lack of reliable PICS determinations that provides part of the motivation for the current work presented in this chapter.

### 4.1.1 Electron ionization of $N_2O$

The dissociative ionization of the $N_2O$ molecule has been investigated by photoionization mass spectrometry,[4,5] electron ionization mass spectrometry,[6-8] and coincidence studies.[9,10] Concentrating on previous investigations of the electron ionization of $N_2O$, Rapp and Englander-Golden[11,12] produced the first measurements of the total electron ionization cross-sections of $N_2O$ from threshold to 1000 eV. Märk *et al*[13] followed this work by producing the first absolute partial electron ionization cross-sections for the formation of $N_2O^+$ from threshold to 180 eV. Oliver *et al*[6-8] investigated the ionization of $N_2O$ at low electron energies (15-40 eV) and observed four dissociation channels using ion kinetic energy and mass analysis. More recently, measurements of the absolute PICSs for the production of fragment ions, formed *via*

electron ionization of $N_2O$, were performed by Iga *et al*,[14] Lopez *et al*[15] and Lindsay *et al*.[16] Iga *et al*[14] used a crossed electron and molecular beam, presenting absolute electron ionization cross-sections for $N_2O$ from threshold to 1000 eV. Lopez *et al*[15] utilized a fast-neutral-beam technique determining absolute cross-section data from threshold to 200 eV.

A recent theoretical determination[17] of the total ionization cross-section of $N_2O$ after electron ionization has been carried out using the binary-encounter-Bethe (BEB) theoretical method, and is shown to agree with data from Rapp *et al*[12] and Iga *et al*.[14]

Most recently, Lindsay *et al*[16] used a TOF mass spectrometer with position sensitive detector to determine absolute partial and total ionization cross-sections from threshold to 1000 eV. It is the lack of consistency displayed between the recent experimental determination of the absolute PICSs by Lindsay *et al*[16] and previous cross-section determinations[14,15] that also provides the motivation for the investigation of the ionization of $N_2O$ detailed here. The experimental technique used in this thesis involves a two-dimensional (2D) ion coincidence technique, described in detail in Chapters 2 and 3. This technique enables the single product ions, pairs of product ions or three product ions formed following ionization of individual $N_2O$ molecules to be detected, identified and quantified. Such an experimental set-up allows the first determination of the relative precursor specific PICSs for the ionization of $N_2O$ to be made. These relative precursor specific PICSs quantify the contribution from various levels of ionization to the individual product ion yields following an electron-molecule collision, and hence add further detail to the understanding of the electron ionization of $N_2O$.

Relative PICSs and relative precursor specific PICSs for electron ionization of $N_2O$ have been determined using TOF mass spectrometry and ion-ion coincidence techniques. Cross-sections are reported for ionizing energies from 30-200 eV and data are presented for the formation of $N^{2+}$, $O^{2+}$, $N^+$, $O^+$, $N_2O^{2+}$, $N_2^+$ and $NO^+$ relative to $N_2O^+$.

## 4.2 Experimental Procedures

The nitrous oxide used in these experiments was purchased from Aldrich with a purity of 99.9% and was used without further purification.

### 4.2.1 Experimental conditions

As discussed in Chapters 2 and 3, the operating conditions employed in these

experiments involve low electron fluxes and target gas pressures, to generate a low ion count rate.[18-20] These conditions ensure that there is less than one ionization event detected per electron gun pulse. This methodology markedly decreases the likelihood of any 'accidental coincidences' in the coincidence spectra,[21-23] as discussed in Chapter 3.

### 4.2.2 Predissociation of $N_2O^+$

Earlier experiments performed by Märk *et al*[13] suggest that the $N_2O^+$ ion may predissociate to produce $NO^+$ and N. If such predissociation occurs, the intensity of $N_2O^+$ and $NO^+$ ions detected here will be skewed, and inaccurate relative PICSs would be determined. To verify that $N_2O^+$ was not readily predissociating in this apparatus, the voltages on the source and the drift tube were altered to vary the flight times of the $N_2O^+$ and $NO^+$ ions, enabling the $NO^+/N_2O^+$ ratio to be monitored as a function of flight time. No change in the $NO^+/N_2O^+$ ratio was observed as a function of flight time. It therefore appears that any in-flight predissociation is negligible in these experiments. A similar conclusion was reached in another recent investigation of the ionization of $N_2O$.[16]

## 4.3 Data Analysis

Mass and coincidence spectra were recorded at ionizing electron energies between 30-200 eV using the experimental apparatus described in Chapter 2. For each electron energy four separate experimental cross-section determinations were made.

### 4.3.1 Singles spectrum

A representative singles spectrum of $N_2O$ following electron ionization at 200 eV is illustrated in Figure 4.1. The singles spectrum shows ion peaks corresponding to $N^{2+}$, $O^{2+}$, $N^+$, $O^+$, $N_2O^{2+}$, $N_2^+$, $NO^+$ and $N_2O^+$. The singles spectrum exhibited traces of $O_2^+$, despite several attempts at purification. This peak is attributed to the residual gas in the TOF mass spectrometer, which contributes slightly to the singles (mass) spectrum as the experiments are performed at low $N_2O$ pressures to keep the accidental coincidence rate low, Section 3.1.1.3.2 of Chapter 3. Typically, the magnitude of the $O_2^+$ signal was 1% of the $N_2O^+$ ion signal. In order to remove the contribution from this residual gas to the $N_2O$ singles spectra the singles spectra of air were recorded at each electron energy. These air mass spectra were subtracted from the $N_2O$ spectra by normalizing the air

spectra to the $O_2^+$ signal in the $N_2O$ spectrum.

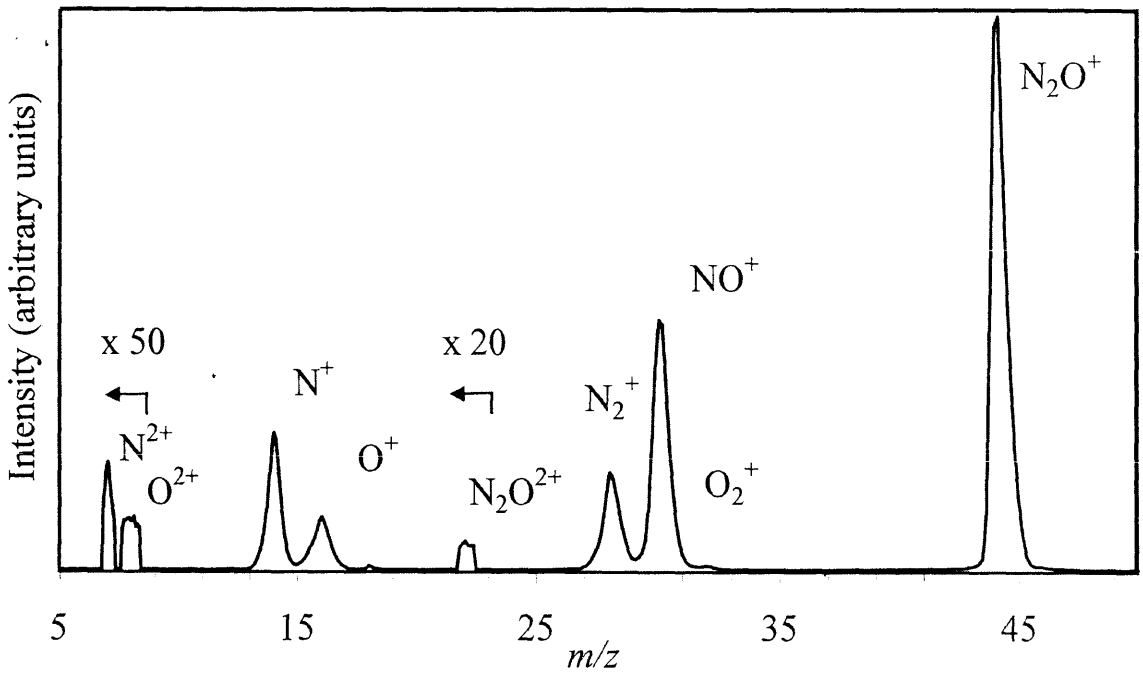


Figure 4.1: A singles (mass) spectrum of $N_2O$ following electron ionization recorded at an electron energy of 200 eV. As indicated in the figure, the intensity scale has been increased by a factor of 50 and 20 over the *m/z* values of 6-9 and 21-23 respectively, to show the signals due to $N^{2+}$, $O^{2+}$ and $N_2O^{2+}$.

## 4.3.2 Pairs spectrum

### 4.3.2.1 Ion pairs

A schematic pairs spectrum recorded at an electron energy of 200 eV following ionization of $N_2O$ is shown in Figure 4.2, and is seen to exhibit eight dissociation channels: $NO^+ + N^+$, $N_2^+ + O^+$, $N^+ + N^+ + O$, $N^+ + O^+ + N$, $N^{2+} + N^+ + O$, $N^{2+} + O^+ + N$, $O^{2+} + N^+ + N$ and $N^{2+} + NO^+$. The dominant fragmentation channel is $NO^+ + N^+$, accounting for 40% of the dissociations detected. The ion pairs involving dications are only present, and then with low intensity, at electron energies above 75 eV.

### 4.3.2.2 Dead-time ion loss

As discussed in Chapters 2 and 3, the experimental set-up is such that no ion pairs are recorded if the second ion arrives within 32 ns of the first ion, due to the dead-time of the discrimination circuitry. Such dead-time losses affect the $N^+ + N^+$ and, to a lesser

extent, the $N^+ + O^+$ peaks in the pairs spectra recorded following electron ionization of $N_2O$. However, these ion losses are easily estimated by extrapolating the visible part of the pairs peak to $t_1=t_2$ using simple geometry.[22,24]

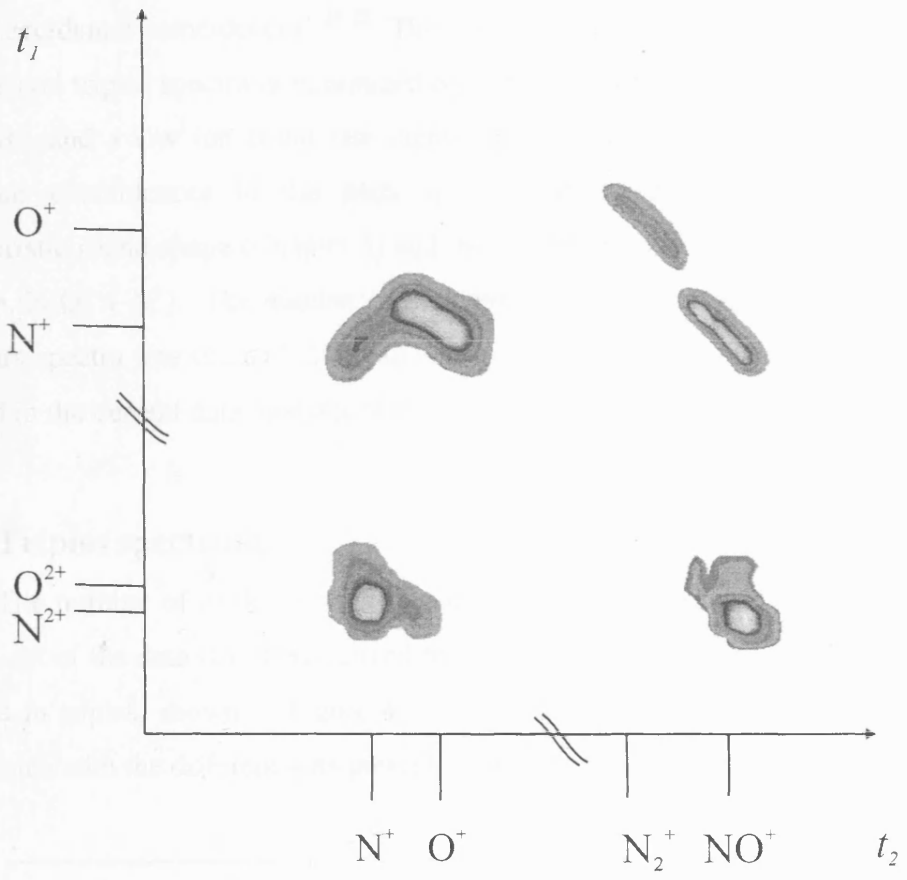


Figure 4.2: A schematic pairs spectrum of $N_2O$ recorded at an electron energy of 200 eV.

#### 4.3.2.3 Notation

As discussed in Section 3.1.1.3.3 of Chapter 3, in the analysis of the pairs spectra, a distinction between the type of ion pair is made: $P_2[X^+]$ and $P_3[X^+]$. $P_2[X^+]$ is the intensity of $X^+$ in pairs of monocations (e.g. $N^+ + O^+$). Such pairs of monocations can arise from double ionization, or from triple ionization if an ion is missed. In contrast, $P_3[X^+]$ represents the intensity of an ion $X^+$ in ion pairs involving a dication and a monocation (e.g. $N^{2+}+ O^+$), and such pairs of ions can only arise from triple ionization, as in the analysis it is assumed that any contribution from quadruple ionization is negligible. As discussed below, only a small contribution from triple ionization is observed at the electron energies studied here, and thus omission of higher order ionization is appropriate.

#### 4.3.2.4 Accidental coincidences

As discussed in Chapter 3, the pairs spectra may contain contributions from ions that did not originate from the same dissociation event but are detected in coincidence, termed 'accidental coincidences'.[21-23] The contribution from accidental coincidences to the pairs and triples spectra is minimized by operating with a low $N_2O$ pressure (below $10^{-6}$ Torr), and a low ion count rate (approximately 200-300 ions per second). Any accidental coincidences in the pairs spectra can be readily identified by their characteristic round shape (Chapter 3) and the combination of observed ion masses (for example, $N_2O^+ + N^+$). The number of accidental coincidences directly observed in the $N_2O$ pairs spectra was small (1-2%) and thus accidental coincidence subtraction was not required in the current data analysis of the $N_2O$ pairs spectra.

### 4.3.3 Triples spectrum

The number of triple coincidences detected is low. As discussed in Chapter 3, this sub-set of the data is first visualized by simply plotting a mass spectrum of the ions recorded in triples, shown in Figure 4.3, and then plotting a series of pairs spectra in coincidence with the different ions present in the mass spectrum of triples.

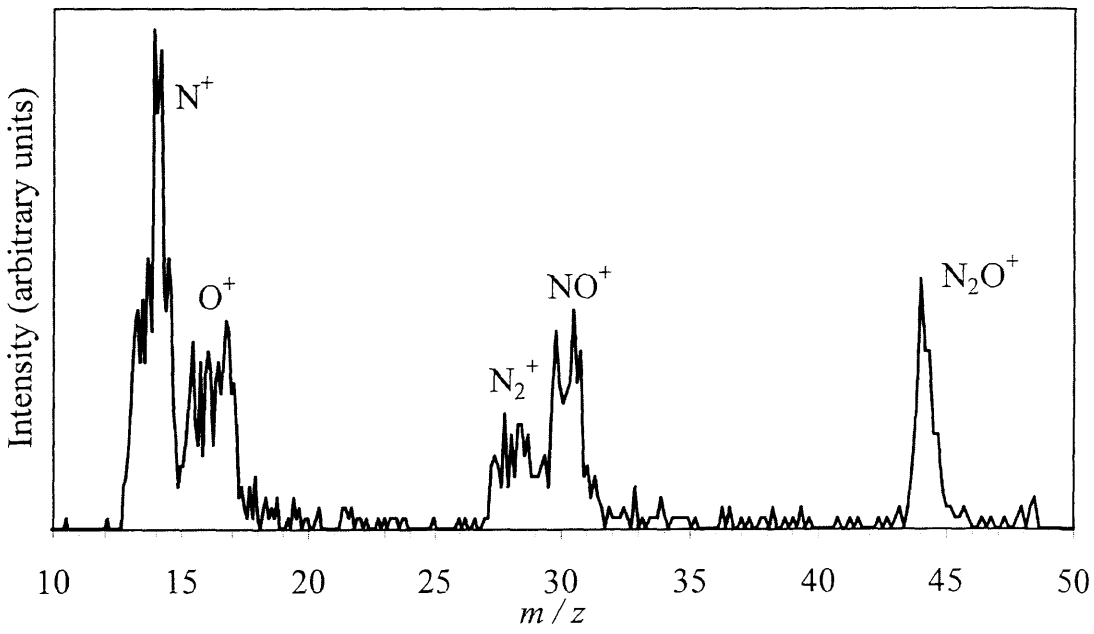


Figure 4.3: A triples mass spectrum recorded at an electron energy of 200 eV. Ion peaks of $N^+$, $O^+$, $N_2^+$, $NO^+$ and $N_2O^+$ are observed. Note the contribution of false coincidences to the spectrum.

The intensities of the peaks in these 'coincident pairs' spectra are determined by summing the counts in each peak to give $T[X^+]$. Figure 4.3 shows the raw triple ion coincidence data. It is clear that the accidental coincidences are significant in this data set, as the observed $N_2^+$, $NO^+$ and $N_2O^+$ ion peaks cannot be formed in the same dissociative ionization event of $N_2O^{3+}$. Accidental coincidence estimation and subtraction was performed, as detailed in Section 3.1.1.4.2 of Chapter 3, and is further detailed below. Following accidental coincidence subtraction, the only real triple event observed following electron ionization of $N_2O$ is the formation of $2N^+ + O^+$. The number of triple ionization events is small, contributing less than 1% to the total ion yield at 200 eV, justifying the neglect of quadruple and higher ionization at these ionizing energies.

#### 4.3.3.1 Accidental coincidences

As discussed in Chapter 3, the triples spectra may contain contributions from ions that did not originate from the same dissociation event but are detected in coincidence, termed 'accidental coincidences'.[21-23] The contribution from accidental coincidences to the triples spectra was minimized by operating with a low $N_2O$ pressure and a low ion count rate. However, accidental coincidences in the triples spectra were frequent, but the false coincidence ion triple peaks were easily identified, as only the formation of the $2N^+ + O^+$ ion triple was possible from the dissociative ionization of $N_2O^{3+}$. Using these false coincidence ion peaks the $2N^+ + O^+$ ion triple was corrected for the contribution from accidental coincidences, as described in Section 3.1.1.4.2 in Chapter 3, to produce a 'true' intensity for this ion triple.

## 4.4 Relative PICSs

The ion intensities recorded in the singles, pairs and triples spectra were processed to yield the relative PICSs and the relative precursor specific PICSs. This data processing is described in detail in Chapter 3 and specifically for the electron ionization of $N_2O$ in Appendix C, and thus only a brief summary is given below.

### 4.4.1 Notation

The relative PICS for the formation of a fragment ion $X^+$ is expressed as $\sigma_r[X^+]$, where the cross-section for the formation of $X^+$ is expressed relative to the cross-section for forming $N_2O^+$. Similarly, the relative precursor specific PICS $\sigma_n[X^+]$ ($n$=1-3)

express the cross-section for forming the fragment ion $X^+$, relative to the cross-section for forming $N_2O^+$, *via* single ($n$=1), double ($n$=2) or triple ($n$=3) ionization.

## 4.4.2 Ion intensities

A full description of the data analysis methods is presented in Chapter 3. To illustrate the data analysis, the equations used to determine relative PICSs are shown for the $N^+$ and $N^{2+}$ fragment ions in Eqs. (4.1) and (4.2). The relative PICSs are expressed as a sum of the individual precursor specific PICSs for formation of the ion *via* single, double and triple ionization, where $N_n[X^+]$ represents the number of $X^+$ ions formed *via* loss of $n$ electrons. These values can in turn be expressed as a sum of the ion intensities from the singles $I[X^+]$, pairs $P_2[X^+]$ and $P_3[X^+]$, and triples spectra $T[X^+]$:

$$\sigma_r[N^+]=\frac{N_1[N^+]+N_2[N^+]+N_3[N^+]}{N_1[N_2O^+]}=\frac{I[N^+]+P_2[N^+]+P_3[N^+]+T[N^+]}{I[N_2O^+]} \quad (4.1),$$

$$\sigma_r[N^{2+}]=\frac{N_2[N^{2+}]+N_3[N^{2+}]}{N_1[N_2O^+]}=\frac{I[N^{2+}]+P_3[N^{2+}]}{I[N_2O^+]} \quad (4.2).$$

Where the intensity of the $N^+$ and $N^{2+}$ ions in the singles, pairs and triples spectrum can be described by the following equations:

$$I[N^{2+}]=f_i N_2[N^{2+}]+f_i(1-f_i)N_3^{\text{pairs}}[N^{2+}] \quad (4.3),$$

$$I[N^+] = f_i N_1[N^+]+f_i(1-f_i)N_2[N^+]+f_i(1-f_i)N_3^{\text{pairs}}[N^+]+f_i(1-f_i)^2 N_3^{\text{triples}}[N^+] \quad (4.4),$$

$$P_3[N^{2+}]=f_i^2 N_3^{\text{pairs}}[N^{2+}] \quad (4.5),$$

$$P_2[N^+]=f_i^2 N_2[N^+]+2f_i^2(1-f_i)N_3^{\text{triples}}[N^+] \quad (4.6),$$

$$P_3[N^+]=f_i^2 N_3^{\text{pairs}}[N^+] \quad (4.7),$$

$$T[N^+]=f_i^3 N_3^{\text{triples}}[N^+] \quad (4.8).$$

The $\sigma_r$ values expressed here do not depend on $f_i$. However, by determining a value for $f_i$ the data analysis can be extended to yield the values of $\sigma_n[X^+]$, quantifying the contribution to each ion yield from single, double and triple ionization.

### 4.4.3 Relative precursor specific PICSs

#### 4.4.3.1 Ion detection efficiency

As discussed in Chapter 3, to enable the $\sigma_n[X^+]$ values to be derived a value for $f_i$ must be determined by recording singles and pairs spectra following ionization of $CF_4$.[18] For the electron ionization experiments of $N_2O$, this procedure resulted in a value of $f_i$=0.17±0.01, in agreement with previous determinations reported in the literature.[18,20]

The expressions used to evaluate the relative precursor specific PICSs for formation of $N^+$ *via* single, double and triple ionization are shown in Eqs. (4.9)-(4.11):

$$\sigma_1[N^+] = \frac{N_1[N^+]}{N_1[N_2O^+]} \qquad (4.9),$$

$$= \frac{I[N^+] - (1-f_i)/f_i P_2[N^+] - (1-f_i)/f_i P_3[N^+] + (1-f_i)^2/f_i^2 T[N^+]}{I[N_2O^+]}$$

$$\sigma_2[N^+] = \frac{N_2[N^+]}{N_1[N_2O^+]} = \frac{P_2[N^+]/f_i - 2(1-f_i)/f_i^2 T[N^+]}{I[N_2O^+]} \qquad (4.10),$$

$$\sigma_3[N^+] = \frac{N_3^{\text{pairs}}[N^+] + N_3^{\text{triples}}[N^+]}{N_1[N_2O^+]} = \frac{P_3[N^+]/f_i + T[N^+]/f_i^2}{I[N_2O^+]} \qquad (4.11).$$

## 4.5 Energetic ion loss

As discussed in Chapter 3, the signals in the ($t_1$-$t_2$) spectrum will have square tops if all the ions are being collected, Figure 4.4 (a). Ions with a kinetic energy greater than 11 eV perpendicular to the TOF axis will not be detected, and such ion losses result in a 'hollowing' of peaks in the TOF difference spectrum. This 'hollowing' involves a loss of counts at the centre of the normally square coincidence peak, Figure 4.4 (b). The TOF difference plots for the $N^+ + O^+$ ion pair show this hollow character, indicative of some degree of energetic ion loss.

To correct for this ion loss, the area of the $N^+ + O^+$ signal is adjusted to create a square coincidence peak which allows for the events missed. The dotted line in Figure 4.4 (b) illustrates how the intensity of the ion pair peak is estimated if there were no energetic ion loss. The intensity of the dotted square topped peak is determined and compared to the intensity of the original ion pair peak. This intensity correction is adequate for the estimation of the missed ion events in the coincidence peaks. Typically, the values determined for the relative PICSs of $N^+$ and $O^+$ increased by 1%, resulting from an 18% increase in the number of ion counts for the $N^+ + O^+$ ion pair. This modelling also corrects the $N^+ + O^+$ signal intensity for events lost due to the dead-

time of the electronics, as the flight times for these two ions are similar. However, it is not possible to quantify any fragment ion loss from single ionization, if such ions are formed with a translational energy component of more than 11 eV perpendicular to the axis of the mass spectrometer.

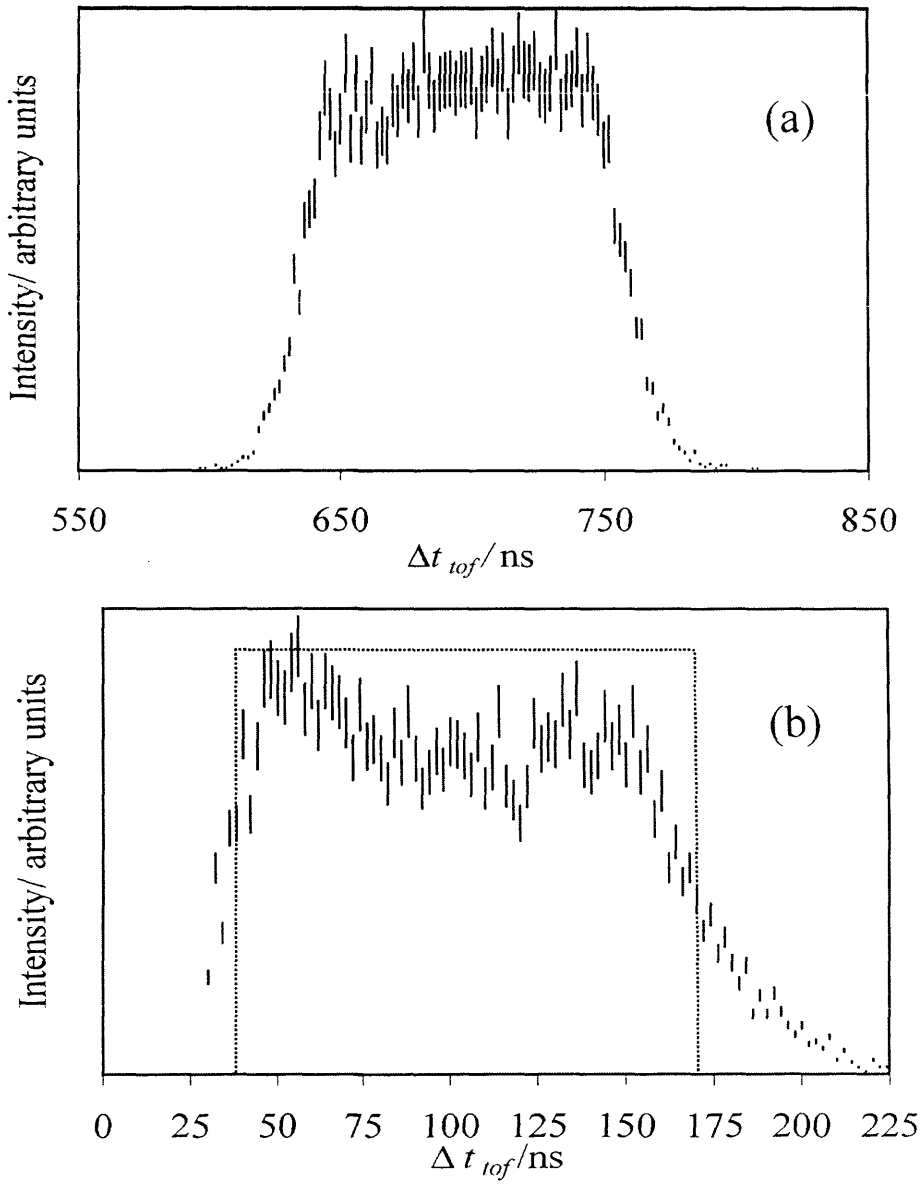


Figure 4.4: Ion coincidence peaks: (a) for the $NO^+ + N^+$ ion pair transformed from the pairs spectrum. This peak forms a 'square' top indicative of complete ion collection. (b) for the $N^+ + O^+$ ion pair transformed from the pairs spectrum. This 'hollow' peak is indicative of energetic ion loss. The manually constructed dotted line illustrates a similar peak with a square top, where no energetic ion loss is occurring. Therefore, by determining the intensity of the dotted peak, the intensity of the ion pair peak if no energetic ion loss was experienced is estimated, and thus the intensity of the missed ions is estimated.

## 4.6 Discussion

The singles and coincidence spectra were processed, as described in Section 4.4, to yield $\sigma_r$ values for the formation of $N^+$, $O^+$, $N_2^+$, $NO^+$, $N^{2+}$, $O^{2+}$ and $N_2O^{2+}$ which are shown as a function of electron energy in Figure 4.5. These $\sigma_r$ values are expressed relative to the $N_2O^+$ ion yield and are displayed in Table 4.1 and Table 4.2. Figure 4.5 shows $N_2O^+$ to be the most abundant ion formed following ionization of $N_2O$ at all the electron energies investigated.

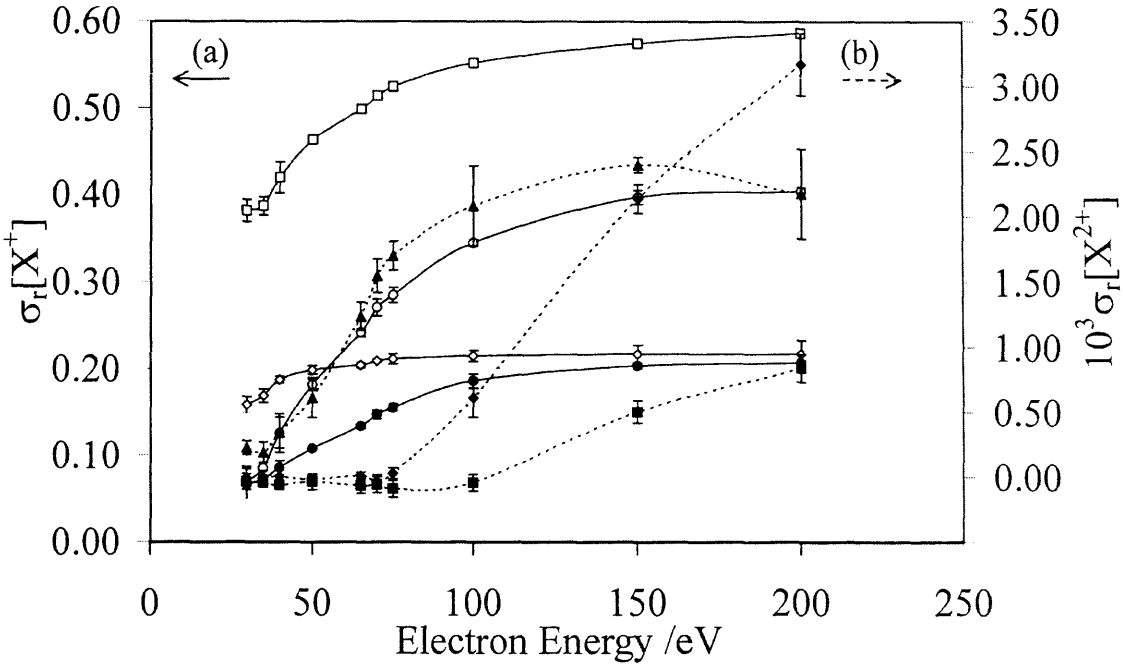


Figure 4.5: Relative PICSs for forming $NO^+$(□) $N^+$(O), $O^+$(●), $N_2^+$(◇), $N_2O^{2+}$(▲), $N^{2+}$(◆) and $O^{2+}$(■) following electron ionization of $N_2O$. The yield of these product ions is expressed relative to the yield of $N_2O^+$. The error bars expressed in this figure represent the standard deviation of 4 separate determinations. Note the $\sigma_r$ values for the formation of the dicationic fragments are joined by dotted lines and the values refer to the right-hand axis.

The $\sigma_n$ values ($n$=1, 2 and 3) derived are displayed within Sections 4.6.1 - 4.6.7 in Figure 4.6 - Figure 4.9 and values are listed in Table 4.3 - Table 4.7.

Table 4.1: Relative PICSs following electron ionization of $N_2O$, expressed relative to the cross-section for forming $N_2O^+$, as a function of electron energy *E*. The standard deviation of the last figure is given in parentheses.

| *E*/eV | $10^3\ \sigma_r[N^{2+}]$ | $10^3\ \sigma_r[O^{2+}]$ | $\sigma_r[N^+]$ | $\sigma_r[O^+]$ |
|---|---|---|---|---|
| 200 | 3.2(2) | 0.8(1) | 0.403(3) | 0.207(5) |
| 150 | 2.1(1) | 0.5(1) | 0.397(8) | 0.203(4) |
| 100 | 0.6(1) | 0.0(2) | 0.344(4) | 0.185(8) |
| 75 | 0.0(1) | 0.0(1) | 0.284(9) | 0.155(4) |
| 70 | 0.0(1) | 0.0(1) | 0.270(10) | 0.147(5) |
| 65 | 0.0(1) | 0.0(1) | 0.241(5) | 0.133(2) |
| 50 | 0.0(1) | 0.0(1) | 0.181(7) | 0.107(2) |
| 40 | 0.0(1) | 0.0(1) | 0.125(22) | 0.085(8) |
| 35 | 0.0(1) | 0.0(1) | 0.085(14) | 0.072(4) |
| 30 | 0.0(1) | 0.0(1) | 0.069(10) | 0.066(6) |

Table 4.2: Relative PICSs following electron ionization of $N_2O$, expressed relative to the cross-section for forming $N_2O^+$, as a function of electron energy *E*. The standard deviation of the last figure is given in parentheses.

| *E*/eV | $10^3\ \sigma_r[N_2O^{2+}]$ | $\sigma_r[N_2^+]$ | $\sigma_r[NO^+]$ |
|---|---|---|---|
| 200 | 2.17(34) | 0.217(16) | 0.586(2) |
| 150 | 2.39(6) | 0.217(10) | 0.574(4) |
| 100 | 2.08(31) | 0.214(6) | 0.551(1) |
| 75 | 1.70(11) | 0.211(6) | 0.524(5) |
| 70 | 1.54(13) | 0.209(2) | 0.514(4) |
| 65 | 1.23(11) | 0.204(3) | 0.499(3) |
| 50 | 0.61(15) | 0.198(5) | 0.463(4) |
| 40 | 0.34(12) | 0.187(4) | 0.419(18) |
| 35 | 0.19(8) | 0.168(8) | 0.386(10) |
| 30 | 0.22(5) | 0.158(9) | 0.381(13) |

The significant aspects of each fragment ion cross-section are discussed in the following sections. Where appropriate, comparisons are made between the $\sigma_r$ values determined here and values derived from the absolute PICSs presented by Iga *et al*,[14] Lopez *et al*[15] and Lindsay *et al*.[16] Values of the absolute PICSs presented by Lopez *et al*[15] have been extracted from the graphs in the publication of Lopez *et al*[15] which introduces an additional error of a few percent into the presented values of their relative cross-sections shown here.

### 4.6.1 $NO^+$ formation

The values of $\sigma_r[NO^+]$ determined here show $NO^+$ to be the second most abundant ion formed following ionization of $N_2O$ (Figure 4.6), constituting 39% of the total ion signals recorded following electron ionization of $N_2O$ at an electron energy of 200 eV. The values of $\sigma_1[NO^+]$, $\sigma_2[NO^+]$ and $\sigma_3[NO^+]$ increase up to the maximum electron energy for these experiments of 200 eV (Figure 4.6) and are displayed in Table 4.3.

Table 4.3: Relative precursor specific PICSs for forming $NO^+$ following electron ionization of $N_2O$, expressed relative to the cross-section for forming $N_2O^+$, as a function of electron energy *E*. The standard deviation of the last figure is given in parentheses.

| *E*/eV | $\sigma_1[NO^+]$ | $\sigma_2[NO^+]$ | $10^3\ \sigma_3[NO^+]$ |
|---|---|---|---|
| 200 | 0.492(1) | 0.094(1) | 0.46(5) |
| 150 | 0.484(3) | 0.090(2) | 0.31(9) |
| 100 | 0.477(2) | 0.074(1) | 0.17(4) |
| 75 | 0.471(3) | 0.053(4) | 0.06(2) |
| 70 | 0.468(3) | 0.046(2) | 0.06(1) |
| 65 | 0.461(1) | 0.037(1) | 0.07(1) |
| 50 | 0.444(3) | 0.019(2) | 0.11(5) |
| 40 | 0.414(14) | 0.006(4) | 0.05(2) |
| 35 | 0.384(9) | 0.002(1) | 0.06(4) |
| 30 | 0.378(12) | 0.003(1) | 0.06(3) |

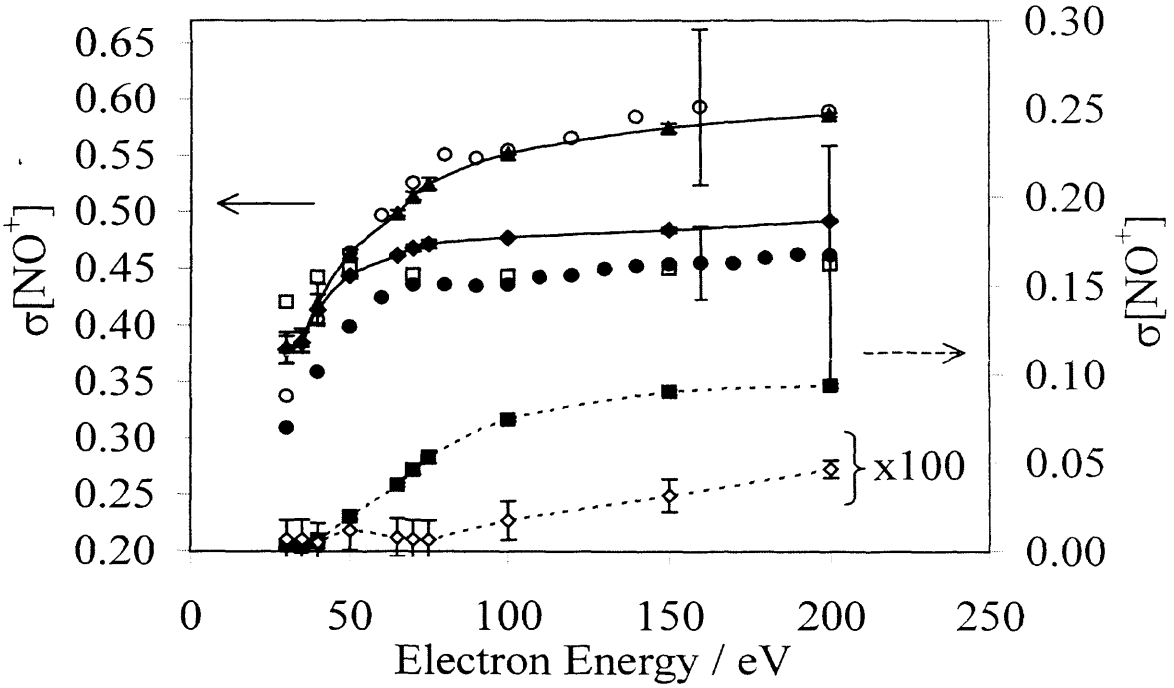


Figure 4.6: Relative precursor specific PICSs for forming $NO^+$ *via* single (◆), double (■) and triple ionization (◇) following electron ionization of $N_2O$. The relative PICS is shown by (▲). These cross-sections are expressed relative to the cross-section for forming $N_2O^+$. The error bars shown in the figure are standard deviations of multiple determinations. Note that the $\sigma_2$ and $\sigma_3$ values, linked by dotted lines, are referenced to the right-hand axis and that the left-hand axis does not start at zero. Relative PICSs extracted from the data of Iga *et al*,[14] (●) Lopez *et al*[15] (□) and Lindsay *et al*[16] (O) are also shown with representative error bars.

Over the whole electron energy range there is agreement between the $\sigma_r[NO^+]$ values determined here and the values derived from the data of Lindsay *et al.*[16] Below 50 eV there is also agreement (Figure 4.6) between the $\sigma_r[NO^+]$ values determined here and the values derived from the data of Iga *et al*[14] and Lopez *et al.*[15] However, above 50 eV the values of $\sigma_r[NO^+]$ determined here are approximately 25% larger than the data of Iga *et al.*[14] Above 50 eV the $\sigma_r[NO^+]$ values determined here and those from Lopez *et al*[15] are within their mutual error limits. However, above 50 eV the actual values from the data of Lopez *et al*[15] are approximately 25% lower than the current data, and in fact are close to the values from the data of Iga *et al.*[14]

Above 50 eV, the contribution to the ion yield from dissociative double ionization becomes significant (Figure 4.6), and this suggests the difference between the data determined here and that of Iga *et al*[14] and Lopez *et al*[15] is as a result of the loss of

energetic ions from multiple ionization. This conclusion is supported by the agreement between the data of Iga *et al*[14] and Lopez *et al*[15] and the values of $\sigma_1[NO^+]$ determined here. Iga *et al*[14] do not detail the detection efficiency of their apparatus for highly translationally energetic fragment ions. However, Lopez *et al*[15] state their apparatus is capable of detecting all ions produced with a kinetic energy of less than 3.5 eV, an upper limit which may well miss a significant number of energetic ions from double ionization.[9] It seems clear the difference between both the values determined here, and those of Lindsay *et al*[16], for $\sigma_r[NO^+]$ and those derived from the data of Iga *et al*[14] and Lopez *et al*[15] is a consequence of the loss of energetic ions in the earlier experiments as also concluded by Lindsay *et al.*[16]

### 4.6.2 $N_2^+$ formation

Figure 4.7 shows that the values of $\sigma_r[N_2^+]$ increase gradually towards an electron energy of 200 eV. The values of $\sigma_1[N_2^+]$ peak at an electron energy of 50 eV (Figure 4.7 and Table 4.4). The values of $\sigma_2[N_2^+]$ become significant above 50 eV and increase towards 200 eV. Note that the left-hand axis of Figure 4.7 does not start at zero. This scale is used to provide a better illustration of the difference between the values derived from the absolute PICS data of Lindsay *et al*[16] and the values of $\sigma_r[N_2^+]$ determined here that are discussed below.

The values derived from the absolute PICS data of Lindsay *et al*[16] agree, within the error limits, with the values of $\sigma_r[N_2^+]$ determined here (Figure 4.7). However, above 50 eV, poor agreement is observed for the values of $\sigma_r[N_2^+]$ determined here and the values derived from the cross-sections of Iga *et al*[14] and Lopez *et al*[15] for all electron energies. The values derived from the cross-sections of Iga *et al*[14] and Lopez *et al*[15] are approximately 40% lower than the values of $\sigma_r[N_2^+]$ determined here. As observed for the $NO^+$ ion, there is agreement between the relative PICSs derived from the data of Iga *et al*[14] and Lopez *et al*[15] and the values of $\sigma_1[N_2^+]$ determined here. These observations again strongly indicate that the differences between the data determined here and that of Iga *et al*[14] and Lopez *et al*[15] are as a result of the loss of energetic ions in the earlier experiments.

No $N_2^+ + O^{2+}$ signals are observed in the pairs spectrum (Figure 4.2), and no detectable amounts of $N_2^+$ are formed by triple ionization over the range of ionizing energies investigated here. In contrast, $NO^+$ is clearly formed by triple ionization as this ion is detected as part of the $NO^+ + N^{2+}$ ion pair, Figure 4.2.

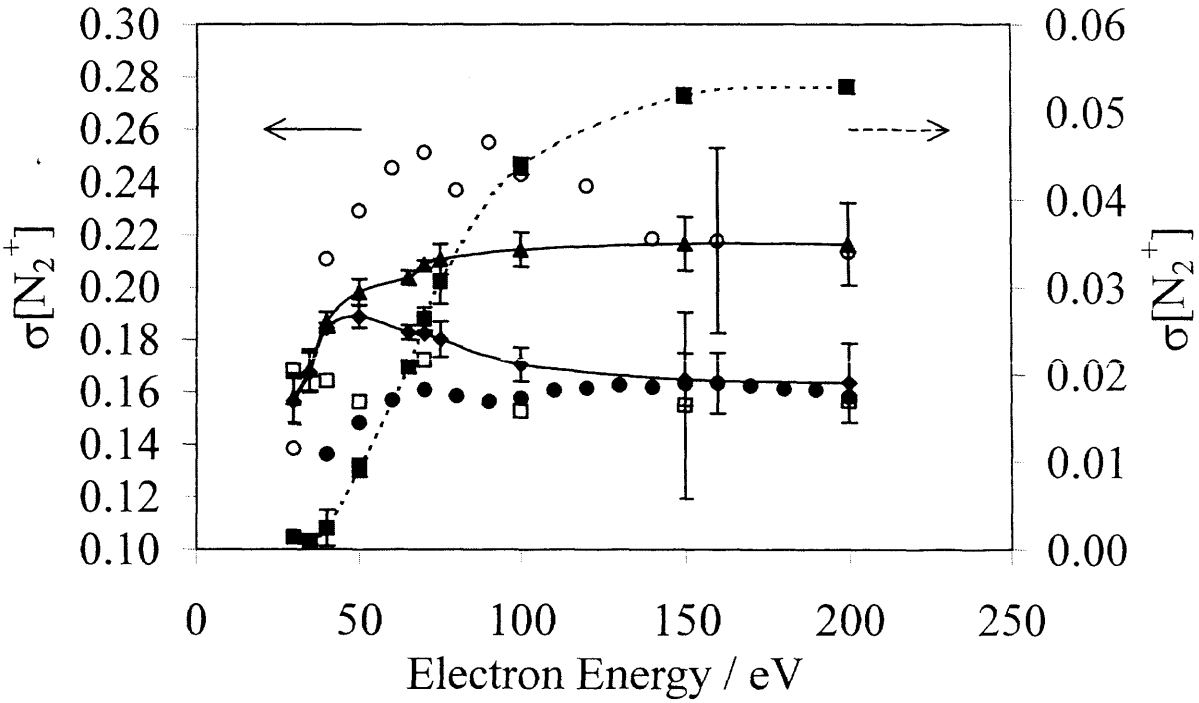


Figure 4.7: Relative precursor specific PICSs for forming $N_2^+$ *via* single (◆) and double ionization (■) following electron ionization of $N_2O$. The relative PICS is shown by (▲). Note that the $\sigma_2$ values, linked by the dotted line, are referenced to the right-hand axis and that the left-hand axis does not start at zero. Relative PICSs extracted from the data of Iga *et al*,[14] (●) Lopez *et al*[15] (□) and Lindsay *et al*[16] (O) are shown with representative error bars (see caption to Figure 4.6 for details).

Table 4.4: Relative precursor specific PICSs for forming $N_2^+$ following electron ionization of $N_2O$, expressed relative to the cross-section for forming $N_2O^+$, as a function of electron energy *E*. The standard deviation of the last figure is given in parentheses.

| *E*/eV | $\sigma_1[N_2^+]$ | $\sigma_2[N_2^+]$ |
|---|---|---|
| 200 | 0.164(15) | 0.053(1) |
| 150 | 0.165(10) | 0.052(1) |
| 100 | 0.171(7) | 0.044(1) |
| 75 | 0.180(7) | 0.031(3) |
| 70 | 0.182(1) | 0.026(1) |
| 65 | 0.183(3) | 0.021(1) |
| 50 | 0.189(4) | 0.009(1) |
| 40 | 0.184(2) | 0.002(2) |
| 35 | 0.167(8) | 0.001(1) |
| 30 | 0.156(9) | 0.001(1) |

### 4.6.3 $N^+$ formation

Figure 4.8 shows that the values of $\sigma_1[N^+]$ derived here peak at an electron energy of 70-75 eV and decrease towards higher ionizing energies. The values of $\sigma_2[N^+]$ rise rapidly with increasing electron energy, becoming larger than the values of $\sigma_1[N^+]$ above an electron energy of 110 eV, showing that double ionization contributes significantly to the $N^+$ ion yield. The values of $\sigma_3[N^+]$ only become significant above 70 eV. These values are also displayed in Table 4.5.

The values of $\sigma_r[N^+]$ derived here are approximately 10% lower than the values derived from the absolute PICSs of Lindsay *et al*,[16] (Figure 4.8). However, the values agree within their mutual error limits for all electron energies. This discrepancy may be a consequence of the current experimental set-up missing highly translationally excited ions (>11eV) from single ionization, discussed in Section 4.5, a loss for which no estimation and correction is possible.

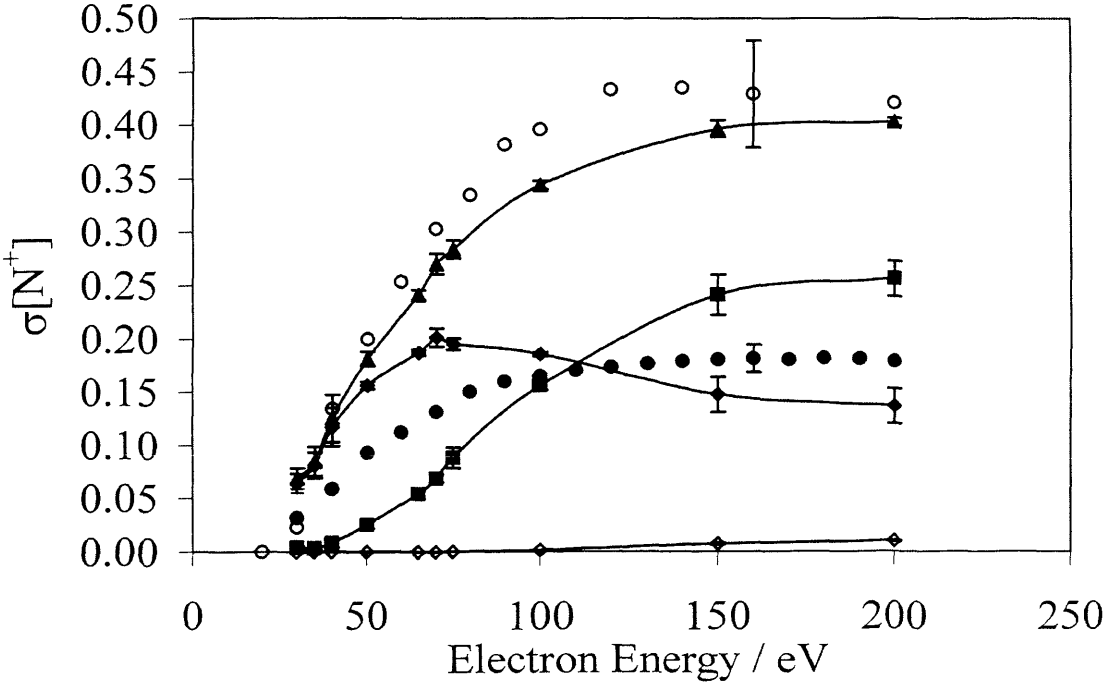


Figure 4.8: Relative precursor specific PICSs for forming $N^+$ *via* single (◆), double (■) and triple ionization (◇) following electron ionization of $N_2O$. The relative PICS is shown by (▲). Relative PICSs extracted from the data of Iga *et al*[14] (●) and Lindsay *et al*[16] (O) are also shown with representative error bars. See the caption to Figure 4.6 for details.

The values of $\sigma_r[N^+]$ derived here are approximately twice the magnitude of the values derived from the data of Iga *et al.*[14] Above 70 eV, where the values of $\sigma_2[N^+]$

are significant, the data of Iga *et al*[14] show better agreement with the values of $\sigma_1[N^+]$ determined here than with the $\sigma_r[N^+]$ values. However, even below 70 eV the relative PICSs derived from the data of Iga *et al,*[14] were significantly lower than the data determined here. This indicates, that as well as missing energetic $N^+$ ions from multiple ionization, the experiments of Iga *et al*[14] may have missed some energetic ions from single ionization.

Table 4.5: Relative precursor specific PICSs for forming $N^+$ following electron ionization of $N_2O$, expressed relative to the cross-section for forming $N_2O^+$, as a function of electron energy *E*. The standard deviation of the last figure is given in parentheses.

| *E*/eV | $\sigma_1[N^+]$ | $\sigma_2[N^+]$ | $10^2\ \sigma_3[N^+]$ |
|---|---|---|---|
| 200 | 0.137(16) | 0.256(17) | 0.99(7) |
| 150 | 0.148(17) | 0.241(19) | 0.74(6) |
| 100 | 0.186(2) | 0.156(4) | 0.17(2) |
| 75 | 0.195(5) | 0.088(10) | 0.03(1) |
| 70 | 0.201(9) | 0.069(4) | 0.00(2) |
| 65 | 0.187(2) | 0.054(4) | 0.00(2) |
| 50 | 0.156(4) | 0.025(3) | 0.00(2) |
| 40 | 0.117(18) | 0.008(4) | 0.00(2) |
| 35 | 0.081(12) | 0.004(1) | 0.00(2) |
| 30 | 0.064(9) | 0.005(1) | 0.00(2) |

### 4.6.4 $O^+$ formation

Figure 4.9 shows the values of $\sigma_1[O^+]$ determined here peak at an electron energy of 70-75 eV and then decrease toward higher ionizing energies, similar to the behaviour of $\sigma_1[N^+]$. At an electron energy of 95 eV, the contribution to the total $O^+$ product ion yield from $O^+$ ions formed *via* dissociative double ionization, becomes greater than the contribution from dissociative single ionization (Figure 4.9). A large percentage of the $O^+$ ion yield results from dissociative double ionization. For example, at an ionizing electron energy of 200 eV, the formation of $O^+$ *via* double ionization constitutes 70% of the total $O^+$ ion yield. As with $\sigma_3[N^+]$, values of $\sigma_3[O^+]$ only become significant above 70 eV. These values are also displayed in Table 4.6.

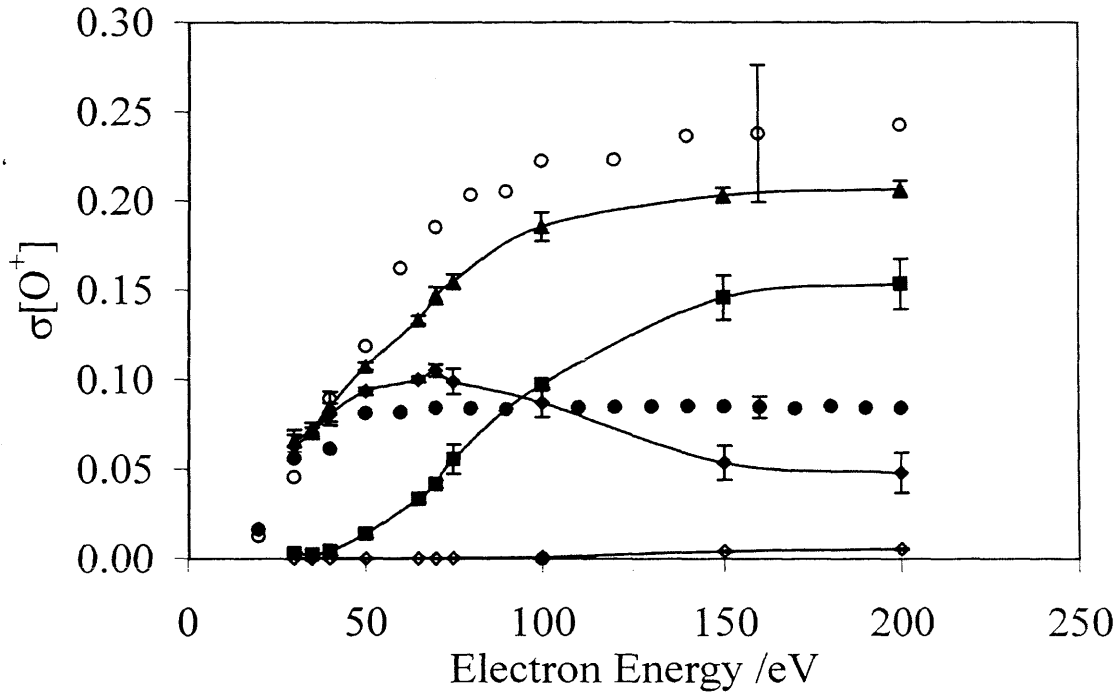


Figure 4.9: Relative precursor specific PICSs for forming $O^+$ *via* single (◆), double (■) and triple ionization (◇) following electron ionization of $N_2O$. The relative PICS is shown by (▲). Relative PICSs extracted from the data of Iga *et al*[14] (●) and Lindsay *et al*[16] (O) are also shown with representative error bars. See the caption to Figure 4.6 for details.

Table 4.6: Relative precursor specific PICSs for forming $O^+$ following electron ionization of $N_2O$, expressed relative to the cross-section for forming $N_2O^+$, as a function of electron energy *E*. The standard deviation of the last figure is given in parentheses.

| *E*/eV | $\sigma_1[O^+]$ | $\sigma_2[O^+]$ | $10^2\,\sigma_3[O^+]$ |
|---|---|---|---|
| 200 | 0.048(11) | 0.153(14) | 0.53(4) |
| 150 | 0.054(10) | 0.146(12) | 0.39(3) |
| 100 | 0.087(8) | 0.097(3) | 0.09(1) |
| 75 | 0.099(7) | 0.056(8) | 0.02(1) |
| 70 | 0.105(3) | 0.042(2) | 0.00(2) |
| 65 | 0.100(2) | 0.033(2) | 0.00(2) |
| 50 | 0.093(2) | 0.014(2) | 0.00(2) |
| 40 | 0.081(6) | 0.004(2) | 0.00(2) |
| 35 | 0.070(3) | 0.002(1) | 0.00(2) |
| 30 | 0.063(6) | 0.003(1) | 0.00(2) |

The values of $\sigma_r[O^+]$ determined here are approximately 15% lower than the values of Lindsay *et al.*[16] However, the $\sigma_r[O^+]$ values determined here do agree with the values derived from the absolute PICSs of Lindsay *et al*[16] within their mutual error limits (Figure 4.9). The relative PICSs derived from the data of Iga *et al*[14] show poor agreement with the values of $\sigma_r[O^+]$ determined here which is indicative of energetic ion loss.

Lopez *et al*[15] cannot resolve the individual contribution of $N^+$ and $O^+$ in their mass spectra. To compare the relative PICSs determined here and the data of Lopez *et al*,[15] the values of $\sigma_r[N^+]$ and $\sigma_r[O^+]$ must be summed, Figure 4.10.

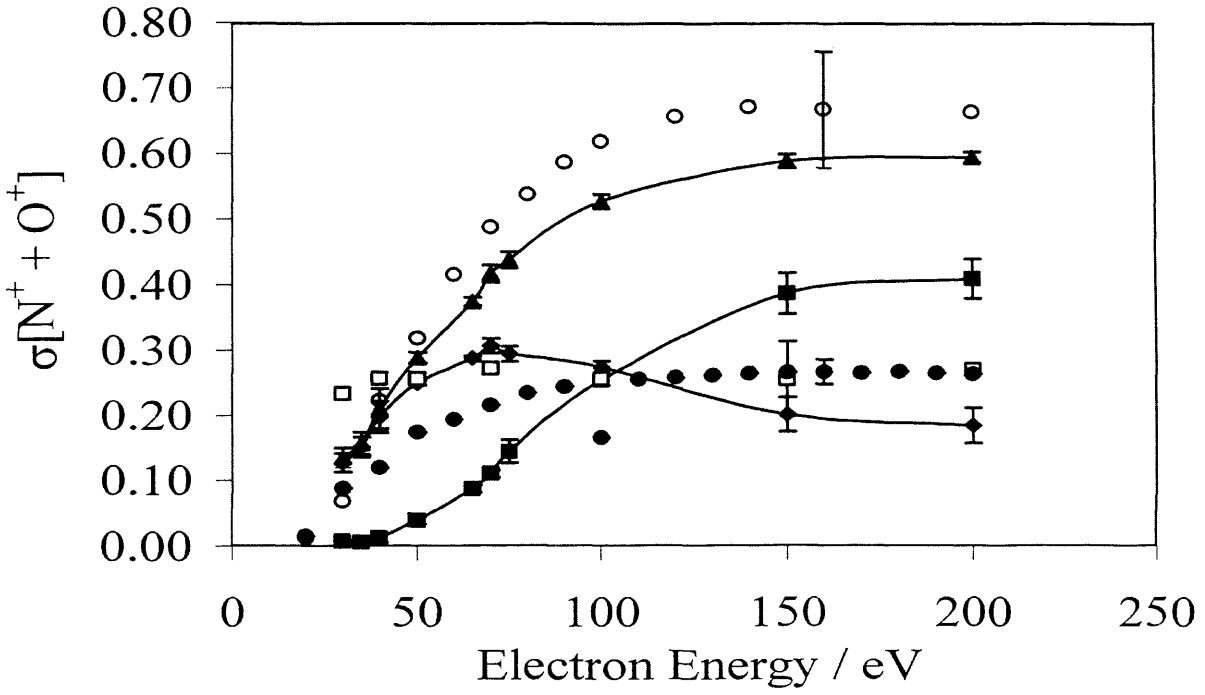


Figure 4.10: Relative precursor specific PICSs for forming $N^+ + O^+$ *via* single (◆) and double ionization (■) following electron ionization of $N_2O$. The relative PICS is shown by (▲). Relative PICSs extracted from the data of Iga *et al*,[14] (●) Lopez *et al*[15] (□) and Lindsay *et al*[16] (O) are also shown with representative error bars. See the caption to Figure 4.6 for details.

The values of $\sigma_r[N^+ + O^+]$ determined here are within the error limits of the data of Lopez *et al*[15] below 65 eV. However, at higher electron energies the values of $\sigma_r[N^+ + O^+]$ determined here are 100% larger than the values of Lopez *et al*,[15] Figure 4.10. It seems probable that this difference is again due to incomplete ion collection of energetic ions from multiple ionization.

### 4.6.5 $N^{2+}$ formation

The values of $\sigma_r[N^{2+}]$ are small (Figure 4.5). The $N^{2+}$ peak in the mass spectrum is only clearly obvious at electron energies above 75 eV and it should be noted that here $\sigma_r[N^{2+}] = \sigma_2[N^{2+}] + \sigma_3[N^{2+}]$. The values determined for both $\sigma_2[N^{2+}]$ and $\sigma_3[N^{2+}]$ are zero below 100 eV (Table 4.7).

### 4.6.6 $O^{2+}$ formation

The values of $\sigma_r[O^{2+}]$ become statistically significant above an electron energy of 100 eV (Figure 4.5 and Table 4.7). Values of $\sigma_2[O^{2+}]$ and $\sigma_3[O^{2+}]$ are only appreciable above an electron energy of 100 eV.

Table 4.7: Relative precursor specific PICSs for forming $N^{2+}$ and $O^{2+}$ following electron ionization of $N_2O$, expressed relative to the cross-section for forming $N_2O^+$, as a function of electron energy *E*. The standard deviation of the last figure is given in parentheses.

| *E*/eV | $10^3\ \sigma_2[N^{2+}]$ | $10^3\ \sigma_3[N^{2+}]$ | $10^3\ \sigma_2[O^{2+}]$ | $10^3\ \sigma_3[O^{2+}]$ |
|---|---|---|---|---|
| 200 | 1.5(2) | 1.6(2) | 0.5(1) | 0.4(1) |
| 150 | 1.2(2) | 0.9(1) | 0.3(1) | 0.2(1) |
| 100 | 0.4(2) | 0.2(1) | 0.0(2) | 0.0(2) |
| 75 | 0.0(2) | 0.1(2) | 0.0(2) | 0.0(2) |
| 70 | 0.0(2) | 0.1(2) | 0.0(2) | 0.0(2) |
| 65 | 0.0(2) | 0.1(2) | 0.0(2) | 0.0(2) |
| 50 | 0.0(2) | 0.1(2) | 0.0(2) | 0.0(2) |
| 40 | 0.0(2) | 0.1(2) | 0.0(2) | 0.0(2) |
| 35 | 0.0(2) | 0.1(2) | 0.0(2) | 0.0(2) |
| 30 | 0.0(2) | 0.1(2) | 0.0(2) | 0.0(2) |

### 4.6.7 $N_2O^{2+}$ formation

The appearance energy for $N_2O^{2+}$ formation (Figure 4.5) lies between 30 and 40 eV, where, within the error limits, the $N_2O^{2+}$ yield was zero at an electron energy of 30 eV and non-zero at 40 eV. An estimate for the appearance energy of $N_2O^{2+}$ was determined, by extrapolation of the three data points above 30 eV, producing a value of 36.0±2.0 eV. This double ionization energy is in agreement with other determinations of the ground state energy of $N_2O^{2+}$ available in the literature.[25-27]

### 4.6.8 The energetics of dissociative double ionization

In principle, the gradient of the peaks in the pairs spectrum can be used to elucidate the dynamics of the dicationic dissociation process, discussed in Chapter 3. However, the temporal resolution in the pairs spectra produced in these experiments, due to the length of the electron pulse, is insufficient to add any information on the dynamics of the three-body dissociation reactions of multiply charged $N_2O$ which have been extensively investigated.[28,29] Table 4.8 shows the gradients and proposed dynamics of the dicationic dissociation processes for the ion pair peaks observed in these experiments compared with PEPIPICO and electron ionization experiments.[9,26,28]

Table 4.8: Gradient determinations and proposed dicationic dissociation processes for ion pair peaks (a) observed in the pairs spectrum recorded currently at 200 eV compared with (b) other experimentally determined gradients using 25.6 nm and 30.4 nm photoionization and 1300 eV electron ionization.[9,26,28]

| | Ion pairs | | | |
|---|---|---|---|---|
| | $NO^+ + N^+$ | $N_2^+ + O^+$ | $N^+ + O^+$ | $N^+ + N^+$ |
| Gradient[(a)] | ≈-1 | ≈-1 | ≈-1 | - |
| Proposed dissociation process[(a)] | Direct | Direct | Inconclusive | Obscured due to dead-time |
| Gradient[(b)] | -1 | -1 | -1.075±0.025 (-1 and -2) | - |
| Proposed dissociation process[(b)] | Direct | Direct | (1) Mixture of concurrent mechanisms<br>(2) Single rapid sequential process | - |

As described in Chapter 3, the peak shapes in the pairs spectrum can be used to estimate the kinetic energy released when the doubly charged parent ion dissociates. The KERs are extracted by forming a TOF difference ($t_2 - t_1$) plot from the pairs data, where the differences in ion flight times are histogrammed for each ion pair of interest and are then compared with a Monte Carlo simulation for the particular dissociation channel. Using the procedure outlined in Section 3.1.4 of Chapter 3, the KER for the

formation of the $NO^+ + N^+$ and $N_2^+ + O^+$ ion pairs was determined at an electron energy of 50 eV, as this electron energy is the lowest which provides sufficient coincidence signals to produce a statistically significant result. A KER of 6.3±1.0 eV was found for the $NO^+ + N^+$ channel, in agreement with the PIPICO determination, at 40.8 eV, of Price *et al*[26] and a more accurate value, less influenced by field inhomogeneities, from Eland and Murphy (7.2±0.4 eV).[28] At 50 eV the $N_2^+ + O^+$ channel cannot be well modelled using only a single KER. The best fit required three kinetic releases of 3.2±1.0, 5.8±1.0, 9.0±1.0 eV with weightings of 10:50:40. These values are in agreement with previous determinations.[26,28] The dominant energy releases in each of these channels have previously been assigned to the fragmentation of the ground $^3\Sigma^-$ state of $N_2O^{2+}$.[26,28]

As the formation of $2N^+ + O^+$ *via* triple ionization of $N_2O$ is very weak, the $N^+ + O^+$ and $N^+ + N^+$ signals can be interpreted in terms of the double ionization of $N_2O$. The KER in the $N^+ + O^+$ channel is well modelled using two energy releases of 5±1 eV and 7±1 eV. These values are in agreement with that of Eland and Murphy (5.2±1.0 eV) obtained using 25.6 nm radiation.[28] The lowest electron energy for which the KER for the $N^+ + N^+ + O$ dissociation channel can be determined is 65 eV. At this electron energy the experimental data can be fitted with two KERs of 5±1 eV and 8±1 eV. These KERs could be interpreted in terms of $N_2O^{2+}$ precursor state energies of 45.6±1 and 48.6±1 eV, assuming one-step double ionization. These potential precursor states lie relatively high in the electronic state manifold[28] of $N_2O^{2+}$ and, hence, no clear identification is possible.

## 4.7 Conclusions

Two-dimensional TOF mass spectrometry has been used to determine the relative PICSs and relative precursor specific PICSs for the formation of $N^{2+}$, $O^{2+}$, $N^+$, $O^+$, $N_2O^{2+}$, $N_2^+$ and $NO^+$ relative to $N_2O^+$ at electron energies from 30-200 eV. This is the first time that relative precursor specific PICSs have been derived for the electron ionization of $N_2O$. At 50 eV double ionization contributes 7% of the total product ion yield and at 100 eV the contribution was 28%. These results highlight the importance of energetic fragment ion collection in the measurement of ionization cross-sections. Similar conclusions have previously been drawn using this experimental apparatus for the electron ionization of $Cl_2$ and HCl.[18,19] For $Cl_2$ and HCl, at 50 eV, double ionization was found to contribute 14% and 3% respectively to the total product ion yield and at 100 eV the contribution was 26% and 12% respectively.[18,19]

Comparison between the cross-section data currently determined and recent electron ionization studies of $N_2O$ by Iga *et al*,[14] Lopez *et al*,[15] and Lindsay *et al*[16] have been made. Agreement between the data determined here and the relative cross-sections derived from the data of Lindsay *et al*[16] was found for the formation of $N^+$, $O^+$, $N_2^+$ and $NO^+$ ions. However, significant differences were found between the relative PICSs for the formation of $N^+$, $O^+$, $N_2^+$ and $NO^+$ determined here and those derived from the cross-sections of Iga *et al*[14] and Lopez *et al.*[15] These differences are consistent with the incomplete collection of translationally energetic ions in some earlier experiments.

## 4.8 References


1 I. E. Eger, *Nitrous oxide* (Edward Arnold Ltd, New York, 1985).

2 R. P. Wayne, *Chemistry of Atmospheres* (Clarendon Press, Oxford, 1985).

3 Database needs for modeling and simulation of plasma processing, National Research Council, (National Academy Press, 1996).

4 D. A. Shaw, D. M. P. Holland, M. A. Macdonald, A. Hopkirk, M. A. Hayes, and S. M. McSweeney, *Chem. Phys.* **163,** 387 (1992).

5 J. Berkowitz and J. H. D. Eland, *J. Chem. Phys.* **67,** 2740 (1977).

6 J. L. Olivier, R. Locht, and J. Momigny, *Chem. Phys.* **68,** 201 (1982).

7 J. L. Olivier, R. Locht, and J. Momigny, *Int. J. Mass Spectrom. Ion Process.* **58,** 293 (1984).

8 J. L. Olivier, R. Locht, and J. Momigny, *Chem. Phys.* **84,** 295 (1984).

9 D. M. Curtis and J. H. D. Eland, *Int. J. Mass Spectrom. Ion Process.* **63,** 241 (1985).

10 J. H. D. Eland, *Vacuum Ultraviolet Photoionization and Photodissociation of Molecules and Clusters* (World Scientific, Singapore, 1991).

11 D. Rapp and P. Englander-Golden, *J. Chem. Phys.* **43,** 1464 (1965).

12 D. Rapp, P. Englander-Golden, and D. D. Briglia, *J. Chem. Phys.* **42,** 4081 (1965).

13 E. Mark, T. D. Mark, Y. B. Kim, and K. Stephan, *J. Chem. Phys.* **75,** 4446 (1981).

14 I. Iga, M. Rao, and S. K. Srivastava, *J. Geophys. Res.-Planets* **101,** 9261 (1996).

15 J. Lopez, V. Tarnovsky, M. Gutkin, and K. Becker, *Int. J. Mass Spectrom.* **225,** 25 (2003).

16 B. G. Lindsay, R. Rejoub, and R. F. Stebbings, *J. Chem. Phys.* **118,** 5894 (2003).

17 Y.-K. Kim, W. Hwang, N. M. Weinberger, M. A. Ali, and M. E. Rudd, *J. Chem. Phys.* **106,** 1026 (1997).

18 P. Calandra, C. S. S. O'Connor, and S. D. Price, *J. Chem. Phys.* **112,** 10821 (2000).

19 S. Harper, P. Calandra, and S. D. Price, *Phys. Chem. Chem. Phys.* **3,** 741 (2001).

20 C. S. S. O'Connor and S. D. Price, *Int. J. Mass Spectrom.* **184,** 11 (1999).

21 M. R. Bruce, C. Ma, and R. A. Bonham, *Chem. Phys. Lett.* **190,** 285 (1992).

22 D. A. Hagan and J. H. D. Eland, *Org. Mass Spectrom.* **27,** 855 (1992).

23 L. J. Frasinski, M. Stankiewicz, P. A. Hatherly, and K. Codling, *Meas. Sci. Technol.* **3,** 1188 (1992).

24 M. R. Bruce, L. Mi, C. R. Sporleder, and R. A. Bonham, *J. Phys. B-At. Mol. Opt. Phys.* **27,** 5773 (1994).

25 A. S. Newton and A. F. Sciamanna, *J. Chem. Phys.* **40,** 718 (1964).

26 S. D. Price, J. H. D. Eland, P. G. Fournier, J. Fournier, and P. Millie, *J. Chem. Phys.* **88,** 1511 (1988).

27 F. M. Harris, C. J. Reid, J. A. Ballantine, and D. E. Parry, *J. Chem. Soc.-Faraday Trans.* **87,** 1681 (1991).

28 J. H. D. Eland and V. J. Murphy, *Rapid Commun. Mass Spectrom.* **5,** 221 (1991).

29 S. Hsieh and J. H. D. Eland, *J. Phys. B-At. Mol. Opt. Phys.* **30,** 4515 (1997).

# Chapter 5

# Electron Ionization of $BCl_3$

## 5.1 Introduction

Boron trichloride ($BCl_3$) is widely used in the plasma etching of semiconductors and metals[1-5] and is also used to dope or deposit boron.[6] A recent report from the National Research Council addressing the 'Database Needs for Modeling and Simulation of Plasma Processing'[7] highlighted the lack of reliable partial ionization cross-sections (PICSs) for industrially important molecules such as $BCl_3$. Accurate values of relevant electron ionization cross-sections are essential for the precise modeling and optimization of plasmas used in industry.[8] It is this lack of reliable determinations that provides the motivation for the current study which is discussed in this chapter.

### 5.1.1 Electron ionization of $BCl_3$

Investigations of the electron ionization and photoionization of $BCl_3$ are limited.[9-12] In a recent review of electron interactions with $BCl_3$ by Christophorou and Olthoff,[13] they remark on the lack of data concerning electron-collision cross-sections with $BCl_3$ and suggest that further experimental measurements of the total electron ionization cross-section for $BCl_3$ are needed. An early study of the electron ionization of $BCl_3$ by Marriott and Craggs, using a Nier 60° mass spectrometer, showed $BCl_2^+$ to be the most abundant ion formed.[9] More recently, Jiao *et al*[10] determined the absolute PICSs of $BCl_3$ using electron ionization and Fourier transform mass spectrometry (FTMS), from threshold to 60 eV. There are no other determinations of the electron ionization cross-sections of $BCl_3$ in the current literature. This lack of data is primarily due to the corrosive and reactive nature of $BCl_3$, which makes it experimentally challenging to use without severe degradation of the experimental apparatus. Therefore, the motivation for the current study of $BCl_3$ is to further investigate the electron ionization of this highly reactive molecule, over a wider energy range then previous experiments, and to

determine the relevant relative PICSs and relative precursor specific PICSs. Relative precursor specific PICSs quantify the contribution from various levels of ionization to the individual product ion yields following an electron-molecule collision. This work enables a distinction to be made between ions formed *via* single and double ionization of $BCl_3$.

This chapter presents determinations of the relative PICSs and relative precursor specific PICSs for the electron ionization of $BCl_3$ using TOF mass spectrometry and ion-ion coincidence techniques, described in Chapter 3. Data for the formation of $B^+$, $BCl_2^{2+}$, $BCl^+$ and $BCl_2^+$ relative to $BCl_3^+$, are reported for ionizing electron energies from 30-200 eV.

## 5.2 Experimental Procedures

The boron trichloride used in these experiments was purchased from Aldrich with a purity of 99.8% and was thus utilised without further purification.

### 5.2.1 Experimental conditions

As discussed in Chapters 2 and 3, the experimental operating conditions employed in these experiments involve low electron fluxes and target gas pressures, producing a low ion count rate.[14-16] These conditions ensure that there is very much less than one ionization event detected per electron gun pulse and thus markedly decreases the likelihood of any accidental coincidences,[17-19] Section 5.3.3. By operating under these conditions of low pressure and low count rate, ions from the background gas in the mass spectrometer can contribute to the singles (mass) spectrum. In principle, by recording singles spectra of the empty spectrometer, the contribution of the background gas can be determined and subtracted from each $BCl_3$ singles spectrum. However, for these experiments using $BCl_3$, no subtraction is necessary, as the gas signals from the background gas do not overlap with any ion signals from $BCl_3$.

### 5.2.2 The corrosive nature of $BCl_3$

The corrosive nature of $BCl_3$ had several detrimental effects on the experimental apparatus and on the data it yielded. Firstly, exposure to $BCl_3$ degraded the pulse height distribution from the multichannel plate (MCP) detector during each experimental run. To ensure that the ion detection efficiency was constant for each experiment, the MCP was 'regenerated' before the next experiment until the mean pulse height from the MCP

returned to its original value. This regeneration was achieved by exposing the MCP to air at a pressure of $1x10^{-6}$ Torr for a period of several hours. The degradation of the MCP also forced the experimental run times to be limited, and restricted the number of experiments at each electron energy to two, so that irreversible MCP degradation did not occur. This curtailment of the data acquisition times increases the statistical uncertainty in the cross-sections reported in this chapter. Secondly, despite repeated attempts to dry the gas inlet system a white deposit was always observed on the glass inlet. This deposit was also reported by Tokunaga *et al*[20] and is attributed to $B(OH)_3$ formation *via* hydrolysis. As a consequence of this hydrolysis of $BCl_3$, $H^{35}Cl^+$ and $H^{37}Cl^+$ ion peaks are observed in the singles spectrum, Figure 5.1. The proximity of these impurity peaks to the $Cl^+$ signals in the singles spectrum, and the potential contribution of dissociative ionization of HCl to these $Cl^+$ signals made the extraction of reliable data for the formation of $Cl^+$ from $BCl_3$ extremely difficult in these experiments. As a result of these problems the cross-sections for the formation of $Cl^+$ from ionization of $BCl_3$ are not presented in this chapter. Tokunaga *et al*[20] also report that $BCl_3$ effectively scavenges $O_2$ and $H_2O$, which is confirmed by the observation of trace quantities of $BClOH^+$ in the present experiment and also in the experiments of Jiao *et al.*[10]

## 5.3 Data Analysis

Mass and coincidence spectra were recorded at ionizing electron energies between 30-200 eV using the experimental apparatus described in Chapter 2.

### 5.3.1 Singles spectrum

A typical singles spectrum is shown in Figure 5.1, recorded at an electron energy of 200 eV. As seen from Figure 5.1, the $BCl_2^+$ ion is the most abundant ion formed following electron ionization of $BCl_3$ at all the electron energies investigated here. Figure 5.1 illustrates the presence of boron ($^{10}B$, $^{11}B$) and chlorine ($^{35}Cl$, $^{37}Cl$) isotopes. However, the intensities of these isotopic peaks are not fully resolved, making any extraction of isotopic specific cross-sections impossible. Therefore, all the isotopic data is summed to give cross-sections for the individual product ions: $B^+$, $Cl^+$, $BCl_2^{2+}$, $BCl^+$, $BCl_2^+$ and $BCl_3^+$.

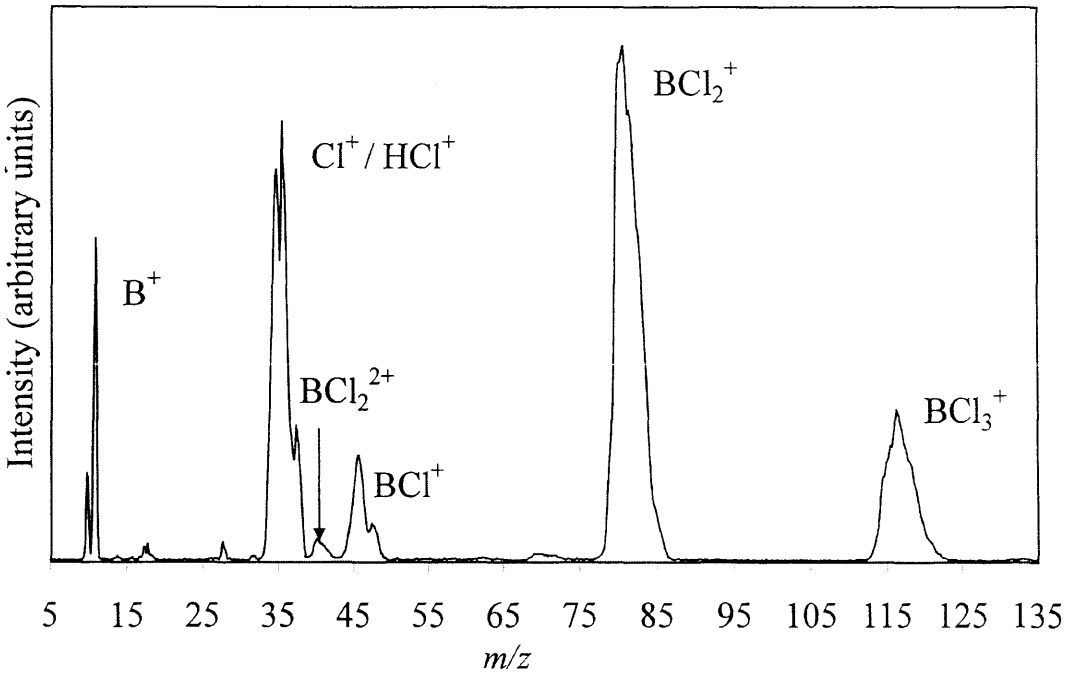


Figure 5.1: A singles (mass) spectrum of $BCl_3$ following electron ionization recorded at an electron energy of 200 eV. Residual gas ion peaks are observed at $m/z$=14,16,18,32 and 70/72. These ion peaks are attributed to the ionization of background air (forming $N^+$, $O^+$, $H_2O^+$, $O_2^+$) and chlorine (forming $Cl_2^+$) in the mass spectrometer.

The singles spectrum also contains small signals of air and water from the residual background gas present in the apparatus. As described above, these residual gas signals are observed as a result of the experimental conditions employed in these experiments. Small signals of $Cl_2^+$ are also observed in the singles spectrum, these signals are attributed to traces of $Cl_2$ present in the $BCl_3$ sample. It is clear from Figure 5.1 that the gas signals from the background gas, and any chlorine present in the sample do not overlap with fragment ion peaks formed following ionization with $BCl_3$. Care was taken to minimise the contribution of this residual background gas to the singles spectrum but the experimental conditions limit the achievable background, Section 5.2.1.

## 5.3.2 Pairs spectrum

### 5.3.2.1 Ion pairs

A schematic diagram of the coincidence spectrum (pairs spectrum) recorded at an electron energy of 200 eV is shown in Figure 5.2.

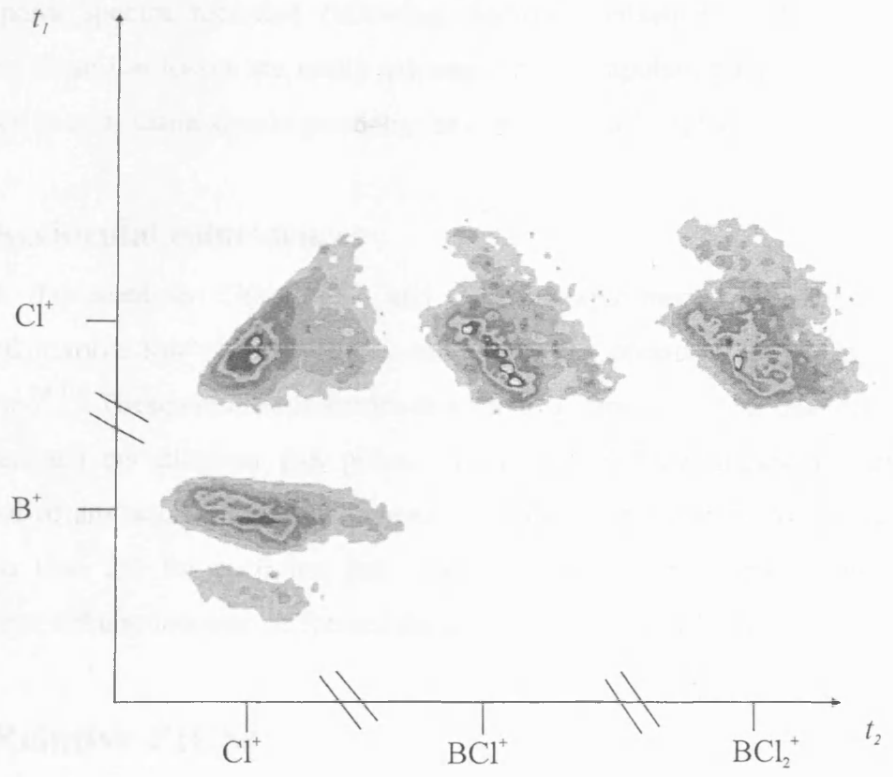


Figure 5.2: A schematic pairs spectrum for $BCl_3$ recorded at an electron energy of 200 eV.

The pairs spectra recorded following ionization of $BCl_3$ exhibited four primary dissociation channels: $B^+ + Cl^+$, $Cl^+ + Cl^+$, $BCl^+ + Cl^+$ and $BCl_2^+ + Cl^+$. At 200 eV the relative intensities of these channels were 1:0.70:0.60:0.71. However, in the one long data collection run performed, for 8000 seconds at an electron energy of 200 eV, where the counting statistics were superior to the 'short' duration spectra (800 seconds) recorded to avoid MCP degradation, traces of a $BCl^+ + Cl_2^+$ dissociation channel were also observed. The presence of boron ($^{10}B$, $^{11}B$) and chlorine ($^{35}Cl$, $^{37}Cl$) isotopes means that at least four ion pair peaks are detected for each dissociation channel except $Cl^+ + Cl^+$. However, these isotopic peaks are not fully resolved in the pairs spectrum again making any extraction of isotopic specific double ionization cross-sections impossible. Therefore, as with the singles data, all the isotopic data is summed to produce cross-sections for the individual product ions.

#### 5.3.2.2 Dead-time ion loss

As discussed in Chapters 2 and 3, the experimental set-up is such that no ion pairs are recorded if the second ion arrives within 32 ns of the first ion, due to the dead-time of the discrimination circuitry. Such dead-time losses affect the $Cl^+ + Cl^+$ ion peak

in the pairs spectra recorded following electron ionization of $BCl_3$, Figure 5.2. However, these ion losses are easily estimated by extrapolating the visible part of the pairs peak to $t_1=t_2$ using simple geometry, as discussed in Chapter 3.[18,21]

### 5.3.3 Accidental coincidences

As discussed in Chapters 2 and 3, the experimental operating conditions employed involve low electron fluxes and target gas pressures, producing a low ion count rate.[14-16] These conditions ensure that there is very much less than one ionization event detected per electron gun pulse. This methodology markedly decreases the likelihood of any accidental coincidences.[17-19] Such contributions to the pairs spectra were less than 2% for each ion pair channel observed and therefore no accidental coincidence subtraction was performed for the pairs spectra of $BCl_3$.

## 5.4 Relative PICSs

The ion intensities recorded in the singles and pairs spectra were processed to yield the relative PICSs and the relative precursor specific PICSs for the formation of the boron containing ions from $BCl_3$ relative to the parent ion $BCl_3^+$. This data processing is described in detail in Chapter 3, and specifically for the electron ionization of $BCl_3$ in Appendix D, and thus only a brief summary is given below. The derived cross-sections are shown in Figure 5.3 - Figure 5.6, and values are given in Table 5.1 - Table 5.4, where the points shown represent the average of two determined data values and the bars extend between the two values. This representation provides a clear view of the scatter of the data. Of course, the data scatter is significantly larger than in previous work because only two determinations are averaged to give the final value, as opposed to 4 or more in work with less corrosive gases.[14-16] As described in Section 5.2.2, the cross-sections for the formation of $Cl^+$ are not reported.

### 5.4.1 Notation

In the data presented here the relative PICSs are abbreviated to $\sigma_r[X^+]$, where $\sigma_r[X^+/BCl_3^+] = \sigma_r[X^+]$. The data presented here for the relative precursor specific PICSs are abbreviated to $\sigma_1[X^+]$ and $\sigma_2[X^+]$; where $\sigma_1[X^+]/\sigma_1[BCl_3^+] = \sigma_1[X^+]$ and $\sigma_2[X^+]/\sigma_1[BCl_3^+] = \sigma_2[X^+]$.

## 5.4.2 Ion intensities

A full description of the data analysis methods is presented in Chapter 3. To illustrate the data analysis, representative equations used to determine the relative PICSs for the $B^+$ and $BCl_2^{2+}$ fragment ions are shown, Eqs. (5.1) and (5.2), expressed relative to the $BCl_3^+$ ion. Note that $\sigma_r[BCl_2^{2+}] = \sigma_2[BCl_2^{2+}]$. The relative PICSs are expressed as a sum of the individual precursor specific PICSs for formation of the ion *via* single and double ionization, where $N_n[X^+]$ represents the number of $X^+$ ions formed *via* loss of $n$ electrons. These values can in turn be expressed as a sum of the ion intensities from the singles $I[X^+]$ and pairs $P[X^+]$ spectra:

$$\sigma_r[B^+] = \frac{N_1[B^+] + N_2[B^+]}{N_1[BCl_3^+]} = \frac{I[B^+] + P[B^+]}{I[BCl_3^+]} \quad (5.1),$$

$$\sigma_r[BCl_2^{2+}] = \frac{N_2[BCl_2^{2+}]}{N_1[BCl_3^+]} = \frac{I[BCl_2^{2+}]}{I[BCl_3^+]} \quad (5.2).$$

Where the intensity of the $B^+$ and $BCl_2^{2+}$ ions in the singles and pairs spectrum can be described by the following equations:

$$I[B^+] = f_i N_1[B^+] + f_i(1 - f_i) N_2[B^+] \quad (5.3),$$

$$I[BCl_2^{2+}] = f_i N_2[BCl_2^{2+}] \quad (5.4),$$

$$P[B^+] = f_i^2 N_2[B^+] \quad (5.5).$$

The $\sigma_r$ values expressed here, Eqs. (5.1) and (5.2), do not depend on $f_i$. However, by determining a value for $f_i$ the data analysis can be extended to yield the values of $\sigma_n[X^+]$, quantifying the contribution to each ion yield from single and double ionization.

## 5.4.3 Relative precursor specific PICSs

### 5.4.3.1 Ion detection efficiency

To extend the data analysis and thus determine relative precursor specific PICSs, $\sigma_n[X^+]$, a value for the ion detection efficiency, $f_i$, was determined, as explained in Chapter 3, by simultaneously recording singles and pairs spectra following ionization of $CF_4$. This procedure resulted in an average $f_i$ value of $0.12 \pm 0.01$ for the electron ionization of $BCl_3$. This value of $f_i$ is lower than other determinations in this thesis, Chapters 4, 6 and 7.[14,16] This lower value of $f_i$ is principally due to MCP degradation during preliminary experiments with $BCl_3$. As described in Section 5.2.2, to ensure that

$f_i$ remains constant for each experiment the pulse height distribution was monitored after every experiment and the MCP regenerated if necessary.

For completeness, representative examples of the equations used to determine the relative precursor specific PICSs are shown below, Eqs. (5.6)-(5.8), for the $B^+$ and $BCl_2^{2+}$ ions.

$$\sigma_1[B^+] = \frac{N_1[B^+]}{N_1[BCl_3^+]} = \frac{I[B^+] - (1-f_i)/f_i P[B^+]}{I[BCl_3^+]} \quad (5.6),$$

$$\sigma_2[B^+] = \frac{N_2[B^+]}{N_1[BCl_3^+]} = \frac{P[B^+]}{f_i I[BCl_3^+]} \quad (5.7),$$

$$\sigma_2[BCl_2^{2+}] = \frac{N_2[BCl_2^{2+}]}{N_1[BCl_3^+]} = \frac{I[BCl_2^{2+}]}{I[BCl_3^+]} \quad (5.8).$$

## 5.5 Discussion

In this section the derived data is discussed for the formation of $B^+$, $BCl_2^{2+}$, $BCl^+$ and $BCl_2^+$ relative to $BCl_3^+$.

### 5.5.1 $BCl_2^+$ and $BCl_2^{2+}$ formation

The values of $\sigma_r[BCl_2^+]$ determined here are in agreement with the values derived from the absolute PICSs recently presented by Jiao *et al*,[10] (Figure 5.3). This agreement clearly indicates that, in our experiment, no $BCl_2$ is produced by the reaction of $BCl_3$ on the surfaces of the spectrometer or the filament. If significant surface formation of $BCl_2$ were occurring, the $BCl_2$ would then be ionized, causing the $\sigma_r[BCl_2^+]$ values to be larger than the data of Jiao *et al*[10] which is not the case. This conclusion, that no neutral $BCl_2$ is generated from reactions of $BCl_3$ in the spectrometer, is important in the data interpretation below. Values for $\sigma_r[BCl_2^+]$, $\sigma_1[BCl_2^+]$ and $\sigma_2[BCl_2^+]$ are shown in Table 5.1.

The $BCl_2^{2+}$ ion is observed in low abundance in the singles spectrum, Figure 5.1. As shown above, since there is no dissociation of $BCl_3$ to form $BCl_2$ in this apparatus, then these $BCl_2^{2+}$ ions must come from dissociative double ionization of $BCl_3$. At 100 eV, the relative PICS for $BCl_2^{2+}$ is 3% of the $BCl_2^+$ relative PICS. The values of $\sigma_r[BCl_2^{2+}]$ determined here are shown in Table 5.2.

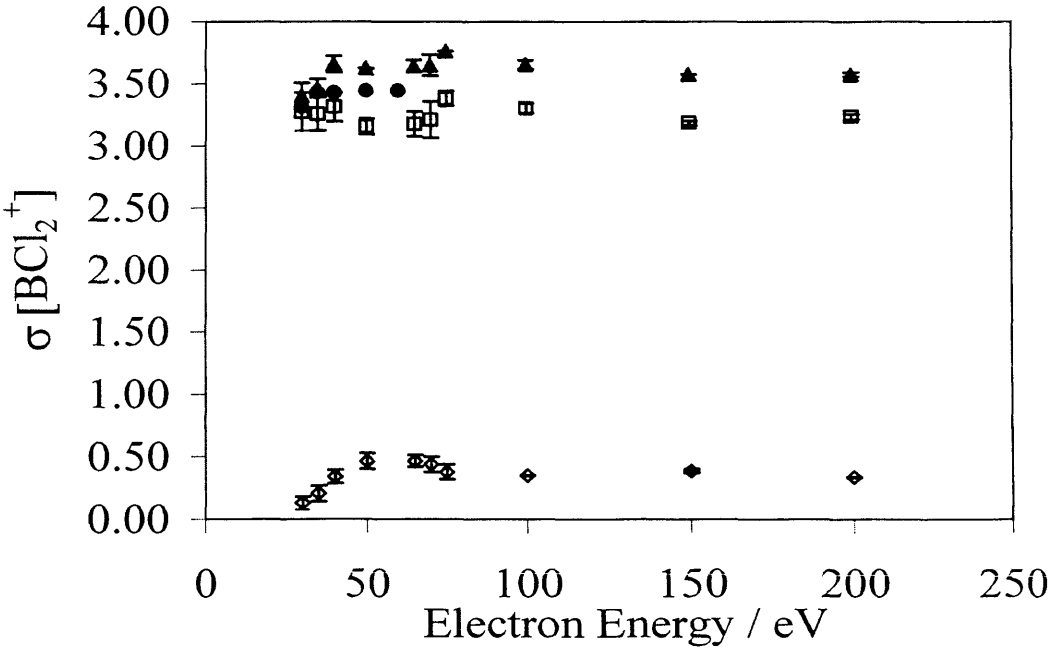


Figure 5.3: The relative PICSs and relative precursor specific PICSs determined for forming $BCl_2^+$ following electron ionization of $BCl_3$. The $\sigma_r[BCl_2^+]$ values are marked with ▲, $\sigma_1[BCl_2^+]$ with □ and $\sigma_2[BCl_2^+]$ with ◇. The markers show the average of two experimental determinations and the bar shown represents how far each data point lies from the average value. Data are expressed relative to the formation of $BCl_3^+$. Comparison is made with relative PICSs derived from the absolute PICSs of Jiao *et al*[10] (●).

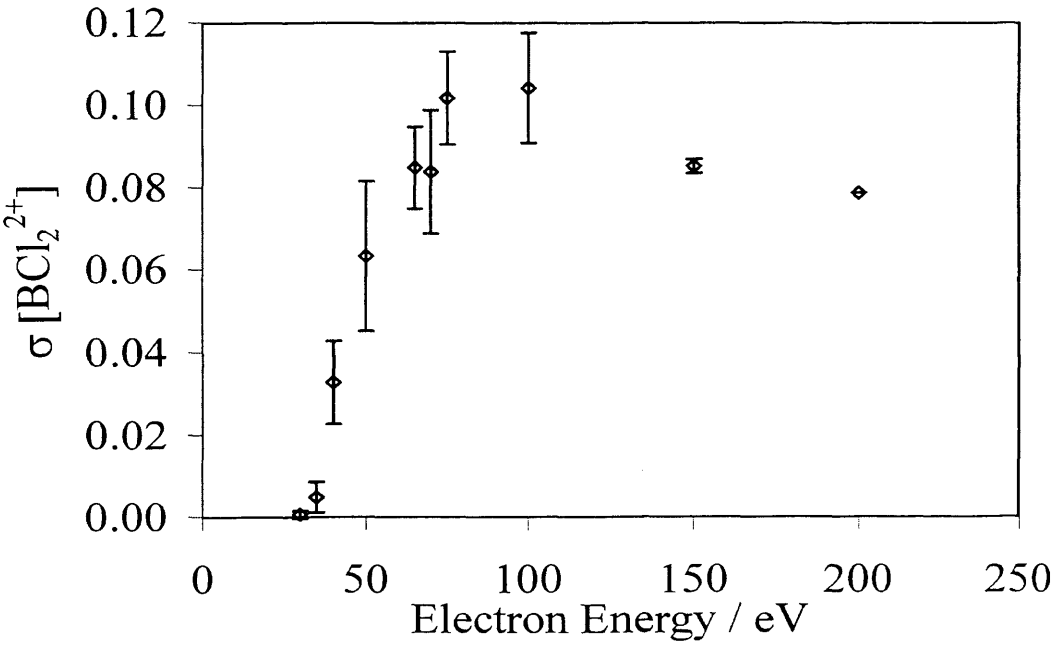


Figure 5.4: The relative PICS for forming $BCl_2^{2+}$ ($\sigma_r[BCl_2^{2+}]$ ) by electron ionization, shown by ◇. See caption to Figure 5.3 for details.

Table 5.1: Relative precursor specific PICSs and relative PICSs for the formation of $BCl_2^+$ from $BCl_3$ as a function of incident electron energy *E*. The values represent the average of two determinations. The numbers in parentheses indicate the difference between the average value and actual data points in the last figure.

| *E*/eV | $\sigma_1[BCl_2^+]$ | $\sigma_2[BCl_2^+]$ | $\sigma_r[BCl_2^+]$ |
|---|---|---|---|
| 200 | 3.24(2) | 0.34(1) | 3.58(2) |
| 150 | 3.19(2) | 0.39(2) | 3.58(1) |
| 100 | 3.30(4) | 0.35(1) | 3.65(4) |
| 75 | 3.38(6) | 0.38(9) | 3.76(1) |
| 70 | 3.21(15) | 0.44(9) | 3.65(8) |
| 65 | 3.18(10) | 0.47(7) | 3.65(5) |
| 50 | 3.16(6) | 0.47(9) | 3.63(1) |
| 40 | 3.31(12) | 0.34(8) | 3.65(7) |
| 35 | 3.26(14) | 0.21(9) | 3.47(7) |
| 30 | 3.27(16) | 0.13(7) | 3.40(10) |

Table 5.2: Relative PICSs for the formation of $BCl_2^{2+}$ from $BCl_3$ as a function of incident electron energy *E*. See the caption to Table 5.1 for details.

| *E*/eV | $\sigma_2[BCl_2^{2+}]$ |
|---|---|
| 200 | 0.08(1) |
| 150 | 0.09(1) |
| 100 | 0.10(2) |
| 75 | 0.10(1) |
| 70 | 0.08(2) |
| 65 | 0.08(1) |
| 50 | 0.06(3) |
| 40 | 0.03(1) |
| 35 | 0.00(1) |
| 30 | 0.00(1) |

## 5.5.2 $BCl^+$ formation

Figure 5.5 illustrates that below 65 eV the $\sigma_r[BCl^+]$ values determined here are 50% larger than those derived from the cross-section determinations of Jiao *et al.*[10] However, the general form of the energy dependence, decreasing with increasing electron energy, is similar for the two sets of results. The values of $\sigma_r[BCl^+]$, $\sigma_1[BCl^+]$ and $\sigma_2[BCl^+]$ determined here are shown in Table 5.3.

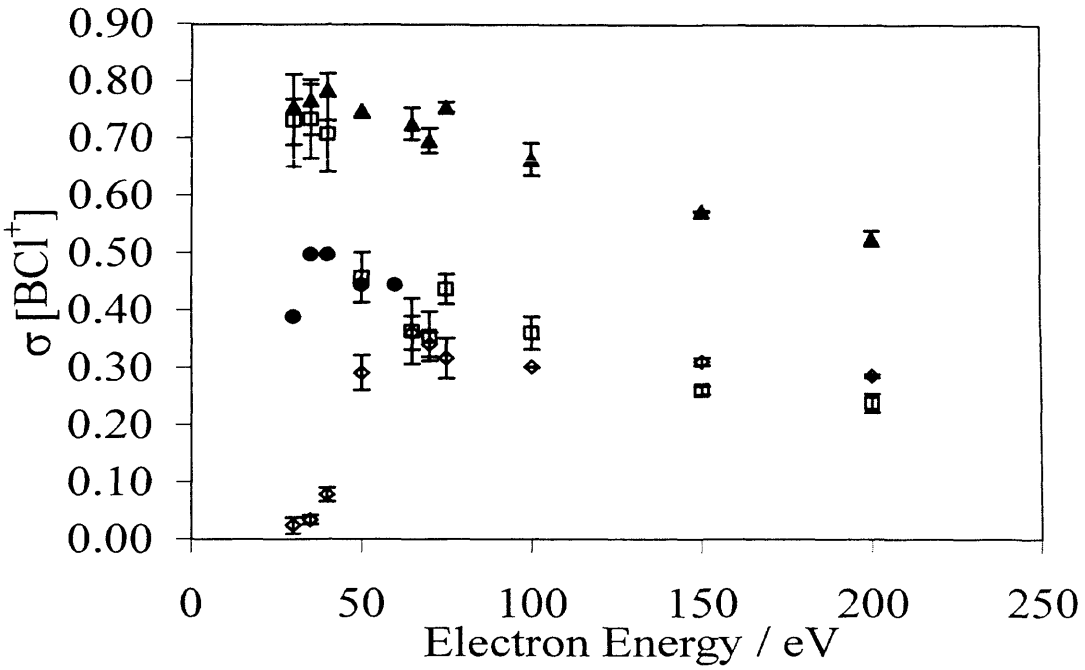


Figure 5.5: The relative PICSs and relative precursor specific PICSs determined for forming $BCl^+$ following electron ionization of $BCl_3$. The $\sigma_r[BCl^+]$ values are marked with ▲, $\sigma_1[BCl^+]$ with □ and $\sigma_2[BCl^+]$ with ◇. Comparison is made with relative PICSs derived from the absolute PICSs of Jiao *et al*[10] (●). See caption for Figure 5.3 for details.

One possible reason for the discrepancy between the $\sigma_r[BCl^+]$ values determined here and the values derived from the cross-section determinations of Jiao *et al*[10] is a difference in efficiency of energetic ion collection between this experiment and the FTMS apparatus used by Jiao *et al.*[10] If $BCl^+$ ions are formed with a significant kinetic energy they may not be efficiently retained and detected in the FTMS employed by Jiao *et al*[10] which requires significant ion residence times. Unfortunately, Jiao *et al*[10] do not detail the detection efficiency of their apparatus for such translationally 'hot' ions. It is well established[22-27] that dissociative multiple ionization is a common source of

energetic monocations and double ionization may well account for some of the difference between the relative PICSs derived from the data of Jiao *et al*[10] and the data presented here. However, Figure 5.5 clearly shows the contribution of dissociative double ionization to the $BCl^+$ yield is low between 30-40 eV, and thus it seems that in this energy region single ionization must contribute significantly to the yield of translationally energetic $BCl^+$ ions which are missed by Jiao *et al.*[10] At 50 and 60 eV where the contribution of double ionization (~40%, Figure 5.5) to the yield of $BCl^+$ is now significant, the data of Jiao *et al*[10] still lie 30% below the values of $\sigma_1[BCl^+]$ determined here, again implicating single ionization in the production of some of the energetic $BCl^+$ ions that Jiao *et al*[10] miss. The formation of highly translationally energetic ions from single and double ionization is well established,[28,29] and as a result, the loss of such ions in the FTMS experiments of Jiao *et al*[10] is the most probable explanation of the differences between their results and the data determined here. To support that conclusion, as discussed below, the observation of a 'real' signal from the dissociation of $BCl_3$ which yields the $B^+$ ion provides evidence for the formation of energetic $B^+$ ions from the dissociative double ionization of $BCl_3$, see Figure 5.2. Yet, Jiao *et al*[10] reported that no $B^+$ ions were formed in the FTMS experiments.

An alternative explanation for the disagreement between the $\sigma_r[BCl^+]$ values determined here and those derived from the data of Jiao *et al*[10] is that the $BCl_3$ neutral is reacting within this spectrometer to produce neutral BCl which is subsequently ionized. Such a possibility is hard to eliminate completely. However, as noted in Section 5.5.1, no evidence for the dissociation of $BCl_3$ to $BCl_2$ was observed in these experiments. In addition, no evidence for the dissociation and subsequent ionization of other reactive molecules has ever been observed in previous experiments with this apparatus.[14-16] In addition, the $BCl^+$ detected from double ionization is formed together with a $Cl^+$ ion and hence, given the definitive absence of degradation of $BCl_3$ to $BCl_2$ in the apparatus, must arise from double ionization of $BCl_3$. Clearly, further investigations are needed to definitively resolve the source of the discrepancy between the current data and that of Jiao *et al*[10] for the formation of $BCl^+$. However, no further investigations were possible using the experimental apparatus detailed in this thesis due to the level of degradation experienced whilst using $BCl_3$ for the experiments described in this chapter.

Table 5.3: Relative precursor specific PICSs and relative PICSs for the formation of $BCl^+$ from $BCl_3$ as a function of incident electron energy *E*. See the caption to Table 5.1 for details.

| *E*/eV | $\sigma_1[BCl^+]$ | $\sigma_2[BCl^+]$ | $\sigma_r[BCl^+]$ |
|---|---|---|---|
| 200 | 0.24(2) | 0.29(1) | 0.53(1) |
| 150 | 0.26(1) | 0.31(1) | 0.57(1) |
| 100 | 0.36(3) | 0.30(1) | 0.66(3) |
| 75 | 0.44(3) | 0.32(5) | 0.76(1) |
| 70 | 0.35(4) | 0.34(3) | 0.69(2) |
| 65 | 0.36(6) | 0.36(4) | 0.72(3) |
| 50 | 0.46(4) | 0.29(4) | 0.75(1) |
| 40 | 0.71(7) | 0.08(2) | 0.79(5) |
| 35 | 0.73(7) | 0.03(1) | 0.76(6) |
| 30 | 0.73(8) | 0.02(2) | 0.75(7) |

### 5.5.3 $B^+$ formation

The observation of significant quantities of the $B^+$ ion in the singles and pairs spectra again does not correspond with the data of Jiao *et al*,[10] where no $B^+$ ions were detected (Figure 5.6 and Table 5.4). As discussed above, the origin of this discrepancy could be inefficient collection of energetic $B^+$ ions in the experiments of Jiao *et al*,[10] or breakdown of $BCl_3$ to boron atoms, which are subsequently ionized in the apparatus used here. However, the observation of $B^+$ ions in a 'real' ion pair peak in the pairs spectra, see Figure 5.2, provides evidence that energetic $B^+$ ions are formed *via* dissociation of doubly ionized $BCl_3$. Indeed the current data show that $\sigma_2[B^+]$ constitutes more than 30% of $\sigma_r[B^+]$ above 100 eV. This data also shows that these energetic $B^+$ ions are present at electron energies as low as 50 eV (Figure 5.6), where no $B^+$ ions are reported by Jiao *et al.*[10] It is therefore concluded that the most likely source of the difference between their results, and those reported here, is due to the loss of energetic ions in the experiments of Jiao *et al.*[10]

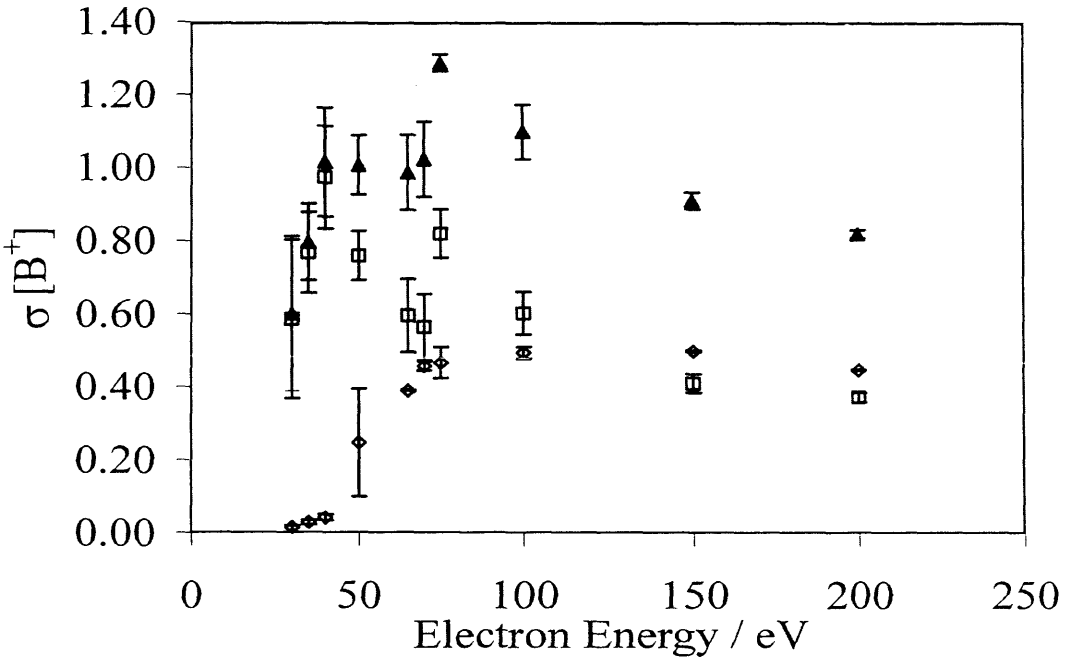


Figure 5.6: The relative PICSs and relative precursor specific PICSs determined for forming $B^+$ following electron ionization of $BCl_3$. The $\sigma_r[B^+]$ values are marked with ▲, $\sigma_1[B^+]$ with □ and $\sigma_2[B^+]$ with ◇. See caption for Figure 5.3 for details.

Table 5.4: Relative precursor specific PICSs and relative PICSs for the formation of $B^+$ from $BCl_3$ as a function of incident electron energy *E*. See the caption to Table 5.1 for details.

| *E*/eV | $\sigma_1[B^+]$ | $\sigma_2[B^+]$ | $\sigma_r[B^+]$ |
|---|---|---|---|
| 200 | 0.37(3) | 0.45(1) | 0.82(1) |
| 150 | 0.41(1) | 0.50(1) | 0.91(2) |
| 100 | 0.60(6) | 0.50(2) | 1.10(7) |
| 75 | 0.82(7) | 0.47(6) | 1.29(2) |
| 70 | 0.57(9) | 0.46(2) | 1.03(10) |
| 65 | 0.60(10) | 0.39(1) | 0.99(10) |
| 50 | 0.76(7) | 0.25(21) | 1.01(8) |
| 40 | 0.97(14) | 0.04(1) | 1.01(15) |
| 35 | 0.77(11) | 0.03(1) | 0.80(10) |
| 30 | 0.59(22) | 0.01(1) | 0.60(21) |

Some contribution to the values of $\sigma_1[B^+]$ determined here resulting from the decomposition of $BCl_3$ to boron atoms, which are then ionized, cannot be ruled out. However, the detection of $B^+$ ions, as discussed below, observed in the $B^+ + Cl^+$ ion pair peak of the pairs spectrum, from the double ionization of $BCl_3$ certainly means that energetic ions are not efficiently detected in the experiments of Jiao *et al.*[10] It is therefore possible that energetic $B^+$ ions from the dissociation of $BCl_3^+$, which may contribute significantly to the $\sigma_1[B^+]$ values determined here, are also not detected.

### 5.5.4 Dissociative double ionization

As mentioned above, the pairs spectra recorded following ionization of $BCl_3$ exhibit four different decay channels: $B^+ + Cl^+$, $Cl^+ + Cl^+$, $BCl^+ + Cl^+$ and $BCl_2^+ + Cl^+$. A pairs spectrum was recorded for 8000 seconds which was sufficient duration to achieve adequate statistics to facilitate the investigation of the mechanism of formation for the $B^+ + Cl^+$ ion pair, which accounts for 35% of the total dication dissociations detected at 200 eV. As discussed in Chapter 3, the gradient of the coincidence peaks in the pairs spectrum can provide an insight into the mechanism of the charge-separating dissociation.[30,31] This insight is possible as the gradient of the peak reflects the correlation between the momenta of the two fragment ions. For the dominant isotopes, the gradient of the $B^+ + Cl^+$ coincidence peak is determined to be -0.45±0.05. Immediately, this gradient reveals that the ion pair does not originate from a simple two-body dissociation of $BCl^{2+}$, which would give a peak with a gradient of –1, as the momenta of the $Cl^+$ and $B^+$ would have to be equal and opposite. A dissociation pathway that would generate a coincidence peak with the observed gradient is a sequential reaction mechanism with initial charge-separation, shown in Reactions [5.I] and [5.II] and calculated using a ratio of masses.

$$BCl_3^{2+} \rightarrow BCl^+ + Cl_2^+ \qquad [5.I],$$

$$\downarrow \quad \downarrow$$

$$B^+ + Cl + Cl^+ + Cl \qquad [5.II].$$

This fragmentation pathway should result in a coincidence peak with a gradient of -0.48 (using a ratio of masses), in excellent agreement with the experimental value. Further support for this dissociation pathway comes from the observation of weak signals corresponding to the fragmentation of $BCl_3^{2+}$ to $BCl^+$ and $Cl_2^+$ in the long duration spectrum recorded at 200 eV, the first step in the proposed route for the

formation of $B^+$ and $Cl^+$, shown in Reaction [5.I].

Considering the other dicationic dissociation channels observed in the pairs spectra, Figure 5.2, the $BCl_2^+ + Cl^+$ ion pair can only originate from direct dissociation of $BCl_3^{2+}$. The $BCl^+ + Cl^+$ ion peak appears to have a gradient of approximately –1, suggesting either a three-body direct dissociation from $BCl_3^{2+}$, or the two-body dissociation of $BCl_2^{2+}$ formed in an initial neutral-loss step from $BCl_3^{2+}$. The latter is perhaps more probable since long-lived $BCl_2^{2+}$ ions are detected. The mechanism for forming the $Cl^+ + Cl^+$ ion pair cannot be definitely determined from the data collected here due to the dead-time in the pairs spectra. This dead-time means a significant fraction of the $Cl^+ + Cl^+$ coincidences are missed, and although these missed ions can be corrected for numerically, no accurate determination of the peak gradient was possible from the visible ion pair peak in the pairs spectra. The possibility that the $Cl^+ + Cl^+$ signal originates from dissociative double ionization of any traces of $Cl_2$ present in the sample is now considered. The $Cl_2^+$ signal in the singles spectrum is only just above the detection limit and much of this signal must result from the dicationic dissociation to $BCl^+ + Cl_2^+$. However, if it is assumed that all of the $Cl_2^+$ signal in the singles spectrum is from ionization of $Cl_2$, then the relevant precursor specific PICS[14] indicate that only 4% of the detected $Cl^+ + Cl^+$ coincidences could originate from dissociative double ionization of $Cl_2$, at 200 eV. It is therefore concluded that the $Cl^+ + Cl^+$ coincidences must come predominantly from ionization of $BCl_3$, as they cannot originate from ionization of BCl and, as shown in Section 5.5.1, there is no ionization of neutral $BCl_2$ occurring in the apparatus used here.

## 5.6 Conclusions

Using electron ionization, coupled with TOF mass spectrometry, the relative PICSs and relative precursor specific PICSs for the formation of $B^+$, $BCl_2^{2+}$, $BCl^+$ and $BCl_2^+$ relative to $BCl_3^+$ have been determined from 30-200 eV. This is the first time that relative precursor PICSs have been derived for $BCl_3$. Comparisons between the data determined here and the only other quantitative study of the electron ionization of $BCl_3$ were made. Agreement with this earlier work is excellent for the formation of $BCl_2^+$, however, some inconsistencies exist for the formation of $BCl^+$ and $B^+$ ions. These inconsistencies may be accounted for by the earlier experiments failing to detect all the energetic fragment ions.

## 5.7 References


1 M. W. Cole, G. F. McLane, D. W. Eckart, and M. Meyyappan, *Scanning* **15,** 225 (1993).

2 S. J. Pearton, W. S. Hobson, C. R. Abernathy, F. Ren, T. R. Fullowan, A. Katz, and A. P. Perley, *Plasma Chem. Plasma Process.* **13,** 311 (1993).

3 A. T. Demos, H. S. Fogler, J. Fournier, and M. E. Elta, *AICHE J.* **41,** 658 (1995).

4 J. W. Lee, J. Hong, E. S. Lambers, C. R. Abernathy, S. J. Pearton, W. S. Hobson, and F. Ren, *Plasma Chem. Plasma Process.* **17,** 155 (1997).

5 K. J. Nordheden, X. D. Hua, Y. S. Lee, L. W. Yang, D. C. Streit, and H. C. Yen, *J. Vac. Sci. Technol. B* **17,** 138 (1999).

6 A. Slaoui, F. Foulon, C. Fuchs, E. Fogarassy, and P. Siffert, *Appl. Phys. A-Mater. Sci. Process.* **50,** 317 (1990).

7 Database needs for modeling and simulation of plasma processing, National Research Council, (National Academy Press, 1996).

8 L. G. Christophorou and J. K. Olthoff, *J. Phys. Chem. Ref. Data* **27,** 1 (1998).

9 J. Marriot and J. D. Craggs, *J. Electron. Control* **3,** 194 (1957).

10 C. Q. Jiao, R. Nagpal, and P. Haaland, *Chem. Phys. Lett.* **265,** 239 (1997).

11 V. H. Dibeler and J. A. Walker, *Inorg. Chem.* **8,** 50 (1969).

12 H. Biehl, K. J. Boyle, D. M. Smith, R. P. Tuckett, K. R. Yoxall, K. Codling, P. A. Hatherly, and M. Stankiewicz, *J. Chem. Soc.-Faraday Trans.* **92,** 185 (1996).

13 L. G. Christophorou and J. K. Olthoff, *J. Phys. Chem. Ref. Data* **31,** 971 (2002).

14 P. Calandra, C. S. S. O'Connor, and S. D. Price, *J. Chem. Phys.* **112,** 10821 (2000).

15 S. Harper, P. Calandra, and S. D. Price, *Phys. Chem. Chem. Phys.* **3,** 741 (2001).

16 C. S. S. O'Connor and S. D. Price, *Int. J. Mass Spectrom.* **184,** 11 (1999).

17 M. R. Bruce, C. Ma, and R. A. Bonham, *Chem. Phys. Lett.* **190,** 285 (1992).

18 D. A. Hagan and J. H. D. Eland, *Org. Mass Spectrom.* **27,** 855 (1992).

19 L. J. Frasinski, M. Stankiewicz, P. A. Hatherly, and K. Codling, *Meas. Sci. Technol.* **3,** 1188 (1992).

20 K. Tokunaga, F. C. Redeker, D. A. Danner, and D. W. Hess, *J. Electrochem. Soc.* **128,** 851 (1981).

21 M. R. Bruce, L. Mi, C. R. Sporleder, and R. A. Bonham, *J. Phys. B-At. Mol. Opt. Phys.* **27,** 5773 (1994).

22 D. M. Curtis and J. H. D. Eland, *Int. J. Mass Spectrom. Ion Process.* **63,** 241 (1985).

23 M. Lundqvist, D. Edvardsson, P. Baltzer, M. Larsson, and B. Wannberg, *J. Phys. B-At. Mol. Opt. Phys.* **29,** 499 (1996).

24 M. Lundqvist, D. Edvardsson, P. Baltzer, and B. Wannberg, *J. Phys. B-At. Mol.*

*Opt. Phys.* **29,** 1489 (1996).

25 D. Edvardsson, M. Lundqvist, P. Baltzer, B. Wannberg, and S. Lunell, *Chem. Phys. Lett.* **256,** 341 (1996).

26 S. Hsieh and J. H. D. Eland, *J. Phys. B-At. Mol. Opt. Phys.* **30,** 4515 (1997).

27 B. G. Lindsay, R. Rejoub, and R. F. Stebbings, *J. Chem. Phys.* **118,** 5894 (2003).

28 D. Rapp, P. Englander-Golden, and D. D. Briglia, *J. Chem. Phys.* **42,** 4081 (1965).

29 J. H. D. Eland, *Photoelectron Spectroscopy*, Second Edition (1984).

30 J. H. D. Eland, F. S. Wort, and R. N. Royds, *J. Elec. Spect. Rel. Phen.* **41,** 297 (1986).

31 J. H. D. Eland, *Mol. Phys.* **61,** 725 (1987).

# Chapter 6

# Electron ionization of $SF_6$

## 6.1 Introduction

The physical properties and dielectric capabilities of sulphur hexafluoride mean it has become widely used for applications in the electrical utility industry, magnesium casting, sound insulation, semiconductor etching, and chemical lasers. When $SF_6$ is released into the atmosphere it is a highly effective greenhouse gas, and thus it is important to provide quantitative data to help reduce the amount of $SF_6$ used within industrial processes such as plasma etching. Accurate electron ionization cross-sections are essential for the modelling and optimization of plasmas, and also for atmospheric modelling. With the widespread use of $SF_6$ in plasmas, it is therefore surprising to learn that a limited number of recent experimental measurements of the electron ionization cross-sections of $SF_6$ are available. Therefore, the main objective here is to provide additional electron ionization cross-section measurements of $SF_6$. The existing electron ionization data for $SF_6$ have been recently evaluated and summarized in a comprehensive review by Christophorou and Olthoff.[1]

### 6.1.1 Electron ionization of $SF_6$

In this section the available experimental electron ionization cross-section data is briefly reviewed. In 1965 Rapp and Englander-Golden[2] measured the total ionization cross-section of $SF_6$ at electron energies up to 300 eV. Partial and total ionization cross-sections have been determined by Stanski and Adamczyk,[3] Margreiter *et al*,[4] Rao and Srivastava[5] and Rejoub *et al.*[6] Stanski and Adamczyk,[3] used a cycloidal mass spectrometer to determine absolute partial ionization cross-sections (PICSs), however, the authors suggest that some energetic ions may not be detected in their experiments due to discrimination effects. Later, Margreiter *et al*[4] determined the absolute PICSs for $SF_6$ from threshold to 180 eV. Rao and Srivastava[5] determined the absolute partial

electron ionization cross-sections for $SF_6$ at 100 eV. The most recent absolute partial electron ionization cross-sections for $SF_6$ were determined by Rejoub *et al*[6] from threshold to 1000 eV. Rejoub *et al*[6] also present absolute ion pair production cross-sections for formation of $(SF_3^+ + F^+)$, $(SF_2^+ + F^+)$, $(SF^+ + F^+)$ and $(S^+ + F^+)$.

Theoretical calculations of the total cross-section for ionizing $SF_6$ have been performed by Hwang *et al*[7] and Kim and Rudd[8] using the binary encounter Bethe (BEB) method, Margreiter *et al*[4] and Deutsch *et al*[9] using the DM formalism and Deutsch *et al*[10] using the modified additivity rule. Joshipura *et al*[11] used a self-developed semi-empirical approach to theoretically determine the total cross-section. Most recently Pal *et al*[12] have extended previous theoretical calculations to include both partial and differential cross-sections of $SF_6$ using an approach based on the Jain-Khare semi-empirical formulation. Pal *et al*[12] find encouraging agreement between their calculated PICSs for $SF_6$ and the most recent experimental data of Rao and Srivastava[5] and Rejoub *et al.*[6]

The available experimental electron ionization cross-section data, discussed above, showed a lack of consistency between the determined absolute PICSs.[3-6] It is this lack of consistency that highlights the need for further cross-section data and provides the motivation for the current investigation of $SF_6$. The experimental technique used in this thesis involves a two-dimensional (2D) ion coincidence technique, described in detail in Chapters 2 and 3. This technique enables the single product ions, pairs of product ions or three product ions, formed following ionization of individual $SF_6$ molecules to be detected, identified and quantified. Such an experimental set-up allows the determination of the relative precursor specific PICSs for the ionization of $SF_6$. These relative precursor specific PICSs quantify the contribution from various levels of ionization to the individual product ion yields following an electron-molecule collision, and hence add further detail to the understanding of the electron ionization of $SF_6$. The determination of relative precursor specific PICSs for ion formation *via* dissociative double ionization allowed the direct comparison with recently determined absolute ion pair production cross-sections, discussed above, by Rejoub *et al.*[6] In addition, this is the first time that the contribution from single and triple ionization to the individual ion yields has been quantified following electron interactions with $SF_6$.

In principle the 2D technique utilised here provides information on the energetics involved in dissociation of any multiply charged ions formed. A high yield of molecular dications, in particular $SF_4^{2+}$ and $SF_2^{2+}$, has been observed in previous

studies of the ionization of $SF_6$[6,13-16] although, as noted by these authors, the $SF_6^{2+}$ ion is not observed experimentally. Using 25.6 nm photoionization of $SF_6$, Field and Eland[17] determined two mean lifetimes for $SF_4^{2+}$ dications to be 45±23 ns and 25000 $\pm\frac{50000}{12500}$ ns. Several authors have reported thresholds for the formation of the $SF_4^{2+}$, $SF_3^{2+}$, $SF_2^{2+}$ and $SF^{2+}$ molecular dications from $SF_6$ and these threshold values differ considerably.[13,14,16,18] Thresholds for ion pair formation have been determined by Frasinski *et al*,[19] using photoelectron-photoion-photoion coincidences (PEPIPICO), and by Lange *et al*[16] using a method similar to PEPIPICO. Lange *et al*[16] also examined the dynamics of the fragmentation processes involved in the formation of the product ion pairs and used *ab-initio* calculations to estimate the appearance energies and vertical ionization potentials for individual ion pairs. Eland and Treves-Brown[20] produced kinetic energy release (KER) determinations for five ion pair channels using the PEPIPCO technique at a wavelength of 25.6 nm. Eland and co-workers[21-23] have extensively studied the dissociation of $SF_6^{2+}$ to $SF_3^+ + F^+ + 2F$. Most recently, Hsieh and Eland[23] used a position sensitive detector to further investigate the formation of the $SF_3^+ + F^+$ coincident ion pair, concluding that it does indeed follow a sequential mechanism as determined previously. An Auger-electron-photoion coincidence study of $SF_6$ following photoionization of the sulphur L-shell found that dications having two holes in the outer valence bands dissociate to various fragments whilst those having one hole in the outer valence and one hole in the inner valence dissociate to $S^+ + F^+$.[24]

In this chapter, the focus is aimed at providing further information regarding the relative PICSs and relative precursor specific PICSs for $SF_6$. As outlined above, there is an abundance of literature detailing the dynamics of multiply charged ion dissociation. There are also numerous threshold studies for both dications and ion pair formation from $SF_6$. Therefore, additional dynamic and threshold information is only presented and discussed where the literature lacks consistency in the available determinations.

## 6.2 Experimental Procedures

The sulphur hexafluoride used in these experiments was purchased from Aldrich with a purity of 99.9% and was used without further purification.

### 6.2.1 Experimental conditions

As discussed in Chapter 2, in contrast to the experiments on $N_2O$ and $BCl_3$, a turbo pump was mounted at the detection region for these experiments to minimise the

time that background gas resides on the surface of the MCP detector to reduce the dark counts from the MCP.

As detailed in Chapter 3, the experimental operating conditions involve low electron fluxes and target gas pressures in order to generate a low ion count rate. These conditions ensure that there is very much less than one ionization event per pulse. However, as discussed in Chapter 3, the pairs and triples spectra may still contain small contributions from ions that did not originate from the same dissociation event, but are detected in coincidence: these events are termed accidental coincidences.[25-27] Any accidental coincidence peaks in the pairs and triples spectra can be readily identified by their characteristic 'round' shape, as the ions in the pairs do not possess any momentum correlation. The contribution from accidental coincidence peaks to 'real' peaks in the pairs and triples spectra is subtracted by normalising the two-dimensional and three-dimensional auto-correlation function of the singles spectrum to a known false peak in the pairs (e.g. $SF_3^+ + SF_5^+$) or triples spectrum (e.g. $F^+ + SF_3^+ + SF_5^+$) respectively, as described in Chapter 3.[26-28] The number of accidental coincidences in the current pairs and triples spectra is not insignificant and so accidental coincidence subtraction has been performed for every ion pair and triple to produce 'true' pairs and triples spectra.[27] At 200 eV accidental coincidences in the pairs spectra were typically less than 1-3% of the ion pair peak intensity, however, the accidental coincidences increased to 30% and 60% respectively for the $SF_4^+ + F^+$ and $SF_5^+ + F^+$ ion pairs. The $SF_4^+ + F^+$ and $SF_5^+ + F^+$ ion pair peaks both have a very low intensity in the pairs spectrum, see Figure 6.2, representing less than 1% of the total ion pair peak yield, and thus accidental coincidences are more important.

## 6.3 Data Analysis

Mass and coincidence spectra were recorded at ionizing electron energies between 30-200 eV using the experimental apparatus described in Chapter 2. For each electron energy four separate experimental cross-section determinations were made.

### 6.3.1 Singles spectrum

A representative singles (mass) spectrum recorded at 200 eV is shown in Figure 6.1. Note that the $SF_6^+$ parent ion and $SF_6^{2+}$ parent dication are not observed at any electron energy.

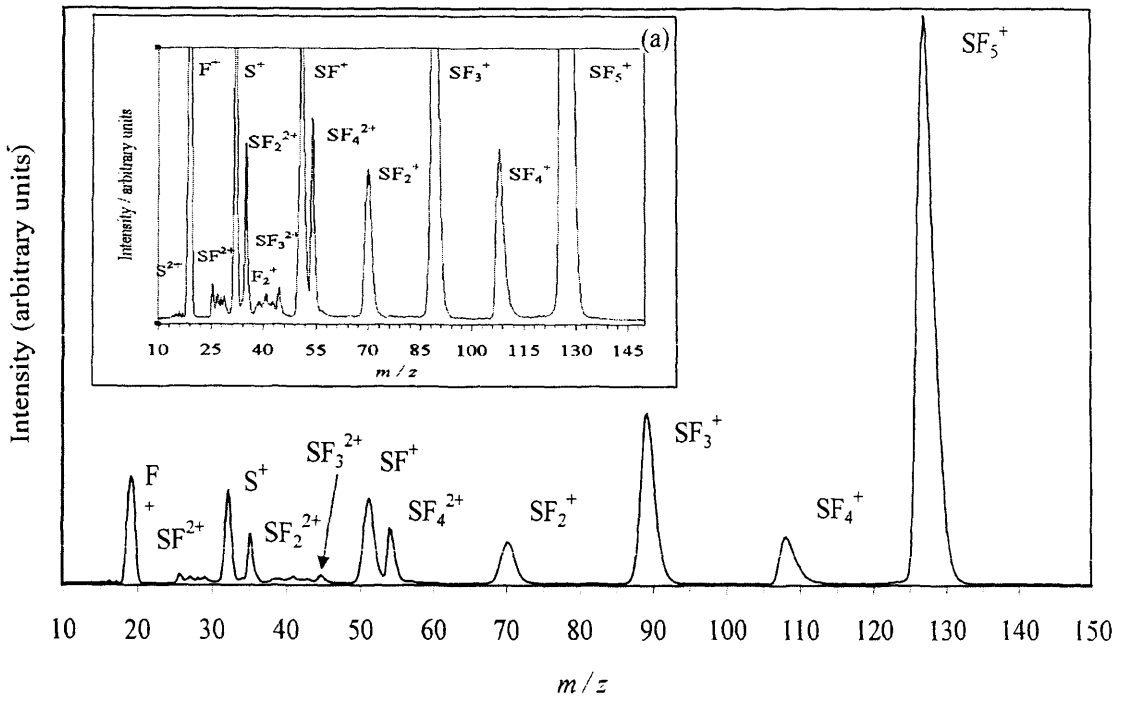


Figure 6.1: A characteristic singles spectrum (mass spectrum) of $SF_6$ following electron ionization recorded at an electron energy of 200 eV. The intensity scale, in part (a) of the above figure, has been increased by a factor of 7.5 over an identical *m/z* range, and shows that trace quantities of background gas were observed at *m/z*=14, 16, 18, 27, 28, 29, 32, 39 and 41. These features are discussed in the text below.

The singles spectra exhibited traces of $H_2O^+$, $N_2^+$, $O_2^+$ and hydrocarbon residual gas at all electron energies. These residual gas peaks contribute to the singles spectra as a result of the operating conditions, namely, low $SF_6$ target gas pressure to minimize the accidental coincidence rate. However, the $H_2O^+$ ion peak becomes obscured at electron energies greater than 70 eV by the $F^+$ ion peak (*m/z*=18 and *m/z*=19 respectively) and the $O_2^+$ peak is obscured by the $S^+$ ion peak (both having *m/z*=32). To remove the contribution from residual gas to the $SF_6$ singles spectra, mass spectra of air were recorded at each electron energy. The intensities of the $H_2O^+$, $N_2^+$ and $O_2^+$ peaks in the air singles spectra were recorded and the ratio of the $H_2O^+/N_2^+$ and $O_2^+/N_2^+$ peaks was determined. These ratios were then normalised to the intensity of the $N_2^+$ ion peak present in the $SF_6$ spectra. Therefore, the intensities of the residual $H_2O^+$ and $O_2^+$ ion signals that contribute to the $SF_6$ singles spectra were determined and subtracted from each $SF_6$ singles spectrum. Typically, the magnitude of the $H_2O^+$ signal was less than

3% of the $F^+$ signal and the magnitude of the $O_2^+$ signal was less than 4% of the $S^+$ signal.

It should be noted that a small ion peak with an *m/z* value of 16 was just detectable in the singles spectra at 200 eV, Figure 6.1. This ion peak consisted of contributions from the fragment ion $S^{2+}$ and also $O^+$, from the residual gas. To remove the contribution from residual gas to the $SF_6$ singles spectra, mass spectra of air were recorded at each electron energy, as described above. Briefly, the intensity of the $O^+$ and $N_2^+$ peaks in the singles spectra of air were recorded, and the ratio of the $O^+/N_2^+$ peaks was determined. This ratio was then normalised to the intensity of the $N_2^+$ ion peak present in the $SF_6$ spectra. The intensity of the $O^+$ ion signal was determined, and subtracted from each $SF_6$ singles spectrum, to yield the $S^{2+}$ signal intensity. The cross-sections determined for $S^{2+}$ were, however, too small to be statistically significant above the background. The relative PICSs for $S^{2+}$ are therefore not presented for any electron energy.

Ion signals at values of *m/z*=9.5 ($F^{2+}$) and *m/z*=10.7 ($S^{3+}$) were not observed in the singles spectra at the electron energies studied here. A small ion peak at *m/z*=38 ($F_2^+$) was observed in the singles spectrum, at an electron energy of 200 eV. However, the contribution from the background gas and neighbouring ion peaks made any accurate peak intensity determination impossible.

Another prominent feature of the singles spectrum is the strong alternation in the relative intensities observed between ions containing an odd and even number of F atoms. Both features have previously been reported and are discussed in detail in the literature.[15,16,29,30] The singles spectra exhibited the ion peaks: $F^+$, $SF^{2+}$, $S^+$, $SF_2^{2+}$, $SF_3^{2+}$, $SF^+$, $SF_4^{2+}$, $SF_2^+$, $SF_3^+$, $SF_4^+$ and $SF_5^+$.

The intensities of these peaks in the singles spectra $I[X^+]$ were determined by summing the counts in the peak and applying a suitable background correction for the non-zero baseline.

### 6.3.2 Pairs spectrum

The pairs spectra recorded following electron ionization of $SF_6$ exhibit nine fragmentation channels: $SF_5^+ + F^+$, $SF_4^+ + F^+$, $SF_3^+ + F^+$, $SF_2^+ + F^+$, $SF^+ + F^+$, $S^+ + F^+$, $F^+ + F^+$, $SF^{2+} + F^+$ and $SF_2^{2+} + F^+$, as shown in Figure 6.2.

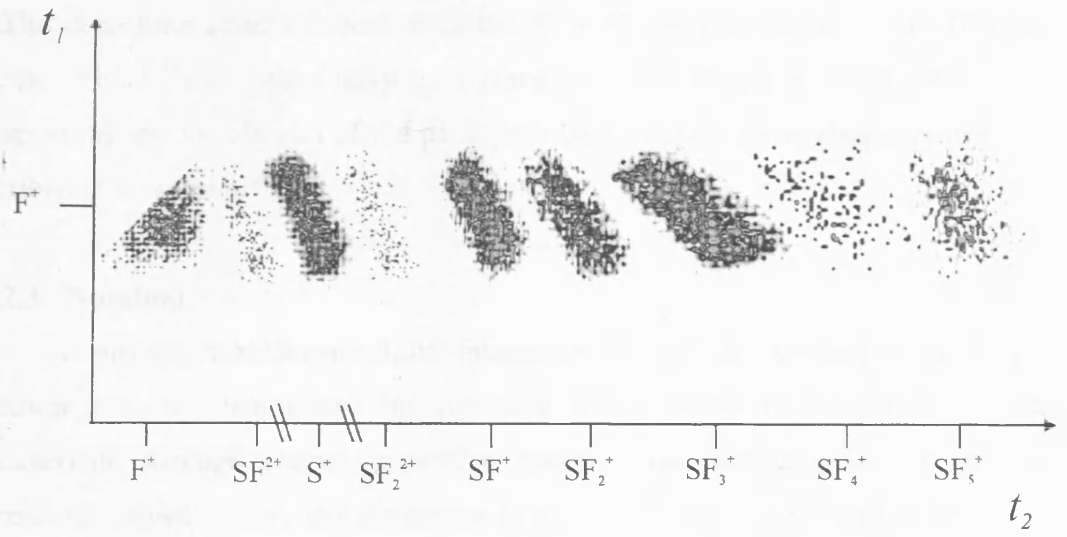


Figure 6.2: A schematic pairs spectrum for $SF_6$ recorded at 200 eV.

### 6.3.2.1 Ion channels

At 200 eV the dominant fragmentation channel is $S^+ + F^+$ accounting for over 30% of the dicationic dissociations detected. A very small $SF_3^+ + F_2^+$ fragmentation channel is also observed. However, the ion pair intensities for the $SF_3^+ + F_2^+$ peak are too low to produce useful precursor specific PICS information. Lange *et al*[16] also observed weak coincidence signals between $F_2^+$ and $SF_3^+/SF_2^+$ following ionization using a 2 MeV $He^{2+}$ ion beam. The $F_2^+$ ion peak was not directly observed in the singles spectra due to the high level of background.

A small 'tail' was observed on the $SF_3^+ + F^+$ coincidence peak that extends towards the diagonal of the coincidence spectrum to the $SF_4^{2+}$ 'self coincidence' peak, discussed in Section 3.1.1.3.6 of Chapter 3. This feature has also been observed by Field and Eland[17] and Lange *et al.*[16] The 'tail' from the $SF_3^+ + F^+$ ion pair peak is produced by a small percentage of metastable $SF_4^{2+}$ ions that dissociate in the source region of the mass spectrometer, or after acceleration towards the detector. As mentioned in Section 6.1.1, Field and Eland[17] estimated mean lifetimes of these metastable $SF_4^{2+}$ dications to be 45±23 ns and $25000 \pm \frac{50000}{12500}$ ns, in the source and field-free drift region respectively, using 25.6 nm photoionization.

### 6.3.2.2 Dead-time

In this experiment no ion pairs are recorded if the second ion arrives within 32 ns of the first ion, due to the dead-time of the discrimination circuitry, shown in Chapter

3. The dead-time affects collection of the $F^+ + F^+$ ion pair signals in the $SF_6$ pairs spectra. The $F^+$ ion counts missed, as a result of the dead-time, were estimated by extrapolating the visible part of the pairs peak back to $t_1=t_2$ using simple geometry, as described in Chapter 3.[26,31]

#### 6.3.2.3 Notation

As discussed in Chapter 3, the intensities of a selected product ion in the pairs spectrum can be determined by summing the number of counts within each characteristic lozenge shaped peak that involves the selected ion. In the data processing, shown below, the distinction is made between $P_2[X^+]$ and $P_3[X^+]$, where $P_2[X^+]$ is the intensity of $X^+$ in pairs of monocations, for example the $S^+ + F^+$ channel. Such pairs of monocations can arise from double ionization or from triple ionization. $P_3[X^+]$ represents the intensity of $X^+$ in ion pairs involving a dication and a monocation, for example $SF_2^{2+} + F^+$, where such ion pairs can only arise from triple or higher levels of ionization. In this analysis it is assumed that any contribution from quadruple ionization is negligible. As discussed below, only a small contribution from triple ionization is observed at the electron energies studied here, and thus the omission of quadruple and higher orders of ionization is appropriate.

### 6.3.3 Triples spectrum

The number of triple coincidences detected is low, as shown in Figure 6.3.

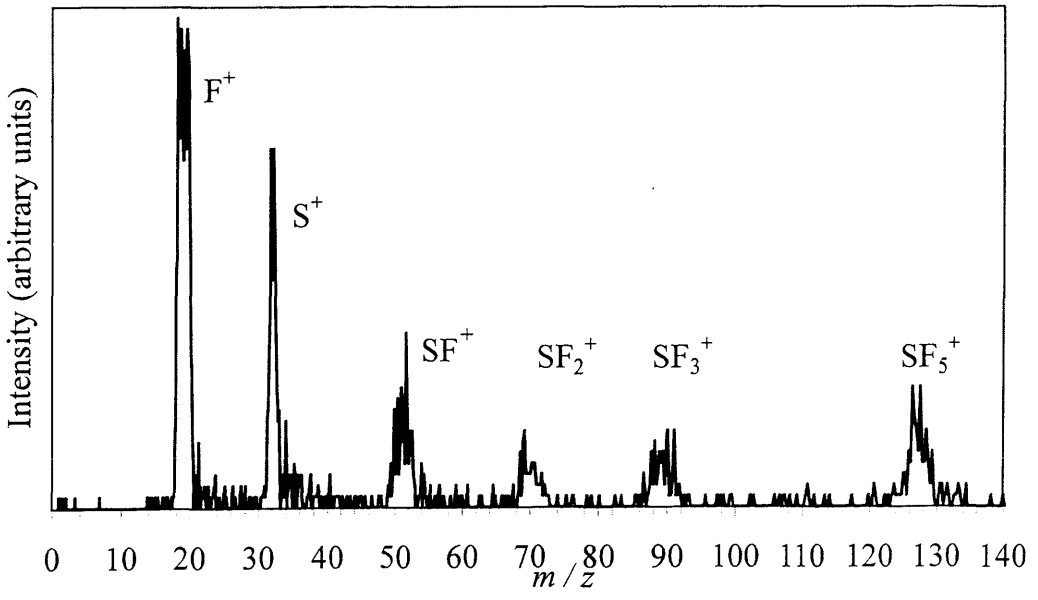


Figure 6.3: A triples mass spectrum recorded at an electron energy of 200 eV. Ion peaks of $F^+$, $S^+$, $SF^+$, $SF_2^+$, $SF_3^+$ and $SF_5^+$ are observed.

As discussed in Chapter 3, this sub-set of the data is first visualized by simply plotting a mass spectrum of the ions recorded as triples, as shown in Figure 6.3, and then plotting a series of pairs spectra, in coincidence, with the different ions present in the mass spectrum of triples. The intensities of the peaks in these 'coincident pairs' spectra are determined by summing the counts in each peak to give $T[X^+]$.

Figure 6.3 shows the raw triple ion coincidence data. It is clear that the accidental coincidences are significant in this data set, as the observed $SF_5^+$ ion peak cannot be formed with any other two fragment monocations in the same dissociative ionization event from $SF_6^{3+}$. Accidental coincidence estimation and subtraction was performed on this data set and is further detailed below.

#### 6.3.3.1 Accidental coincidences

In the triples spectra five ion triple channels were observed in the coincident spectra: the larger $2F^+ + S^+$ and $2F^+ + SF^+$ channels, and minor channels of $3F^+$, $2F^+ + SF_2^+$ and $2F^+ + SF_3^+$. However, following accidental coincidence subtraction, the ion triple intensities of the $3F^+$, $2F^+ + SF_2^+$ and $2F^+ + SF_3^+$ ion triple channels were insufficient to produce reliable cross-section data, and thus are neglected in the analysis. Typically the accidental coincidences in the triples spectra formed 1-3% of the peak intensities. Following accidental coincidence subtraction, the only measurable cross-sections were determined for the formation of $2F^+ + S^+$ and $2F^+ + SF^+$ ion channels.

## 6.4 Relative PICSs

The ion intensities recorded in the singles, pairs and triples spectra were processed to yield the relative PICSs and the relative precursor specific PICSs. This data processing is described in detail in Chapter 3, and specifically for the electron ionization of $SF_6$ in Appendix E, and thus only a brief summary is given below.

### 6.4.1 Notation

The relative PICS for the formation of a fragment ion $X^+$ is symbolized as $\sigma_r[X^+]$, where the cross-section for the formation of $X^+$ is expressed relative to the cross-section for forming $SF_5^+$. Similarly, the relative precursor specific PICS $\sigma_n[X^+]$ ($n$=1-3) expresses the cross-section for forming the fragment ion $X^+$, relative to the cross-section for forming $SF_5^+$, *via* single ($n$=1), double ($n$=2) or triple ($n$=3) ionization.

Typically, relative PICSs are defined relative to the parent ion of the system.

However, the $SF_6^+$ ion is not observed following ionization of $SF_6$, as stated in Section 6.3.1 and discussed in the literature.[15,16,29,30,32] The relative ionization cross-sections presented here, are therefore defined relative to the summation of $\sigma_1[SF_5^+] + \sigma_2[SF_5^+]$, as no evidence was seen in the pairs spectra for $SF_5^+$ ion formation *via* triple ionization ($SF_5^+ + F^{2+}$).

## 6.4.2 Ion intensities

The intensities of the $F^+$, $SF^{2+}$, $S^+$, $SF_2^{2+}$, $SF_3^{2+}$, $SF^+$, $SF_4^{2+}$, $SF_2^+$, $SF_3^+$ and $SF_4^+$ ions observed in the singles pairs and triples spectra are utilised to determine relative PICSs, as detailed in Section 3.1.2 of Chapter 3. The relative PICSs are expressed as a sum of the individual precursor specific PICSs for formation of the ion *via* single, double and triple ionization, where $N_n[X^+]$ represents the number of $X^+$ ions formed *via* loss of $n$ electrons. These values can in turn be expressed as a sum of the ion intensities from the singles $I[X^+]$, pairs $P_2[X^+]$ and $P_3[X^+]$, and triples spectra $T[X^+]$. To illustrate the data analysis used to determine relative PICSs, representative equations are shown for the $F^+$ and $SF^{2+}$ ions:

$$\sigma_r[F^+] = \frac{N_1[F^+] + N_2[F^+] + N_3[F^+]}{N_1[SF_5^+] + N_2[SF_5^+]} = \frac{I[F^+] + P_2[F^+] + P_3[F^+] + T[F^+]}{I[SF_5^+] + P_2[SF_5^+]} \quad (6.1),$$

$$\sigma_r[SF^{2+}] = \frac{N_2[SF^{2+}] + N_3[SF^{2+}]}{N_1[SF_5^+] + N_2[SF_5^+]} = \frac{I[SF^{2+}] + P_3[SF^{2+}]}{I[SF_5^+] + P_2[SF_5^+]} \quad (6.2).$$

Where the intensity of the $F^+$ and $SF^{2+}$ ions in the singles, pairs and triples spectrum can be described by the following equations:

$$I[F^+] = \quad (6.3),$$

$$f_i N_1[F^+] + f_i(1-f_i)N_2[F^+] + f_i(1-f_i)N_3^{\text{pairs}}[F^+] + f_i(1-f_i)^2 N_3^{\text{triples}}[F^+]$$

$$I[SF^{2+}] = f_i N_2[SF^{2+}] + f_i(1-f_i)N_3^{\text{pairs}}[SF^{2+}] \quad (6.4),$$

$$P_2[F^+] = f_i^2 N_2[F^+] + 2f_i^2(1-f_i)N_3^{\text{triples}}[F^+] \quad (6.5),$$

$$P_3[F^+] = f_i^2 N_3^{\text{pairs}}[F^+] \quad (6.6),$$

$$P_3[SF^{2+}] = f_i^2 N_3^{\text{pairs}}[SF^{2+}] \quad (6.7),$$

$$T[F^+] = f_i^3 N_3^{triples}[F^+] \quad (6.8).$$

Note that the $\sigma_r$ values determined here do not depend on $f_i$. However, if a value of $f_i$ is available, then the data analysis can be extended to determine $\sigma_n[X^+]$ values, and thus enable the contributions to each ion yield from single, double and triple ionization to be quantified.

### 6.4.3 Relative precursor specific PICSs

#### 6.4.3.1 Ion detection efficiency

As discussed in Chapter 3, to enable the $\sigma_n[X^+]$ values to be derived a value for $f_i$ must be determined by recording singles and pairs spectra following ionization of $CF_4$.[28] For the electron ionization experiments of $SF_6$, this procedure resulted in a value of $f_i$=0.17±0.02, in agreement with other determinations reported in this thesis, in Chapters 4, 5 and 7.

The expressions used to evaluate the relative precursor specific PICSs for formation of $F^+$ *via* single, double and triple ionization are shown in Eqs. (6.9)-(6.11):

$$\sigma_1[F^+] = \frac{N_1[F^+]}{N_1[SF_5^+] + N_2[SF_5^+]} = \quad (6.9),$$

$$\frac{I[F^+] - (1-f_i)/f_i P_2[F^+] - (1-f_i)/f_i P_3[F^+] + (1-f_i)^2/f_i^2 T[F^+]}{I[SF_5^+] + P_2[SF_5^+]}$$

$$\sigma_2[F^+] = \frac{N_2[F^+]}{N_1[SF_5^+] + N_2[SF_5^+]} = \frac{P_2[F^+]/f_i - 2(1-f_i)/f_i^2 T[F^+]}{I[SF_5^+] + P_2[SF_5^+]} \quad (6.10),$$

$$\sigma_3[F^+] = \frac{N_3^{pairs}[F^+] + N_3^{triples}[F^+]}{N_1[SF_5^+] + N_2[SF_5^+]} = \frac{P_3[F^+]/f_i + T[F^+]/f_i^2}{I[SF_5^+] + P_2[SF_5^+]} \quad (6.11).$$

## 6.5 Discussion

The singles and coincidence spectra were processed, as described in Chapter 3, to yield $\sigma_r$ and $\sigma_n$ values. These values are expressed relative to $SF_5^+$ ion yield, the most abundant ion formed following ionization of $SF_6$ at all ionizing electron energies investigated here.

### 6.5.1 Data Comparison

In this section, the $\sigma_r$ and $\sigma_n$ values (Table 6.1-Table 6.9) determined here are discussed and compared with relative cross-sections derived from the absolute partial and absolute ion pair production cross-sections of Rejoub *et al.*[6] The relative PICS, and relative precursor specific PICS values derived from the data of Rejoub *et al*[6] are defined as, $\sigma_r[X^+]$ and $\sigma_2[X^+]$ respectively. The $\sigma_2[X^+]$ values derived from the ion pair cross-sections data of Rejoub *et al*[6] are equivalent to the $\sigma_2[X^+]$ values determined here. The $\sigma_2[X^+]$ values presented here are determined up to an electron energy of 200 eV, however, the values of $\sigma_2[X^+]$ derived from the data of Rejoub *et al*[6] are generally only determined at electron energies above 100 eV, which restricts the comparison between the data. Following comparison between the values of $\sigma_2[X^+]$ determined here, and the values of $\sigma_2[X^+]$ derived from the data of Rejoub *et al*,[6] their data are generally lower than the values of $\sigma_2[X^+]$ determined here, see Sections 6.5.3 to 6.5.5. To understand why such a discrepancy exists, it is useful to examine the indirect experimental approach used by Rejoub *et al*[6] to determine the ion pair cross-sections. The experimental apparatus used by Rejoub *et al*[6] is only capable of counting one ion arrival per electron pulse. Therefore, when a pair of ions is formed, following a single dicationic dissociation, the 'slower' correlated ion pair partner will not be detected, and thus this loss of ions may lead to an underestimation of particular fragment ion cross-sections. It is clear from Figure 6.2 that the contribution from such dissociation events to the total ion yields is significant. Rejoub *et al*[6] solved the potential loss of fragment ions, and subsequent underestimation of the absolute PICS, by using the fact that for the electron ionization of $SF_6$ every ion pair is formed in coincidence with an $F^+$ ion. By applying a gate to the timing signal, to suppress the detection of the $F^+$ ions, the 'true' absolute PICSs for all other fragment ions formed following electron ionization of $SF_6$ were produced, irrespective of whether an $F^+$ ion is also formed. The same methodology is used for the determination of the 'true' $F^+$ absolute PICSs. The 'apparent' absolute PICSs for each particular ion were determined without the gate applied to the timing signal. By subtracting the apparent absolute PICS from the true absolute PICS, and dividing by the detection efficiency of the system, an absolute precursor specific cross-section for formation of that ion, with its correlated $F^+$ partner, is determined. Rejoub *et al*[6] give a value for the detection efficiency of their system to

be between 40.0% and 40.5% for all ion species. By understanding the methodology used by Rejoub *et al*[6] it is probable that the small discrepancy between the values of $\sigma_2[\dot{X}^+]$ determined here and the $\sigma_2[X^+]$ values derived from the data of Rejoub *et al*[6] may be explained by the differing experimental methodology used in deriving precursor specific cross-section data. For example, Rejoub *et al*[6] may be overestimating the detection efficiency of their system, which would explain why their cross-sections for ion pair formation are generally smaller than the values determined here. Another explanation may be the result of the data analysis used by Rejoub *et al*,[6] where it is assumed that relatively few ionization events result in the formation of three positive ions. Indeed, the values determined from analysis of these triples peaks, observed in the triples spectra, produced small $\sigma_3[X^+]$ values, even at 200 eV.

Agreement within the mutual error limits is seen for all the $\sigma_r$ values determined here and the $\sigma_r[X^+]$ values derived from the data of Rejoub *et al*[6] for all ions formed following electron interaction with $SF_6$. These values are therefore not discussed further in the following Sections. As mentioned in Section 6.1.1, Rao and Srivastava[5] determined absolute PICSs for the electron ionization of $SF_6$ at 100 eV. However, the relative PICS values derived from the absolute PICSs of Rao and Srivastava,[5] especially for the formation of lighter fragment ions, are lower than the $\sigma_r[X^+]$ values determined here, and the $\sigma_r[X^+]$ values derived from the data of Rejoub *et al.*[6] This indicates that the experimental apparatus used by Rao and Srivastava[5] may not have been able to collect all the energetic fragment ions formed following electron interaction with $SF_6$. Rejoub *et al*[6] also draw this conclusion. Therefore, the data of Rao and Srivastava[5] are not shown.

### 6.5.2 $SF_4^+$ formation

Figure 6.4 shows that the values of $\sigma_r[SF_4^+]$ determined here increase towards 100 eV and peak between 100-150 eV. The values of $\sigma_2[SF_4^+]$ are very small even at an electron energy of 200 eV and, hence, the values of $\sigma_1[SF_4^+]$ are approximately equal to the values of $\sigma_r[SF_4^+]$. The values of $\sigma_1[SF_4^+]$, $\sigma_2[SF_4^+]$ and $\sigma_r[SF_4^+]$ are displayed in Table 6.1.

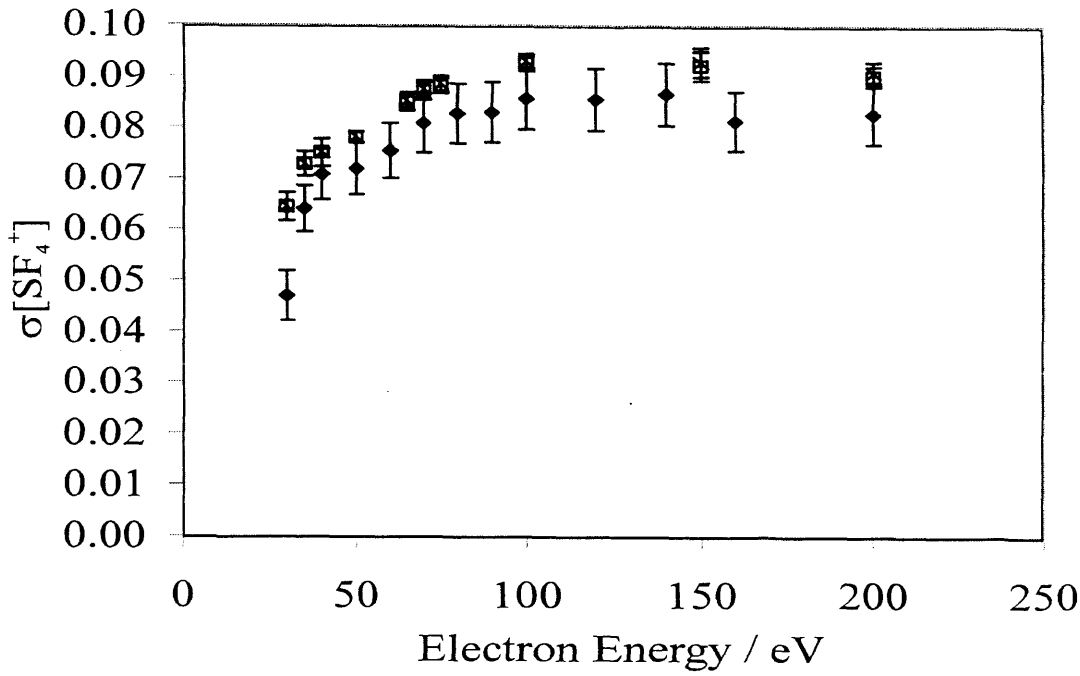


Figure 6.4: Relative precursor specific PICSs for forming $SF_4^+$ *via* single ionization (□) following electron ionization of $SF_6$. The relative PICS is shown by (×). These cross-sections are expressed relative to the cross-section for forming $SF_5^+$. The error bars shown are standard deviations of multiple determinations. Relative PICSs extracted from the data of Rejoub *et al*[6] (◆) are also shown with representative error bars. The relative precursor specific PICSs for forming $SF_4^+$ *via* double ionization are not shown.

Table 6.1: Relative precursor specific PICSs and relative PICSs following electron ionization of $SF_6$, expressed relative to the cross-section for forming $SF_5^+$, as a function of electron energy, *E*. The standard deviation of the last figure is given in parentheses.

| *E*/eV | $\sigma_1[SF_4^+]$ | $\sigma_2[SF_4^+]$ | $\sigma_r[SF_4^+]$ |
|---|---|---|---|
| 200 | 0.090(2) | 0.001(1) | 0.091(2) |
| 150 | 0.092(3) | 0.001(1) | 0.093(3) |
| 100 | 0.092(1) | 0.000(1) | 0.092(1) |
| 75 | 0.088(2) | 0.000(1) | 0.088(1) |
| 70 | 0.087(2) | 0.000(1) | 0.087(2) |
| 65 | 0.085(2) | 0.000(1) | 0.085(2) |
| 50 | 0.078(1) | 0.000(1) | 0.078(1) |
| 40 | 0.075(3) | 0.000(1) | 0.075(3) |
| 35 | 0.073(2) | 0.000(1) | 0.073(2) |
| 30 | 0.064(3) | 0.000(1) | 0.064(3) |

### 6.5.3 $SF_3^+$ formation

Figure 6.5 shows that the values of $\sigma_r[SF_3^+]$ increase gradually towards an electron energy of 200 eV except for a decrease (a 'dip') around 40-50 eV. This dip is also observed in the $\sigma_1[SF_3^+]$ values, as will be discussed below. The values of $\sigma_1[SF_3^+]$, $\sigma_2[SF_3^+]$ and $\sigma_r[SF_3^+]$ are displayed in Table 6.2.

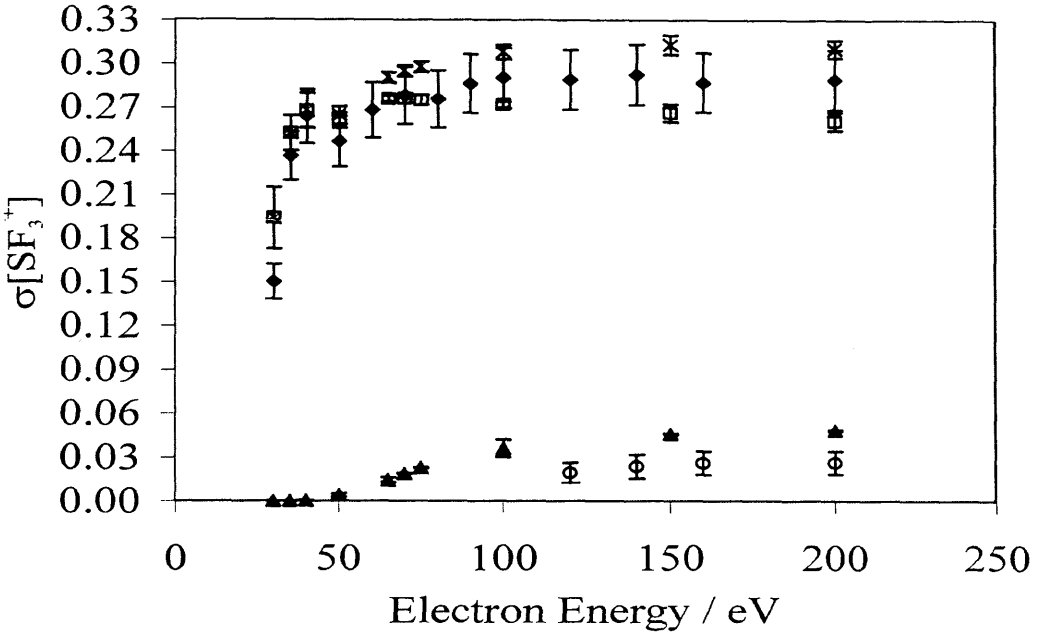


Figure 6.5: Relative precursor specific PICSs for forming $SF_3^+$ *via* single (□), and double ionization (▲) following electron ionization of $SF_6$. The relative PICS is shown by (×). These cross-sections are expressed relative to the cross-section for forming $SF_5^+$. The error bars shown in the figure are standard deviations of multiple determinations. Relative PICSs and cross-sections for ion pair formation extracted from the data of Rejoub *et al*[6] are also shown with representative error bars, (◆) and (O) respectively.

A similar 'dip' in the $SF_3^+$ PICS has previously been reported by Margreiter *et al*[4] and Rejoub *et al.*[6] Most recently a detailed study of the $SF_3^+$ PICS by Feil *et al*[33] using a mass-analyzed ion kinetic energy (MIKE) scan technique investigated this pronounced 'dip' in the $SF_3^+$ PICS. Feil *et al*[33] show that the contribution from the Coulomb explosion of metastable $SF_4^{2+}$ ions forming $SF_3^+ + F^+$ becomes significant around an electron energy of 45.5 eV, whilst the relative PICS for $SF_3^+$ formation *via* single ionization peaks just above 40 eV and decreases towards 200 eV. The conclusions of Feil *et al*[33] are shown schematically in Figure 6.6.

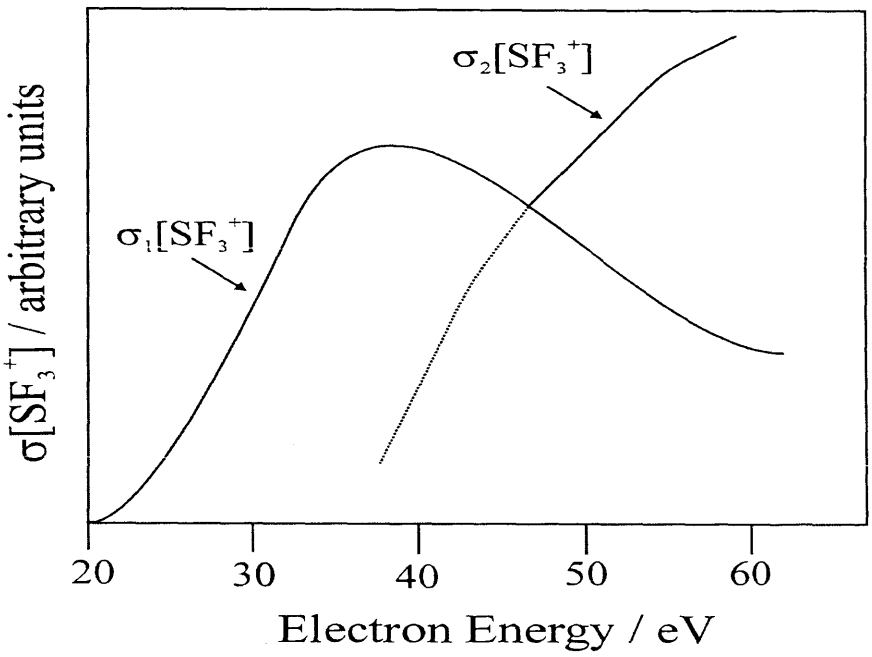


Figure 6.6: A schematic diagram of the relative precursor specific PICSs for forming $SF_3^+$ *via* single and double ionization.

The behaviour of these cross-sections creates a 'dip' feature where the contribution from dissociative single ionization is decreasing and the dissociative double ionization becomes significant at around 45 eV. As mentioned above, this 'dip' feature is observed in the values of $\sigma_r[SF_3^+]$ and also the values of $\sigma_1[SF_3^+]$ determined here. The observation of this dip feature in the precursor specific PICS for formation of $SF_3^+$ *via* single ionization suggested that $SF_3^+$ ions were also being formed from Rydberg states, just above the double ionization threshold, *via* single ionization. The implication from this observation is that this 'dip' feature in the $SF_3^+$ PICS is not only the result of the increasing contribution from metastable $SF_4^{2+}$ dissociation as the contribution from dissociative single ionization decreases, but that there is also a component due to single ionization.

The values of $\sigma_2[SF_3^+]$ determined here are approximately 80% greater than the $\sigma_2[SF_3^+]$ values derived from the data of Rejoub *et al.*[6] Possible explanations for this discrepancy are detailed in Section 6.5.1.

Table 6.2: Relative precursor specific PICSs and relative PICSs following electron ionization of $SF_6$, see caption of Table 6.1 for further details.

| *E*/eV | $\sigma_1[SF_3^+]$ | $\sigma_2[SF_3^+]$ | $\sigma_r[SF_3^+]$ |
|---|---|---|---|
| 200 | 0.261(6) | 0.049(1) | 0.311(6) |
| 150 | 0.267(6) | 0.046(1) | 0.313(7) |
| 100 | 0.272(2) | 0.036(6) | 0.308(5) |
| 75 | 0.275(3) | 0.023(1) | 0.298(4) |
| 70 | 0.277(3) | 0.019(1) | 0.295(4) |
| 65 | 0.276(2) | 0.014(2) | 0.291(4) |
| 50 | 0.261(5) | 0.004(1) | 0.265(6) |
| 40 | 0.268(12) | 0.000(1) | 0.268(12) |
| 35 | 0.253(12) | 0.000(1) | 0.253(12) |
| 30 | 0.194(21) | 0.000(1) | 0.194(21) |

### 6.5.4 $SF_2^+$ formation

Figure 6.7 shows the values of $\sigma_r[SF_2^+]$ and $\sigma_1[SF_2^+]$ determined here peak at 70 eV and decrease towards 200 eV. The values of $\sigma_2[SF_2^+]$ become significant above 50 eV and increase up to 200 eV. The values of $\sigma_1[SF_2^+]$, $\sigma_2[SF_2^+]$ and $\sigma_r[SF_2^+]$ are displayed in Table 6.3.

Comparison between the values of $\sigma_2[SF_2^+]$ determined here and the values of $\sigma_2[SF_2^+]$ derived from the data of Rejoub *et al*[6] shows agreement at 100 eV within the mutual error limits. However, above 100 eV the values determined here are approximately 100% greater than the $\sigma_2[SF_2^+]$ values derived from the data of Rejoub *et al*.[6] Possible reasons for this discrepancy have been discussed in detail within Section 6.5.1.

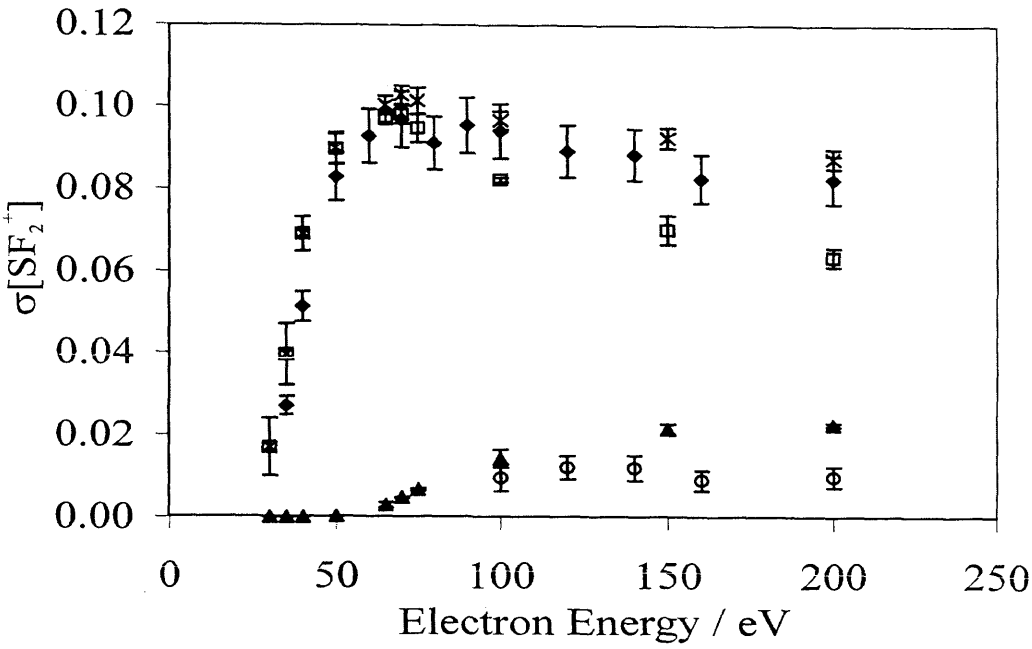


Figure 6.7: Relative precursor specific PICSs for forming $SF_2^+$ *via* single (□), and double ionization (▲) following electron ionization of $SF_6$. The relative PICS is shown by (×). These cross-sections are expressed relative to the cross-section for forming $SF_5^+$. The error bars shown in the figure are standard deviations of multiple determinations. Relative PICSs and cross-sections for ion pair formation extracted from the data of Rejoub *et al*[6] are also shown with representative error bars, (◆) and (O) respectively.

Table 6.3: Relative precursor specific PICSs and relative PICSs following electron ionization of $SF_6$, see caption of Table 6.1 for further details.

| *E*/eV | $\sigma_1[SF_2^+]$ | $\sigma_2[SF_2^+]$ | $\sigma_r[SF_2^+]$ |
|---|---|---|---|
| 200 | 0.064(2) | 0.023(1) | 0.087(2) |
| 150 | 0.070(4) | 0.021(1) | 0.092(2) |
| 100 | 0.082(1) | 0.014(2) | 0.097(2) |
| 75 | 0.095(3) | 0.007(1) | 0.101(3) |
| 70 | 0.098(2) | 0.005(1) | 0.103(2) |
| 65 | 0.097(2) | 0.003(1) | 0.100(2) |
| 50 | 0.090(4) | 0.000(1) | 0.090(4) |
| 40 | 0.069(4) | 0.000(1) | 0.069(4) |
| 35 | 0.040(7) | 0.000(1) | 0.040(7) |
| 30 | 0.017(7) | 0.000(1) | 0.017(7) |

### 6.5.5 $SF^+ + SF_4^{2+}$ formation

It should be noted that Rejoub *et al*[6] are unable to completely separate the $SF^+$ and $SF_4^{2+}$ ion peaks. So for convenient comparison the relative precursor specific PICSs ($\sigma_1[SF^+]$, $\sigma_2[SF^+]$, $\sigma_3[SF^+]$ and $\sigma_2[SF_4^{2+}]$) and a summation of the $SF^+$ and $SF_4^{2+}$ relative PICSs ($\sigma_r[SF^+ + SF_4^{2+}]$), are presented in Figure 6.8. The current experiment enables the $SF^+$ and $SF_4^{2+}$ ion peaks to be individually analysed at electron energies of 75-200 eV in the singles spectrum. Below 75 eV, the overlap observed between the $SF^+$ and $SF_4^{2+}$ ion peaks in the singles spectra becomes significant. Therefore, to obtain accurate $I[SF^+]$ and $I[SF_4^{2+}]$ values, a peak fitting procedure was used below 75 eV. This peak fitting procedure determined the additional ion intensity of each peak obscured by the $SF^+$ and $SF_4^{2+}$ ion peak overlap. However, by using a peak fitting procedure the cross-sections determined for the $SF^+$ and $SF_4^{2+}$ ions have a slightly larger associated error.

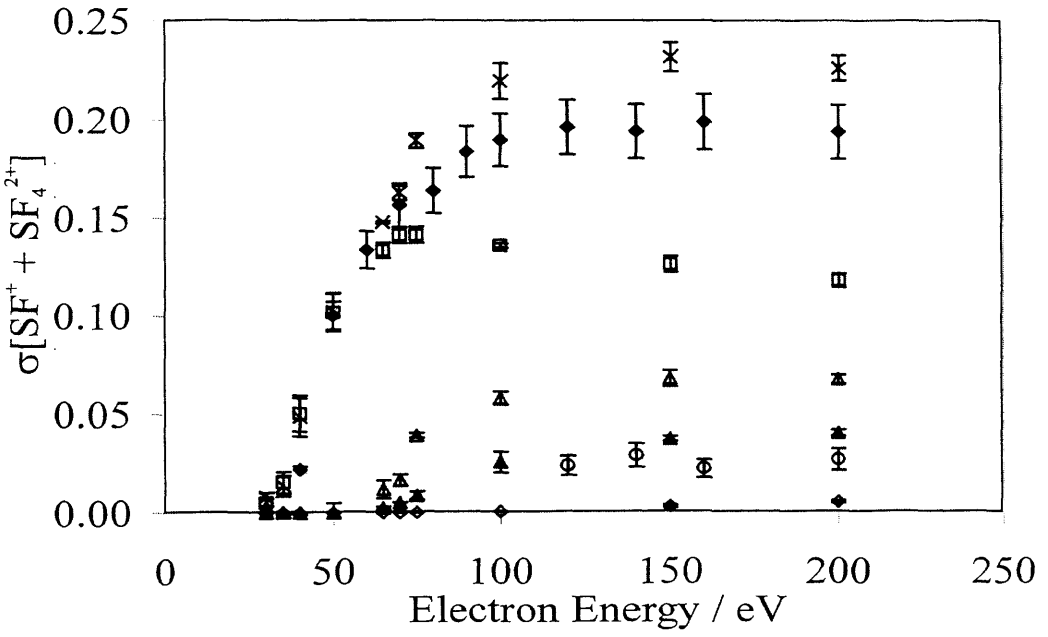


Figure 6.8: Relative precursor specific PICSs for forming $SF^+$ *via* single (□), double (▲) and triple ionization (◇) and formation of $SF_4^{2+}$ *via* double ionization (△) following electron ionization of $SF_6$. The relative PICS for forming $SF^+ + SF_4^{2+}$ is shown by (×). These cross-sections are expressed relative to the cross-section for forming $SF_5^+$. The error bars shown in the figure are standard deviations of multiple determinations. Relative PICSs for forming $SF^+ + SF_4^{2+}$ and cross-sections for ion pair formation ($SF^+ + F^+$) extracted from the data of Rejoub *et al*[6] are also shown with representative error bars, (◆) and (O) respectively.

Figure 6.8 shows that the values of $\sigma_1[SF^+]$ peak at an electron energy of 75 eV. The values of $\sigma_2[SF^+]$ only become significant at 65 eV and increase up to an electron energy of 200 eV. The $\sigma_3[SF^+]$ values are very small even at 150 and 200 eV. Figure 6.8 shows that the $\sigma_r[SF_4^{2+}]$ values only become significant above 50 eV and increase up to 150 eV, where they reach a plateau towards 200 eV. As a result of using a peak fitting procedure on the $SF^+$ and $SF_4^{2+}$ ion peaks, between 30-70 eV, the sensitivity to the onset of the $SF_4^{2+}$ ion peak is decreased. Note that $\sigma_r[SF_4^{2+}]=\sigma_2[SF_4^{2+}]$. These values are displayed in Table 6.4.

The values of $\sigma_r[SF^+ + SF_4^{2+}]$ determined here are in agreement with the $\sigma_r[SF^+ + SF_4^{2+}]$ values derived from the data of Rejoub *et al*[6] at electron energies below 75 eV. However, from 75-200 eV disagreement with the values of $\sigma_r[SF^+ + SF_4^{2+}]$ determined here and the values of $\sigma_r[SF^+ + SF_4^{2+}]$ derived from the data of Rejoub *et al*[6] was observed. At 200 eV the values of $\sigma_r[SF^+ + SF_4^{2+}]$ determined here were 15% greater than the $\sigma_r[SF^+ + SF_4^{2+}]$ values derived from the data of Rejoub *et al.*[6]

At 200 eV the value of $\sigma_2[SF^+]$ determined here is 30% greater than the $\sigma_2[SF^+]$ values derived from the data of Rejoub *et al.*[6] This small discrepancy is again consistent with the reasons detailed in Section 6.5.1. However, for electron energies below 200 eV the values of $\sigma_2[SF^+]$ determined here agree within the mutual error limits with the values of $\sigma_2[SF^+]$ derived from the data of Rejoub *et al.*[6]

Table 6.4: Relative precursor specific PICSs and relative PICSs following electron ionization of $SF_6$, see caption of Table 6.1 for further details.

| *E*/eV | $\sigma_1[SF^+]$ | $\sigma_2[SF^+]$ | $\sigma_3[SF^+]$ | $\sigma_r[SF^+]$ | $\sigma_r[SF_4^{2+}]$ |
|---|---|---|---|---|---|
| 200 | 0.118(4) | 0.040(2) | 0.005(1) | 0.164(4) | 0.068(2) |
| 150 | 0.126(4) | 0.037(1) | 0.003(1) | 0.167(4) | 0.068(4) |
| 100 | 0.136(1) | 0.026(5) | 0.000(1) | 0.162(6) | 0.058(3) |
| 75 | 0.142(4) | 0.009(2) | 0.000(1) | 0.150(3) | 0.039(1) |
| 70 | 0.155(6) | 0.005(1) | 0.000(1) | 0.160(6) | 0.017(3) |
| 65 | 0.147(9) | 0.002(1) | 0.000(1) | 0.149(9) | 0.012(5) |
| 50 | 0.111(12) | 0.000(1) | 0.000(1) | 0.111(12) | 0.000(1) |
| 40 | 0.055(10) | 0.000(1) | 0.000(1) | 0.055(10) | 0.000(2) |
| 35 | 0.018(6) | 0.000(1) | 0.000(1) | 0.018(6) | 0.000(2) |
| 30 | 0.005(2) | 0.000(1) | 0.000(1) | 0.005(2) | 0.000(2) |

### 6.5.6 $S^+$ formation

Figure 6.9 shows the values of $\sigma_r[S^+]$ increase towards 200 eV. The values of $\sigma_1[S^+]$ peak at 100 eV and decrease towards 200 eV. The $\sigma_2[S^+]$ values only become significant above an electron energy of 70 eV and increase up to 200 eV. The values of $\sigma_3[S^+]$ are non-zero above 150 eV. The values of $\sigma_1[S^+]$, $\sigma_2[S^+]$ and $\sigma_r[S^+]$ are displayed in Table 6.5.

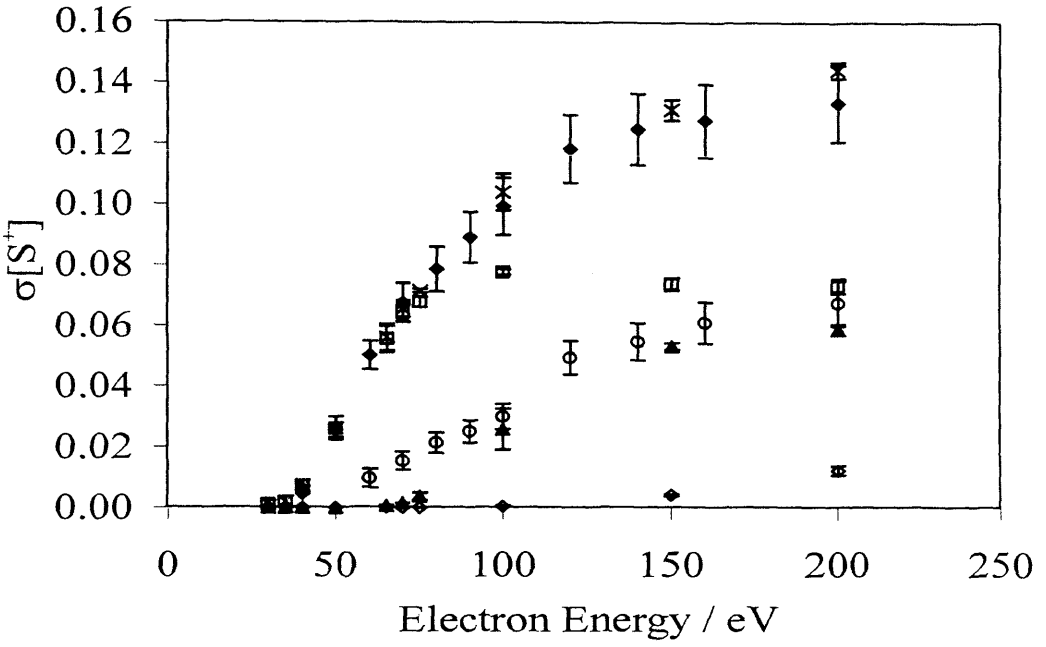


Figure 6.9: Relative precursor specific PICSs for forming $S^+$ *via* single (□), double (▲) and triple ionization (◇) following electron ionization of $SF_6$. The relative PICS is shown by (×). These cross-sections are expressed relative to the cross-section for forming $SF_5^+$. The error bars shown in the figure are standard deviations of multiple determinations. Relative PICSs and cross-sections for ion pair formation extracted from the data of Rejoub *et al*[6] are also shown with representative error bars, (◆) and (O) respectively.

Above 75 eV the values of $\sigma_2[S^+]$ determined here are in agreement with the $\sigma_2[S^+]$ values derived from the data of Rejoub *et al.*[6] However, at electron energies below 75 eV the values for $\sigma_2[S^+]$ determined here are 10 times lower than the $\sigma_2[S^+]$ values derived from the data of Rejoub *et al.*[6] The intensity of the $S^+ + F^+$ ion pair observed in our coincidence spectra does indeed drop rapidly at electron energies below 70 eV. The reasons why there is such a significant discrepancy between the $\sigma_2[S^+]$ values determined here, below 75 eV, and the $\sigma_2[S^+]$ values derived from the data of Rejoub *et*

*al*,[6] are not fully understood. Using a least squares fit procedure at electron energies of 65, 70, 75 and 100 eV, the appearance potential for the $S^+ + F^+$ ion pair was determined to be 62.0±1.5 eV. This value is in disagreement with the $\sigma_2[S^+]$ values derived from the data of Rejoub *et al*[6] which are non-zero at 60 eV. However, the threshold estimate of 62.0±1.5 eV is in good agreement with an experimental photoionization threshold determination of Frasinski *et al*[19] and calculations of Lange *et al.*[16] Frasinski *et al*[19] observed no $S^+ + F^+$ ion pair formation using photon energies of up to 56.4 eV, therefore, this gives a lower threshold limit for the $S^+ + F^+$ ion pair. Lange *et al*[16] calculated the double ionization potential of the $(5a_{1g})^{-2}$ state to be 62.9 eV and postulate that this state may be responsible for this process. By examining the gradient of the $S^+ + F^+$ coincidence peak Lange *et al*[16] conclude that this ion pair is formed *via* an instantaneous dissociation of $SF_6^{2+}$ and thus the threshold for formation of the $S^+ + F^+$ peak may be expected to be above the double ionization threshold, as determined in these experiments.

Table 6.5: Relative precursor specific PICSs and relative PICSs following electron ionization of $SF_6$, see caption of Table 6.1 for further details.

| *E*/eV | $\sigma_1[S^+]$ | $\sigma_2[S^+]$ | $\sigma_3[S^+]$ | $\sigma_r[S^+]$ |
|---|---|---|---|---|
| 200 | 0.073(2) | 0.059(2) | 0.012(2) | 0.144(3) |
| 150 | 0.074(2) | 0.053(1) | 0.004(1) | 0.131(3) |
| 100 | 0.078(1) | 0.026(7) | 0.000(1) | 0.104(6) |
| 75 | 0.068(2) | 0.004(1) | 0.000(1) | 0.072(1) |
| 70 | 0.064(3) | 0.001(1) | 0.000(1) | 0.066(3) |
| 65 | 0.055(4) | 0.001(1) | 0.000(1) | 0.056(4) |
| 50 | 0.026(4) | 0.000(1) | 0.000(1) | 0.026(4) |
| 40 | 0.007(2) | 0.000(1) | 0.000(1) | 0.007(2) |
| 35 | 0.002(2) | 0.000(1) | 0.000(1) | 0.002(2) |
| 30 | 0.001(1) | 0.000(1) | 0.000(1) | 0.001(1) |

### 6.5.7 $F^+$ formation

Figure 6.10 shows the values of $\sigma_r[F^+]$ we determine increase steeply towards 200 eV. The values of $\sigma_1[F^+]$ peak at an electron energy of 75 eV and decrease towards 200 eV. Interestingly, the values of $\sigma_1[F^+]$ only become significant at 50 eV. The values of

$\sigma_2[F^+]$ become significant above 40 eV and steadily increase up to 200 eV, becoming larger than $\sigma_1[F^+]$ above 75 eV, showing that double ionization contributes significantly to the $F^+$ ion yield. The values of $\sigma_2[F^+]$ are expected to be significant, as the $F^+$ ion is the correlated partner ion in all ion pairs observed following multiple ionization. The values of $\sigma_3[F^+]$ determined here become significant above 100 eV. The values of $\sigma_1[F^+]$, $\sigma_2[F^+]$ and $\sigma_r[F^+]$ are displayed in Table 6.6.

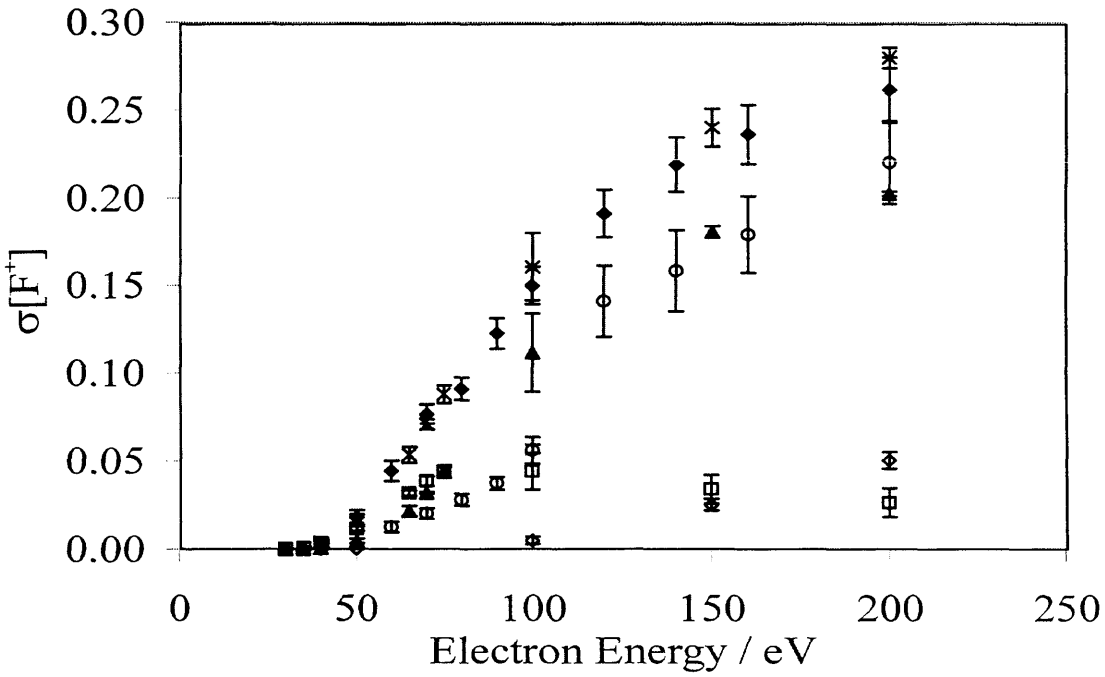


Figure 6.10: Relative precursor specific PICSs for forming $F^+$ *via* single (□), double (▲) and triple ionization (◇) following electron ionization of $SF_6$. The relative PICS is shown by (×). These cross-sections are expressed relative to the cross-section for forming $SF_5^+$. The error bars shown in the figure are standard deviations of multiple determinations. Relative PICSs and cross-sections for ion pair formation extracted from the data of Rejoub *et al*[6] are also shown with representative error bars, (◆) and (O) respectively. It should be noted that for comparison the cross-section values for formation of $F^+$ from the ion pairs data of Rejoub *et al*[6] shown here are a summation of all ion pairs observed by Rejoub *et al*[6] and, as described in the text, a percentage has been added to allow for the $F^+$ + $F^+$ ion pairs not collected by Rejoub *et al.*[6]

Hitchcock *et al*[14] believed that almost all the $F^+$ fragment ions arose from dissociative double ionization of $SF_6$, and hence, did not expect a significant amount of $F^+$ ions to be produced from fragmentation of $SF_6^+$. With reference to Figure 6.10, the

majority of $F^+$ ions are indeed formed *via* dissociative double ionization. For example at 200 eV the value of $\sigma_1[F^+]$ constitutes 10% of the value of $\sigma_2[F^+]$ determined.

The methodology adopted by Rejoub *et al*[6] to determine ion pair cross-sections, described in Section 6.5.1, could not be used to determine the ion pair cross-section for the $F^+ + F^+$ ion pair because of the timing electronics used in their apparatus. From the $SF_6$ pairs spectrum recorded here, the $F^+ + F^+$ ion pair peak intensity constitutes approximately 15% of the ion pairs observed, and represents a significant proportion of the $\sigma_2[F^+]$ yield. The $\sigma_2[F^+]$ values derived from the data of Rejoub *et al*[6] were corrected for the absence of the $F^+ + F^+$ ion pair peak by adding 15% of the total number of $F^+$ ions formed as ion pairs observed by Rejoub *et al*[6] to the total number of $F^+$ ions formed as ion pairs. The $\sigma_2[F^+]$ values of Rejoub *et al*,[6] shown in Figure 6.10, represent the summation of the $\sigma_2[F^+]$ values derived from the data of Rejoub *et al*[6] and the correction for the absence of the $F^+ + F^+$ ion pair peak, described above. Agreement, within the mutual error limits, between the $\sigma_2[F^+]$ values determined here, and the values of $\sigma_2[F^+]$ derived from the data of Rejoub *et al*[6] is observed, see Figure 6.10.

Table 6.6: Relative precursor specific PICSs and relative PICSs following electron ionization of $SF_6$, see caption of Table 6.1 for further details.

| *E*/eV | $\sigma_1[F^+]$ | $\sigma_2[F^+]$ | $\sigma_3[F^+]$ | $\sigma_r[F^+]$ |
|---|---|---|---|---|
| 200 | 0.027(8) | 0.203(1) | 0.051(5) | 0.281(6) |
| 150 | 0.034(8) | 0.181(3) | 0.025(3) | 0.240(11) |
| 100 | 0.044(11) | 0.112(22) | 0.005(2) | 0.161(19) |
| 75 | 0.044(3) | 0.044(3) | 0.000(1) | 0.088(5) |
| 70 | 0.039(3) | 0.032(1) | 0.000(1) | 0.071(3) |
| 65 | 0.032(1) | 0.022(3) | 0.000(1) | 0.054(5) |
| 50 | 0.012(2) | 0.005(1) | 0.000(1) | 0.017(3) |
| 40 | 0.003(1) | 0.001(1) | 0.000(1) | 0.004(1) |
| 35 | 0.001(1) | 0.000(1) | 0.000(1) | 0.001(1) |
| 30 | 0.000(1) | 0.000(1) | 0.000(1) | 0.001(1) |

### 6.5.8 $SF_3^{2+}$ formation

Figure 6.11 shows that the values of $\sigma_r[SF_3^{2+}]$ determined here become significant above an electron energy of 40 eV and increase towards 150 eV where the values reach a plateau. Where $\sigma_r[SF_3^{2+}]=\sigma_2[SF_3^{2+}]$, no $SF_3^{2+}$ ions are observed from triple ionization in this experiment. The values of $\sigma_r[SF_3^{2+}]$ derived from the data of Rejoub *et al*[6] are in agreement with the data determined here at electron energies below 100 eV. Above 100 eV the values of $\sigma_r[SF_3^{2+}]$ determined here are at least 50% greater than the values of $\sigma_r[SF_3^{2+}]$ derived from the data of Rejoub *et al.*[6] However, the intensity of the $SF_3^{2+}$ ion peak observed in the singles spectrum is small, and there are also significant background ion peaks in the area, Figure 6.1. These factors increase the associated errors in the cross-section determinations shown here, see Figure 6.11 and Table 6.7. Consequently, it is concluded that overall agreement between the data determined here and the values of $\sigma_r[SF_3^{2+}]$ derived from the data of Rejoub *et al*[6] is observed.

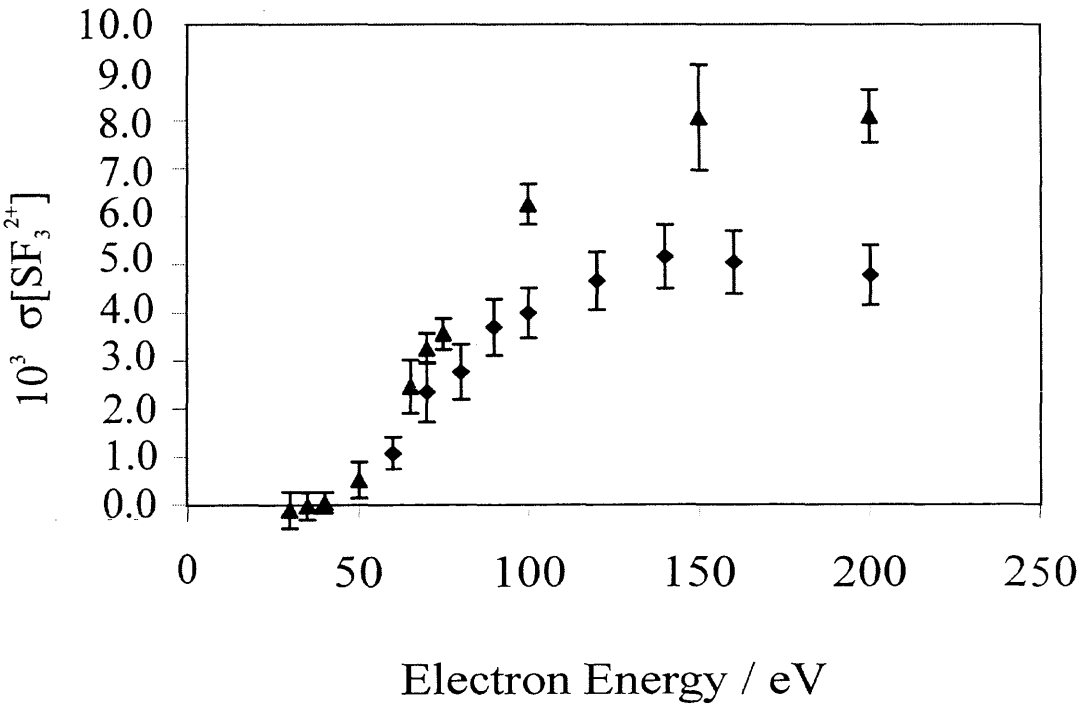


Figure 6.11: Relative precursor specific PICSs for forming $SF_3^{2+}$ *via* double ionization (▲) following electron ionization of $SF_6$. These cross-sections are expressed relative to the cross-section for forming $SF_5^+$. The error bars shown in the figure are standard deviations of multiple determinations. Relative PICSs extracted from Rejoub *et al*[6] (◆) are also shown with representative error bars.

A least squares fit procedure was used to estimate the appearance potential for the formation of $SF_3^{2+}$ using four data values of $\sigma_r[SF_3^{2+}]$ from 50-75 eV. This procedure yielded an estimate of 46±4 eV. The only other experimentally determined threshold for $SF_3^{2+}$ was 42.6 eV by Jochims *et al*,[18] with no error bars given. Subsequently, Lange *et al*[16] calculated the double ionization potential of the $3e_g$ orbital to be 42.6 eV. Therefore, the appearance potential estimated here is in agreement with other, more accurate, determinations available in the literature.[16,18]

Table 6.7: Relative precursor specific PICSs and relative PICSs following electron ionization of $SF_6$, see caption of Table 6.1 for further details.

| *E*/eV | $\sigma_r[SF_3^{2+}]$ |
|---|---|
| 200 | 0.008(1) |
| 150 | 0.008(1) |
| 100 | 0.006(1) |
| 75 | 0.004(1) |
| 70 | 0.003(1) |
| 65 | 0.002(1) |
| 50 | 0.001(1) |
| 40 | 0.000(1) |
| 35 | 0.000(1) |
| 30 | 0.000(1) |

### 6.5.9 $SF_2^{2+}$ formation

The values for $\sigma_r[SF_2^{2+}]$ we determine become significant above 50 eV and increase towards 200 eV, Figure 6.12. The values of $\sigma_3[SF_2^{2+}]$ derived here only become significant above 75 eV and increase towards 200 eV. The values of $\sigma_2[SF_2^{2+}]$, $\sigma_3[SF_2^{2+}]$ and $\sigma_r[SF_2^{2+}]$ are also displayed in Table 6.8.

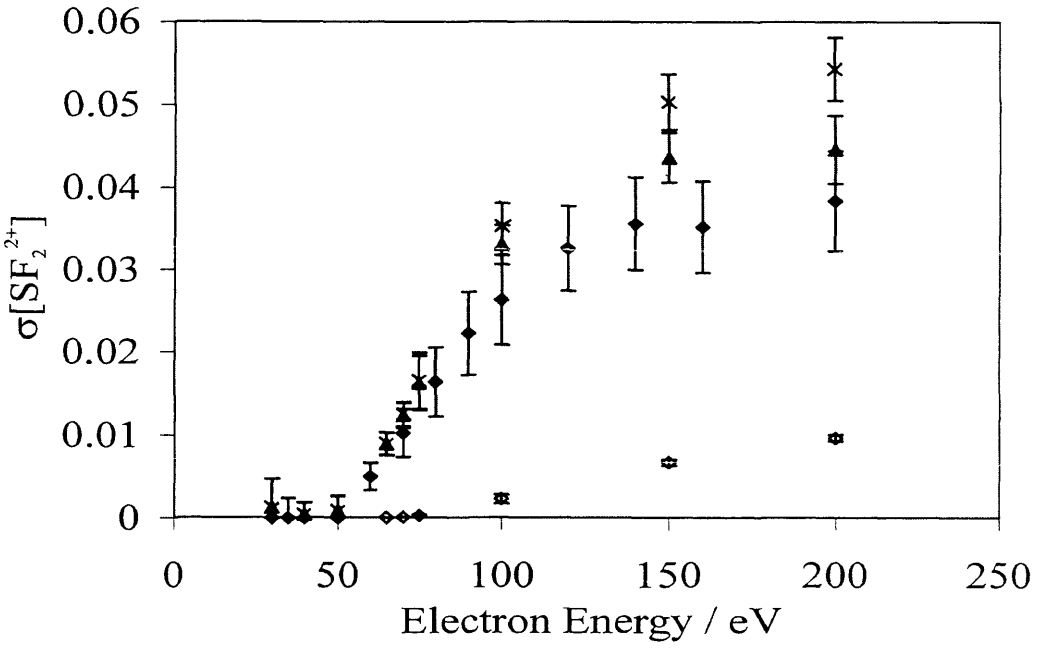


Figure 6.12: Relative precursor specific PICSs for forming $SF_2^{2+}$ *via* double (▲) and triple ionization (◇) following electron ionization of $SF_6$. The relative PICS is shown by (×). These cross-sections are expressed relative to the cross-section for forming $SF_5^+$. The error bars shown in the figure are standard deviations of multiple determinations. Relative PICSs from Rejoub *et al*[6] (◆) are also shown with representative error bars.

The values of $\sigma_r[SF_2^{2+}]$ determined here are in agreement with the values of $\sigma_r[SF_2^{2+}]$ derived from the data of Rejoub *et al*[6] below 150 eV. Above 100 eV the values of $\sigma_r[SF_2^{2+}]$ determined here are 40% greater than the $\sigma_r[SF_2^{2+}]$ values derived from the data of Rejoub *et al.*[6] This deviation appears to occur when the contribution from dissociative triple ionization becomes significant, as agreement between the $\sigma_2[SF_2^{2+}]$ values determined here and the $\sigma_r[SF_2^{2+}]$ values derived from the data of Rejoub *et al*[6] is observed. However, as discussed for the $SF_3^{2+}$ ion in Section 6.5.8, the errors associated with these smaller cross-sections may be greater than shown. Consequently, overall agreement between the values of $\sigma_r[SF_2^{2+}]$ determined here and the values of $\sigma_r[SF_2^{2+}]$ derived from the data of Rejoub *et al*[6] is indicated.

Table 6.8: Relative precursor specific PICSs and relative PICSs following electron ionization of $SF_6$, see caption of Table 6.1 for further details.

| *E*/eV | $\sigma_2[SF_2^{2+}]$ | $\sigma_3[SF_2^{2+}]$ | $\sigma_r[SF_2^{2+}]$ |
|---|---|---|---|
| 200 | 0.045(4) | 0.010(1) | 0.054(4) |
| 150 | 0.044(3) | 0.007(1) | 0.050(3) |
| 100 | 0.033(2) | 0.002(1) | 0.035(2) |
| 75 | 0.016(3) | 0.000(1) | 0.017(3) |
| 70 | 0.012(1) | 0.000(1) | 0.013(1) |
| 65 | 0.009(1) | 0.000(1) | 0.009(1) |
| 50 | 0.001(2) | 0.000(1) | 0.001(2) |
| 40 | 0.000(1) | 0.000(1) | 0.000(1) |
| 35 | 0.000(1) | 0.000(1) | 0.000(1) |
| 30 | 0.001(2) | 0.000(1) | 0.001(1) |

### 6.5.10 $SF^{2+}$ formation

Figure 6.13 shows the values of $\sigma_r[SF^{2+}]$ determined here increase towards 200 eV. The values of $\sigma_2[SF^{2+}]$ and $\sigma_3[SF^{2+}]$ both increase towards 200 eV. The values of $\sigma_3[SF^{2+}]$ are small and only become significant above an electron energy of 100 eV. The values of $\sigma_r[SF^{2+}]$ determined here are in agreement with the values of $\sigma_r[SF^{2+}]$ derived from the data of Rejoub *et al.*[6] The values of $\sigma_1[SF^{2+}]$, $\sigma_2[SF^{2+}]$ and $\sigma_r[SF^{2+}]$ are also displayed in Table 6.9.

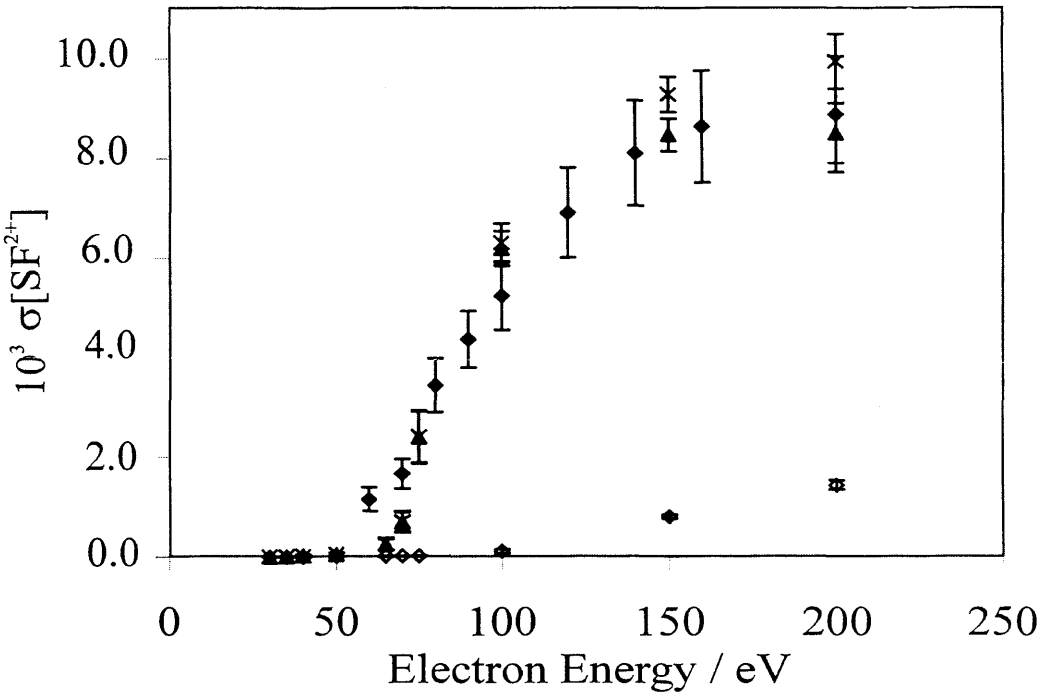


Figure 6.13: Relative precursor specific PICSs for forming $SF^{2+}$ *via* double (▲) and triple ionization (◇) following electron ionization of $SF_6$. The relative PICS is shown by (×). These cross-sections are expressed relative to the cross-section for forming $SF_5^+$. The error bars shown in the figure are standard deviations of multiple determinations. Relative PICSs extracted from Rejoub *et al*[6] (◆) are also shown with representative error bars.

Table 6.9: Relative precursor specific PICSs and relative PICSs following electron ionization of $SF_6$, see caption of Table 6.1 for further details.

| *E*/eV | $\sigma_2[SF^{2+}]$ | $\sigma_3[SF^{2+}]$ | $\sigma_r[SF^{2+}]$ |
|---|---|---|---|
| 200 | 0.009(1) | 0.001(1) | 0.010(1) |
| 150 | 0.008(1) | 0.001(1) | 0.009(1) |
| 100 | 0.006(1) | 0.000(1) | 0.006(1) |
| 75 | 0.002(1) | 0.000(1) | 0.002(1) |
| 70 | 0.001(1) | 0.000(1) | 0.001(1) |
| 65 | 0.000(1) | 0.000(1) | 0.000(1) |
| 50 | 0.000(1) | 0.000(1) | 0.000(1) |
| 40 | 0.000(1) | 0.000(1) | 0.000(1) |
| 35 | 0.000(1) | 0.000(1) | 0.000(1) |
| 30 | 0.000(1) | 0.000(1) | 0.000(1) |

## 6.6 Conclusions

Two-dimensional TOF mass spectrometry has been used to determine the relative PICSs and relative precursor specific PICSs for the formation of $F^+$, $SF^{2+}$, $S^+$, $SF_2^{2+}$, $SF_3^{2+}$, $SF^+$, $SF_4^{2+}$, $SF_2^+$, $SF_3^+$ and $SF_4^+$ relative to $SF_5^+$ from 30-200 eV. This is the first time that the contribution from single and triple ionization to the individual fragment ion yields has been quantified and the second time the contribution from double ionization to the individual fragment ion yields has been quantified following ionization of $SF_6$.

Comparison between the current data and a recent electron ionization study of $SF_6$ by Rejoub *et al*[6] was made. Good agreement between the current data and the relative PICSs derived from the data of Rejoub *et al*[6] was found for the formation of $F^+$, $SF^{2+}$, $S^+$, $SF_2^{2+}$, $SF_3^{2+}$, $SF^+$, $SF_4^{2+}$, $SF_2^+$, $SF_3^+$ and $SF_4^+$ ions.

The cross-section values derived for the formation of ion pairs from the data of Rejoub *et al*[6] were generally lower than the relative precursor specific PICS values for ion formation *via* dissociative double ionization determined here for $SF_3^+$, $SF_2^+$ and $SF^+$ ions. However, agreement was observed between the relative precursor specific PICSs for $F^+$ and $S^+$ formation *via* dissociative double ionization that were determined here, and the cross-section values for ion pair formation of the $S^+$ and $F^+$ (after addition of the $F^+ + F^+$ ion pair peak) ions derived from the data of Rejoub *et al.*[6]

The overall agreement found between the current relative PICSs determined here and the relative PICS values derived from the data of Rejoub *et al*[6] should provide additional confidence in these recently determined PICSs.

## 6.7 References


1 L. G. Christophorou and J. K. Olthoff, *J. Phys. Chem. Ref. Data* **29,** 267 (2000).

2 D. Rapp and P. Englander-Golden, *J. Chem. Phys.* **43,** 1464 (1965).

3 T. Stanski and B. Adamczyk, *Int. J. Mass Spectrom. Ion. Phys.* **46,** 31 (1983).

4 D. Margreiter, G. Walder, H. Deutsch, H. U. Poll, C. Winkler, K. Stephan, and T. D. Mark, *Int. J. Mass Spectrom. Ion Process.* **100,** 143 (1990).

5 M. Rao and S. Srivastava, Proc. 20th Int. Conf. on the Physics of Electronic and Atomic Collisions, (Vienna, 1997), pp. MO151.

6 R. Rejoub, D. R. Sieglaff, B. G. Lindsay, and R. F. Stebbings, *J. Phys. B-At. Mol. Opt. Phys.* **34,** 1289 (2001).

7 W. Hwang, Y.-K. Kim, and M. E. Rudd, *J. Chem. Phys.* **104,** 2956 (1996).

8 Y.-K. Kim and M. E. Rudd, *Comment At. Mol. Phys.* **34,** 309 (1999).

9 H. Deutsch, K. Becker, S. Matt, and T. D. Märk, *Int. J. Mass Spectrom.* **197,** 37 (2000).

10 H. Deutsch, K. Becker, and T. D. Märk, *Int. J. Mass. Spectrom. Ion. Process.* **167/168,** 503 (1997).

11 K. N. Joshipura, M. Vinodkumar, C. G. Limbachiya, and B. K. Antony, *Phys. Rev. A* **69,** 022705 (2004).

12 S. Pal, J. Kumar, and T. D. Märk, *J. Chem. Phys.* **120,** 4658 (2004).

13 V. H. Dibeler and F. L. Mohler, *J. Res. Natl. Bur. Stand.* **40,** 25 (1948).

14 A. P. Hitchcock and M. J. van der Wiel, *J. Phys. B-At. Mol. Opt. Phys.* **12,** 2153 (1979).

15 T. Masuoka and J. A. R. Samson, *J. Chem. Phys.* **75,** 4946 (1981).

16 M. Lange, O. Pfaff, U. Muller, and R. Brenn, *Chem. Phys.* **230,** 117 (1998).

17 T. A. Field and J. H. D. Eland, *Chem. Phys. Lett.* **211,** 436 (1993).

18 H. W. Jochims, E. Rühl, and H. Baumgärtel, BESSY jahresbericht, (Berlin, 1986).

19 L. J. Frasinski, M. Stankiewicz, K. J. Randall, P. A. Hatherly, and K. Codling, *J. Phys. B-At. Mol. Opt. Phys.* **19,** L819 (1986).

20 J. H. D. Eland and B. J. Treves-Brown, Dissociative and multiionization in molecules, (AIP Conference Proceedings, 1992), pp. 100.

21 J. H. D. Eland, F. S. Wort, P. Lablanquie, and I. Nenner, *Z. Phys. D-Atoms Mol. Clusters* **4,** 31 (1986).

22 J. H. D. Eland, *Mol. Phys.* **61,** 725 (1987).

23 S. Hsieh and J. H. D. Eland, *Rapid Commun. Mass Spectrom.* **9,** 1261 (1995).

24 Y. Sato, K. Ueda, H. Chiba, E. Shigemasa, and A. Yagishita, *Chem. Phys. Letts.* **196,** 475 (1992).

25 M. R. Bruce, C. Ma, and R. A. Bonham, *Chem. Phys. Lett.* **190,** 285 (1992).

26 D. A. Hagan and J. H. D. Eland, *Org. Mass Spectrom.* **27,** 855 (1992).

27 L. J. Frasinski, M. Stankiewicz, P. A. Hatherly, and K. Codling, *Meas. Sci. Technol.* **3,** 1188 (1992).

28 P. Calandra, C. S. S. O'Connor, and S. D. Price, *J. Chem. Phys.* **112,** 10821 (2000).

29 V. H. Dibeler and J. A. Walker, *J. Chem. Phys.* **44,** 4405 (1966).

30 A. P. Hitchcock, C. E. Brion, and M. J. van der Wiel, *J. Phys. B-At. Mol. Opt. Phys.* **11,** 3245 (1978).

31 M. R. Bruce, L. Mi, C. R. Sporleder, and R. A. Bonham, *J. Phys. B-At. Mol. Opt. Phys.* **27,** 5773 (1994).

32 A. H. Al-Nasir, M. A. Chaudhry, A. J. Duncan, R. Hippler, D. M. Campbell, and H. Kleinpoppen, *J. Phys. B-At. Mol. Opt. Phys.* **29,** 1849 (1996).

33 S. Feil, K. Gluch, P. Scheier, K. Becker, and T. D. Märk, *J. Chem. Phys.* **120,** 11465 (2004).

# Chapter 7

# Absolute electron ionization cross-sections of $N_2O$ and $C_2H_2$

## 7.1 Introduction

This chapter begins by presenting absolute PICSs and absolute precursor specific PICSs determinations for the $N^+$, $O^+$, $N_2^+$ and $NO^+$ fragment ions formed following electron interaction with nitrous oxide. These determinations serve to extend the previous analysis performed in Chapter 4, and thus form an ideal 'test' molecule to confirm the validity of the absolute PICS and absolute precursor specific PICS methodology. Subsequently, the absolute PICS and absolute precursor specific PICS determinations for the $H^+$, $C^+ + C_2^{2+}$, $CH^+ + C_2H_2^{2+}$, $C_2^+$ and $C_2H^+$ fragment ions formed following electron interaction with acetylene are presented. The methodology used to determine absolute PICSs and absolute precursor specific PICSs was previously described in Chapters 2 and 3.

Nitrous oxide was used as a 'test' case to confirm that the theory and methods described in Chapters 2 and 3 yield accurate absolute PICSs and absolute precursor specific PICSs over the ionizing electron energy range of 30-200 eV. The relative PICSs and relative precursor specific PICSs of nitrous oxide were presented and discussed in detail in Chapter 4. It is therefore satisfying to progress to determine absolute cross-section data. However, due to the shortened experimental runtimes necessary to minimise the gas pressure change over the experimental runtime only absolute PICSs and absolute precursor specific PICSs of $N^+$, $O^+$, $N_2^+$ and $NO^+$ fragment ions formed following electron interactions with $N_2O$ were determined.

Following the 'test' case of nitrous oxide, acetylene was selected as the new target gas for two experiments, one with argon as the reference gas, the other with nitrogen as the reference gas. Acetylene was chosen because of its widespread use in industry and its presence in planetary atmospheres and in the interstellar medium. These important aspects are further discussed in Section 7.5.

# Electron ionization of $N_2O$

## 7.2 Introduction

The motivation for investigating nitrous oxide is detailed in Chapter 4. It is appropriate to return to $N_2O$ to test the theory and methods for determination of absolute PICSs, described in Chapters 2 and 3. The use of $N_2O$ enables the extension of the data analysis to determine absolute precursor specific PICSs for the $N^+$, $O^+$, $N_2^+$ and $NO^+$ ions. The $N^+$, $O^+$, $N_2^+$ and $NO^+$ fragment ions were selected for this study, as these ions are the most abundant ions formed following electron ionization with $N_2O$, except for the parent monocation $N_2O^+$. The $N^{2+}$, $O^{2+}$ and $N_2O^{2+}$ ions formed following electron interaction with $N_2O$ were not suitable for investigation here due to the small cross-sections for their formation, as detailed in Chapter 4.

In Chapter 4, detailed comparisons were made between the $\sigma_r$ values determined here and $\sigma_r$ values derived from the absolute PICSs presented by Iga *et al*,[1] Lopez *et al*[2] and Lindsay *et al*.[3] The $\sigma_r$ values derived from the data of Lindsay *et al*[3] showed good agreement with the $\sigma_r$ values determined in Chapter 4 for the $N^+$, $O^+$, $N_2^+$ and $NO^+$ ions. However, the conclusions drawn in Chapter 4, regarding the $\sigma_r$ values derived from Iga *et al*,[1] and Lopez *et al*[2] suggested that energetic ion loss was occurring in the experiments of Iga *et al*[1] and Lopez *et al*.[2] The methodology used here to determine absolute PICSs and absolute precursor specific PICSs relies on the accurate determination of the absolute PICSs for formation of the parent ion. In the following sections good agreement is observed between the $\sigma'[N_2O^+]$ values determined here and the literature cross-section values for the parent ion. This agreement means that the absolute PICS and absolute precursor PICS values for the formation of the $N^+$, $O^+$, $N_2^+$ and $NO^+$ ions determined here will exhibit the same agreement with the literature cross-section values for the formation of each ion as observed in Chapter 4. Therefore, the conclusions discussed in Chapter 4, and mentioned above, will be mirrored in this chapter. The discussion presented in this chapter is therefore brief, with the emphasis being on the production of accurate absolute PICS and absolute precursor specific PICS values. Hence, in this chapter, no further discussion is presented on the behaviour of the cross-sections, or the comparison with the literature values as this was covered in detail in Chapter 4.

## 7.3 Experimental procedures

Following the conclusions reached in Chapters 2 and 3, argon was chosen as the reference gas. Argon has a similar molecular mass to nitrous oxide ($m/z$=40:$m/z$=44), giving a mass correction factor of 0.95 ($\sqrt{40}/\sqrt{44}$, from the square root of the molecular mass ratio). Argon was also chosen to ensure that there would be no interference between ion peaks produced in the singles and pairs spectra following electron interaction with argon and nitrous oxide.

The argon used in these experiments was purchased from BOC with a purity of 99.5%. The nitrous oxide was purchased from Aldrich with a purity of 99.9%, enabling both gases to be used without further purification.

The modified experimental methodology derived in Section 3.2.1 to 3.2.3 of Chapter 3, was further tested for the determination of $\sigma'[N_2O^+]$ values. Firstly, the experimental conditions involved the introduction of both gases through the gas inlet needles into the source region with various gas pressures. Under these experimental conditions a complete set of data was collected and analysed, and values of $\sigma'[N_2O^+]$ were determined. The second experiment then involved the introduction of both gases through the re-located PTFE tubing, designed to produce a more uniform gas mixture in the source region, (discussed in Chapter 3, for the $N_2$/Ar absolute PICS experiments) with a gas pressure ratio of approximately 1:1. Again, under these experimental conditions a complete set of data was collected and analysed, and values of $\sigma'[N_2O^+]$ were determined. From the $\sigma'[N_2^+]$ values determined for the $N_2$/Ar absolute PICS experiments, discussed in Chapter 3, the second determination of $\sigma'[N_2O^+]$ values was expected to show improvement in accuracy and reproducibility of the data values.

Following the determination of $\sigma'[N_2O^+]$ values, detailed above, the absolute PICSs and absolute precursor specific PICSs for the $N^+$, $O^+$, $N_2^+$ and $NO^+$ ions were determined using the re-located PTFE tubing and a gas pressure ratio of approximately 1:1. These results are presented and discussed in the following sections.

## 7.4 Data Analysis

Singles and pairs spectra were recorded at ionizing electron energies between 30-200 eV. The intensities of the ions observed in the singles and pairs spectra were processed as described in Chapter 3. The pressures of argon and nitrous oxide were

determined, as described in Chapter 3, and the values of $\sigma'[Ar^+]$ were taken from the literature of Straub *et al*,[4] as discussed in Chapter 3.

The absolute PICS and absolute precursor specific PICS values determined here are shown as the average of four individual cross-section determinations. The error presented with these values is the standard deviation of the four individual cross-section determinations. The standard deviation is a better representation of the 'true' error resulting from fluctuations in the experimental apparatus between cross-section determinations.

## 7.4.1 Absolute PICSs for $N_2O^+$

### 7.4.1.1 Singles spectrum

Using Ar and $N_2O$ simultaneously produces a singles spectrum with $N^{2+}$, $O^{2+}$, $N^+$, $O^+$, $Ar^{2+}$, $N_2O^{2+}$, $N_2^+$, $NO^+$, $Ar^+$ and $N_2O^+$ ion peaks, shown in Figure 7.1. The singles spectrum also contains small ion signals resulting from traces of air, water and hydrocarbon residues, present as background gas in the apparatus. The singles spectra were recorded between 30-200 eV.

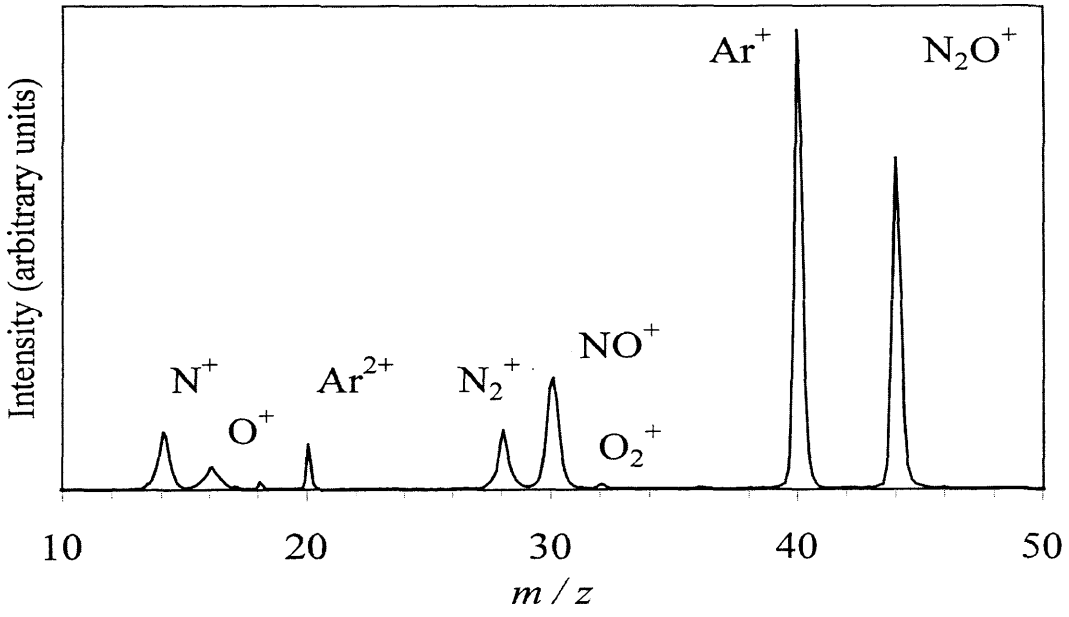


Figure 7.1: A typical singles spectrum for the electron ionization of argon and nitrous oxide at 200 eV. Residual gas peaks are observed at *m/z*=18, 32, 36, 45 and 46 and are attributed to $H_2O^+$, $O_2^+$ and hydrocarbon residues respectively.

The intensities of the $Ar^+$ and $N_2O^+$ ion peaks were determined as described in

Chapter 3. As these ions are not observed in the pairs spectra, $I[Ar^+]=S[Ar^+]$ and $I[N_2O^+]=S[N_2O^+]$. As detailed in Chapter 3, and shown in Eq. (7.1), when each parameter on the right hand side of Eq. (7.1) is determined, over the ionizing electron energy range, the values for $\sigma'[N_2O^+]$ can be determined:

$$\sigma'[N_2O^+] = \frac{S(N_2O^+)}{S(Ar^+)} \times \frac{p_{Ar}}{p_{N_2O}} \times \sigma'[Ar^+] \qquad (7.1).$$

The values for $\sigma'[N_2O^+]$ are displayed in Figure 7.2 and are detailed in Table G.1 of Appendix G.

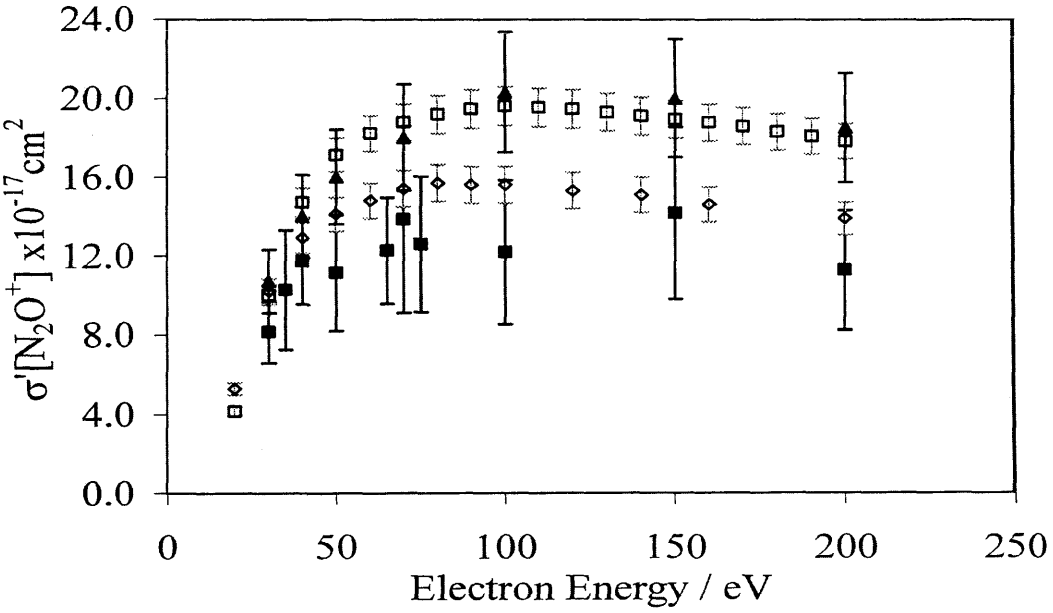


Figure 7.2: Values determined for $\sigma'[N_2O^+]$ (■). This data is compared with recently determined absolute PICSs for $N_2O^+$ of Iga *et al*[1] (□), Lopez *et al*[2] (▲) and Lindsay *et al*[3] (◇), each shown with the appropriate error.

As shown in Figure 7.2, the $\sigma'[N_2O^+]$ values determined here show agreement with the absolute PICS data of Lindsay *et al*[3] within the mutual error limits. As the absolute PICS data of Lindsay *et al*[3] are regarded as the most reliable data, this agreement provides confidence that the technique for determining absolute PICSs is sound. However, as discussed for the $Ar/N_2$ system, in Chapter 3, a significant spread in $\sigma'[N_2O^+]$ values is observed and the values of $\sigma'[N_2O^+]$ determined here are lower than the absolute PICS data of Lindsay *et al.*[3] As discussed in Chapter 3, the deviation in the $\sigma'[N_2O^+]$ values is thought to result from the gases not forming a uniform mixture prior to ionization. This results from the introduction of both gases through the gas inlet needles into the source region and the use of different gas pressure ratios

for each experiment. In the following section the $\sigma'[N_2O^+]$ values were determined again utilising the re-located PTFE tubing and a gas pressure ratio of approximately 1:1 for each experiment.

### 7.4.1.2 Gas pressure ratio and gas flow

To address the deviations in the $\sigma'[N_2O^+]$ values determined here, shown by the error bars in Figure 7.2, a more uniform gas mixture is required in the source region. This was achieved by using an argon and nitrous oxide gas pressure ratio of approximately 1:1, and by introducing the argon and nitrous oxide gas into the source region *via* the re-located PTFE tubing, discussed in Chapter 3. Using these experimental conditions, the $\sigma'[N_2O^+]$ values were re-determined and are displayed in Figure 7.3.

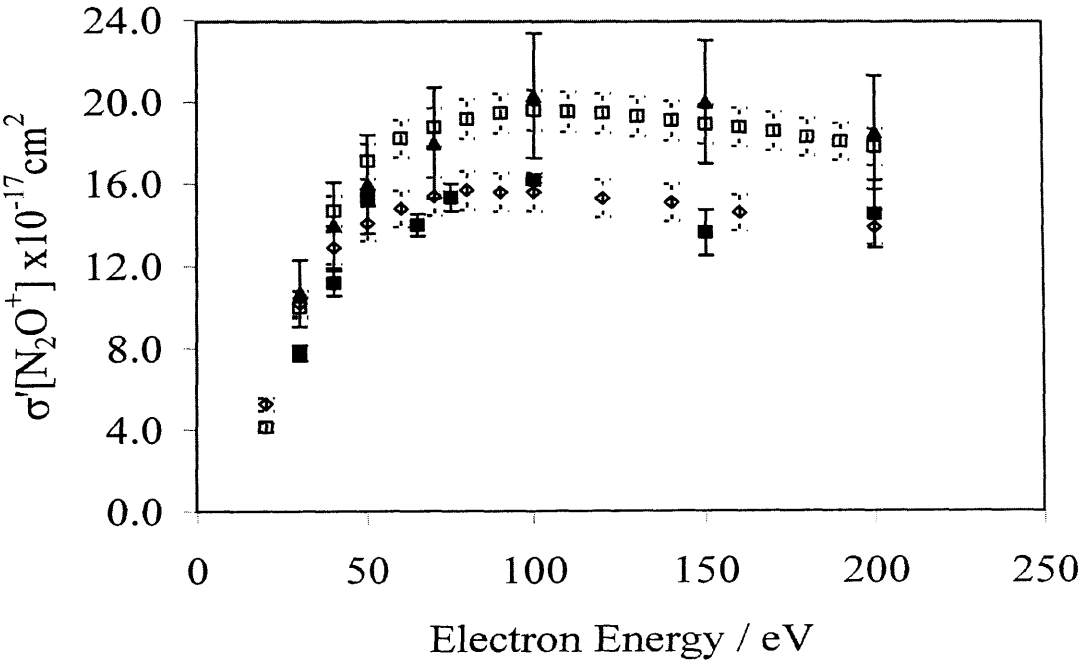


Figure 7.3: Values determined for $\sigma'[N_2O^+]$ (■). This data is compared with recently determined absolute PICSs for $N_2O^+$ of Iga *et al*[1] (□), Lopez *et al*[2] (▲) and Lindsay *et al*[3] (◇), each shown with the appropriate error.

With reference to Figure 7.3, the agreement seen between the $\sigma'[N_2O^+]$ values determined currently and the absolute PICS data of Lindsay *et al*[3] is improved. Additionally, the standard deviation (displayed as error bars) observed for the $\sigma'[N_2O^+]$ values is significantly decreased from Figure 7.2 to Figure 7.3. These results confirm that a more uniform gas mixture is produced by allowing the gases to 'mix' in

the chamber before entering the source region and to a pressure ratio of approximately 1:1, as previously concluded for the $Ar/N_2$ system in Chapter 3. The values of $\sigma'[N_2O^+]$ currently determined are displayed in Table 7.1.

Table 7.1: Values determined for $\sigma'[N_2O^+]$ at each electron energy *E*. The error in the last figure is shown in parentheses. This error is the standard deviation of four individual cross-section determinations.

| *E*/eV | $\sigma'[N_2O^+]$ ($x10^{-17}cm^2$) |
|---|---|
| 200 | 14.5 (17) |
| 150 | 13.6 (11) |
| 100 | 16.2 (1) |
| 75 | 15.3 (7) |
| 65 | 14.0 (5) |
| 50 | 15.4 (4) |
| 40 | 11.2 (6) |
| 30 | 7.8 (4) |

As discussed in Section 7.2, the methodology used to determine absolute PICSs and absolute precursor specific PICSs relies on the accurate determination of the absolute PICSs for formation of the parent ion of the system. The data values obtained above provide additional confidence regarding the 'necessary' experimental conditions required to determine accurate absolute cross-section values. These experimental conditions are summarised below together with the methodology used to determine absolute PICSs and absolute precursor specific PICSs.

#### 7.4.1.3 Conclusions

By modifying the experimental technique to use a 1:1 gas pressure ratio and the re-located gas inlets, the determined values of $\sigma'[N_2O^+]$ show agreement with reliable literature data and improved reproducibility. Consequently, in the following sections the same experimental techniques are employed to determine the absolute PICSs and absolute precursor specific PICSs for the $N^+$, $O^+$, $N_2^+$ and $NO^+$ ions formed following electron interaction with $N_2O$.

### 7.4.2 Absolute PICSs for $N^+$, $O^+$, $N_2^+$ and $NO^+$ ions

The same data analysis methods, discussed in detail in Chapter 3, and used to determine the $\sigma'[N_2O^+]$ values, are used to determine the absolute PICSs for the $N^+$, $O^+$, $N_2^+$ and $NO^+$ ions formed following electron ionization of $N_2O$, Eq. (7.2):

$$\sigma'[X^+] = \frac{S(X^+)}{S(Ar^+)} \times \frac{p_{Ar}}{p_{N_2O}} \times \sigma'[Ar^+] \qquad (7.2).$$

$$\text{where } \sigma'[X^+] = \frac{I[X^+] + P[X^+]}{I[Ar^+]} \times \frac{p_{Ar}}{p_{N_2O}} \times \sigma'[Ar^+]$$

This method is termed 'direct'. With reference to Eq. (7.2), the total ion signal $S$ for the $N^+$, $O^+$, $N_2^+$ and $NO^+$ fragment ions is determined using the ion intensities recorded in the singles and pairs spectra. The pairs spectra recorded following electron ionization of the $Ar/N_2O$ two-gas system is identical to that presented in Chapter 4, and was analysed as described in Chapters 3 and 4.

There are in fact two methods by which the absolute PICSs for the $N^+$, $O^+$, $N_2^+$ and $NO^+$ ions can be determined, a 'direct' method, discussed above, and an 'indirect' method. The indirect method involves determination of the relative PICSs for the formation of the fragment ion $X^+$, symbolized as $\sigma_r[X^+]$, where the cross-section for the formation of $X^+$ is expressed relative to the cross-section for forming the parent ion. The $\sigma_r[X^+]$ values are then multiplied by the $\sigma'[N_2O^+]$ values we determine, as demonstrated in Eq. (7.3). This 'indirect' methodology is shown below:

$$\sigma'[X^+] = \sigma_r[X^+] \times \sigma'[N_2O^+] \qquad (7.3).$$

$$\sigma'[X^+] = \frac{\sigma[X^+]}{\sigma[N_2O^+]} \times \sigma'[N_2O^+]$$

$$\sigma'[X^+] = \frac{I[X^+] + P[X^+]}{I[N_2O^+]} \times \frac{I[N_2O^+]}{I[Ar^+]} \times \frac{p_{Ar}}{p_{N_2O}} \times \sigma'[Ar^+]$$

As demonstrated above, both analysis methods are equivalent and therefore produce the same absolute PICS determinations. In this chapter the 'direct' analysis method was used to determine the absolute PICSs for each fragment ion. Data analysis equations for the $N^+$, $O^+$, $N_2^+$ and $NO^+$ ions are given in Appendix F.

### 7.4.3 Absolute precursor specific PICSs for $N^+$, $O^+$, $N_2^+$ and $NO^+$ ions

As described in Chapter 3, to determine the absolute precursor specific PICSs for the formation of the $N^+$, $O^+$, $N_2^+$ and $NO^+$ ions *via* single and double ionization, the

relative precursor specific PICSs for the formation of the $N^+$, $O^+$, $N_2^+$ and $NO^+$ ions *via* single and double ionization must first be determined. The relative precursor specific PICSs for formation of a fragment ion $X^+$ *via* single and double ionization are symbolized as $\sigma_n[X^+]$ ($n$=1,2), and are expressed relative to the cross-section for forming the parent ion of the system. These $\sigma_n[X^+]$ values are then multiplied by $\sigma'[N_2O^+]$, previously determined in Section 7.4.1. As shown in Eqs. (7.4) and (7.5), the absolute precursor specific PICS can then be derived and are symbolized by $\sigma_n'[X^+]$ ($n$=1,2):

$$\sigma_1'[X^+] = \frac{\sigma_1[X^+]}{\sigma_1[N_2O^+]} \times \sigma'[N_2O^+] \quad (7.4),$$

$$\sigma_2'[X^+] = \frac{\sigma_2[X^+]}{\sigma_1[N_2O^+]} \times \sigma'[N_2O^+] \quad (7.5).$$

As detailed in Chapter 3, the values of $\sigma_n[X^+]$ can only be determined if a value for the ion detection efficiency, $f_i$, is available. The determination of $f_i$ is shown below in Section 7.4.3.1.

It should also be noted that for each ionizing electron energy the sum of the $\sigma_n'[X^+]$ values, for a particular fragment ion $X^+$, is equal to the value of $\sigma'[X^+]$.

The triples data required to quantify the yield of these fragment ions from triple ionization were not recorded as a consequence of the shortened runtimes, used to minimise gas pressure changes over the experimental runtime. As detailed in Chapters 2 and 3, the triples collection was small even over the significant runtimes used in the data collection of relative PICSs and relative precursor specific PICSs. Therefore, the neglect of the triple and higher levels of ionization is appropriate within the accuracy of the absolute cross-sections reported in this chapter.

### 7.4.3.1 Ion detection efficiency

As discussed in Chapter 3, to enable $\sigma_n[X^+]$ values to be derived, and hence $\sigma_n'[X^+]$ values to be determined, a value for $f_i$ is derived by recording the singles and pairs spectra following ionization of $CF_4$. This procedure resulted in a value of $f_i$=0.17±0.02, in agreement with determinations made in Chapters 4-6.

## 7.4.4 Discussion

Using the data analysis described in Sections 7.4.2 and 7.4.3, the absolute PICSs and absolute precursor specific PICSs were determined for the $N^+$, $O^+$, $N_2^+$ and $NO^+$ fragment ions from 30-200 eV. The absolute PICS data exhibit agreement with the absolute PICSs of Lindsay *et al*[3] within the mutual error limits for each fragment ion studied here. As expected poorer agreement is observed between the absolute PICSs of Iga *et al*[1] and Lopez *et al*[2] especially for the $N^+$ and $O^+$ fragment ions. These results are displayed in Figure 7.4-Figure 7.7 and the values are given in Appendix G. These results are in accord with the discussion presented in Chapter 4 and thus no further discussion is presented in this section.

### 7.4.4.1 $N^+$ formation

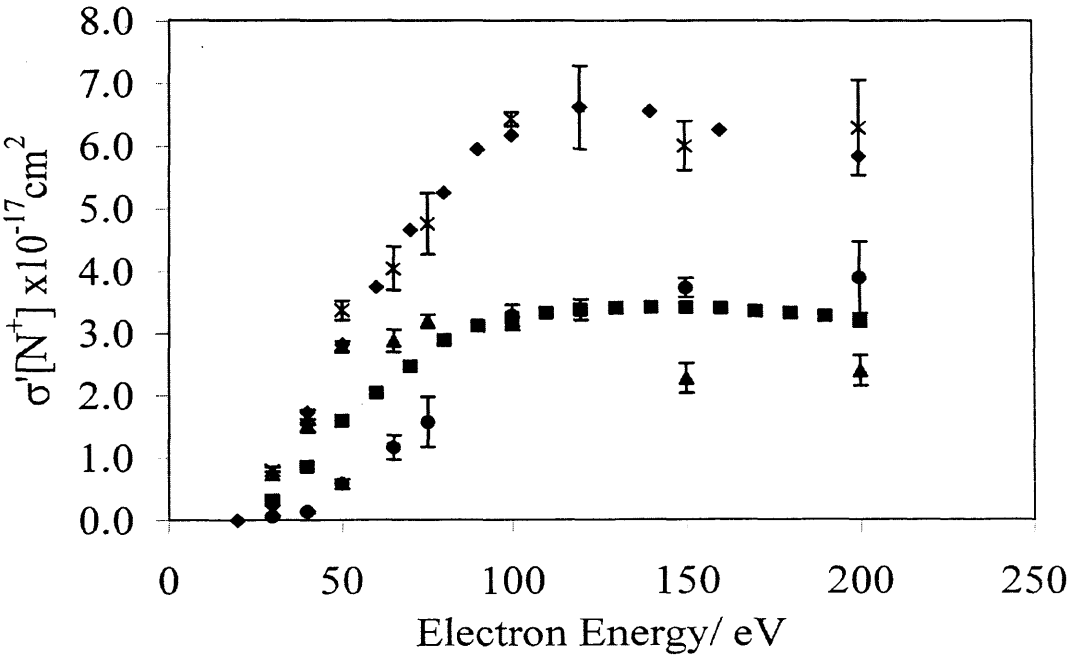


Figure 7.4: Values determined for $\sigma'[N^+]$ (×), $\sigma_1'[N^+]$ (▲) and $\sigma_2'[N^+]$ (●). This data is compared with recently determined absolute PICSs for $N^+$ of Iga *et al*[1] (■) and Lindsay *et al*[3] (◆), with representative error bars shown at 120 eV.

### 7.4.4.2 $O^+$ formation

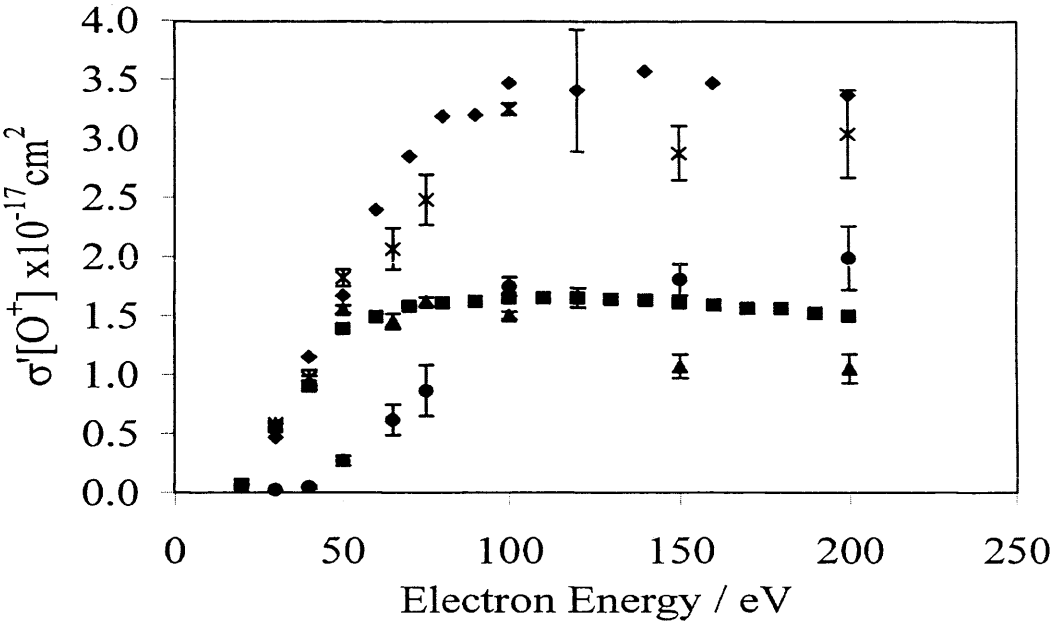


Figure 7.5: Values determined for $\sigma'[O^+]$ (×), $\sigma_1'[O^+]$ (▲) and $\sigma_2'[O^+]$ (●). This data is compared with recently determined absolute PICSs for $O^+$ of Iga *et al*[1] (■) and Lindsay *et al*[3] (◆), with representative error bars shown at 120 eV.

### 7.4.4.3 $N_2^+$ formation

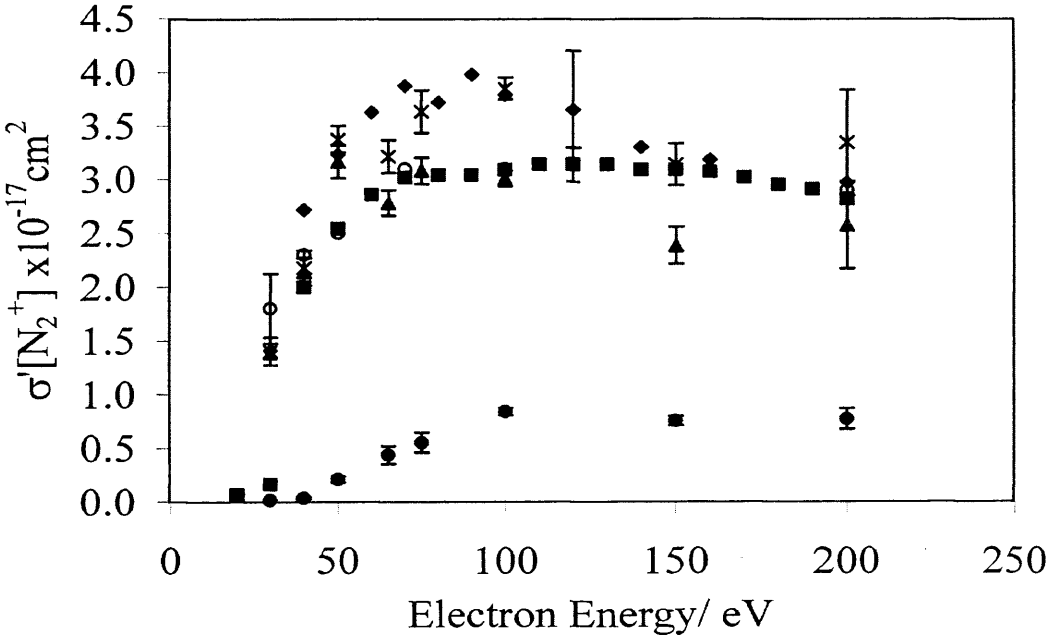


Figure 7.6: Values determined for $\sigma'[N_2^+]$ (×), $\sigma_1'[N_2^+]$ (▲) and $\sigma_2'[N_2^+]$ (●). This data is compared with recently determined absolute PICSs for $N_2^+$ of Iga *et al*[1] (■), Lopez *et al*[2] (○) and Lindsay *et al*[3] (◆), where error bars are shown at 120 eV, 150 eV and 120 eV respectively.

#### 7.4.4.4 $NO^+$ formation

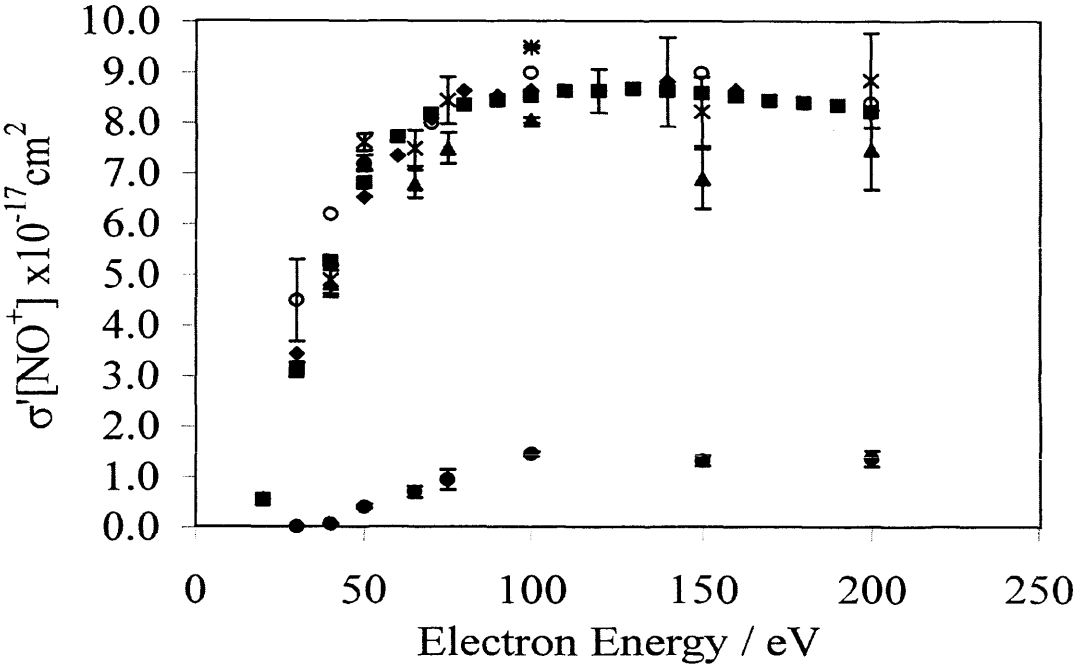


Figure 7.7: Values determined for $\sigma'[NO^+]$ (×), $\sigma_1'[NO^+]$ (▲) and $\sigma_2'[NO^+]$ (●). This data is compared with recently determined absolute PICSs for $NO^+$ of Iga *et al*[1] (■), Lopez *et al*[2] (○) and Lindsay *et al*[3] (◆). Representative error bars are shown at 120 eV, 150 eV and 120 eV for the data of Iga *et al*,[1] Lopez *et al*[2] and Lindsay *et al*.[3]

## 7.4.5 Conclusions

The absolute PICSs and absolute precursor specific PICSs determined for the $N^+$, $O^+$, $N_2^+$ and $NO^+$ ions show agreement when compared to the absolute PICS data of Lindsay *et al*.[3] These results confirm the conclusions made in Chapter 4 for the electron ionization of $N_2O$ and reaffirm the conclusions, made in Chapter 3, that using a gas pressure ratio of 1:1 and re-locating the gas inlets produces accurate and reproducible absolute cross-sections over the ionizing electron energy range studied here.

The following sections detail the determination of absolute PICSs and absolute precursor specific PICSs of selected fragment ions formed following electron interaction with $C_2H_2$.

# Electron ionization of $C_2H_2$

## 7.5 Introduction

Acetylene is the simplest molecule among the hydrocarbons and has $D_{\infty h}$ symmetry. The acetylene molecule is industrially important due largely to its unique molecular structure which produces a high resultant enthalpy of formation and higher than normal combustion temperature.[5] These attributes make $C_2H_2$ widely used for welding and cutting in high temperature flames. Acetylene is also used in the semiconductor industry for the deposition of diamond film.[6] Also, fusion plasma devices regularly use graphite for the inner walls to reduce radiation loss and hydrocarbon products are produced at these walls. Recent studies have demonstrated that the conditions at the region close to these walls (plasma edge) play an important role in achieving, sustaining and controlling thermonuclear fusion plasmas.[7-9] In order to understand the processes occurring in the plasma edge region, and the effect on plasma properties and conditions, it is essential to have quantitative data regarding these processes. The world-wide industrial use of acetylene makes the determination of electron ionization cross-sections of vital importance to enable the processes described above to be streamlined to provide optimum performance in a cost effective manner.

Acetylene is present in planetary atmospheres and the interstellar medium.[10] Distinctive features, characteristic of acetylene, were first recorded in vacuum ultraviolet (VUV) spectra of the atmospheres of Saturn,[11] and later in the atmosphere of Titan,[12] Uranus[13] and Jupiter.[14] In fact, the concentration of acetylene within the Earth's atmosphere is increasing and is expected to double by 2030 because of increasing car useage.[15] To enable the accurate modelling of acetylene in these various planetary atmospheres it is again essential that accurate electron ionization cross-sections are determined.

Electron ionization of acetylene was first studied in 1932 by Tate *et al.*[16] In 1995 Davister and Locht[17-20] produced detailed literature regarding the translational energy distributions and appearance energies of some of the fragment ions formed following the electron ionization of $C_2H_2$. Recently, Feil *et al*[21] utilised a Nier-type electron ionization source to investigate the initial ion kinetic energy distribution of various ions formed from electron ionization of $C_2H_2$.

Concentrating only on previous electron ionization studies of $C_2H_2$, a brief

review of the available experimental electron ionization cross-section data is now presented. Electron ionization cross-sections for the formation of various fragment ions have been determined by Gaudin and Hagemann[22] with a magnetic sector instrument from 100-2000 eV and with a quadrupole mass spectrometer (QMS) and TOF mass spectrometer from threshold to 800 eV by Zheng and Srivastava.[10] The most recent electron ionization study of $C_2H_2$ was conducted by Tian and Vidal[23] using a TOF mass spectrometer, designed to allow complete ion collection from threshold to 600 eV. There is a lack of agreement between the recent cross-section data of Tian and Vidal[23] and the data of Gaudin and Hagemann[22] and Zheng and Srivastava.[10] The latter utilised experiments that may miss some energetic ions formed following electron ionization of $C_2H_2$. Therefore additional cross-section measurements are needed, and this provides the motivation for the current electron ionization study of $C_2H_2$.

## 7.6 Experimental procedures

The acetylene used in these experiments was purchased from BOC with a purity of >98.5% and contained acetone to stablise the gas. Several attempts to minimise the quantity of acetone present in the spectra were made using an acetonitrile slush bath. A trap, packed with glass beads, was filled with nitrogen gas and was allowed to cool for several hours in the acetonitrile slush bath. The acetylene gas was then slowly run through the trap to liquefy the acetone. Using this method, the intensities of acetone (*m/z*=58) and $CH_3CO^+$ (*m/z*=43) were decreased by approximately 40%, whilst the intensity of the $H^+$, $H_2^+$, $C^+ + C_2^{2+}$, $CH^+ + C_2H_2^{2+}$, $C_2^+$, $C_2H^+$ and $C_2H_2^+$ ion peaks remained unchanged. The experiments, detailed below, were therefore performed using the $C_2H_2$ without any further purification.

Experiments were performed to produce determinations of the absolute PICSs and absolute precursor specific PICSs following electron interaction with $C_2H_2$, using both $N_2$ and Ar as reference gases.[4,24] The experimental modifications utilised for the $N_2$/Ar and $N_2O$/Ar two-gas systems should ensure that either reference gas enables accurate absolute PICSs and absolute precursor specific PICSs to be determined. The absolute PICSs and absolute precursor specific PICSs determined using either reference gas are displayed on the same figure to facilitate easy comparison. Both experiments utilised gas introduction *via* the re-located PTFE tubing in the source region and a gas pressure ratio of 1:1.

Following electron ionization of $C_2H_2$ the $H^+$ fragment ion is observed in the singles spectrum. However, $H^+$ ions are also formed *via* sources such as $H_2O$, acetone, and $H_2$ produced by hydrocarbons on the filament, which are also observed in the singles spectrum. The intensity of $H^+$ ions produced from these other sources fluctuates from experiment to experiment, and hence, quantification and subsequent accurate correction is difficult. The intensity of $H^+$ ions from these other sources is estimated by recording air spectra between 30-200 eV. The intensities of the $H^+$ and $H_2O^+$ ions in the air spectra were determined and normalised to the intensity of the $H_2O^+$ ion peak observed in the $C_2H_2$ spectra at each electron energy. The estimated intensity of $H^+$ ions from other sources is subtracted from the $H^+$ intensity recorded in the singles spectrum to produce a more accurate $H^+$ fragment ion intensity from the electron ionization of $C_2H_2$. As a result of using the 'corrected' $H^+$ ion intensity in the determination of the $\sigma'[H^+]$ and $\sigma_1'[H^+]$ values, these values therefore have a larger associated error.

## 7.7 Data Analysis

Singles and pairs spectra were recorded at ionizing electron energies between 30-200 eV. The intensities of the ions observed in the singles and pairs spectra were processed as described in Chapter 3. As discussed in Chapter 3, any contribution from triple ionization is assumed to be negligible in the current analysis of absolute cross-sections.

The values of the absolute PICS and absolute precursor specific PICS shown in the following sections represent the average of four individual cross-section determinations. The error shown with these values represents the standard deviation of the four individual cross-section determinations.

### 7.7.1 Singles spectrum

Singles spectra of the $Ar/C_2H_2$ and $N_2/C_2H_2$ systems were recorded between 30-200 eV. The $H^+$, $H_2^+$, $C^+ + C_2^{2+}$, $CH^+ + C_2H_2^{2+}$, $C_2^+$, $C_2H^+$ and $C_2H_2^+$ fragment ions were observed with the $N^{2+}$, $N^+$, $N_2^+$, $Ar^{2+}$ and $Ar^+$ fragment ions from the reference gases ($N_2$ and Ar), see Figure 7.8 and Figure 7.9. The intensity $I[X^+]$ of the ion peaks was determined as described in Chapter 3.

With reference to Figure 7.8 and Figure 7.9, both singles spectra contain small ion signals resulting from traces of air, water, hydrocarbon residues and acetone, present as background gas in the apparatus and in the acetylene gas.

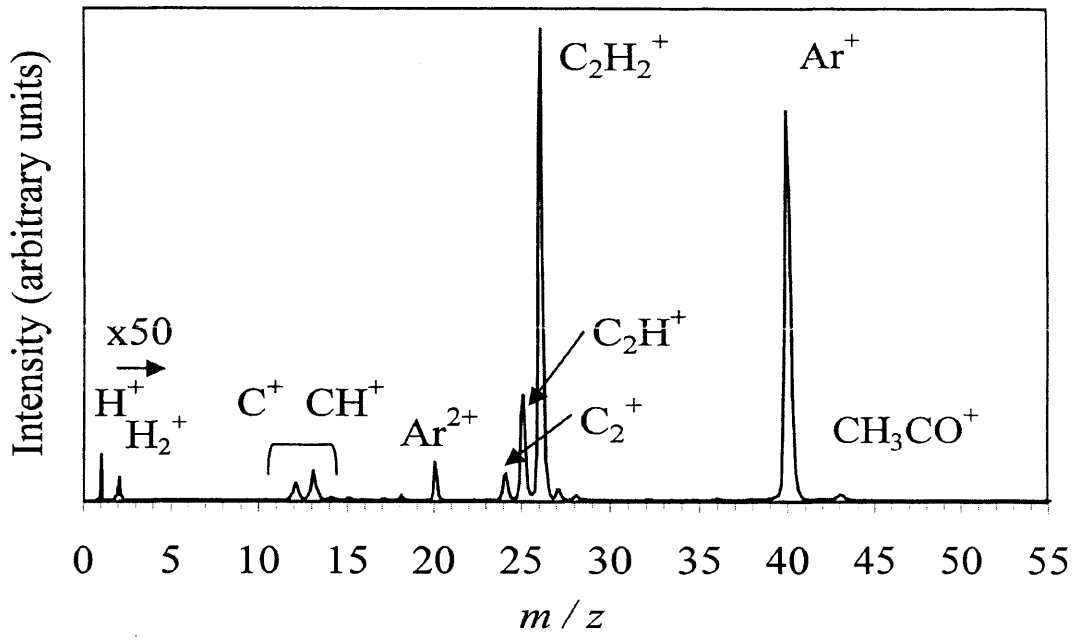


Figure 7.8: Typical singles spectrum for the electron ionization of acetylene and argon at 200 eV. Residual gas peaks are observed at *m/z*=14, 15, 16, 17, 18, 27, 29, 32, 36 and 43 are attributed to $H_2O^+$, $O_2^+$, hydrocarbon residues and acetone. It should be noted that *m/z*=1.5 to 2.5 is expanded by a factor of 50.

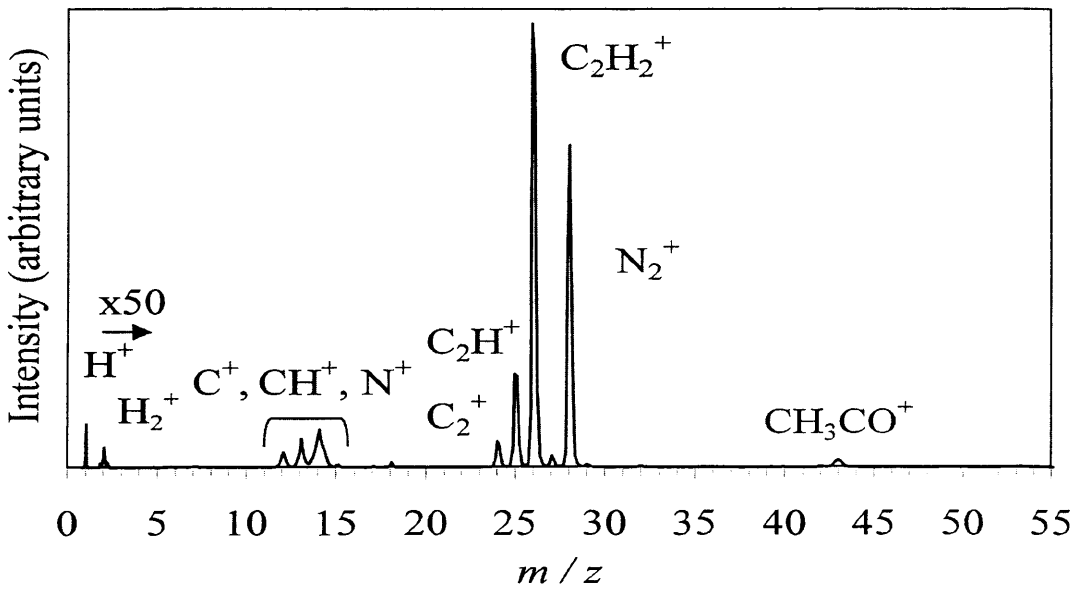


Figure 7.9: Typical singles spectrum for the electron ionization of acetylene and nitrogen at 200 eV. Residual gas peaks are observed at *m/z*=15, 16, 17, 18, 27, 29, 32 and 43 are attributed to $H_2O^+$, $O_2^+$, hydrocarbon residues and acetone. It should be noted that *m/z*=1.5 to 2.5 is expanded by a factor of 50.

The ion peaks observed at *m/z*=12 and 13 are both the combination of a cation and dication peak, and cannot be resolved because they have the same mass number: $C^+ + C_2^{2+}$ and $CH^+ + C_2H_2^{2+}$. The intensities of $C^+ + C_2^{2+}$ and $CH^+ + C_2H_2^{2+}$ ions, recorded in the singles spectra, can therefore only be expressed as a summation of the cation and dication peak intensity; $I[C^+ + C_2^{2+}]$ and $I[CH^+ + C_2H_2^{2+}]$ However, by using the definitions above, a problem arises with the data processing because the $C^+$ and $CH^+$ ions observed in the singles spectrum are formed *via* single ionization, but the $C_2^{2+}$ and $C_2H_2^{2+}$ dications are formed *via* double ionization. Therefore, the intensity summations cannot be used to determine the individual absolute precursor specific PICSs for formation of $C^+$ and $CH^+$ *via* single ionization and for formation of $C_2^{2+}$ and $C_2H_2^{2+}$ *via* double ionization. In this chapter the notation $\sigma_1'[C^+ + C_2^{2+}]$ and $\sigma_1'[CH^+ + C_2H_2^{2+}]$ is replaced by $\sigma_{12}'[C^+ + C_2^{2+}]$ and $\sigma_{12}'[CH^+ + C_2H_2^{2+}]$, to clarify that these cross-sections have contributions from both single and double ionization, although the majority of the $\sigma_{12}'[C^+ + C_2^{2+}]$ and $\sigma_{12}'[CH^+ + C_2H_2^{2+}]$ values will originate from the formation of the $C^+$ and $CH^+$ ions *via* single ionization, as the $\sigma_2'[C_2^{2+}]$ and $\sigma_2'[C_2H_2^{2+}]$ values are very much smaller than the $\sigma_1'[C^+]$ and $\sigma_1'[CH^+]$ values. Unfortunately, this problem cannot be mathematically resolved using the current experimental data, but may be addressed in the future by performing an isotopic experiment using $C_2HD$.

Electron ionization experiments by Locht *et al*[25] emphasise the use of low pressure ($<10^{-6}$ Torr) whilst investigating $C_2H_2$. At higher pressures Locht *et al*[25] observed an ion peak at *m/z*=50, thought to originate from dimeric ions which may also lead to the observation of additional $C_2H^+$ ions. The experimental conditions used for these experiments involve low target gas pressure ($<10^{-6}$ Torr) and therefore with reference to Figure 7.8 and Figure 7.9 as expected, no ion peak is observed at *m/z*=50. The absence of an ion peak at *m/z*=50 provides additional confidence in the accuracy of the $C_2H^+$ ion intensity recorded in the singles spectra following electron ionization of $C_2H_2$.

The absolute PICSs and absolute precursor specific PICSs determined using the $Ar/C_2H_2$ and $N_2/C_2H_2$ systems are compared to available absolute PICS data of Zheng and Srivastava[10] and Tian and Vidal.[23] Tian and Vidal[23] determine absolute PICSs by normalising their data to the recently published absolute PICSs for argon of Straub *et al.*[4] The experimental apparatus used by Tian and Vidal[23] allows separate experiments to be performed for the reference gas and the gas under investigation, as

discussed in Chapter 3. The absolute PICS data of Tian and Vidal[23] also shows complete collection of all the ions and therefore must be considered as the most reliable cross-sections. The absolute PICS data of Zheng and Srivastava[10] may be missing energetic ions due to the use of a QMS to collect some of the fragment ions.

With reference to Figure 7.8 and Figure 7.9 the $H_2^+$ ion peak observed is small. The intensity of the $H_2^+$ ion peak is approximately 0.1% of the intensity of the $C_2H_2^+$ ion peak at 200 eV, and thus the absolute PICS for formation of the $H_2^+$ ion would be approximately 2.4-2.7x$10^{-19}$ $cm^2$ at 200 eV. This conclusion is mirrored by the data of Tian and Vidal[23] where the $H_2^+$ cross-section is determined to be smaller than 5x$10^{-19}$ $cm^2$ at an electron energy of 200 eV.

## 7.7.2 Pairs spectrum

At an electron energy of 200 eV six ion pairs were observed: $C^+ + H^+$, $CH^+ + H^+$, $C_2^+ + H^+$, $C_2H^+ + H^+$, $CH^+ + C^+$ and $CH^+ + CH^+$. The most abundant ion pair was $C_2H^+ + H^+$ at every electron energy studied here. Previously, Thissen *et al*[26] studied the dissociations of $C_2H_2^{2+}$ using a triple coincidence photoelectron-photoion-photoion (PEPIPICO) method, this experiment additionally observed $C^+ + CH_2^+$ and $C_2 + H^+ + H^+$ minor ion channels. These ion channels were not observed with the current experimental set-up. The intensity of both ion channels may be too weak to be observed.

The intensity, $P[X^+]$, of the ions in each ion pair peak was determined using the methods described in Chapter 3.

The dissociations and dynamics of dissociations of the $C_2H_2^{2+}$ dication are not investigated in this chapter, as the primary objective is to provide determinations for the absolute PICSs and absolute precursor specific PICSs of the ions observed following electron interaction with $C_2H_2$. Therefore, only the intensities of the ion pairs observed in the pairs spectrum are studied and thus a pairs spectrum is not presented here.

## 7.7.3 Absolute PICSs for $C_2H_2^+$

Using Eq. (7.6) and the methods described in Chapter 3 to determine each of the parameters in Eq. (7.6) the values for $\sigma'[C_2H_2^+]$ were determined from 30-200 eV.

$$\sigma'[C_2H_2^+] = \frac{S(C_2H_2^+)}{S(Ar^+/N_2^+)} \times \frac{p_{Ar/N_2}}{p_{C_2H_2}} \times \sigma'[Ar^+/N_2^+] \qquad (7.6).$$

From Figure 7.10 agreement is observed between the values determined here for $\sigma'[C_2H_2^+]$ and the absolute PICSs of Zheng and Srivastava[10] and Tian and Vidal[23] within the mutual error limits. The $\sigma'[C_2H_2^+]$ values determined using argon and nitrogen reference gases are typically lower than the absolute PICS values of Zheng and Srivastava[10] and Tian and Vidal[23] but do agree within the mutual error limits.

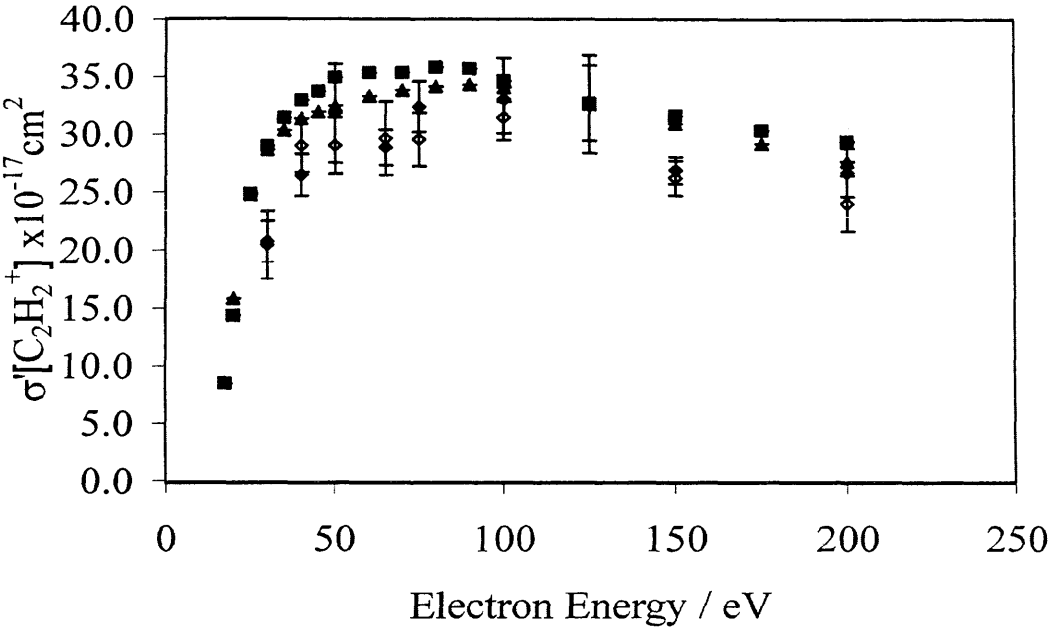


Figure 7.10: Values determined for $\sigma'[C_2H_2^+]$ using $Ar/C_2H_2$ (◆) and $N_2/C_2H_2$ gas mixtures (◇), shown with error bars representing the standard deviation of four cross-section determinations at each electron energy. Data is compared with available absolute PICSs of Zheng and Srivastava[10] (▲) and Tian and Vidal[23] (■), representative errors are shown at 125 eV for both sets of data.

With reference to Figure 7.10 the molecular mass difference between the two gases had no significant effect on the absolute PICS determinations and agreement is observed between both two-gas systems. The cross-sections determined using the argon/acetylene and the nitrogen/acetylene two-gas systems exhibit small variations due principally to the approximate nature of obtaining a gas pressure ratio of 1:1. The $\sigma'[C_2H_2^+]$ values are shown in Table 7.2 for each two-gas system.

Table 7.2: Values determined for $\sigma'[C_2H_2^+]$ at each electron energy $E$ for each two-gas system. The error in the last figure is shown in parentheses. This error is the standard deviation of four individual cross-section determinations.

| | $Ar/C_2H_2$ system | $N_2/C_2H_2$ system |
|---|---|---|
| $E$/eV | $\sigma'[C_2H_2^+]$ ($x10^{-17}cm^2$) | $\sigma'[C_2H_2^+]$ ($x10^{-17}cm^2$) |
| 200 | 26.8 (21) | 24.1 (24) |
| 150 | 27.0 (12) | 26.3 (15) |
| 100 | 33.1 (36) | 31.5 (14) |
| 75 | 32.5 (22) | 29.6 (23) |
| 65 | 28.9 (15) | 29.7 (32) |
| 50 | 31.9 (43) | 29.1 (24) |
| 40 | 26.5 (18) | 29.1 (23) |
| 30 | 20.8 (18) | 20.5 (29) |

The same data analysis methods, discussed in detail in Chapter 3, used to determine the absolute PICSs for $C_2H_2^+$, are also used to determine the absolute PICSs for the $H^+$, $C^+ + C_2^{2+}$, $CH^+ + C_2H_2^{2+}$, $C_2^+$ and $C_2H^+$ fragment ions formed following electron ionization of $C_2H_2$. The absolute PICSs for the $H^+$, $C^+ + C_2^{2+}$, $CH^+ + C_2H_2^{2+}$, $C_2^+$ and $C_2H^+$ fragment ions are defined in Appendix H. For completeness, the $\sigma'[C_2H_2^+]$ values determined using both argon and nitrogen as the reference gases are displayed in Figure 7.10 and values are presented in Table 7.2. As shown in Table 7.2, no significant difference between the $\sigma'[C_2H_2^+]$ values determined using either reference gas was observed. Therefore, no additional discussion is presented in the following sections regarding the mass difference between the two gases utilised for each experiment.

### 7.7.4 Absolute PICSs and absolute precursor specific PICSs

As described in Chapter 3, to enable absolute precursor specific PICSs (Eqs. (7.7) and (7.8)) to be determined, the relative precursor specific PICSs must initially be determined for each fragment ion, Eqs. (7.9) and (7.10). These values are then multiplied by the $\sigma'[C_2H_2^+]$ values determined in Section 7.7.3 and shown in Eq. (7.6). Examples of the data analysis equations are given below for the $H^+$ ion. Data analysis

equations for each fragment ion are given in Appendix H.

$$\sigma_1'[H^+] = \frac{\sigma_1[H^+]}{\sigma_1[C_2H_2^+]} \times \sigma'[C_2H_2^+] \quad (7.7),$$

$$\sigma_2'[H^+] = \frac{\sigma_2[H^+]}{\sigma_1[C_2H_2^+]} \times \sigma'[C_2H_2^+] \quad (7.8),$$

$$\frac{\sigma_1[H^+]}{\sigma_1[C_2H_2^+]} = \frac{N_1[H^+]}{N_1[C_2H_2^+]} = \frac{I[H^+] - (1-f_i)/f_i P[H^+]}{I[C_2H_2^+]} \quad (7.9),$$

$$\frac{\sigma_2[H^+]}{\sigma_1[C_2H_2^+]} = \frac{N_2[H^+]}{N_1[C_2H_2^+]} = \frac{P[H^+]}{I[C_2H_2^+]f_i} \quad (7.10).$$

The absolute precursor specific PICSs were determined for the formation of $H^+$, $C_2^+$ and $C_2H^+$ fragment ions *via* single and double ionization. As discussed in Section 7.7.1, the absolute precursor specific PICSs were determined for the formation of $C^+ + C_2^{2+}$, $CH^+ + C_2H_2^{2+}$ *via* both single and double ionization and the formation of $C^+$ and $CH^+$ *via* double ionization. To enable absolute precursor specific PICSs to be determined the ion detection efficiency must also be derived, as shown in Eqs. (7.9) and (7.10). This value is determined below in Section 7.7.5.

### 7.7.5 Ion detection efficiency

As discussed in Chapter 3, to enable $\sigma_n[X^+]$ values to be derived and hence $\sigma_n'[X^+]$ values to be determined a value for $f_i$ is determined by recording the singles and pairs spectra following ionization of $CF_4$. For the electron ionization of $C_2H_2$ this procedure resulted in a value of $f_i$=0.17±0.02, in agreement with determinations made in Chapters 4-6.

## 7.8 Discussion

### 7.8.1 $C_2H^+$ formation

The values of $\sigma'[C_2H^+]$ determined here peak at 100 eV and decrease towards 200 eV. The values of $\sigma_2'[C_2H^+]$ are small and only become significant at 50 eV, see Figure 7.11 (a) and (b).

Figure 7.11 (a) and (b) demonstrate that agreement is observed between the currently determined $\sigma'[C_2H^+]$ values and the absolute PICS values of Zheng and Srivastava[10] and Tian and Vidal.[23] The values for $\sigma_1'[C_2H^+]$, $\sigma_2'[C_2H^+]$ and $\sigma'[C_2H^+]$ are shown in Table I.1 in Appendix I

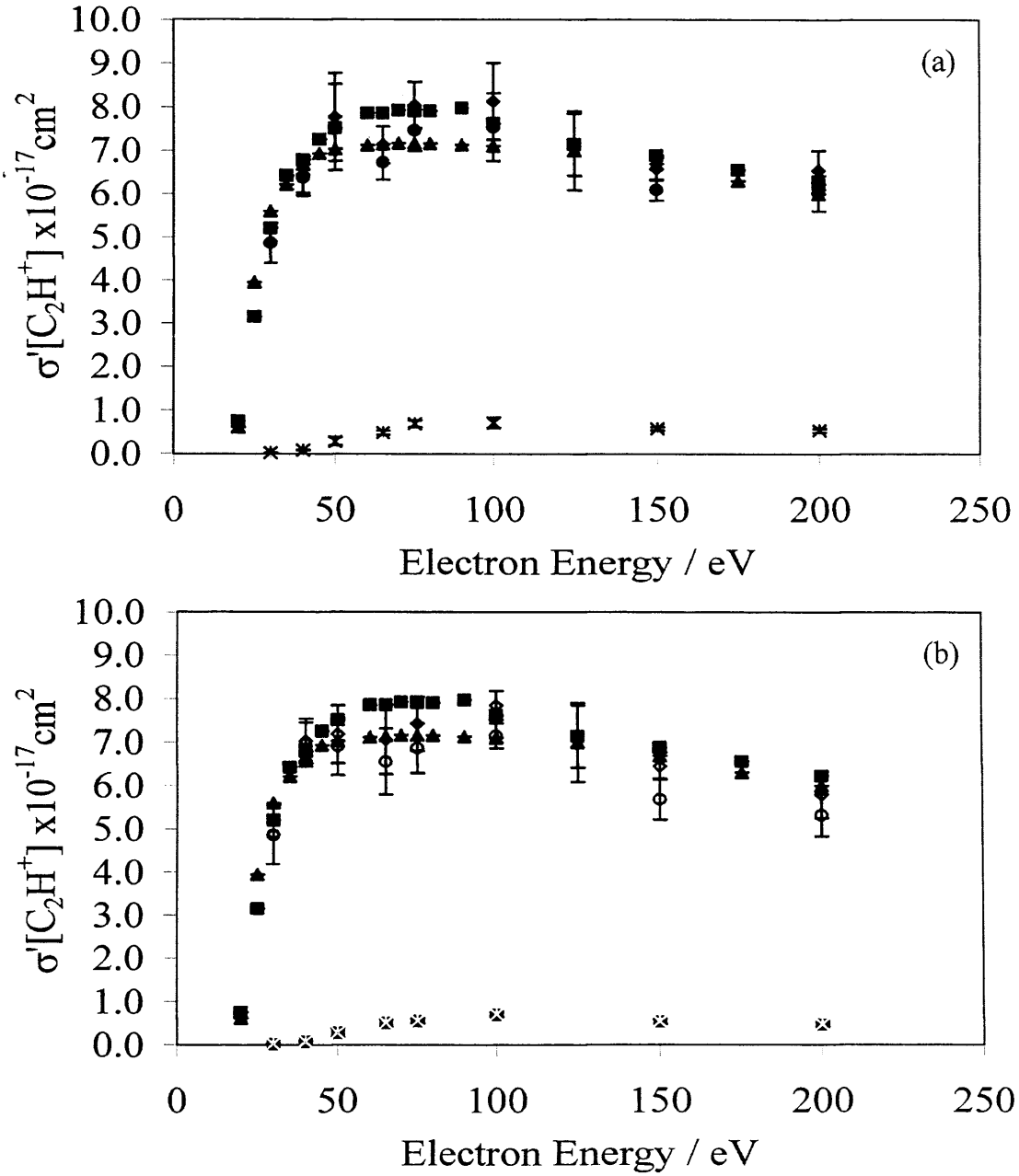


Figure 7.11: (a) Values of $\sigma'[C_2H^+]$ (◆), $\sigma_1'[C_2H^+]$ (●) and $\sigma_2'[C_2H^+]$ (✱) using $Ar/C_2H_2$ gas mixtures. (b) Values of $\sigma'[C_2H^+]$ (◇), $\sigma_1'[C_2H^+]$ (○) and $\sigma_2'[C_2H^+]$ (⊠) using $N_2/C_2H_2$ gas mixtures. Each value is shown with error bars representing the standard deviation of four cross-section determinations at each electron energy. This data is compared with available absolute PICSs of Zheng and Srivastava[10] (▲) and Tian and Vidal[23] (■), representative errors are shown at 125 eV for both sets of data.

### 7.8.2 $C_2^+$ formation

The values of $\sigma'[C_2^+]$ and $\sigma_1'[C_2^+]$ determined here peak between 75-100 eV

and then decrease towards 200 eV. The values of $\sigma_2'[C_2^+]$ become significant above 50 eV and plateau towards 200 eV, shown in Figure 7.12 (a) and (b).

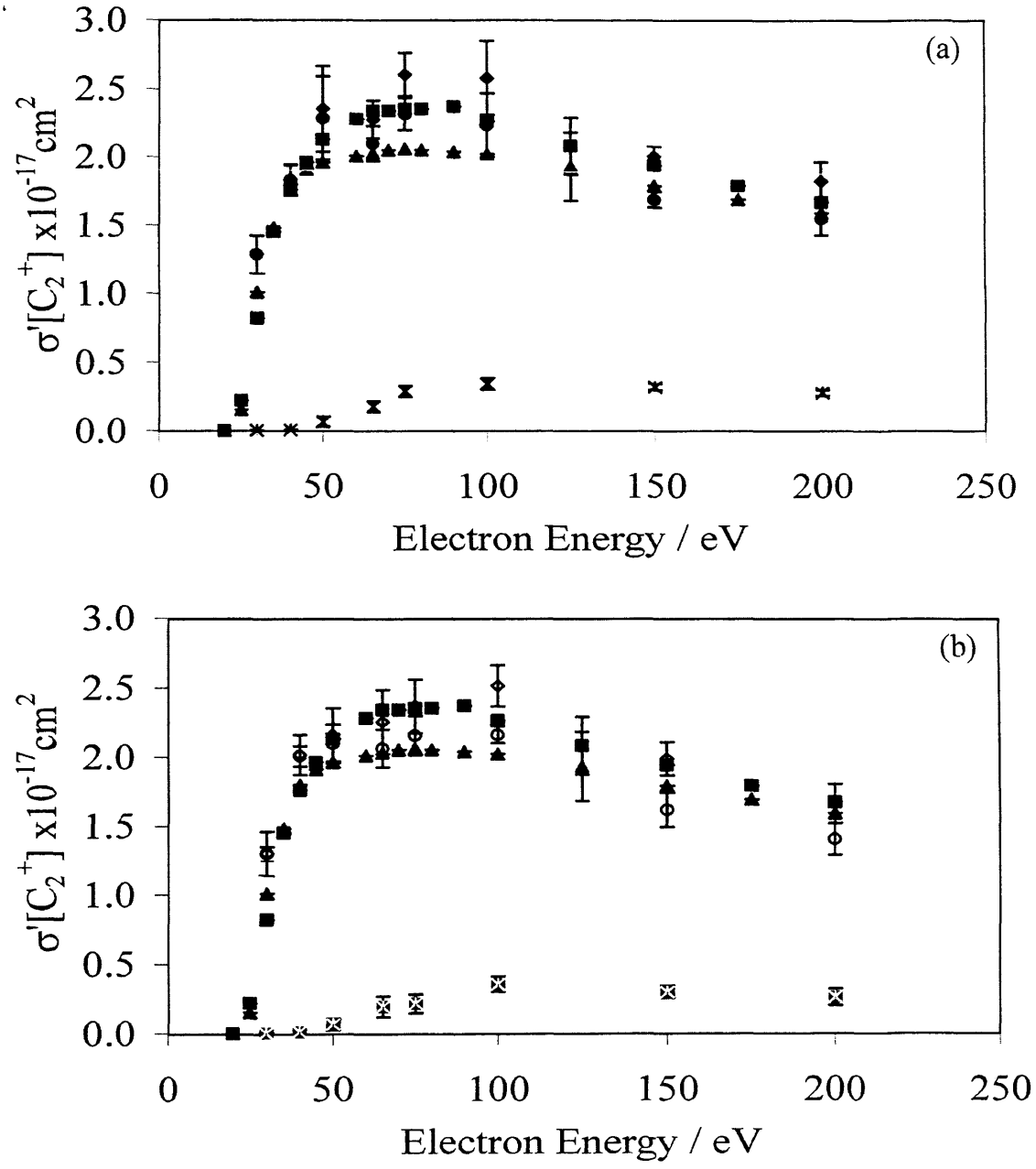


Figure 7.12: (a) Values of $\sigma'[C_2^+]$ (◆), $\sigma_1'[C_2^+]$ (●) and $\sigma_2'[C_2^+]$ (✳) using $Ar/C_2H_2$ gas mixtures. (b) Values of $\sigma'[C_2^+]$ (◇), $\sigma_1'[C_2^+]$ (○) and $\sigma_2'[C_2^+]$ (⊞) using $N_2/C_2H_2$ gas mixtures. Each value is shown with error bars representing the standard deviation of four cross-section determinations at each electron energy. This data is compared with available absolute PICSs of Zheng and Srivastava[10] (▲) and Tian and Vidal[23] (■), representative errors are shown at 125 eV for both sets of data.

With reference to Figure 7.12 (a) and (b), agreement is observed between the current $\sigma'[C_2^+]$ values determined here and the absolute PICS data of Zheng and Srivastava[10] and Tian and Vidal[23] within the mutual error limits. However, between 50-100 eV the absolute PICS values of Zheng and Srivastava[10] are lower than the $\sigma'[C_2^+]$ values and the absolute PICS data of Tian and Vidal,[23] consistent with energetic ion loss from dissociative double ionization. The values for each two-gas system are displayed in Table I.2 in Appendix I.

### 7.8.3 $CH^+ + C_2H_2^{2+}$ formation

The values of $\sigma'[CH^+ + C_2H_2^{2+}]$ and $\sigma_{12}'[CH^+ + C_2H_2^{2+}]$ determined here peak at approximately 100 eV and then decrease towards 200 eV. The values of $\sigma_2'[CH^+]$ determined are non-zero at 40 eV and peak around 100 eV, see Figure 7.13 (a) and (b). The values for each two-gas system are displayed in Table I.3 in Appendix I.

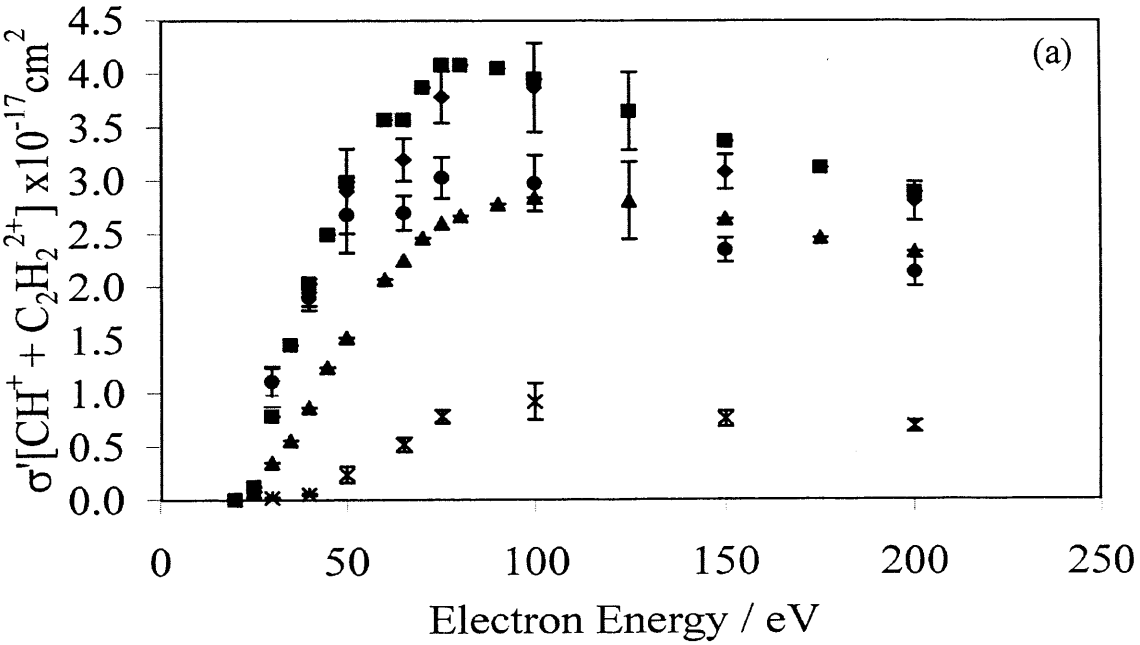

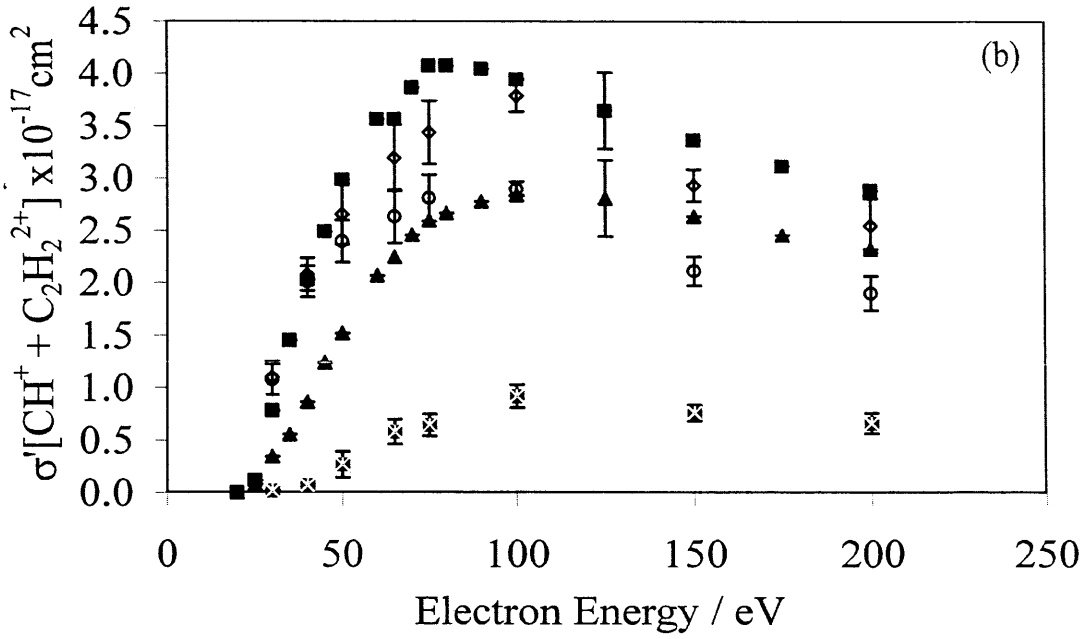


Figure 7.13: (a) Values of $\sigma'[CH^+ + C_2H_2^{2+}]$ (◆), $\sigma_{12}'[CH^+ + C_2H_2^{2+}]$ (●) and $\sigma_2'[CH^+]$ (✱) using $Ar/C_2H_2$ gas mixtures. (b) Values of $\sigma'[CH^+ + C_2H_2^{2+}]$ (◇), $\sigma_{12}'[CH^+ + C_2H_2^{2+}]$ (○) and $\sigma_2'[CH^+]$ (⊠) using $N_2/C_2H_2$ gas mixtures. Each value is shown with error bars representing the standard deviation of four cross-section determinations at each electron energy. This data is compared with available absolute PICSs of Zheng and Srivastava[10] (▲) and Tian and Vidal[23] (■), representative errors are shown at 125 eV for both sets of data.

With reference to Figure 7.13 (a) and (b), the values of $\sigma'[CH^+ + C_2H_2^{2+}]$ determined here and the absolute PICS data of Tian and Vidal[23] show agreement. However, the absolute PICS data of Zheng and Srivastava[10] are approximately 30% lower than the values of $\sigma'[CH^+ + C_2H_2^{2+}]$ determined here and the absolute PICS data of Tian and Vidal.[23] Agreement is observed in the shape of all the cross-sections, Figure 7.13. Below 100 eV the experimental apparatus used by Zheng and Srivastava[10] may miss energetic ions formed *via* single ionization at the lower electron energies (<40 eV) and also some energetic ions formed *via* dissociative double ionization (>40 eV). Tian and Vidal[23] have indeed noted that the $CH^+$ ion peak is broadened because of the kinetic energy associated with the ion during dissociation.

### 7.8.4 $C^+ + C_2^{2+}$ formation

The $\sigma'[C^+ + C_2^{2+}]$ and $\sigma_{12}'[C^+ + C_2^{2+}]$ values determined here peak at 100 eV and decrease towards 200 eV. The values of $\sigma_2'[C^+]$ become significant at 50 eV and

peak around 100 eV where the values plateau towards 200 eV, see Figure 7.14 (a) and (b).

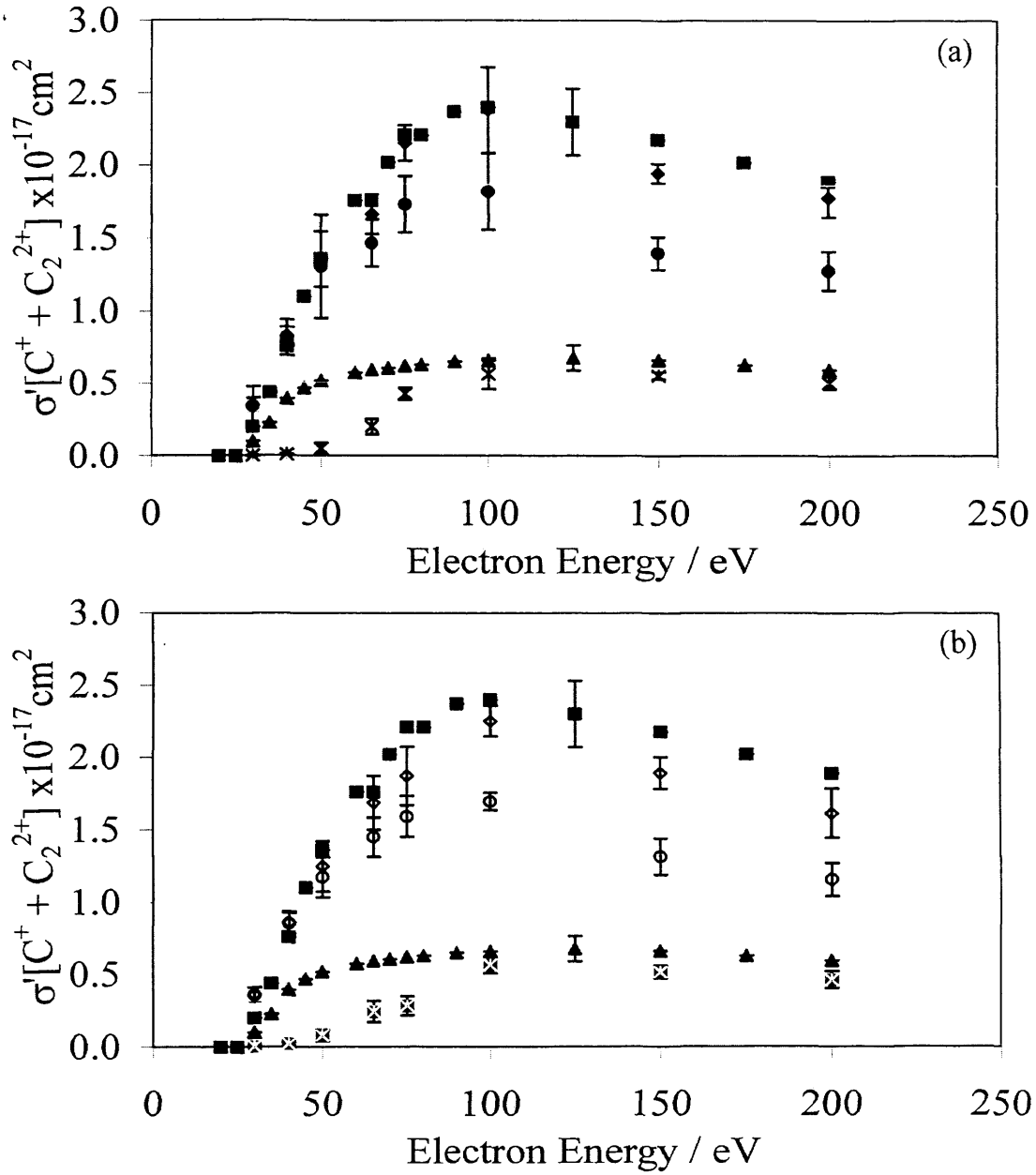


Figure 7.14: (a) Values of $\sigma'[C^+ + C_2^{2+}]$ (◆), $\sigma_{12}'[C^+ + C_2^{2+}]$ (●) and $\sigma_2'[C^+]$ (✱) using $Ar/C_2H_2$ gas mixtures. (b) Values of $\sigma'[C^+ + C_2^{2+}]$ (◇), $\sigma_{12}'[C^+ + C_2^{2+}]$ (○) and $\sigma_2'[C^+]$ (⊞) using $N_2/C_2H_2$ gas mixtures. Each value is shown with error bars representing the standard deviation of four cross-section determinations at each electron energy. This data is compared with available absolute PICSs of Zheng and Srivastava[10] (▲) and Tian and Vidal[23] (■), representative errors are shown at 125 eV for both sets of data.

With reference to Figure 7.14 (a) and (b) the $\sigma'[C^+ + C_2^{2+}]$ values determined

here are in agreement with the absolute PICSs of Tian and Vidal[23] but in disagreement with the absolute PICSs of Zheng and Srivastava.[10] The values determined by Zheng and Srivastava[10] are approximately three times smaller than the $\sigma'[C^+ + C_2^{2+}]$ values determined here and the absolute PICS data of Tian and Vidal.[23] As discussed in Section 7.8.3, a discrepancy of such magnitude suggests that the experiment of Zheng and Srivastava[10] is missing energetic ions formed *via* single and double ionization. The values determined here are displayed in Table I.4 in Appendix I.

### 7.8.5 $H^+$ formation

As discussed in Section 7.6, the values of $\sigma'[H^+]$ are the most difficult to accurately quantify, due to the contribution from $H^+$ ions from other sources such as background $H_2O$, acetone and $H^+$ ions formed on the filament. The values of $\sigma'[H^+]$ determined currently were corrected for any $H^+$ ion contribution from other sources. The error bars shown on Figure 7.15 (a) and (b) represent the standard deviation of four cross-section determinations, however, as detailed in Section 7.6, the associated errors may actually be greater than shown. The values and errors are displayed in Table I.5 in Appendix I.

With reference to Figure 7.15 (a) and (b) the values of $\sigma'[H^+]$ and $\sigma_1'[H^+]$ peak around 75-100 eV and decrease towards 200 eV. The values of $\sigma_2'[H^+]$ determined here become significant at 40 eV, peaking at 100 eV, see Figure 7.15 (a) and (b).

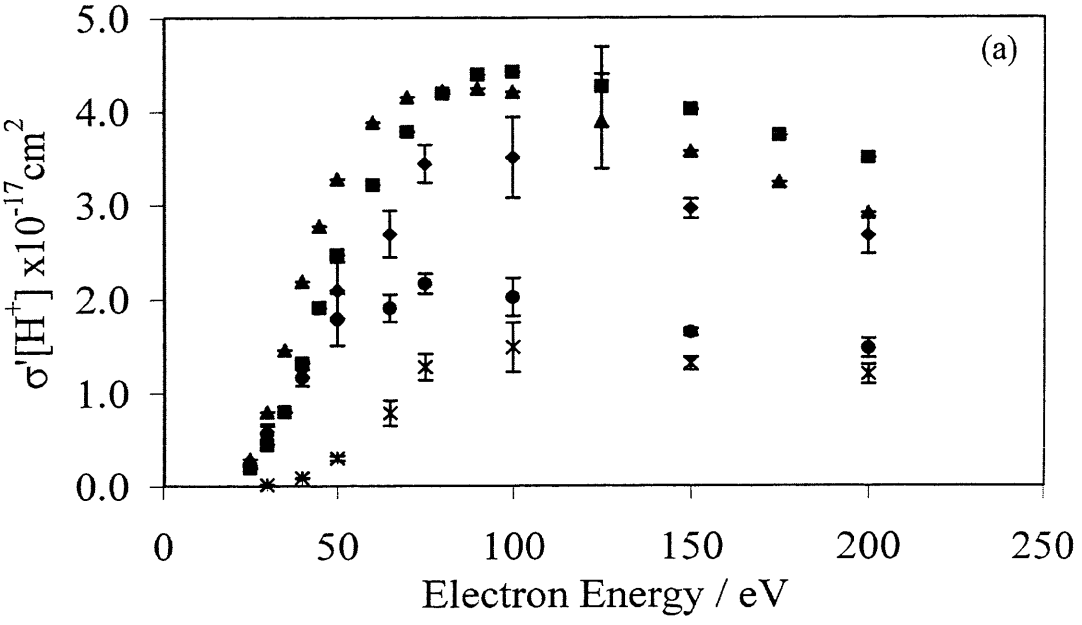

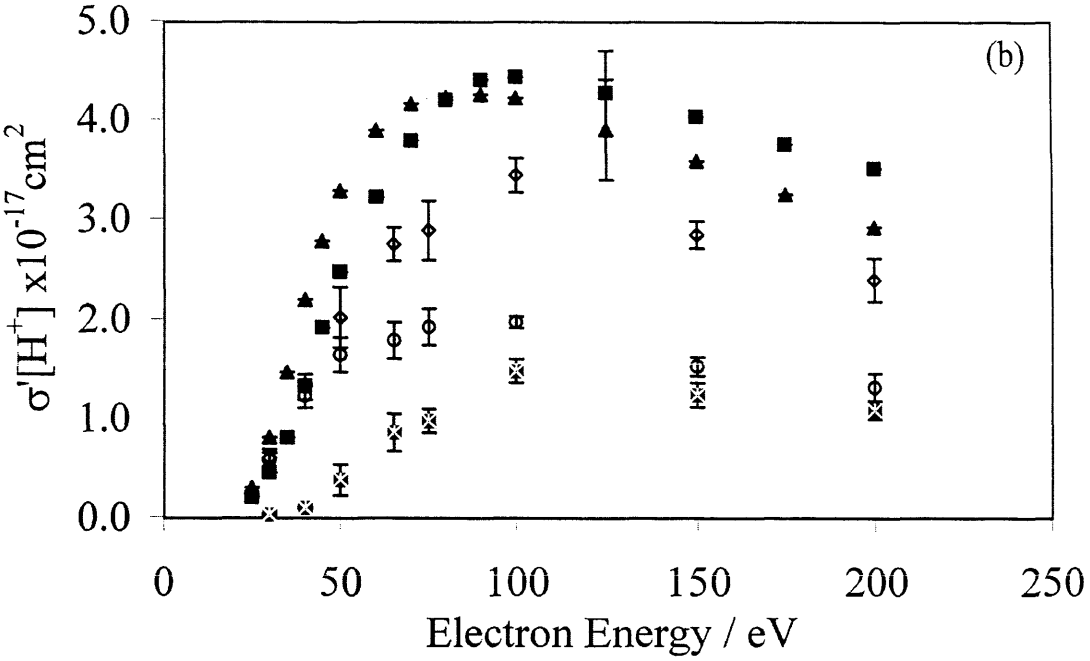


Figure 7.15: (a) Values of $\sigma'[H^+]$ (◆), $\sigma_1'[H^+]$ (●) and $\sigma_2'[H^+]$ (✳) using $Ar/C_2H_2$ gas mixtures. (b) Values of $\sigma'[H^+]$ (◇), $\sigma_1'[H^+]$ (○) and $\sigma_2'[H^+]$ (⊞) using $N_2/C_2H_2$ gas mixtures. Each value is shown with error bars representing the standard deviation of four cross-section determinations at each electron energy. This data is compared with available absolute PICSs of Zheng and Srivastava[10] (▲) and Tian and Vidal[23] (■), representative errors are shown at 125 eV for both sets of data.

Figure 7.15 (a) and (b) show that the values of $\sigma'[H^+]$ determined here are in agreement with the absolute PICSs of Zheng and Srivastava[10] and Tian and Vidal[23] within the mutual error limits. However, the values of $\sigma'[H^+]$ determined here are lower than the values of Zheng and Srivastava[10] and Tian and Vidal.[23] The shape of the absolute PICS determined here and the cross-section shape of Tian and Vidal[23] is similar but the shape of the data by Zheng and Srivastava[10] is different. The $H^+$ ions are the most energetic fragment ions formed following electron interaction with $C_2H_2$. Zheng and Srivastava[10] collected the $H^+$ ions with a segmented TOF mass spectrometer, which means that they would detect more $H^+$ ions, whereas they collected $C^+ + C_2^{2+}$ ions with a QMS which lost more energetic ions. This illustrates that the experimental method used to determine the cross-sections must be carefully considered to ensure complete energetic ion collection.

### 7.8.6 Conclusions

The absolute PICSs of $H^+$, $C^+ + C_2^{2+}$, $CH^+ + C_2H_2^{2+}$, $C_2^+$, $C_2H^+$ and $C_2H_2^+$ ions were determined from 30-200 eV. The absolute PICSs determined here are observed to be in agreement with absolute PICS determinations of Zheng and Srivastava[10] and Tian and Vidal[23] for the $H^+$, $C_2^+$, $C_2H^+$ and $C_2H_2^+$ fragment ions. However, the absolute PICSs determined here for the $C^+ + C_2^{2+}$ and $CH^+ + C_2H_2^{2+}$ fragment ions are greater than the absolute PICS determinations of Zheng and Srivastava.[10] These discrepancies are attributed to the experimental apparatus of Zheng and Srivastava[10] being unable to collect all energetic ions formed. The absolute precursor specific PICSs of $H^+$, $C^+ + C_2^{2+}$, $CH^+ + C_2H_2^{2+}$, $C_2^+$ and $C_2H^+$ ions allows the contribution from various levels of ionization to the individual product ion yields following an electron-molecule collision to be quantified. This data enables differences observed between the absolute PICSs determined here and absolute PICSs used for comparison from the literature to be assessed. For example, the values of $\sigma'[C^+ + C_2^{2+}]$ and $\sigma'[CH^+ + C_2H_2^{2+}]$ determined here suggest that the experimental set-up of Zheng and Srivastava[10] is unable to detect some energetic ions formed *via* single and double ionization.

The $Ar/C_2H_2$ and $N_2/C_2H_2$ two-gas systems produced comparable absolute cross-section data for the fragment ions formed following electron interaction with $C_2H_2$. This information is encouraging; it suggests that over the development of the experimental technique used here to determine absolute ionization cross-sections the parameters under investigation are now better understood. The use of gases with a different molecular mass is shown not to significantly degrade the quality of the cross-section data.

## 7.9 Overall Conclusions

The experimental methods and techniques developed to enable absolute PICSs and absolute precursor specific PICSs to be determined were shown to produce accurate absolute cross-section data for the electron ionization of $N_2O$ and $C_2H_2$.

Following the data displayed in this chapter, this experimental technique can now be used with confidence to study other atmospherically and industrially relevant gases, in the ongoing quest to provide additional absolute cross-section data.

## 7.10 References


1 I. Iga, M. Rao, and S. K. Srivastava, *J. Geophys. Res.-Planets* **101,** 9261 (1996).

2 J. Lopez, V. Tarnovsky, M. Gutkin, and K. Becker, *Int. J. Mass Spectrom.* **225,** 25 (2003).

3 B. G. Lindsay, R. Rejoub, and R. F. Stebbings, *J. Chem. Phys.* **118,** 5894 (2003).

4 H. C. Straub, P. Renault, B. G. Lindsay, K. A. Smith, and R. F. Stebbings, *Phys. Rev. A* **52,** 1115 (1995).

5 A. Williams and D. B. Smith, in *The Combustion and Oxidation of Acetylene* (1969).

6 M. C. McMaster, W. L. Hsu, M. E. Coltrin, D. S. Dandy, and C. Fox, *Diamond Rel. mater.* **4,** 1000 (1995).

7 R. K. Janev, *Atomic and Molecualr Processes in Fusion Edge Plasmas* (Plenum, New York, 1995).

8 H. Tawara and R. A. Phaneuf, *Comm. At. Mol. Phys.* **22,** 963 (1988).

9 H. Tawara, T. Tonuma, H. Kumagai, and T. Matsuo, *J. Phys. B-At. Mol. Opt. Phys.* **25,** L423 (1992).

10 S. H. Zheng and S. K. Srivastava, *J. Phys. B-At. Mol. Opt. Phys.* **29,** 3235 (1996).

11 H. W. Moos and J. T. Clarke, *Astrophys. J.* **229,** L107 (1979).

12 P. T. Smith, K. Yoshino, and W. H. Parkinson, *J. Geophys. Res.* **96,** 17529 (1991).

13 F. Herbert, B. R. Sandel, R. V. Yelle, J. B. Holberg, A. L. Broadfoot, D. E. Shemansky, S. K. Atreya, and P. N. Romani, *J. Geophys. Res.* **92,** 15093 (1987).

14 T. C. Owen, J. Caldwel, A. R. Rivolo, V. Moore, A. L. Lane, C. Sagan, H. Hunt, and C. Ponnamperuma, *Astrophys. J.* **236,** L39 (1987).

15 P. Varanasi, L. P. Giver, and F. P. Valero, *Quant. Spectrosc. Radiat. Transfer.* **30,** 497 (1983).

16 J. T. Tate and P. T. Smith, *Phys. Rev.* **39,** 270 (1932).

17 M. Davister and R. Locht, *Chem. Phys.* **189,** 805 (1994).

18 M. Davister and R. Locht, *Chem. Phys.* **191,** 333 (1995).

19 R. Locht and M. Davister, *Chem. Phys.* **195,** 443 (1995).

20 R. Locht and C. Servais, *Z. Phys. C-At. Mol. Clusters* **195,** 153 (1996).

21 S. Feil, A. Bacher, M. Zangerl, W. Schustereder, K. Gluch, and P. Scheier, *Int. J. Mass. Spectrom.* **233,** 325 (2004).

22 A. Gaudin and R. Hagemann, *J. Chem. Phys.* **64,** 1209 (1967).

23 C. C. Tian and C. R. Vidal, *J. Phys. B-At. Mol. Opt. Phys.* **31,** 895 (1998).

24 H. C. Straub, P. Renault, B. G. Lindsay, K. A. Smith, and R. F. Stebbings, *Phys. Rev. A* **54,** 2146 (1996).

25 C. Servais and R. Locht, *Chem. Phys. Letts.* **236,** 96 (1995).

26 R. Thissen, J. Delwiche, J. M. Robbe, D. Duflot, J. P. Flament, and J. H. D. Eland, *J. Chem. Phys.* **99,** 6590 (1993).

# Chapter 8

# Further Work

As has been illustrated in the preceding chapters, a large amount of information regarding the electron ionization cross-sections and additional information on the dynamics of multiply charged ion dissociation has been obtained from a relatively simple piece of apparatus. However, as is also apparent from these chapters, there is always scope for the improvement of the experimental apparatus to obtain, for example, threshold and low energy electron spectra and positional information for two or more ion arrivals following dicationic and tricationic dissociation events. These points are discussed below.

At electron energies below 30 eV the electron pulses produced by the current electron gun, described in Chapter 2, become broader, and thus the widths of the ion peaks in the mass spectra increase. This increased pulse width is not suitable for the production of accurate electron ionization cross-sections. Therefore, to produce well-collimated electron pulses from threshold to 100 eV an electron monochromator is currently being designed and commissioned. It is hoped that the use of an electron monochromator will enable threshold electron energies to be reliably investigated. However, the set-up of the current experimental apparatus will initially constrain the ability to include this monochromator due to a lack of space available at the source end of the chamber. Such low-energy data is vital for the modelling of discharges used in low temperature plasmas, as most of the significant processes occur in the energy range below 100 eV. It is this 'low-energy' region that should be focussed on for future electron ionization cross-section measurements of molecules used in plasma processing.[1]

The addition of a position sensitive detector (PSD) to the experimental apparatus would increase the amount of information obtainable from the experimental investigations detailed in this thesis. Using the 2D ion coincidence technique with position sensitive detection would enable both ion arrival times and positions to be determined. Having the timing and positional information of each charged product ion

would then enable the initial velocity vectors of both product ions to be determined. As discussed in Chapter 1, such information allows the determination of both dynamic and kinematic details for each dissociation event.[2] The PSD required would be similar to the design of Price and co-workers which was introduced to study the bimolecular reactions of molecular dications.[2] The PSD would consist of a commercial microchannel plate (MCP) with a dual delay line anode, one delay line for the $x$ dimension and one for the $y$ dimension.[3,4] The advantage of using a delay line anode is its capability to encode each ion arrival time and the positional information detected by the MCP with high accuracy and with a high repetition rate,[2] thereby complementing the high repetition rate employed in these experiments. Indeed, a position sensitive coincident technique[5,6] has been used successfully to provide complete descriptions of the kinematics of the unimolecular dissociations of triatomic molecules, following double photoionization.[7]

As detailed in Chapters 4 and 6, the intensity of the triples spectra recorded for $N_2O$ and $SF_6$ were low, due in part to the experimental runtimes. It is hoped that by increasing the experimental runtimes to the order of days, the collection of triples data will be improved. Such data will then lead to the determination of accurate precursor specific partial ionization cross-sections for ions formed *via* triple ionization. With improved statistics the investigation of the dynamics of tricationic dissociation events may also then be a possibility. The installation of precision leak valves for both gas inlet systems may also allow triple ionization to be studied for the absolute ionization cross-section experiments, detailed in Chapter 3. The addition of precision leak valves would also increase the experimental runtimes and thus improve the quality of the data recorded for the absolute ionization cross-section experiments.

Finally, the constantly increasing demand for smaller feature sizes and higher quality devices in the semiconductor industry[8,9] requires the development of sophisticated models able to predict the details of the plasmas used to etch features, deposit materials and indeed clean the reactor chambers.[8-10] The demand for fundamental electron collision cross-section data is therefore increasing, and such data is central to these industrial processes being efficient and well-optimised. In addition, environmental concerns continue to warrant the more efficient use of global warming gases in plasma processes. Consequently, future investigations of the single, double and triple ionization of other small molecules such as $NF_3$, used in reactor cleaning,[1] will be both necessary and relevant.

## References


1 L. G. Christophorou and J. K. Olthoff, *Appl. Sur. Sci.* **192,** 309 (2002).

2 W. P. Hu, S. M. Harper, and S. D. Price, *Meas. Sci. Technol.* **13,** 1512 (2002).

3 I. Ali, R. Dorner, O. Jagutzki, S. Nuttgens, V. Mergel, L. Spielberger, K. Khayyat, T. Vogt, H. Brauning, K. Ullmann, R. Moshammer, J. Ullrich, S. Hagmann, K. O. Groeneveld, C. L. Cocke, and H. Schmidt-Bocking, *Nucl. Instrum. Methods. Phys. Res.* **149,** 490 (1999).

4 A. Oelsner, O. Schmidt, M. Schicketanz, M. Klais, G. Schonhense, V. Mergel, O. Jagutzki, and H. Schmidt-Bocking, *Rev. Sci. Instrum.* **72,** 3968 (2001).

5 J. H. D. Eland and A. H. Pearson, *Meas. Sci. Technol.* **1,** 36 (1990).

6 J. H. D. Eland, *Meas. Sci. Technol.* **5,** 1501 (1994).

7 S. Hsieh and J. H. D. Eland, *J. Phys. B-At. Mol. Opt. Phys.* **30,** 4515 (1997).

8 Database needs for modeling and simulation of plasma processing, National Research Council (National Academy Press), 1996.

9 E. Meeks and P. Ho, *Thin Solid Films* **365,** 334 (2000).

10 L. G. Christophorou and J. K. Olthoff, *Adv. At. Mol. Opt. Phys.* **44,** 59 (2001).

# Appendix A

# Determination of ion flight times for a two-field TOF mass spectrometer

The ion flight time in a time-of-flight (TOF) mass spectrometer can be derived using electrostatic equations and Newtonian mechanics. It is found that the TOF of an ion, $t_{tof}$, travelling a certain distance in a given set of electric fields is proportional to the square root of its mass $m$, Eq. (A.10).[1] The derivation of this expression is presented below.

The TOF mass spectrometer utilised in the experiments and discussed in this thesis is a two-field device, a schematic diagram is shown in Figure 2.1.1 of Chapter 2. The TOF mass spectrometer consists of a source region of length $2D_1$, acceleration region of length $D_2$ and field-free drift region of length $D_3$. Where the two electric fields are termed $E_{S_1}$ and $E_{D_2}$ in the source and acceleration region respectively. The flight time $t_{tof}$ of an ion of mass $m$ in the TOF mass spectrometer formed at a point in the centre of the source region (where $S_1$=$D_1$) and detected at the end of the drift region can be expressed as a sum of the time taken for the ion to travel through each of the regions of the mass spectrometer, Eq. (A.1)

$$t_{tof}(U_0, S_1) = t_{S_1} + t_{D_2} + t_{D_3} \qquad \text{(A.1).}$$

To determine $t_{S_1}$, that is the time taken for the ion to travel from the centre of the source region to the start of the second acceleration region, Newtonian mechanics can be used to produce Eq. (A.2). Where $v_0$ is the ion's initial velocity, $a$ is the acceleration due to the source electric field $E_{S_1}$ and $v_{S_1}$ is the ion's velocity following acceleration through the distance $S_1$. Where $v_{S_1}$ is determined from:

$$t_{S_1} = \frac{v_{S_1} - v_0}{a} \quad \text{and} \quad v_{S_1}{}^2 = v_0{}^2 + 2aS_1 \qquad \text{(A.2).}$$

Therefore, by substituting for $v_{S_1}$ :

$$t_{S_1} = \frac{\sqrt{v_0{}^2 + 2aS_1} \pm v_0}{a} \qquad \text{(A.3),}$$

where the ± in Eq. (A.3) arises as a result of ions being formed with initial velocities moving towards the detector (+) and away from the detector (-).

The final energy, $U$, gained by an ion of charge $q$ after moving through the mass spectrometer is expressed in terms of the energy gained as the ions moves through the electric fields in each region of the spectrometer, Eq. (A.4):

$$U = U_0 + qS_1E_{S_1} + qD_2E_{D_2} \tag{A.4},$$

where $U_0$ is the ion's initial energy. The ion's initial kinetic energy can then be defined by Eq. (A.5):

$$v_0 = \left(\frac{2U_0}{m}\right)^{\frac{1}{2}} \tag{A.5}.$$

The ion's acceleration can then be expressed in terms of mass, charge and the accelerating electric field, using Newton's second law. Therefore, $t_{S_1}$ can be defined:

$$t_{S_1} = 1.02\frac{(2m)^{\frac{1}{2}}}{qE_{S_1}}\left[(U_0 + qE_{S_1}S_1)^{\frac{1}{2}} \pm (U_0)^{\frac{1}{2}}\right] \tag{A.6}.$$

The ion flight time in the second acceleration region, $t_{D_2}$, is derived in the same fashion, Eq. (A.7):

$$t_{D_2} = 1.02\frac{(2m)^{\frac{1}{2}}}{qE_{D_2}}\left[(U)^{\frac{1}{2}} - (U_0 + qE_{S_1}S_1)^{\frac{1}{2}}\right] \tag{A.7}.$$

Finally, the ion flight time through the field-free drift region can be determined, Eq. (A.8). There is no accelerating electric field in the drift tube, consequently, the ions travel through the drift tube at a constant speed, $v_{D_3}$.

$$t_{D_3} = 1.02\frac{(2m)^{\frac{1}{2}}D_3}{2U^{\frac{1}{2}}} \tag{A.8}.$$

The total ion flight time can be determined by summing Eqs. (A.6)-(A.8):

$$t_{\text{tof}} = 1.02(2m)^{\frac{1}{2}}\left[\left(\frac{(U_0 + qE_{S_1}S_1)^{\frac{1}{2}} \pm (U_0)^{\frac{1}{2}}}{qE_{S_1}}\right) + \left(\frac{(U)^{\frac{1}{2}} - (U_0 + qE_{S_1}S_1)^{\frac{1}{2}}}{qE_{D_2}}\right) + \frac{D_3}{2U^{\frac{1}{2}}}\right] \tag{A.9}.$$

Eq. (A.9) illustrates that the ion flight time is proportional to the square root of the ion's mass. As a consequence of the electric fields and dimensions of the mass spectrometer being constant, together with the charge on an ion, Eq. (A.9) can be abbreviated to yield Eq. (A.10):

$$t_{tof} = k\sqrt{m} + c \qquad \text{(A.10).}$$

The constant $k$ is dependent on the electrostatics and dimensions of the spectrometer, whilst the parameter $c$ arises due to the delays in the electronic timing equipment.[1] As discussed in Chapters 2 and 3, these constants are determined by solving two simultaneous equations for two ions of different mass.

## Reference

1 W. C. Wiley and I. H. McLaren, Rev. Sci. Instrum. **26**, 1150 (1955).

# Appendix B

# First-order focussing in a two-field TOF mass spectrometer

## Space focusing

As mentioned in Chapter 2, the resolution of ions in the mass spectrum is affected by a condition termed space focusing. By focusing the ions in the spectrometer the width or time spread of the mass peak observed in the mass spectrum is reduced to be as small as possible. In an 'ideal' mass spectrometer, all ions would be formed with an initial energy, $U_0$, of zero at a single position in the source region. Under such conditions all ions of the same mass, $m$, would possess the same kinetic energy and therefore would have the same time-of-flight (TOF). However, ions are formed with an initial distribution of kinetic energies and positions in the source region, these factors increase the TOF, which causes a reduction in the mass resolution of the mass spectrometer. To attempt to overcome these factors Wiley and McLaren[1] developed a twin electric field design of TOF mass spectrometer to produce the best possible space focus conditions. Wiley and McLaren[1] assumed that the ion's initial kinetic energy, $U_0$, is zero and that ions of charge $q$ are all formed at a point in the centre of the source region (where $D_1$=$S_1$). They also introduced a new parameter $k_0$.

$$U = qS_1E_{S_1} + qD_2E_{D_2} \qquad \text{(B.1)},$$

$$k_0 = \frac{(S_1E_{S_1} + D_2E_{D_2})}{S_1E_{S_1}} \qquad \text{(B.2)},$$

where $E_{S_1}$ and $E_{D_2}$ represent the electric field strengths in the source and accelerating regions respectively, shown in Figure 2.1.1. It is the ratios of electric field strength and lengths both with respect to the source region that are key in the space focusing conditions. By substituting Eqs. (B.1) and (B.2) into the total ion time of flight $t_{tof}$, Eq. (A.9) (Appendix A), an expression for the ion flight time $t_{tof}$ (0, $S_1$) in terms of $k_0$ is determined:

$$t_{tof}(0,S_1)=\left(\frac{m}{2U}\right)^{\frac{1}{2}}\left(2k_0^{\frac{1}{2}}S_1+\frac{2k_0^{\frac{1}{2}}}{k_0^{\frac{1}{2}}+1}D_2+D_3\right) \qquad \text{(B.3).}$$

The substitution of the parameter $k_0$ enables the TOF equation to be simplified. The conditions for first-order space focussing are found by setting the first differential of Eq. (B.3) to equal zero, under conditions where $U_0$=0 and $S_1$=$D_1$, as shown in Chapter 2. Therefore, an expression for the length of the drift tube region $D_3$ is obtained:

$$D_3=2S_1k_0^{\frac{3}{2}}\left(1-\frac{D_2}{S_1(k_0+k_0^{\frac{1}{2}})}\right) \qquad \text{(B.4).}$$

Therefore, 'space focusing' can be achieved by adjusting the ratio of $E_{D_2}/E_{S_1}$, with fixed values of $S_1$, $D_2$ and $D_3$ values for a two-field experiment in contrast with a one-field TOF mass spectrometer which only has geometric space focusing independent of the electric field strengths ($D_3$=2$S_1$).[1] The lengths of $D_1$, $D_2$ and $D_3$ used currently are 0.5, 1.8 and 23.1 cm respectively and the electric fields strengths used are given in Chapter 3.

## Energy Resolution

In practice, the ion distribution in the source region will have a finite size and thus limit the achievable mass resolution. Focusing the ions helps to reduce the distribution of ion flight times arising because of the ion's initial position in the source region, but the effects caused by ions having differing initial velocities are harder to reduce. For example, consider two ions of identical mass and position in the source region, with initial velocity, $v_0$, of equal magnitude but of opposing direction. Each ion has a trajectory along the axis of the spectrometer, one towards the detector, the second away from the detector. The second ion requires a finite time for the source electric field $E_{S_1}$ to decelerate it, until its speed is zero. The source electric field then accelerates this ion back towards the detector. When this second ion reaches its initial formation position, $S_1$, in the source region, it will have the same speed as it started with but in the opposing direction. Therefore, at this point, ion two will have the same initial velocity as ion one. The difference in the flight times of the two ions is simply the time taken for ion two to initially set off in the opposite direction and return to its original position, which is known as 'turn-around time.' The turn-around time adds to the width of the distribution of ion flight times (resolvable mass), and thus may be considered as

energy focusing.

The time-of-flight spread, $\Delta t_{tof}$, due to the turn-around time can be expressed simply as twice the time taken for the ion having the highest initial velocity away from the detector to be decelerated to zero velocity by the source field. Take an ion of mass, $m$, with a maximum initial kinetic energy, $U_0$, the turn-around time can be expressed by Eq. (B.5):

$$\Delta t_{tof} = 1.02\frac{2mv_0}{qE_{S_1}} = 1.02\frac{2}{qE_{S_1}}(2mU_0)^{\frac{1}{2}} \qquad \text{(B.5).}$$

By only considering the effects of initial energy, the maximum resolvable mass, $M_0$, can be defined, Eq. (B.6). This is achieved by substituting expressions into Eq. (B.5), where the energy time spread is equal to the time between adjacent mass peaks ($M_0=t_{tof}/2\Delta t_{tof}$),[1] the ion flight time, Eq. (B.3) and the turn-around time. The focus condition is then used, Eq. (B.4), to yield the maximum resolvable mass:

$$M_0 = \frac{1}{4}\left(\frac{U}{U_0}\right)^{\frac{1}{2}}\left(\frac{k_0+1}{k_0^{\frac{1}{2}}} - \frac{k_0^{\frac{1}{2}}-1}{k_0+k_0^{\frac{1}{2}}}\frac{D_2}{S_1}\right) \qquad \text{(B.6).}$$

In general $M_0$ is increased by increasing $D_3$ and/or decreasing $D_1$ and $D_2$.[1]

## Reference

1 W. C. Wiley and I. H. McLaren, *Rev. Sci. Instrum.* **26,** 1150 (1955).

# Appendix C

## Relative partial ionization cross-section and relative precursor specific partial ionization cross-section equations for $N_2O$

The ion intensities recorded in the singles, pairs and triples spectra are processed to yield the relative PICSs and the precursor specific PICSs. This data processing is described in detail in Chapter 3. We symbolize the relative PICS for the formation of fragment ion $X^+$ as $\sigma_r[X^+]$, where the cross-section for the formation of $X^+$ is expressed relative to the cross-section for forming $N_2O^+$. Similarly, the precursor specific PICS $\sigma_n[X^+]$ ($n$=1-3) express the cross-section for forming the fragment ion $X^+$, relative to the cross-section for forming $N_2O^+$, *via* single ($n$=1), double ($n$=2) or triple ($n$=3) ionization. In this analysis we assume any contribution from quadruple ionization is negligible.

The intensity of each product ion in the singles spectrum can be described by the following equations, neglecting any contribution from dissociative quadruple ionization:

$$I[N^{2+}] = f_i N_2[N^{2+}] + f_i(1-f_i)N_3^{\text{pairs}}[N^{2+}] \quad \text{(C.1)},$$

$$I[O^{2+}] = f_i N_2[O^{2+}] + f_i(1-f_i)N_3^{\text{pairs}}[O^{2+}] \quad \text{(C.2)},$$

$$I[N^+] = f_i N_1[N^+] + f_i(1-f_i)N_2[N^+] + f_i(1-f_i)N_3^{\text{pairs}}[N^+] + f_i(1-f_i)^2 N_3^{\text{triples}}[N^+] \quad \text{(C.3)},$$

$$I[O^+] = f_i N_1[O^+] + f_i(1-f_i)N_2[O^+] + f_i(1-f_i)N_3^{\text{pairs}}[O^+] + f_i(1-f_i)^2 N_3^{\text{triples}}[O^+] \quad \text{(C.4)},$$

$$I[N_2O^+] = f_i N_1[N_2O^+] \quad \text{(C.5)},$$

$$I[N_2^+] = f_i N_1[N_2^+] + f_i(1-f_i)N_2[N_2^+] \quad \text{(C.6)},$$

$$I[NO^+] = f_i N_1[NO^+] + f_i(1-f_i)N_2[NO^+] + f_i(1-f_i)N_3^{\text{pairs}}[NO^+] \quad \text{(C.7)}.$$

In the above equations, the experimental ion detection efficiency is denoted by $f_i$ and

$N_n[X^+]$ represents the number of $X^+$ ions formed *via* ionizing events involving the loss of $n$ electrons. The distinction is made between dissociative triple ionization events $N_3^{pairs}[X^+]$ which generate a pair of fragment ions, a dication and a monocation such as $N^{2+}$ + $O^+$, and triple ionization events $N_3^{triples}[X^+]$ which form $N^+$ + $N^+$ + $O^+$. For example, in Eq. (C.6) the term involving $N_2[X^+]$ represents the contribution to the singles spectrum from dissociative double ionization events forming $X^+$, where the second ion from the dissociative double ionization event is not detected. Such ion losses occur ($f_i$<1) because of the 90% transmission of the grids that define the electric fields in the apparatus, and the less than unit efficiency of the electronics and detector.

To determine the $\sigma_r$ values, it is noted that $\sigma_r[X^+]$, the relative PICS for formation of a fragment ion $X^+$ with respect to the parent ion $Y^+$, is equal to the sum of the relative precursor specific PICSs, $\sigma_n[X^+]$:

$$\sigma_r[X^+] = \frac{\sum_{n=1}^{n=3}\sigma_n[X^+]}{\sum_{n=1}^{n=1}\sigma_n[N_2O^+]} = \frac{\sigma_1[X^+]+\sigma_2[X^+]+\sigma_3[X^+]}{\sigma_1[N_2O^+]} \qquad \text{(C.8).}$$

Now, under our experimental conditions of low electron flux and ionization rate, $N_n[X^+]$ is proportional to $\sigma_n[X^+]$:

$$\sigma_n[X^+] = kN_n[X^+] \qquad \text{(C.9),}$$

where $k$ is a constant for each experiment and is dependent on experimental variables such as the target gas pressure, electron flux in the source region, the duration of the experiment and electron path within the ionization volume.

To determine relative PICSs, the data from the pairs and triples spectra must also be utilised in addition to the singles data.

$$P_2[N^+] = f_i^2 N_2[N^+] + 2f_i^2(1-f_i)N_3^{triples}[N^+] \qquad \text{(C.10),}$$

$$P_2[O^+] = f_i^2 N_2[O^+] + 2f_i^2(1-f_i)N_3^{triples}[O^+] \qquad \text{(C.11),}$$

$$P_2[N_2^+] = f_i^2 N_2[N_2^+] \qquad \text{(C.12),}$$

$$P_2[NO^+] = f_i^2 N_2[NO^+] \qquad \text{(C.13),}$$

$$P_3[N^{2+}] = f_i^2 N_3^{pairs}[N^{2+}] \qquad \text{(C.14),}$$

$$P_3[O^{2+}] = f_i^{\,2} N_3^{\,\text{pairs}}[O^{2+}] \quad \text{(C.15)},$$

$$P_3[N^{+}] = f_i^{\,2} N_3^{\,\text{pairs}}[N^{+}] \quad \text{(C.16)},$$

$$P_3[O^{+}] = f_i^{\,2} N_3^{\,\text{pairs}}[O^{+}] \quad \text{(C.17)},$$

$$P_3[NO^{+}] = f_i^{\,2} N_3^{\,\text{pairs}}[NO^{+}] \quad \text{(C.18)},$$

$$T[N^{+}] = f_i^{\,3} N_3^{\,\text{triples}}[N^{+}] \quad \text{(C.19)},$$

$$T[O^{+}] = f_i^{\,3} N_3^{\,\text{triples}}[O^{+}] \quad \text{(C.20)}.$$

By using the expressions for the intensities of the signals in the singles, pairs and triples spectra, Eq. (C.9) can now be re-cast to express relative PICSs in terms of the intensities determined from the spectra recorded and presented in this thesis:

$$\sigma_r[N^{2+}] = \frac{N_2[N^{2+}] + N_3[N^{2+}]}{N_1[N_2O^{+}]} = \frac{I[N^{2+}] + P_3[N^{2+}]}{I[N_2O^{+}]} \quad \text{(C.21)},$$

$$\sigma_r[O^{2+}] = \frac{N_2[O^{2+}] + N_3[O^{2+}]}{N_1[N_2O^{+}]} = \frac{I[O^{2+}] + P_3[O^{2+}]}{I[N_2O^{+}]} \quad \text{(C.22)},$$

$$\sigma_r[N^{+}] = \frac{N_1[N^{+}] + N_2[N^{+}] + N_3[N^{+}]}{N_1[N_2O^{+}]} = \frac{I[N^{+}] + P_2[N^{+}] + P_3[N^{+}] + T[N^{+}]}{I[N_2O^{+}]} \quad \text{(C.23)},$$

$$\sigma_r[O^{+}] = \frac{N_1[O^{+}] + N_2[O^{+}] + N_3[O^{+}]}{N_1[N_2O^{+}]} = \frac{I[O^{+}] + P_2[O^{+}] + P_3[O^{+}] + T[O^{+}]}{I[N_2O^{+}]} \quad \text{(C.24)},$$

$$\sigma_r[N_2O^{2+}] = \frac{N_2[N_2O^{2+}]}{N_1[N_2O^{+}]} = \frac{I[N_2O^{2+}]}{I[N_2O^{+}]} \quad \text{(C.25)},$$

$$\sigma_r[N_2^{+}] = \frac{N_1[N_2^{+}] + N_2[N_2^{+}]}{N_1[N_2O^{+}]} = \frac{I[N_2^{+}] + P_2[N_2^{+}]}{I[N_2O^{+}]} \quad \text{(C.26)},$$

$$\sigma_r[NO^{+}] = \frac{N_1[NO^{+}] + N_2[NO^{+}] + N_3[NO^{+}]}{N_1[N_2O^{+}]} = \frac{I[NO^{+}] + P_2[NO^{+}] + P_3[NO^{+}]}{I[N_2O^{+}]} \quad \text{(C.27)}.$$

The $\sigma_r$ values expressed here do not depend on $f_i$. However, by determining a value for $f_i$ the data analysis can be extended to yield the values of $\sigma_n[X^{+}]$, quantifying the contribution to each ion yield from single, double and triple ionization. As described in the literature, a value for the ion detection efficiency is found by recording the singles and pairs spectra following ionization of $CF_4$, described in Chapter 3. Having defined a value for the ion detection efficiency relative precursor specific PICSs can be defined for all the fragment ions detected following electron ionization of $N_2O$. The expressions used to evaluate the relative precursor specific PICSs for fragment ion formation *via* single, double and triple ionization are shown below:

$$\sigma_2[N^{2+}] = \frac{N_2[N^{2+}]}{N_1[N_2O^+]} = \frac{I[N^{2+}] - (1-f_i)/f_i P_3[N^{2+}]}{I[N_2O^+]} \quad \text{(C.28)},$$

$$\sigma_3[N^{2+}] = \frac{N_3^{\text{pairs}}[N^{2+}]}{N_1[N_2O^+]} = \frac{P_3[N^{2+}]/f_i}{I[N_2O^+]} \quad \text{(C.29)},$$

$$\sigma_2[O^{2+}] = \frac{N_2[O^{2+}]}{N_1[N_2O^+]} = \frac{I[O^{2+}] - (1-f_i)/f_i P_3[O^{2+}]}{I[N_2O^+]} \quad \text{(C.30)},$$

$$\sigma_3[O^{2+}] = \frac{N_3^{\text{pairs}}[O^{2+}]}{N_1[N_2O^+]} = \frac{P_3[O^{2+}]/f_i}{I[N_2O^+]} \quad \text{(C.31)},$$

$$\sigma_1[O^+] = \frac{N_1[O^+]}{N_1[N_2O^+]} \quad \text{(C.32)},$$

$$= \frac{I[O^+] - (1-f_i)/f_i P_2[O^+] - (1-f_i)/f_i P_3[O^+] + (1-f_i)^2/f_i^2 T[O^+]}{I[N_2O^+]}$$

$$\sigma_2[O^+] = \frac{N_2[O^+]}{N_1[N_2O^+]} = \frac{P_2[O^+]/f_i - 2(1-f_i)/f_i^2 T[O^+]}{I[N_2O^+]} \quad \text{(C.33)},$$

$$\sigma_3[O^+] = \frac{N_3^{\text{pairs}}[O^+] + N_3^{\text{triples}}[O^+]}{N_1[N_2O^+]} = \frac{P_3[O^+]/f_i + T[O^+]/f_i^2}{I[N_2O^+]} \quad \text{(C.34)},$$

$$\sigma_2[N_2O^{2+}] = \frac{N_2[N_2O^{2+}]}{N_1[N_2O^+]} = \frac{I[N_2O^{2+}]}{I[N_2O^+]} \quad \text{(C.35)},$$

$$\sigma_1[N_2^+] = \frac{N_1[N_2^+]}{N_1[N_2O^+]} = \frac{I[N_2^+] - (1-f_i)/f_i P_2[N_2^+]}{I[N_2O^+]} \quad \text{(C.36)},$$

$$\sigma_2[N_2^+] = \frac{N_2[N_2^+]}{N_1[N_2O^+]} = \frac{P_2[N_2^+]/f_i}{I[N_2O^+]} \quad \text{(C.37)},$$

$$\sigma_1[NO^+] = \frac{N_1[NO^+]}{N_1[N_2O^+]} \quad \text{(C.38)},$$

$$= \frac{I[NO^+] - (1-f_i)/f_i P_2[NO^+] - (1-f_i)/f_i P_3[NO^+]}{I[N_2O^+]}$$

$$\sigma_2[NO^+] = \frac{N_2[NO^+]}{N_1[N_2O^+]} = \frac{P_2[NO^+]/f_i}{I[N_2O^+]} \quad \text{(C.39)},$$

$$\sigma_3[NO^+] = \frac{N_3^{\text{pairs}}[NO^+]}{N_1[N_2O^+]} = \frac{P_3[NO^+]/f_i}{I[N_2O^+]} \quad \text{(C.40)}.$$

# Appendix D

## Relative partial ionization cross-section and relative precursor specific partial ionization cross-section equations for $BCl_3$

The ion intensities recorded in the singles, pairs and triples spectra are processed to yield the relative PICSs and the precursor specific PICSs. This data processing is described in detail in Chapter 3. The relative PICS for the formation of fragment ion $X^+$ are expressed as $\sigma_r[X^+]$, where the cross-section for the formation of $X^+$ is expressed relative to the cross-section for forming $BCl_3^+$. Similarly, the precursor specific PICSs $\sigma_n[X^+]$ ($n$=1-2) express the cross-section for forming the fragment ion $X^+$, relative to the cross section for forming $BCl_3^+$, *via* single ($n$=1) and double ($n$=2) ionization. In this analysis it is assumed that any contribution from triple ionization is negligible.

The intensity of each product ion in the singles spectrum can be described by the following equations:

$$I[B^+] = f_i N_1[B^+] + f_i(1-f_i)N_2[B^+] \quad \text{(D.1)},$$

$$I[BCl_2^{2+}] = f_i N_2[BCl_2^{2+}] \quad \text{(D.2)},$$

$$I[BCl^+] = f_i N_1[BCl^+] + f_i(1-f_i)N_2[BCl^+] \quad \text{(D.3)},$$

$$I[BCl_2^+] = f_i N_1[BCl_2^+] + f_i(1-f_i)N_2[BCl_2^+] \quad \text{(D.4)},$$

$$I[BCl_3^+] = f_i N_1[BCl_3^+] \quad \text{(D.5)}.$$

In the above equations, the experimental ion detection efficiency is denoted by $f_i$ and $N_n[X^+]$ represents the number of $X^+$ ions formed *via* ionizing events involving the loss of $n$ electrons. For example, in Eq. (D.1) the term involving $N_2[X^+]$ represents the contribution to the singles spectrum from dissociative double ionization events forming $X^+$, where the second ion from the dissociative double ionization event is not detected. Such ion losses occur ($f_i$<1) because of the 90% transmission of the grids that define the electric fields in the apparatus, and the less than unit efficiency of the electronics and detector.

To determine the $\sigma_r$ values, it is noted that $\sigma_r[X^+]$, the relative PICS for

formation of a fragment ion $X^+$ with respect to the parent ion $Y^+$, is equal to the sum of the relative precursor specific PICSs, $\sigma_n[X^+]$:

$$\sigma_r[X^+] = \frac{\sum_{n=1}^{n=2}\sigma_n[X^+]}{\sigma_n[BCl_3^+]} = \frac{\sigma_1[X^+]+\sigma_2[X^+]}{\sigma_1[BCl_3^+]} \quad \text{(D.6).}$$

Under the experimental conditions of low electron flux and ionization rate, $N_n[X^+]$ is proportional to $\sigma_n[X^+]$:

$$\sigma_n[X^+] = kN_n[X^+] \quad \text{(D.7),}$$

where $k$ is a constant for each experiment and is dependent on experimental variables such as the target gas pressure, electron flux in the source region, the duration of the experiment and electron path within the ionization volume.

To determine relative PICSs, the data from the pairs spectra must also be used in addition to the singles data. The intensity of each product ion in the pairs spectra is described in the following equations. The $Cl^+$ ion is not displayed, as discussed in the text of Chapter 5.

$$P[B^+] = f_i^2 N_2[B^+] \quad \text{(D.8),}$$

$$P[BCl^+] = f_i^2 N_2[BCl^+] \quad \text{(D.9),}$$

$$P[BCl_2^+] = f_i^2 N_2[BCl_2^+] \quad \text{(D.10).}$$

By using the expressions for the intensities of the signals in the singles and pairs spectra, Eq. (D.7) can be re-cast to express relative PICSs in terms of the intensities determined from the spectra recorded and presented in this thesis. Hence, we can now express the relative PICSs:

$$\sigma_r[B^+] = \frac{N_1[B^+]+N_2[B^+]}{N_1[BCl_3^+]} = \frac{I[B^+]+P[B^+]}{I[BCl_3^+]} \quad \text{(D.11),}$$

$$\sigma_r[BCl_2^{2+}] = \frac{N_2[BCl_2^{2+}]}{N_1[BCl_3^+]} = \frac{I[BCl_2^{2+}]}{I[BCl_3^+]} \quad \text{(D.12),}$$

$$\sigma_r[BCl^+] = \frac{N_1[BCl^+]+N_2[BCl^+]}{N_1[BCl_3^+]} = \frac{I[BCl^+]+P[BCl^+]}{I[BCl_3^+]} \quad \text{(D.13),}$$

$$\sigma_r[BCl_2^+] = \frac{N_1[BCl_2^+]+N_2[BCl_2^+]}{N_1[BCl_3^+]} = \frac{I[BCl_2^+]+P[BCl_2^+]}{I[BCl_3^+]} \quad \text{(D.14).}$$

The $\sigma_r$ values expressed above do not depend on $f_i$. However, by determining a value for $f_i$ the data analysis can be extended to yield the values of $\sigma_n[X^+]$, quantifying the contribution to each ion yield from single and double ionization. As described in

Chapter 3, a value for the ion detection efficiency is found by recording the singles and pairs spectra following ionization of $CF_4$. Having determined a value for the ion detection efficiency, relative precursor specific PICSs can be defined for all the fragment ions detected following electron ionization of $BCl_3$. These expressions used to evaluate the relative precursor specific PICSs for fragment ion formation *via* single and double ionization are shown below:

$$\sigma_1[B^+] = \frac{N_1[B^+]}{N_1[BCl_3^+]} = \frac{I[B^+] - (1-f_i)/f_i P[B^+]}{I[BCl_3^+]} \quad \text{(D.15)},$$

$$\sigma_2[BCl_2^{2+}] = \frac{N_2[BCl_2^{2+}]}{N_1[BCl_3^+]} = \frac{I[BCl_2^{2+}]}{I[BCl_3^+]} \quad \text{(D.16)},$$

$$\sigma_1[BCl^+] = \frac{N_1[BCl^+]}{N_1[BCl_3^+]} = \frac{I[BCl^+] - (1-f_i)/f_i P[BCl^+]}{I[BCl_3^+]} \quad \text{(D.17)},$$

$$\sigma_1[BCl_2^+] = \frac{N_1[BCl_2^+]}{N_1[BCl_3^+]} = \frac{I[BCl_2^+] - (1-f_i)/f_i P[BCl_2^+]}{I[BCl_3^+]} \quad \text{(D.18)},$$

$$\sigma_2[B^+] = \frac{N_2[B^+]}{N_1[BCl_3^+]} = \frac{P[B^+]}{f_i I[BCl_3^+]} \quad \text{(D.19)},$$

$$\sigma_2[BCl^+] = \frac{N_2[BCl^+]}{N_1[BCl_3^+]} = \frac{P[BCl^+]}{f_i I[BCl_3^+]} \quad \text{(D.20)},$$

$$\sigma_2[BCl_2^+] = \frac{N_2[BCl_2^+]}{N_1[BCl_3^+]} = \frac{P[BCl_2^+]}{f_i I[BCl_3^+]} \quad \text{(D.21)}.$$

# Appendix E

## Relative partial ionization cross-section and relative precursor specific partial ionization cross-section equations for $SF_6$

The ion intensities recorded in the singles, pairs and triples spectra are processed to yield the relative PICSs and the precursor specific PICSs. This data processing is described in detail in Chapter 3. The relative PICS for the formation of fragment ion $X^+$ are expressed as $\sigma_r[X^+]$, where the cross-section for the formation of $X^+$ is expressed relative to the cross-section for forming $SF_5^+$. Similarly, the precursor specific PICS $\sigma_n[X^+]$ ($n$=1-3) express the cross-section for forming the fragment ion $X^+$, relative to the cross section for forming $SF_5^+$, *via* single ($n$=1), double ($n$=2) or triple ($n$=3) ionization. In this analysis it is assumed that any contribution from quadruple ionization is negligible.

The intensity of each product ion in the singles spectrum can be described by the following equations:

$$I[F^+] = f_i N_1[F^+] + f_i(1-f_i)N_2[F^+] + f_i(1-f_i)N_3^{\text{pairs}}[F^+] + f_i(1-f_i)^2 N_3^{\text{triples}}[F^+] \quad \text{(E.1)},$$

$$I[SF^{2+}] = f_i N_2[SF^{2+}] + f_i(1-f_i)N_3^{\text{pairs}}[SF^{2+}] \quad \text{(E.2)},$$

$$I[S^+] = f_i N_1[S^+] + f_i(1-f_i)N_2[S^+] + f_i(1-f_i)^2 N_3^{\text{triples}}[S^+] \quad \text{(E.3)},$$

$$I[SF_2^{2+}] = f_i N_2[SF_2^{2+}] + f_i(1-f_i)N_3^{\text{pairs}}[SF_2^{2+}] \quad \text{(E.4)},$$

$$I[SF_3^{2+}] = f_i N_2[SF_3^{2+}] \quad \text{(E.5)},$$

$$I[SF^+] = f_i N_1[SF^+] + f_i(1-f_i)N_2[SF^+] + f_i(1-f_i)^2 N_3^{\text{triples}}[SF^+] \quad \text{(E.6)},$$

$$I[SF_4^{2+}] = f_i N_2[SF_4^{2+}] \quad \text{(E.7)},$$

$$I[SF_3^+] = f_i N_1[SF_3^+] + f_i(1-f_i)N_2[SF_3^+] \quad \text{(E.8)},$$

$$I[SF_4^+] = f_i N_1[SF_4^+] + f_i(1-f_i)N_2[SF_4^+] \quad \text{(E.9)},$$

$$I[SF_5^+] = f_i N_1[SF_5^+] + f_i(1-f_i)N_2[SF_5^+] \quad \text{(E.10)}.$$

In the above equations, the experimental ion detection efficiency is denoted by $f_i$ and $N_n[X^+]$ represents the number of $X^+$ ions formed *via* ionizing events involving the loss of $n$ electrons. The distinction is made between dissociative triple ionization events $N_3^{pairs}[X^+]$ which generate a pair of fragment ions, a dication and a monocation such as $SF^{2+}$ + $F^+$, and triple ionization events $N_3^{triples}[X^+]$ which form $F^+$ + $F^+$ + $S^+$. For example, in Eq. (E.1), the term involving $N_2[X^+]$ represents the contribution to the singles spectrum from dissociative double ionization events forming $X^+$, where the second ion from the dissociative double ionization event is not detected. Such ion losses occur ($f_i$<1) because of the 90% transmission of the grids that define the electric fields in the apparatus, and the less than unit efficiency of the electronics and detector.

To determine the $\sigma_r$ values, it is noted that $\sigma_r[X^+]$, the relative PICS for formation of a fragment ion $X^+$ with respect to the parent ion $Y^+$, is equal to the sum of the relative precursor specific PICSs, $\sigma_n[X^+]$:

$$\sigma_r[X^+] = \frac{\sum_{n=1}^{n=3}\sigma_n[X^+]}{\sum_{n=1}^{n=2}\sigma_n[SF_5^+]} = \frac{\sigma_1[X^+]+\sigma_2[X^+]+\sigma_3[X^+]}{\sigma_1[SF_5^+]+\sigma_2[SF_5^+]} \quad \text{(E.11)}.$$

Under the experimental conditions of low electron flux and ionization rate, $N_n[X^+]$ is proportional to $\sigma_n[X^+]$:

$$\sigma_n[X^+] = kN_n[X^+] \quad \text{(E.12)},$$

where $k$ is a constant for each experiment and is dependent on experimental variables such as the target gas pressure, electron flux in the source region, the duration of the experiment and electron path within the ionization volume.

To determine relative PICSs, the data from the pairs and triples spectra must also be used in addition to the singles data. The intensity of each product ion in the pairs and triples spectra is described in the following equations:

$$P_2[F^+] = f_i^2 N_2[F^+] + 2f_i^2(1-f_i)N_3^{triples}[F^+] \quad \text{(E.13)},$$

$$P_2[S^+] = f_i^2 N_2[S^+] + 2f_i^2(1-f_i)N_3^{triples}[S^+] \quad \text{(E.14)},$$

$$P_2[SF^+] = f_i^2 N_2[SF^+] + 2f_i^2(1-f_i)N_3^{triples}[SF^+] \quad \text{(E.15)},$$

$$P_2[SF_2^+] = f_i^2 N_2[SF_2^+] \quad \text{(E.16)},$$

$$P_2[SF_3^+] = f_i^2 N_2[SF_3^+] \quad \text{(E.17)},$$

$$P_2[SF_4^+] = f_i^2 N_2[SF_4^+] \quad \text{(E.18)},$$

$$P_2[SF_5^+] = f_i^2 N_2[SF_5^+] \quad \text{(E.19)},$$

$$P_3[F^+] = f_i^2 N_3^{\text{pairs}}[F^+] \quad \text{(E.20)},$$

$$P_3[SF^{2+}] = f_i^2 N_3^{\text{pairs}}[SF^{2+}] \quad \text{(E.21)},$$

$$P_3[SF_2^{2+}] = f_i^2 N_3^{\text{pairs}}[SF_2^{2+}] \quad \text{(E.22)},$$

$$T[F^+] = f_i^3 N_3^{\text{triples}}[F^+] \quad \text{(E.23)},$$

$$T[S^+] = f_i^3 N_3^{\text{triples}}[S^+] \quad \text{(E.24)},$$

$$T[SF^+] = f_i^3 N_3^{\text{triples}}[SF^+] \quad \text{(E.25)}.$$

By using the expressions for the intensities of the signals in the singles, pairs and triples spectra, Eq. (E.12) can be re-cast to express relative PICSs in terms of the intensities determined from the spectra recorded and presented in this thesis:

$$\sigma_r[F^+] = \frac{N_1[F^+] + N_2[F^+] + N_3[F^+]}{N_1[SF_5^+] + N_2[SF_5^+]} = \frac{I[F^+] + P_2[F^+] + P_3[F^+] + T[F^+]}{I[SF_5^+] + P_2[SF_5^+]} \quad \text{(E.26)},$$

$$\sigma_r[SF^{2+}] = \frac{N_2[SF^{2+}] + N_3[SF^{2+}]}{N_1[SF_5^+] + N_2[SF_5^+]} = \frac{I[SF^{2+}] + P_3[SF^{2+}]}{I[SF_5^+] + P_2[SF_5^+]} \quad \text{(E.27)},$$

$$\sigma_r[S^+] = \frac{N_1[S^+] + N_2[S^+] + N_3[S^+]}{N_1[SF_5^+] + N_2[SF_5^+]} = \frac{I[S^+] + P_2[S^+] + T[S^+]}{I[SF_5^+] + P_2[SF_5^+]} \quad \text{(E.28)},$$

$$\sigma_r[SF_2^{2+}] = \frac{N_2[SF_2^{2+}] + N_3[SF_2^{2+}]}{N_1[SF_5^+] + N_2[SF_5^+]} = \frac{I[SF_2^{2+}] + P_3[SF_2^{2+}]}{I[SF_5^+] + P_2[SF_5^+]} \quad \text{(E.29)},$$

$$\sigma_r[SF_3^{2+}] = \frac{N_2[SF_3^{2+}]}{N_1[SF_5^+] + N_2[SF_5^+]} = \frac{I[SF_3^{2+}]}{I[SF_5^+] + P_2[SF_5^+]} \quad \text{(E.30)},$$

$$\sigma_r[SF^+] = \frac{N_1[SF^+] + N_2[SF^+] + N_3[SF^+]}{N_1[SF_5^+] + N_2[SF_5^+]} = \frac{I[SF^+] + P_2[SF^+] + T[SF^+]}{I[SF_5^+] + P_2[SF_5^+]} \quad \text{(E.31)},$$

$$\sigma_r[SF_4^{2+}] = \frac{N_2[SF_4^{2+}]}{N_1[SF_5^+] + N_2[SF_5^+]} = \frac{I[SF_4^{2+}]}{I[SF_5^+] + P_2[SF_5^+]} \quad \text{(E.32)},$$

$$\sigma_r[SF_2^+] = \frac{N_1[SF_2^+] + N_2[SF_2^+]}{N_1[SF_5^+] + N_2[SF_5^+]} = \frac{I[SF_2^+] + P_2[SF_2^+]}{I[SF_5^+] + P_2[SF_5^+]} \quad \text{(E.33)},$$

$$\sigma_r[SF_3^+] = \frac{N_1[SF_3^+] + N_2[SF_3^+]}{N_1[SF_5^+] + N_2[SF_5^+]} = \frac{I[SF_3^+] + P_2[SF_3^+]}{I[SF_5^+] + P_2[SF_5^+]} \quad \text{(E.34)},$$

$$\sigma_r[SF_4^+] = \frac{N_1[SF_4^+] + N_2[SF_4^+]}{N_1[SF_5^+] + N_2[SF_5^+]} = \frac{I[SF_4^+] + P_2[SF_4^+]}{I[SF_5^+] + P_2[SF_5^+]} \quad \text{(E.35).}$$

The $\sigma_r$ values expressed above do not depend on $f_i$. However, by determining a value for $f_i$ the data analysis can be extended to yield the values of $\sigma_n[X^+]$, quantifying the contribution to each ion yield from single, double and triple ionization. As described in Chapter 3, a value for the ion detection efficiency is found by recording the singles and pairs spectra following ionization of $CF_4$. Having determined a value for the ion detection efficiency, relative precursor specific PICSs can be defined for all the fragment ions detected following electron ionization of $SF_6$. The relative ionization cross-sections are defined relative to the summation of $\sigma_1[SF_5^+] + \sigma_2[SF_5^+]$, $(I[SF_5^+]/f_i + P_2[SF_5^+]/f_i)$. The expressions used to evaluate the relative precursor specific PICSs for fragment ion formation *via* single, double and triple ionization are shown below:

$$\sigma_1[F^+] = \frac{N_1[F^+]}{N_1[SF_5^+] + N_2[SF_5^+]} \quad \text{(E.36),}$$

$$= \frac{I[F^+] - (1-f_i)/f_i P_2[F^+] - (1-f_i)/f_i P_3[F^+] + (1-f_i)^2/f_i^2 T[F^+]}{I[SF_5^+] + P_2[SF_5^+]}$$

$$\sigma_2[F^+] = \frac{N_2[F^+]}{N_1[SF_5^+] + N_2[SF_5^+]} = \frac{P_2[F^+]/f_i - 2(1-f_i)/f_i^2 T[F^+]}{I[SF_5^+] + P_2[SF_5^+]} \quad \text{(E.37),}$$

$$\sigma_3[F^+] = \frac{N_3^{\text{pairs}}[F^+] + N_3^{\text{triples}}[F^+]}{N_1[SF_5^+] + N_2[SF_5^+]} = \frac{P_3[F^+]/f_i + T[F^+]/f_i^2}{I[SF_5^+] + P_2[SF_5^+]} \quad \text{(E.38),}$$

$$\sigma_2[SF^{2+}] = \frac{N_2[SF^{2+}]}{N_1[SF_5^+] + N_2[SF_5^+]} = \frac{I[SF^{2+}] - (1-f_i)/f_i P_3[SF^{2+}]}{I[SF_5^+] + P_2[SF_5^+]} \quad \text{(E.39),}$$

$$\sigma_3[SF^{2+}] = \frac{N_3^{\text{pairs}}[SF^{2+}]}{N_1[SF_5^+] + N_2[SF_5^+]} = \frac{P_3[SF^{2+}]/f_i}{I[SF_5^+] + P_2[SF_5^+]} \quad \text{(E.40),}$$

$$\sigma_1[S^+] = \frac{N_1[S^+]}{N_1[SF_5^+] + N_2[SF_5^+]} \quad \text{(E.41),}$$

$$= \frac{I[S^+] - (1-f_i)/f_i P_2[S^+] + (1-f_i)^2/f_i^2 T[S^+]}{I[SF_5^+] + P_2[SF_5^+]}$$

$$\sigma_2[S^+] = \frac{N_2[S^+]}{N_1[SF_5^+] + N_2[SF_5^+]} = \frac{P_2[S^+]/f_i - 2(1-f_i)/f_i^2 T[S^+]}{I[SF_5^+] + P_2[SF_5^+]} \quad \text{(E.42),}$$

$$\sigma_3[S^+] = \frac{N_3^{\text{triples}}[S^+]}{N_1[SF_5^+] + N_2[SF_5^+]} = \frac{T[S^+]/f_i^2}{I[SF_5^+] + P_2[SF_5^+]} \quad \text{(E.43)},$$

$$\sigma_2[SF_2^{2+}] = \frac{N_2[SF_2^{2+}]}{N_1[SF_5^+] + N_2[SF_5^+]} = \frac{I[SF_2^{2+}] - (1-f_i)/f_i P_3[SF_2^{2+}]}{I[SF_5^+] + P_2[SF_5^+]} \quad \text{(E.44)},$$

$$\sigma_3[SF_2^{2+}] = \frac{N_3^{\text{pairs}}[SF_2^{2+}]}{N_1[SF_5^+] + N_2[SF_5^+]} = \frac{P_3[SF_2^{2+}]/f_i}{I[SF_5^+] + P_2[SF_5^+]} \quad \text{(E.45)},$$

$$\sigma_2[SF_3^{2+}] = \frac{N_2[SF_3^{2+}]}{N_1[SF_5^+] + N_2[SF_5^+]} = \frac{I[SF_3^{2+}]}{I[SF_5^+] + P_2[SF_5^+]} \quad \text{(E.46)},$$

$$\sigma_1[SF^+] = \frac{N_1[SF^+]}{N_1[SF_5^+] + N_2[SF_5^+]} \quad \text{(E.47)},$$

$$= \frac{I[SF^+] - (1-f_i)/f_i P_2[SF^+] + (1-f_i)^2/f_i^2 T[SF^+]}{I[SF_5^+] + P_2[SF_5^+]}$$

$$\sigma_2[SF^+] = \frac{N_2[SF^+]}{N_1[SF_5^+] + N_2[SF_5^+]} = \frac{P_2[SF^+]/f_i - 2(1-f_i)/f_i^2 T[SF^+]}{I[SF_5^+] + P_2[SF_5^+]} \quad \text{(E.48)},$$

$$\sigma_3[SF^+] = \frac{N_3^{\text{triples}}[SF^+]}{N_1[SF_5^+] + N_2[SF_5^+]} = \frac{T[SF^+]/f_i^2}{I[SF_5^+] + P_2[SF_5^+]} \quad \text{(E.49)},$$

$$\sigma_2[SF_4^{2+}] = \frac{N_2[SF_4^{2+}]}{N_1[SF_5^+] + N_2[SF_5^+]} = \frac{I[SF_4^{2+}]}{I[SF_5^+] + P_2[SF_5^+]} \quad \text{(E.50)},$$

$$\sigma_1[SF_2^+] = \frac{N_1[SF_2^+]}{N_1[SF_5^+] + N_2[SF_5^+]} = \frac{I[SF_2^+] - (1-f_i)/f_i P_2[SF_2^+]}{I[SF_5^+] + P_2[SF_5^+]} \quad \text{(E.51)},$$

$$\sigma_2[SF_2^+] = \frac{N_2[SF_2^+]}{N_1[SF_5^+] + N_2[SF_5^+]} = \frac{P_2[SF_2^+]/f_i}{I[SF_5^+] + P_2[SF_5^+]} \quad \text{(E.52)},$$

$$\sigma_1[SF_3^+] = \frac{N_1[SF_3^+]}{N_1[SF_5^+] + N_2[SF_5^+]} = \frac{I[SF_3^+] - (1-f_i)/f_i P_2[SF_3^+]}{I[SF_5^+] + P_2[SF_5^+]} \quad \text{(E.53)},$$

$$\sigma_2[SF_3^+] = \frac{N_2[SF_3^+]}{N_1[SF_5^+] + N_2[SF_5^+]} = \frac{P_2[SF_3^+]/f_i}{I[SF_5^+] + P_2[SF_5^+]} \quad \text{(E.54)},$$

$$\sigma_1[SF_4^+] = \frac{N_1[SF_4^+]}{N_1[SF_5^+] + N_2[SF_5^+]} = \frac{I[SF_4^+] - (1-f_i)/f_i P_2[SF_4^+]}{I[SF_5^+] + P_2[SF_5^+]} \quad \text{(E.55)}$$

$$\sigma_2[SF_4^+] = \frac{N_2[SF_4^+]}{N_1[SF_5^+] + N_2[SF_5^+]} = \frac{P_2[SF_4^+]/f_i}{I[SF_5^+] + P_2[SF_5^+]} \quad \text{(E.56)}$$

# Appendix F

# Absolute PICS and absolute precursor specific PICS equations for $N_2O$

The processing of the ion intensities recorded in the singles and pairs spectra to yield the relative PICSs, $\sigma_r[X^+]$, and the relative precursor specific PICSs, $\sigma_n[X^+]$, has previously been discussed in detail in Chapter 3. The ion intensities in the singles and pairs spectra are also used to yield the absolute PICSs, $\sigma'[X^+]$, and absolute precursor specific PICSs, $\sigma_n'[X^+]$, together with the gas pressures of argon, $p_{Ar}$, (reference gas) and nitrous oxide, $p_{N2O}$, and the literature values of $\sigma'[Ar^+]$. Eq. (F.1) shows how the absolute PICS for formation of a fragment ion $X^+$ may be determined, using a 'direct' method. The total ion signal, $S$, for each ion is expressed in Eqs. (F.3)-(F.8) in terms of the ion intensity in the singles spectrum, $I[X^+]$, and the ion intensity in the pairs spectrum, $P[X^+]$. In this data analysis it is assumed that any contributions from triple ionization are negligible, and are discussed within the text of Chapter 7.

$$\sigma'[X^+] = \frac{S(X^+)}{S(Ar^+)} \times \frac{p_{Ar}}{p_{N_2O}} \times \sigma'[Ar^+] \qquad \text{(F.1).}$$

Eq. (F.2) shows an example for the parent ion $N_2O^+$, formed following electron ionization of $N_2O$. The total ion signal $S$ for each ion is expressed in Eqs. (F.3)-(F.8).

$$\sigma'[N_2O^+] = \frac{S(N_2O^+)}{S(Ar^+)} \times \frac{p_{Ar}}{p_{N_2O}} \times \sigma'[Ar^+] \qquad \text{(F.2),}$$

$$\sigma'[N_2O^+] = \frac{I[N_2O^+]}{I[Ar^+]} \times \frac{p_{Ar}}{p_{N_2O}} \times \sigma'[Ar^+]$$

$$S(N^+) = I[N^+] + P[N^+] \qquad \text{(F.3),}$$

$$S(O^+) = I[O^+] + P[O^+] \qquad \text{(F.4),}$$

$$S(N_2^+) = I[N_2^+] + P[N_2^+] \qquad \text{(F.5),}$$

$$S(NO^+) = I[NO^+] + P[NO^+] \qquad \text{(F.6),}$$

$$S(N_2O^+) = I[N_2O^+] \qquad \text{(F.7),}$$

$$S(Ar^+) = I[Ar^+] \quad \text{(F.8)}.$$

The intensities of the $N^+$, $O^+$, $N_2^+$, $NO^+$ and $N_2O^+$ ions in the singles spectrum, $I$, and pairs spectrum, $P$, can be described by the following equations:

$$I[N^+] = f_i N_1[N^+] + f_i(1-f_i)N_2[N^+] \quad \text{(F.9)},$$

$$I[O^+] = f_i N_1[O^+] + f_i(1-f_i)N_2[O^+] \quad \text{(F.10)},$$

$$I[N_2^+] = f_i N_1[N_2^+] + f_i(1-f_i)N_2[N_2^+] \quad \text{(F.11)},$$

$$I[NO^+] = f_i N_1[NO^+] + f_i(1-f_i)N_2[NO^+] \quad \text{(F.12)},$$

$$I[N_2O^+] = f_i N_1[N_2O^+] \quad \text{(F.13)},$$

$$I[Ar^+] = f_i N_1[Ar^+] \quad \text{(F.14)},$$

$$P[N^+] = f_i^2 N_2[N^+] \quad \text{(F.15)},$$

$$P[O^+] = f_i^2 N_2[O^+] \quad \text{(F.16)},$$

$$P[N_2^+] = f_i^2 N_2[N_2^+] \quad \text{(F.17)},$$

$$P[NO^+] = f_i^2 N_2[NO^+] \quad \text{(F.18)}.$$

In the above equations, the experimental ion detection efficiency is denoted by $f_i$ and $N_n[X^+]$ represents the number of $X^+$ ions formed *via* ionizing events involving the loss of $n$ electrons. For example, in Eq. (F.9) the term involving $N_2[X^+]$ represents the contribution to the singles spectrum from dissociative double ionization events forming $X^+$, where the second ion from the dissociative double ionization event is not detected. Such ion losses occur ($f_i$<1) because of the 90% transmission of the grids that define the electric fields in the apparatus, and the less than unit efficiency of the electronics and detector.

Eq. (F.1) can now be expressed in terms of the ion intensities recorded in the singles and pairs spectra, defined above. Eqs. (F.19)- (F.22) define the absolute PICSs for the formation of the $N^+$, $O^+$, $N_2^+$ and $NO^+$ ions:

$$\sigma'[N^+] = \frac{I[N^+] + P[N^+]}{I[Ar^+]} \times \frac{p_{Ar}}{p_{N_2O}} \times \sigma'[Ar^+] \quad \text{(F.19)},$$

$$\sigma'[O^+] = \frac{I[O^+] + P[O^+]}{I[Ar^+]} \times \frac{p_{Ar}}{p_{N_2O}} \times \sigma'[Ar^+] \quad \text{(F.20)},$$

$$\sigma'[N_2^+] = \frac{I[N_2^+] + P[N_2^+]}{I[Ar^+]} \times \frac{p_{Ar}}{p_{N_2O}} \times \sigma'[Ar^+] \quad \text{(F.21)},$$

$$\sigma'[NO^+] = \frac{I[NO^+] + P[NO^+]}{I[Ar^+]} \times \frac{p_{Ar}}{p_{N_2O}} \times \sigma'[Ar^+] \quad \text{(F.22)}.$$

As discussed in Chapter 7, there is also an 'indirect' method of determining $\sigma'[X^+]$ values. It should be noted that this 'indirect' technique was not used in the current analysis but is provided for completeness, and is mathematically identical to the 'direct' analysis method. For example, for the $Ar/N_2O$ two-gas system, the relative PICS for each fragment ion is expressed relative to the cross-section for the formation of the $N_2O^+$ parent ion. The relative PICS for the formation of a particular fragment ion is multiplied by the value of $\sigma'[N_2O^+]$, which enables the absolute PICS for formation of that particular ion to be determined. This 'indirect' method is shown in Eq. (F.23):

$$\sigma'[X^+] = \sigma_r[X^+] \times \sigma'[N_2O^+] \quad \text{(F.23)}.$$

The data analysis can be extended to determine absolute precursor specific PICS for the formation of the $N^+$, $O^+$, $N_2^+$ and $NO^+$ fragment ions *via* single and double ionization. This analysis uses the 'indirect' technique expressed in Eq. (F.23), by replacing $\sigma_r[X^+]$ with $\sigma_n[X^+]$ values (where $n$=1,2). The relative precursor specific PICSs for the formation of the fragment ions $N^+$, $O^+$, $N_2^+$ and $NO^+$ *via* single ionization are detailed below. These expressions are then used with Eq. (F.2) to determine absolute precursor specific PICSs for ion formation *via* single ionization, as shown in (F.24):

$$\sigma_1'[X^+] = \frac{\sigma_1[X^+]}{\sigma_1[N_2O^+]} \times \sigma'[N_2O^+] \quad \text{(F.24)},$$

$$\sigma_1'[X^+] = \sigma_1[X^+] \times \sigma'[N_2O^+]$$

$$\sigma_1[N^+] = \frac{N_1[N^+]}{N_1[N_2O^+]} = \frac{I[N^+] - (1-f_i)/f_i P[N^+]}{I[N_2O^+]} \quad \text{(F.25)},$$

$$\sigma_1[O^+] = \frac{N_1[O^+]}{N_1[N_2O^+]} = \frac{I[O^+] - (1-f_i)/f_i P[O^+]}{I[N_2O^+]} \quad \text{(F.26)},$$

$$\sigma_1[N_2^+] = \frac{N_1[N_2^+]}{N_1[N_2O^+]} = \frac{I[N_2^+] - (1-f_i)/f_i P[N_2^+]}{I[N_2O^+]} \quad \text{(F.27)},$$

$$\sigma_1[NO^+] = \frac{N_1[NO^+]}{N_1[N_2O^+]} = \frac{I[NO^+] - (1-f_i)/f_i P[NO^+]}{I[N_2O^+]} \quad \text{(F.28).}$$

Eqs. (F.30)-(F.33) can be used with Eq. (F.2) to determine absolute precursor specific PICSs for ion formation *via* double ionization, as shown in (F.29). The relative precursor specific PICSs for formation of the fragment ions $N^+$, $O^+$, $N_2^+$ and $NO^+$ *via* double ionization are detailed below:

$$\sigma_2'[X^+] = \frac{\sigma_2[X^+]}{\sigma_1[N_2O^+]} \times \sigma'[N_2O^+] \quad \text{(F.29),}$$

$$\sigma_2'[X^+] = \sigma_2[X^+] \times \sigma'[N_2O^+]$$

$$\sigma_2[N^+] = \frac{N_2[N^+]}{N_1[N_2O^+]} = \frac{P[N^+]}{f_i I[N_2O^+]} \quad \text{(F.30),}$$

$$\sigma_2[O^+] = \frac{N_2[O^+]}{N_1[N_2O^+]} = \frac{P[O^+]}{f_i I[N_2O^+]} \quad \text{(F.31),}$$

$$\sigma_2[N_2^+] = \frac{N_2[N_2^+]}{N_1[N_2O^+]} = \frac{P[N_2^+]}{f_i I[N_2O^+]} \quad \text{(F.32)}$$

$$\sigma_2[NO^+] = \frac{N_2[NO^+]}{N_1[N_2O^+]} = \frac{P[NO^+]}{f_i I[N_2O^+]} \quad \text{(F.33).}$$

As detailed in Chapter 3, a value for $f_i$ must be determined to enable the values of $\sigma_n[X^+]$ to be determined, and thus values of $\sigma_n'[X^+]$. A value for the ion detection efficiency is found by recording the singles and pairs spectra following ionization of $CF_4$.

As the determination of the $\sigma_r[X^+]$ and $\sigma_n[X^+]$ values are discussed in detail in Chapter 3, no additional information is presented here. For completeness the relative PICS for the formation of the $N^+$, $O^+$, $N_2^+$ and $NO^+$ fragment ions are expressed below:

$$\sigma_r[N^+] = \frac{N_1[N^+] + N_2[N^+]}{N_1[N_2O^+]} = \frac{I[N^+] + P[N^+]}{I[N_2O^+]} \quad \text{(F.34),}$$

$$\sigma_r[O^+] = \frac{N_1[O^+] + N_2[O^+]}{N_1[N_2O^+]} = \frac{I[O^+] + P[O^+]}{I[N_2O^+]} \quad \text{(F.35),}$$

$$\sigma_r[N_2^+] = \frac{N_1[N_2^+] + N_2[N_2^+]}{N_1[N_2O^+]} = \frac{I[N_2^+] + P[N_2^+]}{I[N_2O^+]} \quad \text{(F.36),}$$

$$\sigma_r[NO^+] = \frac{N_1[NO^+] + N_2[NO^+]}{N_1[N_2O^+]} = \frac{I[NO^+] + P[NO^+]}{I[N_2O^+]} \quad \text{(F.37).}$$

# Appendix G

# Absolute PICS and absolute precursor specific PICS values for electron ionization of $Ar/N_2O$

The values of $\sigma'[N_2O^+]$, $\sigma'[N^+]$, $\sigma'[O^+]$, $\sigma'[N_2^+]$ and $\sigma'[NO^+]$, are shown below. The values of $\sigma_1'[N^+]$, $\sigma_2'[N^+]$, $\sigma_1'[O^+]$, $\sigma_2'[O^+]$, $\sigma_1'[N_2^+]$, $\sigma_2'[N_2^+]$, $\sigma_1'[NO^+]$ and $\sigma_2'[NO^+]$ are also shown. These values were determined as described within the text of Chapter 7, and are shown in Figures 7.2, 7.4, 7.5, 7.6 and 7.7.

Table G.1: Values for $\sigma'[N_2O^+]$, as a function of electron energy *E*. The error in the last figure is shown in parentheses. This error is the standard deviation of four individual cross-section determinations.

| *E*/eV | $\sigma'[N_2O^+]$ ($x10^{-17}cm^2$) |
|---|---|
| 200 | 11.3 (3.0) |
| 150 | 14.2 (4.4) |
| 100 | 12.2 (3.7) |
| 75 | 12.6 (3.4) |
| 70 | 13.8 (4.7) |
| 65 | 12.3 (2.7) |
| 50 | 11.1 (2.9) |
| 40 | 11.7 (2.2) |
| 35 | 10.3 (3.0) |
| 30 | 8.2 (1.5) |

Table G.2: Values for the $\sigma_1'[N^+]$, $\sigma_2'[N^+]$ and $\sigma'[N^+]$, as a function of electron energy *E*. The error in the last figure is shown in parentheses. This error is the standard deviation of four individual cross-section determinations.

| *E*/eV | $\sigma_1'[N^+]$ ($\times 10^{-17}$cm$^2$) | $\sigma_2'[N^+]$ ($\times 10^{-17}$cm$^2$) | $\sigma'[N^+]$ ($\times 10^{-17}$cm$^2$) |
|---|---|---|---|
| 200 | 2.40 (24) | 3.90 (58) | 6.30 (76) |
| 150 | 2.28 (24) | 3.74 (15) | 6.02 (39) |
| 100 | 3.16 (10) | 3.29 (17) | 6.45 (11) |
| 75 | 3.20 (11) | 1.57 (40) | 4.77 (49) |
| 65 | 2.88 (18) | 1.17 (20) | 4.05 (35) |
| 50 | 2.79 (8) | 0.58 (8) | 3.37 (16) |
| 40 | 1.52 (11) | 0.14 (1) | 1.66 (12) |
| 30 | 0.75 (4) | 0.06 (2) | 0.81 (5) |

Table G.3: Values for the $\sigma_1'[O^+]$, $\sigma_2'[O^+]$ and $\sigma'[O^+]$, as a function of electron energy *E*. The error in the last figure is shown in parentheses. This error is the standard deviation of four individual cross-section determinations.

| *E*/eV | $\sigma_1'[O^+]$ ($\times 10^{-17}$cm$^2$) | $\sigma_2'[O^+]$ ($\times 10^{-17}$cm$^2$) | $\sigma'[O^+]$ ($\times 10^{-17}$cm$^2$) |
|---|---|---|---|
| 200 | 1.05 (12) | 1.99 (27) | 3.04 (37) |
| 150 | 1.07 (10) | 1.81 (13) | 2.88 (23) |
| 100 | 1.50 (3) | 1.75 (8) | 3.25 (5) |
| 75 | 1.62 (4) | 0.86 (21) | 2.48 (21) |
| 65 | 1.45 (7) | 0.61 (13) | 2.06 (17) |
| 50 | 1.55 (3) | 0.27 (4) | 1.82 (7) |
| 40 | 0.93 (6) | 0.05 (1) | 0.98 (7) |
| 30 | 0.56 (3) | 0.02 (1) | 0.58 (3) |

Table G.4: Values for the $\sigma_1'[N_2^+]$, $\sigma_2'[N_2^+]$ and $\sigma'[N_2^+]$, as a function of electron energy *E*. The error in the last figure is shown in parentheses. This error is the standard deviation of four individual cross-section determinations.

| *E*/eV | $\sigma_1'[N_2^+]$ ($x10^{-17}cm^2$) | $\sigma_2'[N_2^+]$ ($x10^{-17}cm^2$) | $\sigma'[N_2^+]$ ($x10^{-17}cm^2$) |
|---|---|---|---|
| 200 | 2.57 (40) | 0.77 (10) | 3.34 (49) |
| 150 | 2.39 (17) | 0.75 (4) | 3.14 (19) |
| 100 | 3.01 (7) | 0.84 (3) | 3.85 (10) |
| 75 | 3.08 (12) | 0.55 (9) | 3.63 (20) |
| 65 | 2.78 (10) | 0.43 (8) | 3.21 (15) |
| 50 | 3.17 (12) | 0.21 (3) | 3.38 (13) |
| 40 | 2.14 (15) | 0.03 (1) | 2.17 (16) |
| 30 | 1.39 (13) | 0.01 (1) | 1.40 (13) |

Table G.5: Values for the $\sigma_1'[NO^+]$, $\sigma_2'[NO^+]$ and $\sigma'[NO^+]$, as a function of electron energy *E*. The error in the last figure is shown in parentheses. This error is the standard deviation of four individual cross-section determinations.

| *E*/eV | $\sigma_1'[NO^+]$ ($x10^{-17}cm^2$) | $\sigma_2'[NO^+]$ ($x10^{-17}cm^2$) | $\sigma'[NO^+]$ ($x10^{-17}cm^2$) |
|---|---|---|---|
| 200 | 7.48 (78) | 1.37 (16) | 8.85 (94) |
| 150 | 6.90 (59) | 1.33 (10) | 8.23 (69) |
| 100 | 8.05 (6) | 1.46 (4) | 9.51 (2) |
| 75 | 7.50 (30) | 0.95 (20) | 8.45 (47) |
| 65 | 6.79 (27) | 0.70 (11) | 7.49 (36) |
| 50 | 7.21 (15) | 0.41 (4) | 7.62 (17) |
| 40 | 4.83 (26) | 0.07 (1) | 4.91 (28) |
| 30 | 3.12 (13) | 0.02 (1) | 3.14 (14) |

# Appendix H

## Absolute PICS and absolute precursor specific PICS equations for $C_2H_2$

The processing of the ion intensities recorded in the singles and pairs spectra to yield the relative PICSs, $\sigma_r[X^+]$, and the relative precursor specific PICSs, $\sigma_n[X^+]$, has previously been discussed in detail, see Chapter 3. The ion intensities in the singles and pairs spectra are also used to yield the absolute PICSs, $\sigma'[X^+]$, and absolute precursor specific PICSs, $\sigma_n'[X^+]$, along with the gas pressures of argon and nitrogen, $p_{Ar/N2}$, and acetylene, $p_{C2H2}$, and the literature values of $\sigma'[Ar^+/N_2^+]$. The total ion signal, $S$, for each ion is expressed in Eqs. (H.3)-(H.10), where the ion intensity in the singles spectrum is represented by $I[X^+]$, and the ion signal intensity in the pairs spectrum is represented by $P[X^+]$. In this analysis it is assumed that any contributions from triple ionization are negligible, as discussed within the text of Chapter 7. Eq. (H.1). shows how the absolute PICS for formation of a fragment ion $X^+$ may be determined, using a 'direct' method.

$$\sigma'[X^+] = \frac{S(X^+)}{S(Ar^+)} \times \frac{p_{Ar}}{p_{C_2H_2}} \times \sigma'[Ar^+] \qquad \text{(H.1).}$$

$$\sigma'[X^+] = \frac{S(X^+)}{S(N_2^+)} \times \frac{p_{N_2}}{p_{C_2H_2}} \times \sigma'[N_2^+]$$

Eq. (H.2) shows an example for the parent ion $C_2H_2^+$:

$$\sigma'[C_2H_2^+] = \frac{S(C_2H_2^+)}{S(Ar^+/N_2^+)} \times \frac{p_{Ar/N_2}}{p_{C_2H_2}} \times \sigma'[Ar^+/N_2^+] \qquad \text{(H.2),}$$

$$\sigma'[C_2H_2^+] = \frac{I[C_2H_2^+]}{I[Ar^+/N_2^+]} \times \frac{p_{Ar/N_2}}{p_{C_2H_2}} \times \sigma'[Ar^+/N_2^+]$$

$$S(H^+) = I[H^+] + P[H^+] \qquad \text{(H.3),}$$

$$S(C^+ + C_2^{2+}) = I[C^+ + C_2^{2+}] + P[C^+] \qquad \text{(H.4),}$$

$$S(CH^+ + C_2H_2^{2+}) = I[CH^+ + C_2H_2^{2+}] + P[CH^+] \qquad \text{(H.5),}$$

$$S(C_2^+) = I[C_2^+] + P[C_2^+] \quad \text{(H.6)},$$

$$S(C_2H^+) = I[C_2H^+] + P[C_2H^+] \quad \text{(H.7)},$$

$$S(C_2H_2^+) = I[C_2H_2^+] \quad \text{(H.8)},$$

$$S(Ar^+) = I[Ar^+] \quad \text{(H.9)},$$

$$S(N_2^+) = I[N_2^+] \quad \text{(H.10)}.$$

The intensities of the $H^+$, $C^+ + C_2^{2+}$, $CH^+ + C_2H_2^{2+}$, $C_2^+$ and $C_2H^+$ ions in the singles spectrum $I$ and pairs spectrum $P$ can be described by the following equations:

$$I[H^+] = f_i N_1[H^+] + f_i(1 - f_i) N_2[H^+] \quad \text{(H.11)},$$

$$I[C^+ + C_2^{2+}] = f_i N_{12}[C^+ + C_2^{2+}] + f_i(1 - f_i) N_2[C^+] \quad \text{(H.12)},$$

$$I[CH^+ + C_2H_2^{2+}] = f_i N_{12}[CH^+ + C_2H_2^{2+}] + f_i(1 - f_i) N_2[CH^+] \quad \text{(H.13)},$$

$$I[C_2^+] = f_i N_1[C_2^+] + f_i(1 - f_i) N_2[C_2^+] \quad \text{(H.14)},$$

$$I[C_2H^+] = f_i N_1[C_2H^+] + f_i(1 - f_i) N_2[C_2H^+] \quad \text{(H.15)},$$

$$I[C_2H_2^+] = f_i N_1[C_2H_2^+] \quad \text{(H.16)},$$

$$I[Ar^+] = f_i N_1[Ar^+] \quad \text{(H.17)},$$

$$I[N_2^+] = f_i N_1[N_2^+] \quad \text{(H.18)},$$

$$P[H^+] = f_i^2 N_2[H^+] \quad \text{(H.19)},$$

$$P[C^+] = f_i^2 N_2[C^+] \quad \text{(H.20)},$$

$$P[CH^+] = f_i^2 N_2[CH^+] \quad \text{(H.21)},$$

$$P[C_2^+] = f_i^2 N_2[C_2^+] \quad \text{(H.22)},$$

$$P[C_2H^+] = f_i^2 N_2[C_2H^+] \quad \text{(H.23)}.$$

In the above equations, the experimental ion detection efficiency is denoted by $f_i$ and $N_n[X^+]$ represents the number of $X^+$ ions formed *via* ionizing events involving the loss of $n$ electrons. For example, in Eq. (H.11) the term involving $N_2[X^+]$ represents the contribution to the singles spectrum from dissociative double ionization events forming $X^+$, where the second ion from the dissociative double ionization event is not detected. Such ion losses occur ($f_i$<1) because of the 90% transmission of the grids that define the electric fields in the apparatus, and the less than unit efficiency of the electronics and

detector. As detailed in Chapter 7, the intensity of the $C^+$+$C_2^{2+}$ and $CH^+$+$C_2H_2^{2+}$ ions recorded in the singles spectra can only be analysed as a summation of ion intensities. Therefore, in Eqs. (H.12) and (H.13), $N_{12}[X^+ + X^{2+}]$ represents the number of $X^+$ and $X^{2+}$ ions formed *via* single and double ionization respectively.

Equations showing how the absolute PICSs for the formation of the $H^+$, $C^+$+$C_2^{2+}$, $CH^+$+$C_2H_2^{2+}$, $C_2^+$ and $C_2H^+$ ions are determined are given below:

$$\sigma'[H^+] = \frac{I[H^+] + P[H^+]}{I[Ar^+/N_2^+]} \times \frac{p_{Ar/N_2}}{p_{C_2H_2}} \times \sigma'[Ar^+/N_2^+] \quad \text{(H.24)},$$

$$\sigma'[C^+ + C_2^{2+}] = \frac{I[C^+ + C_2^{2+}] + P[C^+]}{I[Ar^+/N_2^+]} \times \frac{p_{Ar/N_2}}{p_{C_2H_2}} \times \sigma'[Ar^+/N_2^+] \quad \text{(H.25)},$$

$$\sigma'[CH^+ + C_2H_2^{2+}] = \frac{I[CH^+ + C_2H_2^{2+}] + P[CH^+]}{I[Ar^+/N_2^+]} \times \frac{p_{Ar/N_2}}{p_{C_2H_2}} \times \sigma'[Ar^+/N_2^+] \quad \text{(H.26)},$$

$$\sigma'[C_2^+] = \frac{I[C_2^+] + P[C_2^+]}{I[Ar^+/N_2^+]} \times \frac{p_{Ar/N_2}}{p_{C_2H_2}} \times \sigma'[Ar^+/N_2^+] \quad \text{(H.27)},$$

$$\sigma'[C_2H^+] = \frac{I[C_2H^+] + P[C_2H^+]}{I[Ar^+/N_2^+]} \times \frac{p_{Ar/N_2}}{p_{C_2H_2}} \times \sigma'[Ar^+/N_2^+] \quad \text{(H.28)}.$$

As discussed in Chapter 7, there is also an 'indirect' method of determining the absolute PICSs. It should be noted that this 'indirect' technique was not used in the current analysis, but is provided for completeness and is mathematically identical to the 'direct' analysis method. The relative PICSs for each fragment ion formed following electron ionization of $C_2H_2$ are expressed relative to the cross-section for formation of the parent ion $C_2H_2^+$. Therefore, to determine the absolute PICS for formation of a particular fragment ion, the relative PICS is multiplied by the value of $\sigma'[C_2H_2^+]$. This 'indirect' method is shown in Eq. (H.29):

$$\sigma'[X^+] = \sigma_r[X^+] \times \sigma'[C_2H_2^+] \quad \text{(H.29)}.$$

The data analysis can be extended to determine absolute precursor specific PICSs for the $H^+$, $C^+$+$C_2^{2+}$, $CH^+$+$C_2H_2^{2+}$, $C_2^+$ and $C_2H^+$ fragment ions formed *via* single and double ionization. This analysis uses the 'indirect' technique expressed in Eq. (H.29), by replacing $\sigma_r[X^+]$ with $\sigma_n[X^+]$ values (where $n$=1,2). The relative precursor specific PICSs for formation of the fragment ions $H^+$, $C_2^+$ and $C_2H^+$ *via* single ionization are detailed below. The intensities of the $C^+$+$C_2^{2+}$ and $CH^+$+$C_2H_2^{2+}$ ions are expressed in Eq. (H.12) and (H.13). As detailed in Chapter 7, however, the $C^+$ and $CH^+$ ions observed in the singles spectrum are formed *via* single ionization but the $C_2^{2+}$ and

$C_2H_2^{2+}$ dications are formed *via* double ionization, the normal notation $\sigma_1'[C^+ + C_2^{2+}]$ and $\sigma_1'[CH^+ + C_2H_2^{2+}]$ is replaced by $\sigma_{12}'[C^+ + C_2^{2+}]$ and $\sigma_{12}'[CH^+ + C_2H_2^{2+}]$, to clarify that these cross-sections have contributions from both single and double ionization, shown in Eqs. (H.34) and (H.35).

The relative precursor specific PICSs for the formation of the fragment ions *via* single ionization are detailed below. Eqs. (H.31)-(H.33) are then used with Eq. (H.2) to determine absolute precursor specific PICSs for ion formation *via* single ionization, as shown in Eq. (H.30).

$$\sigma_1'[X^+] = \frac{\sigma_1[X^+]}{\sigma_1[C_2H_2^+]} \times \sigma'[C_2H_2^+] \qquad \text{(H.30)},$$

$$\sigma_1'[X^+] = \sigma_1[X^+] \times \sigma'[C_2H_2^+]$$

$$\sigma_1[H^+] = \frac{N_1[H^+]}{N_1[C_2H_2^+]} = \frac{I[H^+] - (1-f_i)/f_i P[H^+]}{I[C_2H_2^+]} \qquad \text{(H.31)},$$

$$\sigma_1[C_2^+] = \frac{N_1[C_2^+]}{N_1[C_2H_2^+]} = \frac{I[C_2^+] - (1-f_i)/f_i P[C_2^+]}{I[C_2H_2^+]} \qquad \text{(H.32)},$$

$$\sigma_1[C_2H^+] = \frac{N_1[C_2H^+]}{N_1[C_2H_2^+]} = \frac{I[C_2H^+] - (1-f_i)/f_i P[C_2H^+]}{I[C_2H_2^+]} \qquad \text{(H.33)}.$$

Eqs.(H.34) and (H.35) represent the contributions from both single and double ionization, necessary because of the intensity summation of the $C^+ + C_2^{2+}$ and $CH^+ + C_2H_2^{2+}$ ions.

$$\sigma_{12}[C^+ + C_2^{2+}] = \frac{N_{12}[C^+ + C_2^{2+}]}{N_1[C_2H_2^+]} \qquad \text{(H.34)},$$

$$= \frac{I[C^+ + C_2^{2+}] - (1-f_i)/f_i P[C^+]}{I[C_2H_2^+]}$$

$$\sigma_{12}[CH^+ + C_2H_2^{2+}] = \frac{N_{12}[CH^+ + C_2H_2^{2+}]}{N_1[C_2H_2^+]} \qquad \text{(H.35)}.$$

$$= \frac{I[CH^+ + C_2H_2^{2+}] - (1-f_i)/f_i P[CH^+]}{I[C_2H_2^+]}$$

The relative precursor specific PICSs for formation of the fragment ions $H^+$, $C^+$, $CH^+$, $C_2^+$ and $C_2H^+$ *via* double ionization are detailed below. Eqs. (H.37)-(H.41) can then be used with Eq. (H.2) to determine absolute precursor specific PICSs for ion formation *via* double ionization.

$$\sigma_2[X^+] = \frac{\sigma_2[X^+]}{\sigma_1[C_2H_2^+]} \times \sigma[C_2H_2^+] \quad \text{(H.36)},$$

$$\sigma_2'[X^+] = \sigma_2[X^+] \times \sigma'[C_2H_2^+]$$

$$\sigma_2[H^+] = \frac{N_2[H^+]}{N_1[C_2H_2^+]} = \frac{P[H^+]}{f_i I[C_2H_2^+]} \quad \text{(H.37)},$$

$$\sigma_2[C^+] = \frac{N_2[C^+]}{N_1[C_2H_2^+]} = \frac{P[C^+]}{f_i I[C_2H_2^+]} \quad \text{(H.38)},$$

$$\sigma_2[CH^+] = \frac{N_2[CH^+]}{N_1[C_2H_2^+]} = \frac{P[CH^+]}{f_i I[C_2H_2^+]} \quad \text{(H.39)},$$

$$\sigma_2[C_2^+] = \frac{N_2[C_2^+]}{N_1[C_2H_2^+]} = \frac{P[C_2^+]}{f_i I[C_2H_2^+]} \quad \text{(H.40)},$$

$$\sigma_2[C_2H^+] = \frac{N_2[C_2H^+]}{N_1[C_2H_2^+]} = \frac{P[C_2H^+]}{f_i I[C_2H_2^+]} \quad \text{(H.41)}.$$

As detailed in Chapter 3, a value for $f_i$ was determined to enable the values of $\sigma_n[X^+]$ to be determined, and thus values of $\sigma_n'[X^+]$. A value for the ion detection efficiency is found by recording the singles and pairs spectra following ionization of $CF_4$.

As the determination of the $\sigma_r[X^+]$ and $\sigma_n[X^+]$ values are discussed in detail in Chapter 3, no additional information is presented here. For completeness the relative PICSs for the formation of the $H^+$, $C^+ + C_2^{2+}$, $CH^+ + C_2H_2^{2+}$, $C_2^+$ and $C_2H^+$ fragment ions are expressed below:

$$\sigma_r[H^+] = \frac{N_1[H^+] + N_2[H^+]}{N_1[C_2H_2^+]} = \frac{I[H^+] + P[H^+]}{I[C_2H_2^+]} \quad \text{(H.42)},$$

$$\sigma_r[C^+ + C_2^{2+}] = \frac{N_1[C^+] + N_2[C_2^{2+}] + N_2[C^+]}{N_1[C_2H_2^+]} = \frac{I[C^+ + C_2^{2+}] + P[C^+]}{I[C_2H_2^+]} \quad \text{(H.43)},$$

$$\sigma_r[CH^+ + C_2H_2^{2+}] = \frac{N_1[CH^+] + N_2[C_2H_2^{2+}] + N_2[CH^+]}{N_1[C_2H_2^+]} \quad \text{(H.44)},$$

$$= \frac{I[CH^+ + C_2H_2^{2+}] + P[C^+]}{I[C_2H_2^+]}$$

$$\sigma_r[C_2^+] = \frac{N_1[C_2^+] + N_2[C_2^+]}{N_1[C_2H_2^+]} = \frac{I[C_2^+] + P[C_2^+]}{I[C_2H_2^+]} \quad \text{(H.45)},$$

$$\sigma_r[C_2H^+] = \frac{N_1[C_2H^+] + N_2[C_2H^+]}{N_1[C_2H_2^+]} = \frac{I[C_2H^+] + P[C_2H^+]}{I[C_2H_2^+]} \quad \text{(H.46)}.$$

# Appendix I

# Absolute PICS and absolute precursor specific PICS determinations for both the $Ar/C_2H_2$ and $N2/C_2H_2$ systems

The values of $\sigma'[C_2H^+]$, $\sigma'[C_2^+]$, $\sigma'[CH^+ + C_2H_2^{2+}]$, $\sigma'[C^+ + C_2^{2+}]$ and $\sigma'[H^+]$, are shown below, for each two-gas system $Ar/C_2H_2$ and $N_2/C_2H_2$. The values of $\sigma_1'[C_2H^+]$, $\sigma_2'[C_2H^+]$, $\sigma_1'[C_2^+]$, $\sigma_2'[C_2^+]$, $\sigma_{12}'[CH^+ + C_2H_2^{2+}]$, $\sigma_2'[CH^+]$, $\sigma_{12}'[C^+ + C_2^{2+}]$, $\sigma_2'[C^+]$, $\sigma_1'[H^+]$ and $\sigma_2'[H^+]$ are also shown. These values were determined as described within the text of Chapter 7, and are shown in Figures 7.11, 7.12, 7.13, 7.14 and 7.15.

Table I.1: Values for the $\sigma_1'[C_2H^+]$, $\sigma_2'[C_2H^+]$ and $\sigma'[C_2H^+]$, as a function of electron energy $E$, for each two-gas system. The error in the last figure is shown in parentheses. This error is the standard deviation of four individual cross-section determinations.

| $Ar/C_2H_2$ system | | | |
|---|---|---|---|
| $E$/eV | $\sigma_1'[C_2H^+]$ ($x10^{-17}cm^2$) | $\sigma_2'[C_2H^+]$ ($x10^{-17}cm^2$) | $\sigma'[C_2H^+]$ ($x10^{-17}cm^2$) |
| 200 | 6.02 (41) | 0.53 (5) | 6.55 (45) |
| 150 | 6.01 (24) | 0.58 (4) | 6.59 (26) |
| 100 | 7.54 (79) | 0.71 (12) | 8.25 (88) |
| 75 | 7.47 (48) | 0.69 (8) | 8.16 (53) |
| 65 | 6.73 (41) | 0.48 (4) | 7.21 (43) |
| 50 | 7.54 (99) | 0.28 (9) | 7.82 (101) |
| 40 | 6.37 (42) | 0.08 (1) | 6.45 (42) |
| 30 | 4.86 (45) | 0.02 (2) | 4.88 (45) |

| $N_2/C_2H_2$ system | | | |
|---|---|---|---|
| $E$/eV | $\sigma_1'[C_2H^+]$ ($x10^{-17}cm^2$) | $\sigma_2'[C_2H^+]$ ($x10^{-17}cm^2$) | $\sigma'[C_2H^+]$ ($x10^{-17}cm^2$) |
| 200 | 5.32 (49) | 0.47 (5) | 5.79 (54) |
| 150 | 5.69 (48) | 0.53 (6) | 6.22 (31) |
| 100 | 7.15 (29) | 0.70 (5) | 7.85 (33) |
| 75 | 6.87 (57) | 0.56 (6) | 7.43 (62) |
| 65 | 6.56 (76) | 0.50 (8) | 7.06 (80) |
| 50 | 6.91 (66) | 0.28 (11) | 7.19 (66) |
| 40 | 6.95 (51) | 0.08 (1) | 7.03 (52) |
| 30 | 4.87 (68) | 0.02 (2) | 4.89 (68) |

Table I.2: Values for the $\sigma_1'[C_2^+]$, $\sigma_2'[C_2^+]$ and $\sigma'[C_2^+]$, as a function of electron energy *E*, for each two-gas system. The error in the last figure is shown in parentheses. This error is the standard deviation of four individual cross-section determinations.

| $Ar/C_2H_2$ system | | | |
|---|---|---|---|
| *E*/eV | $\sigma_1'[C_2^+]$ ($x10^{-17}cm^2$) | $\sigma_2'[C_2^+]$ ($x10^{-17}cm^2$) | $\sigma'[C_2^+]$ ($x10^{-17}cm^2$) |
| 200 | 1.55 (12) | 0.28 (2) | 1.83 (14) |
| 150 | 1.69 (6) | 0.32 (2) | 2.01 (7) |
| 100 | 2.24 (23) | 0.34 (4) | 2.58 (27) |
| 75 | 2.32 (12) | 0.29 (4) | 2.61 (16) |
| 65 | 2.10 (13) | 0.18 (4) | 2.28 (14) |
| 50 | 2.29 (31) | 0.07 (4) | 2.36 (31) |
| 40 | 1.83 (11) | 0.01 (1) | 1.84 (11) |
| 30 | 1.29 (13) | 0.01 (1) | 1.30 (14) |

| $N_2/C_2H_2$ system | | | |
|---|---|---|---|
| *E*/eV | $\sigma_1'[C_2^+]$ ($x10^{-17}cm^2$) | $\sigma_2'[C_2^+]$ ($x10^{-17}cm^2$) | $\sigma'[C_2^+]$ ($x10^{-17}cm^2$) |
| 200 | 1.40 (12) | 0.26 (3) | 1.66 (14) |
| 150 | 1.62 (15) | 0.30 (3) | 1.92 (12) |
| 100 | 2.16 (12) | 0.35 (4) | 2.51 (15) |
| 75 | 2.15 (17) | 0.21 (3) | 2.36 (19) |
| 65 | 2.06 (25) | 0.19 (5) | 2.25 (23) |
| 50 | 2.09 (19) | 0.06 (3) | 2.15 (19) |
| 40 | 2.01 (14) | 0.01 (1) | 2.02 (14) |
| 30 | 1.30 (16) | 0.01 (1) | 1.31 (16) |

Table I.3: Values for the $\sigma_{12}'[CH^+ + C_2H_2^{2+}]$, $\sigma_2'[CH^+]$ and $\sigma'[CH^+ + C_2H_2^{2+}]$, as a function of electron energy $E$, for each two-gas system. The error in the last figure is shown in parentheses. This error is the standard deviation of four individual cross-section determinations.

| $Ar/C_2H_2$ system | | | |
|---|---|---|---|
| $E$/eV | $\sigma_{12}'[CH^+ + C_2H_2^{2+}]$ ($x10^{-17}cm^2$) | $\sigma_2'[CH^+]$ ($x10^{-17}cm^2$) | $\sigma'[CH^+ + C_2H_2^{2+}]$ ($x10^{-17}cm^2$) |
| 200 | 2.14 (13) | 0.68 (5) | 2.82 (18) |
| 150 | 2.35 (11) | 0.76 (7) | 3.11 (16) |
| 100 | 2.98 (26) | 0.92 (17) | 3.90 (41) |
| 75 | 3.03 (19) | 0.78 (6) | 3.81 (24) |
| 65 | 2.70 (16) | 0.51 (7) | 3.21 (20) |
| 50 | 2.68 (36) | 0.23 (8) | 2.91 (40) |
| 40 | 1.90 (12) | 0.05 (1) | 1.95 (13) |
| 30 | 1.12 (13) | 0.01 (1) | 1.13 (14) |

| $N_2/C_2H_2$ system | | | |
|---|---|---|---|
| $E$/eV | $\sigma_{12}'[CH^+ + C_2H_2^{2+}]$ ($x10^{-17}cm^2$) | $\sigma_2'[CH^+]$ ($x10^{-17}cm^2$) | $\sigma'[CH^+ + C_2H_2^{2+}]$ ($x10^{-17}cm^2$) |
| 200 | 1.91 (16) | 0.67 (10) | 2.58 (25) |
| 150 | 2.12 (14) | 0.76 (8) | 2.88 (16) |
| 100 | 2.90 (7) | 0.92 (11) | 3.82 (16) |
| 75 | 2.81 (22) | 0.65 (11) | 3.46 (30) |
| 65 | 2.64 (26) | 0.58 (12) | 3.22 (32) |
| 50 | 2.40 (20) | 0.27 (13) | 2.67 (29) |
| 40 | 2.01 (15) | 0.07 (1) | 2.08 (16) |
| 30 | 1.08 (15) | 0.02 (2) | 1.10 (15) |

Table I.4: Values for the $\sigma_{12}'[C^+ + C_2^{2+}]$, $\sigma_2'[C^+]$ and $\sigma'[C^+ + C_2^{2+}]$, as a function of electron energy $E$, for each two-gas system. The error in the last figure is shown in parentheses. This error is the standard deviation of four individual cross-section determinations.

| $Ar/C_2H_2$ system | | | |
|---|---|---|---|
| $E$/eV | $\sigma_{12}'[C^+ + C_2^{2+}]$ ($x10^{-17}cm^2$) | $\sigma_2'[C^+]$ ($x10^{-17}cm^2$) | $\sigma'[C^+ + C_2^{2+}]$ ($x10^{-17}cm^2$) |
| 200 | 1.28 (10) | 0.51 (4) | 1.79 (13) |
| 150 | 1.40 (4) | 0.56 (3) | 1.96 (7) |
| 100 | 1.82 (20) | 0.57 (11) | 2.39 (30) |
| 75 | 1.73 (8) | 0.43 (4) | 2.16 (12) |
| 65 | 1.47 (9) | 0.20 (5) | 1.67 (14) |
| 50 | 1.31 (17) | 0.05 (4) | 1.36 (19) |
| 40 | 0.82 (6) | 0.01 (1) | 0.83 (6) |
| 30 | 0.35 (5) | 0.01 (1) | 0.36 (5) |

| $N_2/C_2H_2$ system | | | |
|---|---|---|---|
| $E$/eV | $\sigma_{12}'[C^+ + C_2^{2+}]$ ($x10^{-17}cm^2$) | $\sigma_2'[C^+]$ ($x10^{-17}cm^2$) | $\sigma'[C^+ + C_2^{2+}]$ ($x10^{-17}cm^2$) |
| 200 | 1.16 (11) | 0.46 (6) | 1.62 (17) |
| 150 | 1.31 (13) | 0.52 (4) | 1.83 (11) |
| 100 | 1.70 (6) | 0.57 (6) | 2.27 (11) |
| 75 | 1.59 (14) | 0.28 (7) | 1.87 (20) |
| 65 | 1.45 (14) | 0.25 (7) | 1.70 (19) |
| 50 | 1.17 (14) | 0.08 (4) | 1.25 (17) |
| 40 | 0.86 (7) | 0.02 (1) | 0.88 (8) |
| 30 | 0.36 (5) | 0.01 (1) | 0.37 (5) |

Table I.5: Values for the $\sigma_1'[H^+]$, $\sigma_2'[H^+]$ and $\sigma'[H^+]$, as a function of electron energy $E$, for each two-gas system. The error in the last figure is shown in parentheses. This error is the standard deviation of four individual cross-section determinations.

| $Ar/C_2H_2$ system | | | |
|---|---|---|---|
| $E$/eV | $\sigma_1'[H^+]$ ($x10^{-17}cm^2$) | $\sigma_2'[H^+]$ ($x10^{-17}cm^2$) | $\sigma'[H^+]$ ($x10^{-17}cm^2$) |
| 200 | 1.48 (10) | 1.20 (11) | 2.68 (20) |
| 150 | 1.65 (3) | 1.32 (7) | 2.97 (10) |
| 100 | 2.02 (20) | 1.49 (26) | 3.51 (43) |
| 75 | 2.17 (11) | 1.28 (14) | 3.45 (20) |
| 65 | 1.91 (15) | 0.79 (14) | 2.70 (25) |
| 50 | 1.79 (28) | 0.31 (3) | 2.10 (30) |
| 40 | 1.17 (9) | 0.09 (1) | 1.26 (9) |
| 30 | 0.57 (8) | 0.02 (2) | 0.59 (9) |

| $N_2/C_2H_2$ system | | | |
|---|---|---|---|
| $E$/eV | $\sigma_1'[H^+]$ ($x10^{-17}cm^2$) | $\sigma_2'[H^+]$ ($x10^{-17}cm^2$) | $\sigma'[H^+]$ ($x10^{-17}cm^2$) |
| 200 | 1.31 (14) | 1.08 (9) | 2.39 (22) |
| 150 | 1.52 (10) | 1.23 (12) | 2.75 (21) |
| 100 | 1.97 (6) | 1.47 (12) | 3.44 (17) |
| 75 | 1.91 (18) | 0.97 (12) | 2.88 (30) |
| 65 | 1.78 (18) | 0.86 (19) | 2.64 (26) |
| 50 | 1.64 (17) | 0.38 (16) | 2.02 (30) |
| 40 | 1.22 (12) | 0.09 (1) | 1.31 (13) |
| 30 | 0.57 (8) | 0.03 (2) | 0.60 (9) |